

SYNTHETIC INFLOW BOUNDARY CONDITIONS FOR THE NUMERICAL SIMULATION OF TURBULENCE

A THESIS SUBMITTED TO THE UNIVERSITY OF MANCHESTER
FOR THE DEGREE OF DOCTOR OF PHILOSOPHY
IN THE FACULTY OF ENGINEERING AND PHYSICAL SCIENCES

2008

Nicolas Jarrin

School of Mechanical, Aerospace and Civil Engineering
The University of Manchester
Manchester M60 1QD, United Kingdom

Contents

List of Figures	5
List of Tables	17
Abstract	21
Declaration	23
Copyright	25
Acknowledgements	27
Nomenclature	29
1 Introduction	33
1.1 Motivation	33
1.2 Objectives	34
1.3 Outline of the Thesis	36
2 Turbulence Modelling	37
2.1 Introduction to Turbulence Theory	37
2.1.1 The origin of turbulence	37
2.1.2 Spectral range in isotropic turbulence	38
2.1.3 Wall turbulence	40
2.2 Numerical Simulation of Turbulence	43
2.2.1 Direct Numerical Simulation (DNS)	43
2.2.2 Large-Eddy Simulation (LES)	45
2.2.3 Reynolds Averaged Navier-Stokes (RANS)	48
2.2.4 Hybrid RANS-LES	51
3 Generation of Inflow Boundary Conditions for LES and DNS	53
3.1 Introduction	53
3.2 Recycling Methods	54
3.3 Synthetic Turbulence	58

3.3.1	Algebraic methods	59
3.3.2	Spectral methods	62
3.3.3	Mixed methods	66
3.4	Forcing Techniques	68
4	The Synthetic Eddy Method	69
4.1	Introduction	69
4.2	Basic Equations of the Synthetic Eddy Method	70
4.3	Derivation of Exact Results	72
4.3.1	A stationary ergodic process	72
4.3.2	Mean flow and Reynolds stresses	73
4.3.3	Two-point and two-time correlations	75
4.3.4	Probability density function and higher order statistics	78
4.4	Simulation of Instantaneous Signals	80
5	Computational Techniques	91
5.1	Introduction	91
5.2	Governing Equations	91
5.3	Numerical Method	94
5.3.1	Time discretization	94
5.3.2	Space discretization	95
5.3.3	Boundary Conditions	98
6	Periodic Channel Flow Computations	101
6.1	Introduction	101
6.2	Simulations Performed	101
6.3	Tests of Mesh Refinement	102
6.4	Meshing Strategy	108
6.5	Concluding Remarks	115
7	Synthetic Inlet Conditions for Spatially Developing Channel Flow Computations	119
7.1	Introduction	119
7.2	Synthetized Turbulence with a Modified SEM	120
7.2.1	Description of the modified SEM	120
7.2.2	Validation of the modified SEM	121
7.3	Spatially Developing Channel Flow Simulation with Optimal SEM Input Parameters	126
7.4	Sensitivity Analysis of the SEM to its Input Parameters	131

7.4.1	Influence of the prescribed mean velocity profile	135
7.4.2	Influence of the prescribed Reynolds stress tensor	137
7.4.3	Influence of the prescribed length and time scales	144
7.5	Concluding Remarks	150
8	Interface Conditions for RANS-to-LES Coupling of Simple Wall Flows	155
8.1	Introduction	155
8.2	SEM Parametrization for RANS-to-LES Coupling	156
8.2.1	Physical parameters	156
8.2.2	Numerical parameters	157
8.3	Channel Flow Results	161
8.3.1	Presentation of the case	161
8.3.2	Influence of the Reynolds number	162
8.3.3	Comparisons of methods of generation of inlet conditions for LES	169
8.4	Boundary Layer Flow Results	178
8.4.1	Presentation of the case	178
8.4.2	Results and discussion	181
8.5	Duct Flow Results	186
8.5.1	Presentation of the case	186
8.5.2	Results and discussion	189
8.6	Concluding Remarks	199
9	Interface Conditions for RANS-to-LES Coupling of Wall Flows with Recirculation	201
9.1	Introduction	201
9.2	Flow Over a Backward Facing Step	202
9.2.1	Presentation of the case	202
9.2.2	Results and discussions	206
9.3	Flow Over an Airfoil Trailing Edge	217
9.3.1	Presentation of the case	217
9.3.2	Results and discussions	223
9.4	Concluding Remarks	237
10	Conclusions and Future Directions	243
10.1	Conclusions	243
10.2	Future Directions	245

List of Figures

1.1	Sketch of the typical RANS and LES regions in the simulation of the flow over a two-element airfoil. LES fluctuations need to be reconstructed explicitly at the interface between the RANS and the LES region.	35
2.1	Instability of an axisymmetric jet. A laminar stream of air flows from a cylindrical tube at $Re = 10,000$ and is made visible by a smoke wire. The edge of the jet develops axisymmetric oscillations, rolls up into vortex rings, and then abruptly becomes turbulent. Taken from Van Dyke (1982).	38
2.2	Growth of a mixing layer at (a) a moderate and at (b) a higher Reynolds number. Large scale structures are not affected by the Reynolds number whereas more small scale structures can be observed in the higher Reynolds number case. Taken from Van Dyke (1982)	40
2.3	Sketch of the near-wall coherent structures responsible for the production of turbulence in wall-bounded flows.	43
3.1	Sketch of a LES using a precursor simulation dedicated to the generation of the inflow data.	55
3.2	Sketch of the rescaling/recycling method of Lund et al. (1998) to generate inlet conditions for a zero pressure gradient boundary layer.	56
4.1	Set of points $S = \{\mathbf{x}_1, \mathbf{x}_2, \dots, \mathbf{x}_s\}$ on which the SEM signal is going to be computed and the surrounding box of eddies B	70
4.2	128 \times 128 two-dimensional grid, box of eddies and initial population of eddies. Simulation of isotropic turbulence with the SEM.	81
4.3	Time history and velocity field of u , v and w from top to bottom. Simulation of isotropic turbulence with the SEM.	82

4.4 Time history of time averaged u_i (top left), $u'_i u'_j$ (top right), skewness (bottom left) and flatness (bottom right) at point $(x, y) = (\pi, \pi)$. Simulation of isotropic turbulence with the SEM.	83
4.5 Two-point correlations (top) and one dimensional energy spectra (bottom) in the y direction for the velocity components of the simulated SEM signal: dashed lines represent the expected values as calculated in the previous section.	85
4.6 Simulation of isotropic turbulence with the SEM using different number of eddies. From top to bottom: $N = 10,000$, $N = 1,000$, $N = 100$ and $N = 10$; From left to right: Time history of v , probability density function of v and instantaneous contours of w	87
4.7 Simulation of isotropic turbulence with the SEM using different shape functions. From top to bottom: f is a tent function, a step function and a truncated gaussian function; From left to right: Shape function f , one-dimensional energy spectrum of v in the y -direction and instantaneous contours of w	88
4.8 Simulation of isotropic turbulence with the SEM using different values of σ . From top to bottom: $\sigma = 0.25m$ (DIT G), $\sigma = 0.5m$ (DIT A) and $\sigma = 1m$ (DIT H); From left to right: Time history of v , probability density function of v and instantaneous contours of w	89
5.1 Notations for the spatial discretization of an internal face. For clarity, the representation is two-dimensional even though <i>Code_Saturne</i> is three-dimensional.	95
5.2 Notations for the spatial discretization of a boundary face. For clarity, the representation is two-dimensional even though <i>Code_Saturne</i> is three-dimensional.	99
6.1 Sketch of a channel flow and the coordinate system adopted.	102
6.2 Periodic channel flow simulations at $Re_\tau = 395$. Profiles of the mean streamwise velocity. .	104
6.3 Periodic channel flow simulations at $Re_\tau = 395$. Profiles of (a) the turbulent kinetic energy k and the three normal Reynolds stresses (b) $\langle u'^2 \rangle$, (c) $\langle v'^2 \rangle$ and (d) $\langle w'^2 \rangle$	105
6.4 Two-point correlations of the wall-normal velocity fluctuations at $y^+ = 5$ in channel flow at $Re_\tau = 395$. Streamwise separations (left), and spanwise separations (right).	106
6.5 Integral length scale of the wall-normal velocity in the streamwise (left) and in the spanwise (right) directions in channel flow $Re_\tau = 395$	107
6.6 Streamwise velocity fluctuations on a plane parallel to the wall at $y^+ = 15$ in channel flow $Re_\tau = 395$: (a) run A; (b) run B; (c) run C; (d) run D and (e) run E.	109
6.7 Isosurfaces of $Q = 250$ (u_τ/δ) 2 in channel flow $Re_\tau = 395$: (a) run A; (b) run B; (c) run C; (d) run D and (e) run E.	110

6.8	Periodic channel flow simulations at different Reynolds numbers Re_τ . Profiles of the mean velocity for runs F, G, H and I. Individual profiles are separated with a vertical offset of 4.	112
6.9	Periodic channel flow simulations at different Reynolds numbers Re_τ . Profiles of (a) the turbulent kinetic energy k , (b) $\langle u'^2 \rangle$, (c) $\langle v'^2 \rangle$, (d) $\langle w'^2 \rangle$ and (e) $\langle u'v' \rangle$	113
6.10	Periodic channel flow simulations at different Reynolds numbers Re_τ . Two-point correlations of the three velocity components in the spanwise direction at $y^+ = 5$. Spanwise separation distance z is normalized by δ on the left and by $\delta_v = v/u_\tau$ on the right. Correlations of (a) the streamwise fluctuations, (b) the wall-normal fluctuations and (c) the spanwise fluctuations.	114
6.11	Periodic channel flow simulations at different Reynolds numbers Re_τ . Integral lengthscale in the spanwise direction for the three velocity components. Lengthscales are normalized by δ_v on the left handside and by δ on the right handside. Integral spanwise lengthscale (a) of the streamwise velocity fluctuations, (b) wall-normal velocity fluctuations and (c) spanwise velocity fluctuations. Symbols represent reference DNS data at $Re_\tau = 395$. Thin dashed line represents the mixing length $L = \kappa y$	116
7.1	Profiles of the mean streamwise velocity of the modified SEM signal and the reference periodic LES.	121
7.2	Profiles of the Reynolds stresses of the modified SEM signal and the reference periodic LES.	122
7.3	Profiles of the integral length scales of the three velocity components of the modified SEM signal and the reference periodic LES.	123
7.4	Profiles of the integral time scales of the three velocity components of the modified SEM signal and the reference periodic LES	124
7.5	Two-point v correlations in the spanwise direction for the modified SEM signal and the reference periodic LES	124
7.6	One-dimensional spanwise energy spectra of the wall-normal fluctuations for the modified SEM signal and the reference periodic LES	125
7.7	Instantaneous streamwise velocity contours (left) and velocity vectors (right) of (a) the modified SEM signal and (b) the periodic LES signal. Streamwise velocity contours are evenly spaced at 0, 2, 4, ..., 22. Velocity vectors are projected onto the (Ozy) plane.	126
7.8	Downstream development of the coefficient of friction C_f	127

7.9	Downstream development of the error in the Reynolds stresses.	127
7.10	Downstream development of the error in the Reynolds shear stress profile in the inner and outer layer.	129
7.11	Spatially developing channel flow at $Re_\tau = 395$. Profiles of the Reynolds stresses at various streamwise locations.	130
7.12	Spatially developing channel flow at $Re_\tau = 395$. One-dimensional spanwise energy spectra (a) E_{uu} , (b) E_{vv} and (c) E_{ww} at various streamwise locations at $y^+ = 5$ (left) and at $y/\delta = 1$ (right): Lines represent spatially developing simulation with the SEM at different locations; $\circ\circ\circ$ represent reference periodic LES.	132
7.13	Spatially developing channel flow at $Re_\tau = 395$. Streamwise velocity fluctuations at different y locations. (a) Plane $y^+ = 5$, (b) plane $y^+ = 100$ and (c) plane $y/\delta = 1$. Velocity planes at the same y location for the periodic LES (run G) are provided for comparisons. Contour lines are evenly spaced at $\pm 0.5, \pm 1.5, \pm 2.5, \pm 3.5$ and ± 4.5 for the planes at $y/\delta = 1$ and at $\pm 2, \pm 3, \pm 4, \pm 5$ and ± 6 for the planes at $y^+ = 5$ and $y^+ = 100$. Grey lines indicate negative value contours.	133
7.14	Spanwise velocity fluctuations on a plane of constant in the spatially developing (top) and in the periodic LES (bottom) of channel flow at $Re_\tau = 395$. Contour lines are evenly spaced at $\pm 0.5, \pm 1.5, \pm 2.5, \pm 3.5$ and ± 4.5 . Grey lines indicate negative value contours.	134
7.15	Instantaneous isosurfaces of $Q = 250 (u_\tau^2/\delta)^2$ in the lower half of the channel in the spatially developing (top) and in the periodic LES (bottom) case.	134
7.16	Comparisons of different prescribed inlet velocity profiles.	136
7.17	Downstream development of (a) the coefficient of friction and (b) the error in the turbulent kinetic energy profile for the modified SEM inlet conditions with different prescribed mean velocity profiles.	136
7.18	Profiles of (a) mean velocity and (b) turbulent kinetic energy. Modified SEM inflow with a different inflow mean velocity profile, run UL25.	137
7.19	Production of Reynolds shear stress $P_{\langle u'v' \rangle}$. Modified SEM inflow: (a) run UL25 and (b) reference simulation with the exact mean inflow velocity profile. Contour lines are evenly spaced at $\pm 4, \pm 8, \pm 12, \pm 16$ and ± 20 . Grey lines indicate negative value contours.	138
7.20	Downstream development of (a) the coefficient of friction and the errors in (b) the turbulent kinetic energy, and (c) the Reynolds shear stress profiles.	139

7.21 Downstream development of the error in the turbulent kinetic energy profile: (a) integration of the error for $y^+ < 50$ and (b) integration of the error for $y/\delta > 0.5$. Same legend as in Fig. 7.20.	140
7.22 Downstream development of (a) the coefficient of friction and the errors in (b) the turbulent kinetic energy, and (c) the Reynolds shear stress profiles.	142
7.23 Downstream development of the error (integrated for $y^+ < 50$) in (a) the wall-normal fluctuations and in (b) the Reynolds shear stress profiles. Same legend as in Fig. 7.22. . .	143
7.24 Downstream development of (a) the coefficient of friction and the errors in (b) the turbulent kinetic energy, and (c) the Reynolds shear stress profiles.	145
7.25 Downstream development of the error in the Reynolds shear stress profile: (a) integration of the error for $y^+ < 50$ and (b) integration of the error for $y/\delta > 0.5$. Same legend as in Fig. 7.24.	146
7.26 Contours of streamwise velocity fluctuations u^+ at $y^+ = 5$: Modified SEM with (a) -75% , (b) exact, and (c) $+100\%$ of optimal inflow length scale. Contour lines are evenly spaced at $\pm 2, \pm 3, \pm 4, \pm 5$ and ± 6 . Grey lines indicate negative value contours.	147
7.27 Contours of spanwise velocity fluctuations u^+ at $y/\delta = 1$: Modified SEM with (a) -75% , (b) exact, and (c) $+100\%$ of optimal inflow length scale. Contour lines are evenly spaced at $\pm 0.5, \pm 1.5, \pm 2.5, \pm 3.5$ and ± 4.5 . Grey lines indicate negative value contours.	147
7.28 Contours of streamwise velocity fluctuations u^+ at $y/\delta = 1$: Modified SEM with (a) -75% , (b) exact, and (c) $+100\%$ of optimal inflow length scale. Contour lines are evenly spaced at $\pm 0.5, \pm 1.5, \pm 2.5, \pm 3.5$ and ± 4.5 . Grey lines indicate negative value contours.	148
7.29 Downstream development of (a) the coefficient of friction and the errors in (b) the turbulent kinetic energy, and (c) the Reynolds shear stress profiles.	149
7.30 Downstream development of (a) the coefficient of friction and the errors in (b) the turbulent kinetic energy, and (c) the Reynolds shear stress profiles.	151
7.31 Contours of streamwise velocity fluctuations u^+ at $y^+ = 5$: Modified SEM with (a) -75% , (b) exact, and (c) $+100\%$ of optimal inflow length and time scales. Contour lines are evenly spaced at $\pm 2, \pm 3, \pm 4, \pm 5$ and ± 6 . Grey lines indicate negative value contours.	152
7.32 Contours of streamwise velocity fluctuations u^+ at $y/\delta = 1$: Modified SEM with (a) -75% , (b) exact, and (c) $+100\%$ of optimal inflow length and time scales. Contour lines are evenly spaced at $\pm 2, \pm 3, \pm 4, \pm 5$ and ± 6 . Grey lines indicate negative value contours.	152

8.1	Downstream development of the coefficient of friction for different number of eddies. . .	158
8.2	Downstream development of the flatness of the wall-normal fluctuations at $y^+ = 5$. Modified SEM with optimal parameters and different number of eddies. Same legend as in Fig. 8.1.	158
8.3	Contours of streamwise velocity fluctuations u^+ at $y^+ = 5$: Modified SEM with (a) $N = 50$, (b) $N = 1,000$ and (c) $N = 100,000$. Contour lines are evenly spaced at $\pm 2, \pm 3, \pm 4, \pm 5$ and ± 6 . Grey lines indicate negative value contours.	159
8.4	Downstream development of the coefficient of friction for different number of eddies. . .	160
8.5	Contours of streamwise velocity fluctuations u^+ at $y^+ = 5$: Modified SEM with (a) tent function, and (b) truncated Gaussian function. Contour lines are evenly spaced at $\pm 2, \pm 3, \pm 4, \pm 5$ and ± 6 . Grey lines indicate negative value contours.	160
8.6	Sketch of the hybrid RANS/LES channel flows configuration.	161
8.7	SEM turbulent kinetic energy and Reynolds shear stress profiles extracted from the SST simulation of plane channel flow at $Re_\tau = 395$, $Re_\tau = 590$ and $Re_\tau = 950$	164
8.8	SEM input length and time scales extracted from the SST simulation of plane channel flow at $Re_\tau = 395$, $Re_\tau = 590$ and $Re_\tau = 950$	165
8.9	Channel flow at $Re_\tau = 395$ (\triangle), $Re_\tau = 590$ (\circ) and $Re_\tau = 950$ (\square). Downstream development of the error in the turbulent kinetic energy profiles for $y^+ < 50$ as a function of (a) x/δ and (b) x^+	166
8.10	Channel flow at $Re_\tau = 395$ (\triangle), $Re_\tau = 590$ (\circ) and $Re_\tau = 950$ (\square). Downstream development of the error in the Reynolds shear stress profiles for $y^+ < 50$ as a function of (a) x/δ and (b) x^+	166
8.11	Channel flow at $Re_\tau = 395$ (\triangle), $Re_\tau = 590$ (\circ) and $Re_\tau = 950$ (\square). Downstream development of $C_f/C_{f,ref}$ as a function of (a) y/δ and (b) y^+ . $C_{f,ref}$ denotes the friction coefficient of the periodic LES simulation at the corresponding Reynolds number.	167
8.12	Channel flow at $Re_\tau = 395$ (\triangle), $Re_\tau = 590$ (\circ) and $Re_\tau = 950$ (\square). Downstream development of the error in the turbulent kinetic energy profiles (a) for $y^+ < 50$ and (b) for $y/\delta > 0.5$	168
8.13	Channel flow at $Re_\tau = 395$ (\triangle), $Re_\tau = 590$ (\circ) and $Re_\tau = 950$ (\square). Downstream development of the error in the Reynolds shear stress profiles (a) for $y^+ < 50$ and (b) for $y/\delta > 0.5$	168

8.14 Channel flows at (a) $Re_\tau = 395$, (b) $Re_\tau = 590$ and (c) $Re_\tau = 950$. Contours of streamwise velocity fluctuations u^+ at $y^+ = 5$. Contour lines are evenly spaced at $\pm 2, \pm 3, \pm 4, \pm 5$ and ± 6 . Grey lines indicate negative value contours.	169
8.15 Channel flows at (a) $Re_\tau = 395$, (b) $Re_\tau = 590$ and (c) $Re_\tau = 950$. Contours of spanwise velocity fluctuations w^+ on a plane of constant z . Contour lines are evenly spaced at $\pm 0.5, \pm 1.5, \pm 2.5, \pm 3.5$ and ± 4.5 . Grey lines indicate negative value contours.	170
8.16 Inlet conditions for hybrid RANS-LES simulation. Streamwise velocity contours (left) and velocity vectors (right) for (a) run P1, (b) S1, (c) B1, and (d) R1.	171
8.17 Two-point correlations $R_{vv}(y_1, y_2, \Delta z)$ of the wall-normal velocity fluctuations at $y_1/\delta = 0.25$ as a function of wall-normal distance y_2/δ (left), and as a function of spanwise separation Δz (right).	172
8.18 Hybrid RANS-LES simulation of channel flow at $Re_\tau = 395$. Downstream development of the coefficient of friction.	173
8.19 Hybrid RANS-LES simulation of channel flow at $Re_\tau = 395$. Profiles of the mean velocity at various streamwise locations.	174
8.20 Hybrid RANS-LES simulation of channel flow at $Re_\tau = 395$. Profiles of the turbulent kinetic energy at various streamwise locations.	175
8.21 Hybrid RANS-LES simulation of channel flow at $Re_\tau = 395$. Profiles of the Reynolds shear stress at various streamwise locations.	176
8.22 Hybrid RANS-LES simulation of channel flow at $Re_\tau = 395$. Contours of the instantaneous streamwise velocity fluctuations u^+ at $y^+ = 5$	177
8.23 Hybrid RANS-LES simulation of channel flow at $Re_\tau = 395$. Contours of spanwise velocity fluctuations w^+ on a plane of constant z : (a) precursor simulation inlet conditions, (b) SEM inlet conditions, (c) Batten et al. (2004) inlet conditions and (d) random method inlet conditions. Contour lines are evenly spaced at $\pm 0.5, \pm 1.5, \pm 2.5, \pm 3.5$ and ± 4.5 . Grey lines indicate negative value contours.	178
8.24 Hybrid RANS-LES simulation of channel flow at $Re_\tau = 395$. Instantaneous isosurfaces of $Q = 300$: (a) precursor simulation inlet conditions, (b) SEM inlet conditions, (c) Batten et al. (2004) inlet conditions and (d) random method inlet conditions.	179
8.25 Sketch of the configuration of (a) the reference LES and (b) the hybrid RANS-LES simulations of the turbulent boundary layer over a flat plate.	180
8.26 Hybrid RANS-LES simulation of a zero pressure gradient turbulent boundary layer. Streamwise evolution of the coefficient of friction C_f as a function of Re_θ	182

8.27 Hybrid RANS-LES simulation of a zero pressure gradient turbulent boundary layer. Streamwise evolution of the shape factor H	183
8.28 Hybrid RANS-LES simulation of a zero pressure gradient turbulent boundary layer. Streamwise evolution of the momentum thickness θ . Same legend as in Fig. 8.26.	184
8.29 Hybrid RANS-LES simulation of a zero pressure gradient turbulent boundary layer. Profiles of the mean velocity at various streamwise locations.	185
8.30 Hybrid RANS-LES simulation of a zero pressure gradient turbulent boundary layer. Profiles of turbulent kinetic energy (left) and Reynolds shear stress (right) at various streamwise locations: (a) SEM inlet conditions, (b) Batten's method inlet conditions and (c) random number method inlet conditions.	187
8.31 Hybrid RANS-LES simulation of a zero pressure gradient turbulent boundary layer at $Re_\theta = 900$. Contours of the instantaneous streamwise velocity fluctuations u^+ at $y^+ = 5$: (a) SEM inlet conditions, (b) Batten et al. (2004) inlet conditions and (c) random method inlet conditions. Contour lines are evenly spaced at $\pm 2, \pm 3, \pm 4, \pm 5$ and ± 6 . Grey lines indicate negative value contours.	188
8.32 Hybrid RANS-LES simulation of a zero pressure gradient turbulent boundary layer at $Re_\theta = 900$. Contours of spanwise velocity fluctuations w^+ on a plane of constant z : (a) SEM inlet conditions, (c) Batten et al. (2004) inlet conditions and (d) random method inlet conditions. Contour lines are evenly spaced at $\pm 0.5, \pm 1.5, \pm 2.5, \pm 3.5$ and ± 4.5 . Grey lines indicate negative value contours.	188
8.33 Comparison of mean streamwise velocity contours (left) and transverse velocity vectors (right) between (a) the LES, (b) the SST, and (c) the reference DNS data of Huser and Biringen (1993). Contour lines are evenly space between 0.3, 0.4, ..., 1.2.	190
8.34 Development of the coefficient of friction averaged in the lateral direction along the bottom wall $\overline{C}_f(x)$	192
8.35 Development of the maximum intensity of the secondary motion V_{\max}/U_b . Same legend as in Fig. 8.34.	193
8.36 Development of the kinetic energy over a duct cross-section $\bar{k}(x)$. Same legend as in Fig. 8.34.	193
8.37 Transverse velocity vectors at $x/D = 2$: Hybrid simulations with (a) SEM, (b) Batten's method, (c) the random method and (d) reference periodic LES.	195

8.38 Mean streamwise velocity U distribution normalized by U_b at $x/D = 2$: Hybrid simulations with (a) SEM, (b) Batten's method, (c) the random method and (d) reference periodic LES. Contours lines are evenly space between 0.3, 0.4, ..., 1.2.	196
8.39 Transverse velocity vectors at $x/D = 15$: Hybrid simulations with (a) SEM, (b) Batten's method, (c) the random method and (d) reference periodic LES.	197
8.40 Mean streamwise velocity U distribution normalized by U_b at $x/D = 15$: Hybrid simulations with (a) SEM, (b) Batten's method, (c) the random method and (d) reference periodic LES. Contours lines are evenly space between 0.3, 0.4, ..., 1.2.	198
8.41 Streamwise velocity fluctuations at $y^+ = 4$: Hybrid simulations with (a) SEM, (b) Batten's method, (c) the random method and (d) reference periodic LES. Contour lines are evenly spaced at $\pm 1, \pm 2, \pm 3, \pm 4$ and ± 5 . Grey lines indicate negative value contours.	199
9.1 Sketch of the hybrid RANS-LES simulations of the backward facing-step flow configuration.	202
9.2 RANS (red line) and embedded LES (black line) computational domains used in the hybrid simulations (top), and different close-up views of the shortest LES mesh near the step (bottom).	204
9.3 Streamlines of the mean flow: (a) reference LES run P3, and (b) DNS of Le et al. (1997).	206
9.4 Comparison of coefficient of friction C_f between run P3, the DNS of Le et al. (1997), and the experiment of Jovic and Driver (1994).	207
9.5 Streamlines of the mean flow for different methods of generation of inflow data	208
9.6 Comparison of coefficient of friction C_f for different methods of generation of inflow data	209
9.7 Backward-facing step. Mean streamwise velocity profiles.	210
9.8 Evolution of the integrated turbulent kinetic energy profile \bar{k} in the inlet section boundary layer and downstream of the step.	210
9.9 Contours of wall-normal velocity fluctuations with different methods of generation of inflow data: (a) precursor simulation (run P3); (b) SEM (run S3); (c) Batten's method (run B3); (d) random method (run R3). Contour lines of are evenly spaced at $\pm 0.5, \pm 1.5, \pm 2.5, \pm 3.5$ and ± 4.5 . Grey lines indicate negative value contours.	212
9.10 Isosurfaces $Q = 0.5U_0^2/h$ with different methods of generation of inflow data: (a) precursor simulation (run P3); (b) SEM (run S3); (c) Batten's method (run B3); (d) random method (run R3).	214

9.11 Profiles of Reynolds stresses with different methods of generation of inflow data. From top to bottom: $\langle u'^2 \rangle^{1/2} / U_0$, $\langle v'^2 \rangle^{1/2} / U_0$ and $-\langle u'v' \rangle / U_0^2$	215
9.12 Streamlines of the mean flow for different lengths of the inlet section.	216
9.13 Coefficient of friction using the SEM for different lengths of the inlet section.	216
9.14 Coefficient of friction using the SEM for different lengths of the inlet section.	217
9.15 Profiles of Reynolds stresses using the SEM for different lengths of the inlet section. From top to bottom: $\langle u'^2 \rangle^{1/2} / U_0$, $\langle v'^2 \rangle^{1/2} / U_0$ and $-\langle u'v' \rangle / U_0^2$	218
9.16 Isosurfaces $Q = 0.5U_0^2/h$ with different methods of generation of inflow data: (a) run P3 ($L_i = 10h$); (b) run S3 ($L_i = 10h$); (c) run S2 ($L_i = 10h$); (d) run S1 ($L_i = 10h$).	219
9.17 Sketch of the hybrid RANS-LES simulations of the airfoil trailing edge.	220
9.18 RANS (red line) and embedded LES (black line) computational domains used in the hybrid simulations (top), and different close-up views of the LES mesh near the airfoil trailing edge (bottom).	222
9.19 Comparison between the full domain trailing edge SST solution and the reference LES data of Wang and Moin (2000): (a) Boundary layer edge velocity U_e normalized by U_0 of the lower and upper boundary layer, (b) boundary layer momentum thickness θ normalized by h on the upper surface near the trailing edge.	225
9.20 Coefficient of friction on the low-pressure side near the trailing edge for run S1, the SST calculation and the reference LES.	226
9.21 Streamwise velocity fluctuations in a plane parallel to the wall at $y^+ = 1$ on the low-pressure side (run S1).	226
9.22 Profiles of the mean velocity magnitude normalized by the edge velocity as a function of vertical distance from the upper surface, at $x/h = -3.125, -2.125, -1.625, -1.125, -0.625$	227
9.23 Profiles of the rms streamwise velocity fluctuations normalized by the edge velocity as a function of vertical distance from the upper surface, at $x/h = -4.625, -2.125, -1.625, -1.125, -0.625$	228
9.24 Profiles of the mean streamwise velocity normalized by the free-stream velocity at $x/h = 0, 0.5, 1, 2, 4$	228
9.25 Profiles of the rms streamwise velocity fluctuations normalized by the free-stream velocity at $x/h = 0, 0.5, 1, 2, 4$	229
9.26 Coefficient of friction on the low-pressure side near the trailing edge for run S1, run S2, run S3 and the reference LES.	230

9.27 Profiles of (a) the mean velocity magnitude and (b) the rms streamwise velocity fluctuations normalized by the edge velocity as a function of vertical distance from the upper surface, at $x/h = -3.125, -2.125, -1.625, -1.125, -0.625$	231
9.28 Profiles of (a) the mean streamwise velocity and (b) the rms streamwise velocity fluctuations normalized by the free-stream velocity at $x/h = 0, 0.5, 1, 2, 4$	232
9.29 Streamwise velocity fluctuations in a plane parallel to the wall at $y^+ = 1$ for hybrid simulations with different LES domains: (a) run S1, (b) run S2, and (c) run S3.	233
9.30 Coefficient of friction C_f for different methods of generation of inflow data.	233
9.31 Profiles of (a) the mean velocity magnitude and (b) the rms streamwise velocity fluctuations normalized by the edge velocity as a function of vertical distance from the upper surface, at $x/h = -3.125, -2.125, -1.625, -1.125, -0.625$	235
9.32 Profiles of (a) the mean streamwise velocity and (b) the rms streamwise velocity fluctuations normalized by the free-stream velocity at $x/h = 0, 0.5, 1, 2, 4$	236
9.33 Streamwise velocity fluctuations in a plane parallel to the wall at $y^+ = 1$ for hybrid simulations with different LES inflow data: (a) SEM, (b) method of Batten et al. (2004) and (c) random method.	237
9.34 Isosurfaces $Q = 10U_0^2/h^2$ for hybrid simulations with different LES inflow data: (a) SEM, (b) method of Batten et al. (2004) and (c) random method.	238
9.35 Contours of v' -velocity fluctuations with different LES inflow data: (a) SEM, (b) method of Batten et al. (2004) and (c) random method. Contour lines are evenly spaced at ± 0.05 , ± 0.015 , ± 0.025 , ± 0.035 and ± 0.045 . Grey lines indicate negative value contours. . . .	239
9.36 Frequency spectrum of the v fluctuations in the near wake at $x/h = 4$ and $y/h = 0.5$	240

List of Tables

4.1	Parameter settings used in the simulation of isotropic turbulence with the SEM.	84
5.1	Coefficients of the SST model.	93
6.1	Parameter settings used in the LES computations of the fully developed turbulent channel flow. The parameters not listed here are kept constant for all simulations.	103
6.2	Mean flow properties obtained from LES computations of the periodic channel flow at $Re_\tau = 395$ and reference DNS of Iwamoto et al. (2002).	104
6.3	Mean flow properties obtained from LES computations of fully developed channel flow at Re_τ between 180 and 950. Reference data are taken from the DNS of Hoyas and Jimenez (2006) for run F and I, from the DNS of Iwamoto et al. (2002) for run G, and from the DNS of Moser et al. (1999) for run H.	111
8.1	Parameter settings used in the hybrid RANS-LES simulations of the channel flow. The parameters not listed here are kept constant for all simulations.	162
8.2	Mean flow properties obtained from LES computations of the periodic duct flow.	191
9.1	Parameter settings used in the hybrid RANS/LES computations of the backward facing step. The parameters not listed here are kept constant for all simulations.	205
9.2	Parameter settings used in the hybrid RANS/LES computations of the flow over an airfoil trailing edge. The parameters not listed here are kept constant for all simulations.	223

Abstract

This thesis describes the development and validation of a new method for the generation of synthetic inlet conditions, referred to as the Synthetic Eddy Method (SEM), for Large-Eddy Simulation (LES). The motivation for this work is the growing interest of the engineering community in hybrid methods coupling Reynolds-averaged Navier-Stokes (RANS) approaches in regions of the flow that are at equilibrium (where RANS can be trusted), with LES approaches elsewhere. The focus of this thesis is on the RANS-to-LES interface inside attached turbulent boundary layers, where an unsteady LES content has to be explicitly generated from a steady RANS solution. The SEM is a stochastic algorithm that generates instantaneous velocity fluctuations from input statistical quantities that are typically available from a RANS solution. The method is based on the classical view of turbulence as a superposition of eddies. The signal is expressed as a sum of synthetic eddies with random position and intensity, and which are subsequently convected through the LES domain inlet. The method generates stochastic signals with prescribed mean velocity, Reynolds stresses, and length and time scale distributions. The SEM is implemented into the unstructured finite volume code, *Code_Saturne*, and used to generate inflow data for the LES of plane channel flow. It is shown that the robustness of the SEM depends strongly on the correct specification of its input parameters (i.e. mean velocity, turbulent kinetic energy, and integral length and time scales). Equations to compute all the input parameters of the SEM from simple RANS statistics are then derived, and the SEM is used to couple an upstream RANS simulation with a LES in the case of simple wall-bounded flows (i.e. channel, boundary layer and duct flows). Generally with synthetic turbulence, some distance is required downstream of the inlet for realistic fluctuations to develop. With the SEM, this development length is found to be approximately 3,000 wall units for all the cases simulated - much shorter than other comparable methods of generation of synthetic turbulence. Hybrid simulations of more complicated turbulent flows involving separation and reattachment (i.e. the flow over a backward facing step and over an airfoil trailing edge) are then performed. The SEM is compared to (and found to perform better than) other existing methods of generation of synthetic turbulence. It is shown that when the SEM is used, the RANS-to-LES interface can be placed only 1 – 2 boundary layer thicknesses upstream of the region of interest (where the flow separates) without significantly altering the results.

Declaration

No portion of the work referred to in the thesis has been submitted in support of an application for another degree or qualification of this or any other university or other institution of learning.

Copyright

The author of this thesis (including any appendices and/or schedules to this thesis) owns any copyright in it (the “Copyright”) and he has given The University of Manchester the right to use such Copyright for any administrative, promotional, educational and/or teaching purposes.

Copies of this thesis, either in full or in extracts, may be made only in accordance with the regulations of the John Rylands University Library of Manchester. Details of these regulations may be obtained from the Librarian. This page must form part of any such copies made.

The ownership of any patents, designs, trade marks and any and all other intellectual property rights except for the Copyright (the “Intellectual Property Rights”) and any reproductions of copyright works, for example graphs and tables (“Reproductions”), which may be described in this thesis, may not be owned by the author and may be owned by third parties. Such Intellectual Property Rights and Reproductions cannot and must not be made available for use without the prior written permission of the owner(s) of the relevant Intellectual Property Rights and/or Reproductions.

Further information on the conditions under which disclosure, publication and exploitation of this thesis, the Copyright and any Intellectual Property Rights and/or Reproductions described in it may take place is available from the Head of the School of Mechanical, Aerospace and Civil Engineering and the Dean of the Faculty of Life Sciences, for Faculty of Life Sciences’ candidates.

Acknowledgements

I would like to express my sincere gratitude to my supervisor, Dr. Robert Prosser, for his invaluable help during the course of this work and for his willingness to be interrupted and to invest time with me whenever I sought his attention. Without his guidance, his patience and his encouragement, this work would have surely fallen far short of its present form.

I would also like to thank Prof. Dominique Laurence for his continuous involvement in this work. He has continually made connections that have identified further sources of input and further applicability to the work to others. Working with him has been an invaluable source of inspiration and motivation which helped me reach the present stage.

This research was made possible with the financial support of the European Community through the Desider project¹. I wish also to thank the EDF team in Chatou for hosting me for 5 months during this work. The many fruitful discussions and the kindness with which they welcomed me are all very appreciated. Very special thanks also go to Dr. A. Revell, Dr. J. Uribe for their often much needed help and advice, and to Dr. C. Moulinec for his very helpful and critical reviewing of the present manuscript.

Finally, I would like to thank all my office mates, house mates, friends and relatives that have been a constant source of inspiration and support for me during this time in Manchester. By alphabetical order and only providing first names I would like to give special thanks to Alistair, Anaïs, Andy, Anna, Aziz, Bea, Birin, Charles, Christian, Claire, Claude, Dalila, David M., David P., Eoghan, Fidel, Flavien, Florian, George, Hanna, Hannah, Ignacio, Jack, Jacques, James, Jeanne, Jess, Jonna, Johana (with extra special thanks), Johanna, Juan, Karina, Keith, Lise, Lorenzo, Maguy, Marc, Marcel, Martin, Michael, Michèle, Natasha, Nate, Nicole, Nina, Patricia, Pauline, Rui, Régine, René, Sandra, Sofiane, Stefano, Stuart, Thibaut, Thomas J., Thomas P., Tristan, Ulka, Win, Yacine A., Yacine K. and ZeGroop.

¹The Desider project (Detached Eddy Simulation for Industrial Aerodynamics) is a collaboration between Alenia, ANSYS-AEA, Chalmers University, CNRS-Lille, Dassault, DLR, EADS Military Aircraft, EUROCOPTER Germany, EDF, FOI-FFA, IMFT, Imperial College London, NLR, NTS, NUMECA, ONERA, TU Berlin, and UMIST. Contract No. AST3-CT-2003-502842.

Nomenclature

Greek letters

Δ	grid spacing
δ	channel half-height or boundary layer thickness
δ^*	boundary layer displacement thickness
δ_v	viscous length scale
δ_{ij}	Kronecker symbol
ϵ	dissipation rate
η	Kolmogorov length scale
κ	von Karman constant
λ	Taylor microscale
μ	molecular viscosity
ν	dynamic viscosity
ν_t	turbulent viscosity
ω	dissipation rate per unit of kinetic energy in the SST model
Ω_{ij}	rotation rate tensor
$\bar{\Delta}$	LES filter width
ρ	density
σ	length scale of the eddies in the SEM
τ_{ij}^R	subgrid-sale stress tensor
τ_w	wall shear stress

θ boundary layer momentum thickness

Latin letters

u	velocity
U	mean velocity
\mathcal{F}_k	Fourier transform at wavenumber k
$\mathcal{N}(0, 1)$	normal distribution of mean 0 and variance 1
$\mathcal{U}(B)$	uniform distribution over B
B	box of eddies
C	airfoil chord
C_f	coefficient of friction
C_S	Smagorinsky constant
D	Diameter of the square duct
e_V	integrated error in the profile of variable V
E_{uu}, E_{vv}, E_{ww}	energy spectra of the streamwise, wall-normal and spanwise fluctuations
f	shape function of the eddies
h	step height or airfoil thickness
k	turbulent kinetic energy
L	integral lengthscale of the flow
N	number of eddies used in the SEM
p	pressure
Q	second invariant of the velocity-gradient tensor
R_{uu}, R_{vv}, R_{ww}	two-point correlations of the streamwise, wall-normal and spanwise fluctuations
Re	Reynolds number based on U_b and 2δ in a channel flow
Re_τ	Reynolds number based on u_τ and δ in a channel flow
Re_θ	Reynolds number based on θ and U_∞ in a boundary layer
t	time

u, v, w	streamwise, wall-normal and spanwise components of the velocity
U_∞, U_0	free stream velocity
u_τ	friction velocity
U_b	bulk velocity in a channel or in a pipe
U_e	boundary layer edge velocity
u_i	general notation for velocity components: $u_1 = u, u_2 = v, u_3 = w$
V_B	volume of the box of eddies B
x, y, z	streamwise, wall-normal and spanwise spatial coordinates
x_i	general notation for spatial coordinates: $x_1 = x, x_2 = y, x_3 = z$

Conventions

$'$	fluctuations from the mean
$.+$	variable normalized in wall units
$\langle \cdot \rangle$	Time averaged or statistical mean
$\bar{\cdot}$	filtered variable in LES regions and Reynolds averaged variables in RANS regions
$\hat{\cdot}$	second-order tensor

Acronyms

<i>CFD</i>	Computational Fluid Dynamics
<i>CPU</i>	Central Processing Unit
<i>DES</i>	Detached-Eddy Simulation
<i>DNS</i>	Direct Numerical Simulation
<i>LES</i>	Large-Eddy Simulation
<i>PDF</i>	Probability Density Function
<i>RANS</i>	Reynolds Averaged Navier-Stokes
<i>rms</i>	root mean square
<i>SEM</i>	Synthetic Eddy Method
<i>SST</i>	Shear Stress Transport

Chapter 1

Introduction

1.1 Motivation

Turbulence plays a major role in many engineering applications. In aeronautics for instance the flows around aircrafts are turbulent, the mixing of fuel and air in the engines takes place in a turbulent flow and noise is generated by turbulent vortices on the surface of the aircraft. Accurate predictions of turbulent flows are thus desperately needed in order to improve design processes to build cheaper, cleaner and faster aircrafts.

Although predictions in simple flows (such as pipe flow) have become routine, a tractable quantitative theory that could be used to calculate quantities of practical relevance in the general case does not exist, and is unlikely to be discovered in the foreseeable future. Instead, scientists and engineers alike hope to use the ever-increasing power of computers to simulate numerically the relevant properties of turbulent flows. Computational Fluid Dynamics (CFD) has been growing as an important tool in fluid prediction and control over the past 40 years. It can support faster and cheaper design processes when compared to experimental work, but is still far from being the only and absolute tool. At the moment, the main problems with the use of CFD as a design process in the industry are its lack of reliability and the important computer resources it can sometimes require.

Turbulence is a process that is very difficult to simulate because of the complexity and extreme sensitivity to initial conditions of turbulent flow fields. There is a very large range of time scales and length scales, which places huge demands on computer resources. In order to simplify the problem at hand, engineers use turbulence models, which reduce the level of description of the flow field. There is a broad range of models, which vary in complexity, accuracy, cost of use and which are more or less specifically derived for certain types of flows.

In Direct Numerical Simulation (DNS), all of the fluid scales of motion are resolved. The available computational resources currently restrict DNS simulations to low Reynolds numbers and simple geometries.

Reynolds-averaged Navier-Stokes (RANS) simulations offer a more practical alternative to simulate high Reynolds number flows that are prevalent in engineering applications. RANS simulations resolve only the mean motion and a turbulence model is used to represent the turbulence. RANS methods are simple to use and economical, thus appealing to industry for all kinds of problems. However, it is not possible to have a universal RANS model that will be able to cope with all turbulent flows. RANS models are tuned to behave in an appropriate way on certain classes of flows and therefore a certain degree of engineering accuracy cannot be reached in truly new and original configurations.

Somewhere between RANS and DNS lies Large-Eddy Simulation (LES). LES spatially filters the equations of motion and resolves eddies larger than the filter size, while the smaller ones are modelled. The main advantage of LES models is that they tend to be simpler and more reliable than RANS models, as they only have to model scales smaller than the filter size and not the entire range of turbulence. Although less resource demanding than DNS, the cost of a LES still exceeds by several order of magnitude the cost of a RANS simulation, and this difference only increases with increasing Reynolds number.

Hybrid methods coupling RANS and LES have recently caught the attention of industry, since they aim to combine the accuracy of LES and the cheap computational cost of RANS. The major issue with these hybrid approaches is the theoretical problem caused by the matching of a steady RANS solution and a turbulent, unsteady, LES solution. Many ideas have been developed to address the issue but up to date no consensus has been reached.

1.2 Objectives

The large number of grid points required to perform LES at high Reynolds numbers, complex geometries and large domains is the main obstacle to the application of LES to flows of industrial relevance. In the aeronautical or automotive industry, engineers are interested in LES because it provides an unsteady turbulent flow field which allows to compute the aeroacoustic noise generated by the vehicle or the airfoil. In practise only a small specific region of interest such as the trailing edge of an airfoil or the rear view mirror of a car is computed with LES. The specification of the upstream flow conditions for the embedded LES domain requires the simulation of the whole geometry, which can be achieved using RANS techniques at a relatively cheap computational cost. Fig. 1.1 shows the LES region of a typical hybrid simulation of a two-element airfoil, where LES behavior of the solution is intended before the region

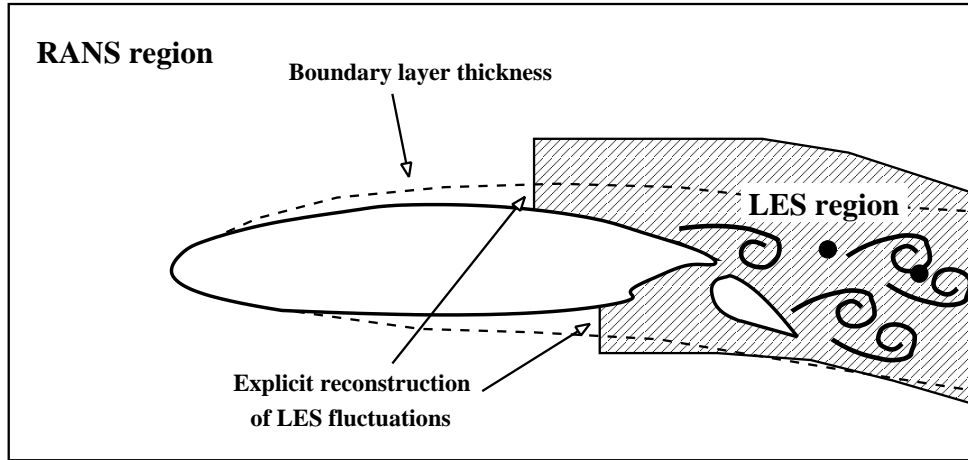


Figure 1.1: Sketch of the typical RANS and LES regions in the simulation of the flow over a two-element airfoil. LES fluctuations need to be reconstructed explicitly at the interface between the RANS and the LES region.

of interest (main airfoil trailing edge and flap airfoil). The challenge is to generate a mature unsteady turbulent LES solution from a steady RANS solution within as short a distance as possible to achieve both a reduction of the total computational cost of the simulation by limiting the size of the embedded LES domain, and a better accuracy of the simulation by using a LES model in the region of interest. The present investigation thus focuses on the RANS-to-LES interface, for what is often referred to in the literature as zonal hybrid RANS-LES methods, where LES and RANS regions use separate domains. In this case unsteady turbulent velocity fluctuations must be explicitly reconstructed and prescribed at the inflow of the LES region from a steady upstream RANS solution.

The main objectives of this research are:

1. To review and (if necessary) to derive a method to generate inflow boundary conditions for LES at a cheap computational cost from a reduced set of statistics available from a RANS simulation.
2. To evaluate the performance of the proposed method compared to existing methods used to generate inflow data for LES.
3. To evaluate the capability of the method to generate realistic boundary conditions for LES in a wide range of turbulent flows.

1.3 Outline of the Thesis

The work carried out during the course of this thesis is presented as follows. Chapter 2 gives some background theory on the nature of turbulence and reviews the main turbulence modelling strategies (already briefly introduced in the present chapter) used in the numerical simulation of turbulence. In Chapter 3, existing methods of generation of inflow data for LES are presented and critically evaluated. A new method, named the Synthetic Eddy Method (SEM), based on the decomposition of a turbulent flow field into stochastic coherent structures is presented in Chapter 4. The characteristics of the velocity signal generated by the SEM are studied thoroughly and illustrative examples of the capabilities of the method are provided. Details of the governing equations and computational techniques used are given in Chapter 5. In Chapter 6, tests of mesh refinement are performed for LES of fully developed turbulence in a plane channel flow, and a meshing strategy used throughout this thesis for LES of several other wall flows is proposed. The last chapters of this thesis are dedicated to the applications of the SEM to the generation of inflow boundary conditions for LES and RANS-to-LES coupling. In Chapter 7, we investigate the ability of the SEM to generate inlet boundary conditions for the LES of a spatially developing plane channel flow. The effect of the various input parameters of the method on the flow downstream of the inlet is investigated and guidelines for the specification of realistic inlet boundary conditions for LES are derived. A parametrization of the SEM - suitable to generate accurate inflow data for LES from reduced information available from a RANS simulation - is proposed in Chapter 8. Several simple wall-bounded flows at different Reynolds numbers are then investigated, including channel flow, duct flow and boundary layer flow. The SEM is compared with other existing methods of reconstruction of turbulent fluctuations for LES. In Chapter 9, building on the experience gained from the use of our RANS-to-LES coupling methodology in the preceding chapter, the flow over a backward facing step and over an airfoil trailing edge are simulated. These flows are of practical engineering relevance and include complex phenomena such as boundary layer acceleration, deceleration and separation. The capability of the SEM to provide accurate upstream boundary conditions for the LES of these highly non-equilibrium flows as close as possible to the region of interest is investigated and the present coupling methodology is compared with other existing methods of generation of inflow data for LES. Finally, Chapter 10 includes conclusions together with recommendations for future work.

Chapter 2

Turbulence Modelling

2.1 Introduction to Turbulence Theory

Some important aspects of turbulence are briefly summarized in this section. Only those aspects which are most relevant to the numerical simulation and modelling techniques employed in this thesis will be considered here. For a thorough introduction to turbulence theory, one can refer to the textbooks of Tennekes and Lumley (1972), Lesieur (1997) or Pope (2000).

2.1.1 The origin of turbulence

Smooth, or *laminar*, motion is maintained only if a flow moves sufficiently slowly or occurs on a sufficiently small scale, otherwise the motion becomes unstable and varies more and more significantly and irregularly in space and in time. This regime of the flow is called *turbulent*.

Reynolds (1883) first defined a non-dimensional number controlling the transition between the two flow regimes. The Reynolds number is defined as

$$Re = \frac{UL}{v}, \quad (2.1)$$

where U and L are respectively a characteristic velocity and scale of the flow, and v is the *kinematic viscosity* of the fluid. The transition between the two regimes occurs when the Reynolds number reaches a critical value. Below this critical value, small perturbations that occur in the flow are damped by the viscous stresses and the flow does not change with time. Above this limit, small perturbations that occur in the flow amplify exponentially to yield spatially organized large scale coherent structures (Lesieur, 1997).

These structures are often referred to as eddies or vortices, since they are usually associated with rotating motions of the fluid flow. The creation of these eddies is generally associated with regions of

shear. Their characteristic size l is typically of the order of the thickness of the shear layer. The large scale eddies eventually become unstable and fragment into smaller eddies. This picture of the process leading to turbulence from an initially smooth laminar flow is maybe best illustrated by directly observing fluid flows. Fig. 2.1 shows the growth of large scale coherent structures in a laminar flow, and their subsequent breaking up into smaller and smaller eddies. It should be noted that large scale coherent eddies are not always the remnants of some instabilities in a laminar flow profile, but can also be generated by instabilities of the turbulent flow field itself (Holmes et al., 1996). Turbulence is not a purely random phenomenon even at very high Reynolds numbers, since among the background turbulence coherent vortices are still present, and play a major role in the mechanism of both production (Jimenez and Pinelli, 1999) and dissipation (Jimenez and Wray, 1988) of the turbulent kinetic energy.



Figure 2.1: Instability of an axisymmetric jet. A laminar stream of air flows from a cylindrical tube at $Re = 10,000$ and is made visible by a smoke wire. The edge of the jet develops axisymmetric oscillations, rolls up into vortex rings, and then abruptly becomes turbulent. Taken from Van Dyke (1982).

2.1.2 Spectral range in isotropic turbulence

The process by which large scale coherent structures break-up into smaller pieces was first studied by Richardson (1922). He proposed that turbulence is organized into a hierarchy of eddies of various scales, each generation taking energy from its immediately larger neighbour in a *cascade* process of eddy-breakdown, until the cascade reaches the smallest scales of turbulence at which the energy is dissipated.

Kolmogorov (1941) quantified the energy cascade of Richardson. He assumed that with each energy transfer towards smaller scales, the anisotropic influence of the large scales is gradually lost, such that at sufficiently small scales the flow is statistically homogeneous and isotropic. This range of scales is called the *equilibrium range* and is universal. The second assumption is that at sufficiently high Reynolds numbers, there is a range of scales, called *inertial scales*, where the break-up process is essentially inviscid and whose role is simply to transfer energy at a constant rate ϵ to the smaller scales where it is dissipated. The dissipation rate ϵ is independent of the small scale structures in the cascade and the fluid properties since it only depends on the rate at which large scale eddies transfer energy into the cascade. Denoting by u the characteristic velocity of the large scale eddies, this can be expressed by the fundamental relation of turbulence,

$$\epsilon = \frac{u^3}{l}. \quad (2.2)$$

The last hypothesis of Kolmogorov's (1941) theory is that the smallest scales of motion at which energy is dissipated are determined by the rate of kinetic energy transfer ϵ and the kinematic viscosity ν of the fluid. From dimensional analysis, the size η of the smallest scale of turbulence at which energy is dissipated can be derived as

$$\eta = \left(\frac{\nu^3}{\epsilon} \right)^{1/4}. \quad (2.3)$$

This is referred to as the *Kolmogorov scale*. For distances shorter than η , viscosity dissipates the eddies before they have time to decay into smaller ones and the flow is smooth.

The ratio between the size l of the large scale eddies and the Kolmogorov length scale η defines the range of scales active in a given turbulent flow. Using Eq. (2.3) and Eq. (2.2), it reads

$$\frac{l}{\eta} = Re^{3/4} \quad \text{where} \quad Re = \frac{u l}{\nu} \quad (2.4)$$

where Re is a turbulent Reynolds number characteristic of the large scale eddies. The small structures thus become smaller and smaller as the Reynolds number increases. Fig. 2.2 shows the growth of a mixing layer at two different Reynolds numbers. It can clearly be seen that while the large scale coherent structures are unaffected by the Reynolds number, the small scale activity increases with the Reynolds number. Typical industrial flows have Reynolds numbers between 10^4 and 10^6 , for which the Kolmogorov scales are up to 10,000 times smaller than the largest eddies of the flow. For such Reynolds numbers, the range of scales present in the flow is so large that direct numerical simulations are currently impractical. Instead, modelling assumptions have to be employed to reduce the complexity of the system to be simulated, and these rely on Kolmogorov's (1941) theory of isotropic turbulence briefly presented above.

One of the assumption of Kolmogorov's (1941) theory is that the Reynolds number is very high, or in other words, there exists a substantial inertial range between the large eddies and the Kolmogorov



Figure 2.2: Growth of a mixing layer at (a) a moderate and at (b) a higher Reynolds number. Large scale structures are not affected by the Reynolds number whereas more small scale structures can be observed in the higher Reynolds number case. Taken from Van Dyke (1982)

eddies. This assumption is valid in a wide range of flows, such as free shear flows away from solid surfaces where the thickness of the shear layer, and hence the size l of the large eddies is unaffected by the viscosity, and hence by the Reynolds number. For such flows at sufficiently high Reynolds number, the Kolmogorov scales are sufficiently small to include a wide inertial range of scales over which the energy cascade representation is valid. However there is an important class of flows for which the largest eddies are always dependent on the viscosity, regardless of the Reynolds number. They are flows over rigid walls. Their dynamics are sensibly different to the picture of the Kolmogorov cascade and they are of paramount engineering importance.

2.1.3 Wall turbulence

Prandtl (1925) first postulated that all wall-bounded flows are characterized by a thin region close to the wall, called the *inner layer*, where the behavior of turbulence is to a large extent universal, independent of the rest of the flow and determined by the viscosity ν and the viscous shear stress at the wall τ_w . As a result of dimensional analysis, the characteristic velocity scale u_τ and length scale δ_ν in the inner layer are obtained as,

$$u_\tau = \sqrt{\frac{\tau_w}{\rho}} \quad , \quad \delta_\nu = \frac{\nu}{u_\tau}. \quad (2.5)$$

u_τ is referred to as the *friction velocity* and δ_ν as the *viscous length scale*. Quantities normalized by δ_ν

and u_τ are said to be expressed in *wall units*. Different regions in the near-wall flow are defined as a function of $y^+ = y/\delta_v$, where y is the distance from the wall. The magnitude of y^+ determines the relative importance of inertial and viscous effects and thus it is similar to a local Reynolds number.

The region of the flow where inertial effects can be neglected when compared with viscous effects is called the *viscous sublayer*, and here the mean velocity profile has a universal form, which follows the *law of the wall*, $U^+ = y^+$. The viscous sublayer is restricted to a very thin region near the wall (typically $y^+ < 5$) whose thickness decreases with increasing Reynolds number. Since the characteristic length scale δ_v of the large eddies in this region is strongly affected by viscosity, there cannot be an inertial subrange. Antonia et al. (1992) found from their experiments in a turbulent channel flow that δ_v is essentially the same as the Kolmogorov length-scale η at the wall ($\eta^+ \approx 1.5 - 42$) without any dependence on Reynolds number.

Further away from the wall, the influence of the viscosity becomes negligible and the size of the large eddies becomes independent of the Reynolds number, and scales with the characteristic geometrical length scale of the flow δ . Unlike the law of the wall, the velocity profile is not universal in this region and is different for different flows (see Chapter 7 of Pope (2000) for instance).

Between these two regions, there is an overlap region where $y^+ \gg 1$ and $y/\delta \ll 1$, where the length scale of the dominant eddies is proportional to the distance to the wall. Assuming that there is a local equilibrium between production and dissipation of energy, the *log-law* of the wall for the mean velocity profile can be derived (von Karman, 1930),

$$U^+ = \frac{1}{\kappa} \log y^+ + A \quad \text{with} \quad \kappa \approx 0.4 \quad \text{and} \quad A \approx 5. \quad (2.6)$$

Experiments (Pope, 2000) confirmed the validity of the above relation for $y^+ > 30$ and $y/\delta < 0.3$.

The ratio of the size δ of the large eddies in the core of the channel to the size of the large eddies δ_v in the near wall region is the *friction Reynolds number*,

$$Re_\tau = \frac{\delta}{\delta_v} = \frac{\delta u_\tau}{v}. \quad (2.7)$$

It plays the same role in wall turbulence as the turbulent Reynolds number defined in Eq. (2.4) for the Kolmogorov cascade. The crucial difference between the turbulence of the Kolmogorov cascade and wall turbulence is that in the latter, large and small scale eddies are segregated in space by the wall whereas both large scale eddies and Kolmogorov eddies coexist at a given location in the Kolmogorov cascade. In wall-bounded flows, the vicinity of the wall is dominated by viscous effects which determines the size δ_v of the near wall structures, whereas further away from the wall, the flow is dominated by large scale eddies of characteristic size δ and the Kolmogorov energy cascade is able to generate a full range of length scales at high Reynolds numbers.

Another major difference between free shear turbulence and wall turbulence is that in wall turbulence, the turbulent kinetic energy is mainly produced in the small scales very close to the wall, with a peak at $y^+ = 12$ (see Antonia et al. (1992) for instance). The near-wall region containing the smallest scales of motion is a net source of turbulent kinetic energy, which is transported towards the centre of the flow (Kim et al., 1987). The core of the flow is a sink of energy and dissipates energy through the classical Kolmogorov energy cascade. Unlike the Kolmogorov theory which explains the behaviour of freely decaying turbulence, a statistical theory describing the energy transfers between small scales and large scales of wall flows is still missing. In order to better understand wall turbulence, much work has been undertaken to understand the structure and the dynamics of the turbulent structures themselves.

The near wall region ($y^+ < 40$) of a channel flow is dominated by two types of structures shown in Fig. 2.3: quasi-streamwise *vortices* or *rolls* with the downstream end slightly further from the wall, and streamwise velocity *streaks* (Robinson, 1991). The streaks are regions of relatively slow and fast moving fluid. Their streamwise length can exceed 1,000 wall units and their average spanwise separation is around 100 wall units. The rolls have diameters of around 50 wall units and have a length typically no more than 200 wall units in the near wall region (Moin and Moser, 1989). They sometimes occur alone, or with a companion of opposite rotation when they are then called *counter rotating vortices*. The low speed streaks $u' < 0$ can be found on the side of the roll where $v' > 0$ and several vortices can be associated with each streak (see Fig. 2.3).

As the counter rotating vortices are being convected, the intensity of the defect in the streamwise velocity profile grows until a critical value at which the slow moving fluid of the streak is ejected from the wall. This part of the evolution, known as the *ejection* phase, is accompanied by a *sweep* phase on the other side of the roll where $v' < 0$ where fast moving fluid is more gently brought towards the wall. Ejection and sweep events cause a burst of Reynolds shear stress which is largely responsible for the production of the turbulence in the boundary layer (Kim et al., 1971).

The origin of the streamwise rolls can be explained by a simple mechanism that leads to the formation of similar structures in all turbulent shear flows. The mean shear $\frac{\partial U}{\partial y}$ of the velocity profile produces cross-stream vorticity ω_z . Infinitesimal fluctuations perturb the streamwise convection of these vortex lines and the lines that are perturbed upward move faster than the ones perturbed downward. A streamwise component of the vorticity then appears. It is more and more stretched by the mean shear as the upper part of the vortex line is carried faster downstream. These stretched and intensified components become the rolls. They become more and more parallel to the wall as the stretching goes on. In a typical flow field there are many different examples of such lines at various points in their life cycle making various angles with the wall, depending on their wall distance. Some of the vortices of the near wall region are

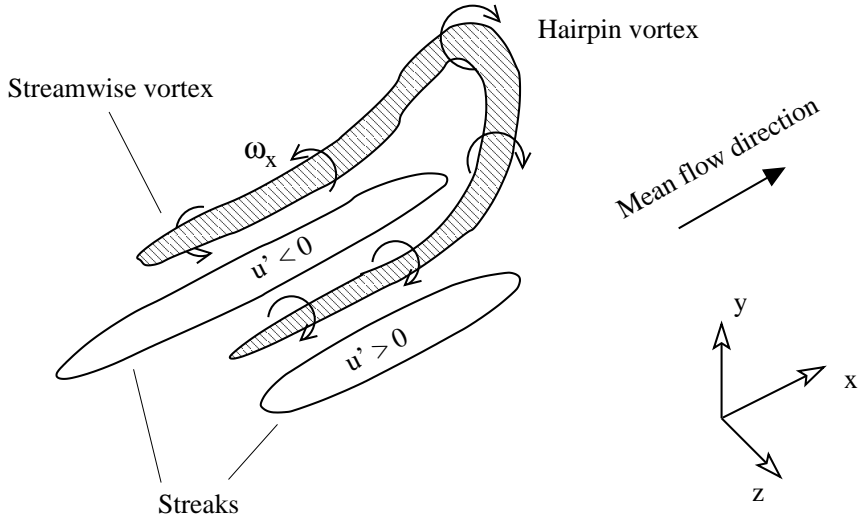


Figure 2.3: Sketch of the near-wall coherent structures responsible for the production of turbulence in wall-bounded flows.

connected to the trailing legs of *hairpin* vortices which can be found in the outer layer of the boundary layer (see Fig. 2.3). The width of the hairpin vortices scales with δ_v but their length can be of order δ (Head and Bandyopadhyay, 1981). They are in average inclined at 45 degrees to the wall.

2.2 Numerical Simulation of Turbulence

In this section, we present the main modelling techniques used in the numerical simulation of turbulence. DNS, RANS, LES and hybrid RANS-LES methods, briefly introduced in Chapter 1, are reviewed in the present section in terms of their main modelling assumptions, computational cost and current applications. This is done largely in qualitative terms with more detailed aspects of governing equations and computational techniques employed in the present work relegated to Chapter 5.

2.2.1 Direct Numerical Simulation (DNS)

DNS of turbulent flow is the simulation of the Navier-Stokes equations without any modelling assumption. All the scales of motions are accurately resolved by the numerical grid used and the only sources of error stem from the numerical method employed. The major difficulty when performing DNS resides in the wide range of scales that needs to be simulated.

We saw in the previous section that the length scales which contain energy are much larger than those at which it is dissipated, and that both are linked by an inertial range which is isotropic and universal. The ratio between the size of the largest and the smallest eddies was shown to grow as $Re^{3/4}$. Since

turbulence is three-dimensional, the number of grid points necessary to resolve a cube whose size is of the same order as the length scale of the largest eddies is proportional to $Re^{9/4}$.

The above derivation is valid for flows whose dynamics is controlled by the Kolmogorov energy cascade. For wall-bounded flows, the Reynolds number dependence is even stricter. We saw that the size of the smallest structures in the near wall layer is proportional to the viscous length scale $\delta_v = v/u_\tau$. Since the size of the large eddy in the core of the flow scales with the geometrical length scale δ , the number of grid points necessary to discretize a wall-bounded flow (assuming a fully homogeneous and structured mesh) is proportional to Re_τ^3 . The Reynolds number,

$$Re = \frac{2U_b\delta}{v}, \quad (2.8)$$

based on the bulk velocity U_b (averaged mean streamwise velocity across the flow) and the channel half width δ is often used to characterize the flow through a channel. Defining the coefficient of friction as,

$$C_f = \frac{u_\tau^2}{\frac{1}{2}\rho U_b^2}, \quad (2.9)$$

and using the empirical correlation $C_f = 0.073 Re^{-0.25}$ suggested by Dean (1978), the number of grid points necessary to discretize a wall-bounded flow is proportional to $Re^{2.625}$. Slight differences with other previous estimates (Chapman (1979), Reynolds (1990), Pope (2000)) stem from the differences in the assumed power law dependence of the friction coefficient with the Reynolds number. Assuming a power law of the form $C_f \propto Re^{-2\alpha}$, typical values of α range from 0.1 to 0.125, yielding a grid points requirement proportional to $Re^{3(1-\alpha)}$ in the range $Re^{2.625-2.7}$.

Additionally, the time integration of the equations require that the time step dt must be small to capture the highest frequencies of the flow. Those scale as η/U where U is a characteristic convection velocity of the flow. The compilation of statistics additionally require that the averaging sample contains a wide variety of flow events. The simulation should thus be run for a period T equals to several l/U , where l is the size of the large scale eddies. Therefore the total number of time steps T/dt needed for one simulation is also proportional to $Re^{3/4}$. This means the total computational cost of a DNS scales with Re^3 for flows away from walls and approximately with $Re^{3.7}$ when the near-wall layer is simulated.

Because of this prohibitive resolution requirement, DNS has been limited to the simulation of turbulent flows at low Reynolds numbers. In the first DNS Orszag and Patterson (1972) simulated the decay of isotropic turbulence at a Reynolds number of 35 based on the Taylor microscale (see Pope (2000) for a definition) with 32^3 grid points. The first DNS of a wall bounded flow was conducted by Kim et al. (1987) at a Reynolds number of 3,300 based on the bulk velocity and channel half width (see Eq. (2.8)) with about 4×10^6 grid points. Computer resources allow now to simulate wall flows at much higher

Reynolds numbers. The more recent DNS of del Alamo et al. (2004) managed to compute channel flows at Reynolds numbers of up to $Re = 87,000$ with over 400×10^6 grid points.

Since the pioneering work on isotropic turbulence of Orszag and Patterson (1972), DNS has been successfully used as a research tool to provide reliable databases (Le et al., 1997) to validate the assumptions used in turbulence models, to provide information which is difficult to obtain through experiment (del Alamo et al., 2004), or to test proposed control strategies (Dandois et al., 2007). Although higher Reynolds number flows than previously achievable can be simulated, DNS of flows of practical engineering interest such as the flow over airfoil trailing edges or the flow in the core of nuclear reactors will remain out of reach of future super computer capabilities for many years.

2.2.2 Large-Eddy Simulation (LES)

LES aims to reduce the prohibitive computational cost of DNS by only simulating directly the large scales of turbulence, while using a turbulence model to represent the smaller scales. From a computational point of view, LES is a very attractive method; in the DNS of isotropic turbulence at moderate Reynolds number for instance, over 99% of the effort is devoted to resolving scales in the dissipation range (Pope, 2000). In terms of modelling, LES finds its justification in the Kolmogorov theory which suggests that the small scales in the inertial and dissipative range have a universal behavior and can be parametrized solely by the energy transfer rate entering the cascade.

LES has its origin in the meteorological community with the pioneering work of Smagorinsky (1963). The first LES of an engineering flow was performed by Deardorff (1970) for a fully developed channel flow. With an increase in Central Processing Unit (CPU) power, the 1980s and 1990s saw an increase in the number of LES performed at least in the research community. However, CPU power still remained lower than that needed to treat realistic engineering applications so that the range of flows remained oriented towards simple geometries and fundamental issues. The flows simulated included non-rotating (Moin and Kim, 1982) as well as rotating channel flows (Piomelli and Liu, 1995) at low Reynolds numbers, isotropic turbulence (Lesieur and Rogallo, 1989), transitional flows (Huai et al., 1999), free shear flows such as mixing layers (Vreman et al., 1997) or simple flows with separation (Kaltenbach et al., 1999). Since the 1990s the number of applications and flow conditions treated with LES has kept growing. In situations where the focus is on structural and temporal details of the turbulent motion, LES is currently used in the industry as a research tool. This includes unsteady pressure fluctuations to predict acoustic noise (Wang and Moin, 2000) or heat transfer extrema to predict thermal fatigue (Niceno et al., 2002). In the case of aeronautical flows however, the demand of LES in terms of both numerical accuracy and grid resolution still limits its use as a practical engineering tool to simple geometries and moderate

Reynolds numbers (Davidson et al., 2003).

The computational cost of a LES can be estimated assuming that the following criterion is met: the filter width is located in the inertial subrange so that the large energy containing eddies are simulated while the dissipative ones are modelled. In practical applications of LES the grid spacing dictates the filter width, so that the above requirement on the size of the filter width can directly translate into a requirement for the grid resolution. Baggett et al. (1997) estimated that the grid spacing employed needs to be ten times smaller than the integral length scale defined as $L = k^{3/2}/\epsilon$ in order for the small scales to be isotropic. For flows away from walls driven by large scale shear, such as jets or mixing layers, the large eddies are controlled by the geometry of the flow, making the integral length scale independent of the Reynolds number. This implies that the number of grid points necessary to resolve accurately such flows is independent of the Reynolds number, which makes LES very appealing compared to DNS.

However, the above arguments do not hold for flows in which the size of the large scales depends on the Reynolds number (such as wall bounded flows). Reynolds (1990) found that the number of grid points required to resolve an attached boundary layer of thickness δ is proportional to $Re^{0.4}$ for the outer layer (assuming it begins at some fixed fraction of δ) and to $Re^{2.4}$ in the inner layer. This requirement was derived by assuming that the grid spacing must remain a fixed fraction of the integral length scale. For wall flows at high Reynolds numbers, the cost of computing the inner layer exceeds by several orders of magnitudes the cost of simulating the outer layer. In this case, the cost of a LES is driven by the inner layer resolution requirement, making LES as computationally costly as DNS. In order to circumvent this issue, LES using block-structured or fully unstructured grids where the grid is locally refined as the wall is approached have been performed (see Kravchenko et al. (1996), Jansen (1996) or Addad et al. (2003) among others), although some doubts remain about the impact of the numerical method employed in such LES applications (Piomelli et al., 2006). Other areas of research include improved subgrid scales models that can represent accurately a broader range of scales than simply the dissipative ones or hybrid RANS-LES approaches where the simulation is stopped at some fixed fraction from the wall so that only the outer layer is simulated (this is the aim of hybrid RANS-LES approaches briefly reviewed in the next section).

The derivation of the governing equations for LES is described in more details in Chapter 5. Here only the main results are used in order to discuss some aspects of LES modelling. The separation of large scales and small scales is done via a low-pass filtering operation, which is defined as a convolution product

$$\bar{\mathbf{u}} = G \star \mathbf{u} = \int_{-\infty}^{+\infty} \mathbf{u}(\mathbf{y}) G_{\Delta}(\mathbf{x} - \mathbf{y}) d\mathbf{y} \quad (2.10)$$

where $G_{\bar{\Delta}}$ is the convolution kernel characteristic of the filter used and $\bar{\Delta}$ is the associated cutoff scale. The convolution product defined by Eq. (2.10) renders the velocity \mathbf{u} smoother in the sense that motions smaller than the cutoff scale are removed. More information on the properties of popular spatial filters (Gaussian filter, box filter, spectral filter, etc.) can be found in Sagaut (2001). Applying this filter to the Navier-Stokes equations results in a new set of equations for the filtered velocity $\bar{\mathbf{u}}$ which differ from the original Navier-Stokes equations by the presence of unclosed terms. These are correlations of small-scale motions $\underline{\tau}^R = \bar{\mathbf{u}} \otimes \bar{\mathbf{u}} - \bar{\mathbf{u}} \otimes \bar{\mathbf{u}}$ and are referred to as the *subgrid-scale*, or *residual* stresses. In order for the filtered Navier-Stokes equations to be closed, $\underline{\tau}^R$ needs to be modelled as a function of known quantities.

The most popular model for the subgrid-scale stresses are eddy viscosity models, such as the model proposed by Smagorinsky (1963) which is used in this thesis. It assumes that the anisotropic part of the subgrid-scale stress tensor is proportional to the resolved rate of strain tensor \bar{S}_{ij} through a *turbulent viscosity* v_t acting like a proportionality coefficient,

$$\tau_{ij}^R - \frac{1}{3}\tau_{kk}^R\delta_{ij} = -2v_t\bar{S}_{ij}. \quad (2.11)$$

The eddy viscosity is modelled as the product of a velocity scale and a length scale l_{LES} proportional to the filter size $\bar{\Delta}$ through the Smagorinsky constant C_S ,

$$l_{LES} = C_S \bar{\Delta}. \quad (2.12)$$

The value of the Smagorinsky constant C_S is not universal, and can be tuned to one set of conditions. Assuming a filter width in the inertial range, Lilly (1967) derived the theoretical value of the Smagorinsky constant for freely decaying isotropic turbulence as $C_S \approx 0.18$. The constant value of C_S in the original Smagorinsky (1963) model makes it unconditionally dissipative. Its role is merely to drain energy from large eddies to smaller ones at the correct rate. It cannot account for local *backscatter* of energy from small to large scales which locally appear in the Kolmogorov cascade. A more problematic aspect of the constant value of C_S is observed for laminar flows and wall flows. In laminar flows, the subgrid-scale viscosity does not vanish causing the model to dissipate the small perturbations which could otherwise have lead to turbulence. In the case of wall flows, a constant value of C_S does not provide the requisite asymptotic near-wall decay of $v_t \propto y^{+3}$. In order to circumvent this issue, a lower value of C_S is usually used for wall flows (Deardorff, 1970) together with a damping function for the Smagorinsky constant in order to lower its value as the wall is approached (Van Driest, 1956).

Motivated by the need for using a fixed constant in the Smagorinsky model, the dynamic procedure proposed by Germano et al. (1991) calculates the Smagorinsky constant adaptively as the simulation is advanced in time. The principle of the model is to assess the subgrid-scale stresses at two different levels

of filtering: the first is the LES filter, with a filter width equal to the grid size; the second filter has a width twice that of the first filter, and is referred to as the test filter. By using the same model to represent both subgrid-scale stress tensors, constants in the model can be computed. The dynamic model makes the Smagorinsky constant vanish in laminar flows and tend towards zero as the wall is approached. It also admits backscatter in the Kolmogorov cascade although this is achieved by having negative values of the Smagorinsky constant, which renders the simulations more unstable. This problem is addressed by introducing some kind of averaging process and limiters to prevent the Smagorinsky constant from varying too erratically (see Meneveau et al. (1996) or Piomelli and Liu (1995) among others).

Other formulations of the subgrid-scale stress tensor include the scale similarity model of Bardina et al. (1980), the mixed scale model of Sagaut (1996), the WALE (Wall-Adapting Local Eddy Viscosity) model of Nicoud and Ducros (1999), the approximate deconvolution model of Stolz and Adams (1999) or models involving the resolution of a transport equation for the subgrid-scale energy (Schumann (1975) or Yoshizawa (1986) among others). Some of these models have been coupled with the dynamic procedure of Germano et al. (1991) to compute the constants involved in them. After almost 30 years of intensive research on subgrid-scale modelling, the general agreement is that although effective in reducing the empiricism in the original Smagorinsky model and therefore being able to simulate a wider range of flows, current subgrid-scale models are unable to represent accurately the near-wall eddies when the filter width is larger than the integral length scale of the flow. A direct consequence is that the near wall grid resolution requirements derived at the beginning of this section cannot be alleviated by current subgrid scale models, which still makes LES of wall flows computationally impracticable at high Reynolds numbers. Alternative approaches to make LES applicable at high Reynolds numbers based on the use of RANS turbulence models in the inner layer are reviewed in Section 2.2.4.

2.2.3 Reynolds Averaged Navier-Stokes (RANS)

The first approach used in the numerical simulation of turbulence was to simulate only averaged quantities. The total velocity \mathbf{u} was decomposed into a sum of its averaged component $\bar{\mathbf{u}}$ and its fluctuating component $\mathbf{u}' = \mathbf{u} - \bar{\mathbf{u}}$. Following the formalism of Labourasse and Sagaut (2002), this averaging operator (usually referred to as Reynolds average) can be defined as an ensemble average over the set of samples Ω

$$\bar{\mathbf{u}} = \frac{1}{N} \sum_{i \in \Omega} \mathbf{u}_{(i)} \quad (2.13)$$

where N is the number of samples in Ω and $\mathbf{u}_{(i)}$ denotes realization i of the sample of realization Ω . The ensemble averaging operator defined by Eq. (2.13) can be seen as a classical mean average or a

conditional average depending on the size of the set of samples Ω . Therefore it can represent both steady and unsteady solutions. Additionally the ergodic theorem states that for a statistically stationary signal with finite integral time scale, this ensemble average can be interpreted asymptotically as a time-average operator. The RANS equations governing the evolution of the averaged velocity and pressure are derived in Chapter 5. As is the case in LES, unclosed terms $\overline{u'_i u'_j}$ (referred to here as the *Reynolds stresses*) appear in the governing equations for the averaged quantities. They represent the effect of the fluctuating velocities on the averaged ones. Recalling that an important property of turbulence is its ability to mix momentum, the Reynolds stresses are often considered to be proportional to the mean rate of strain by introducing a simple eddy viscosity ν_t ,

$$\overline{u'_i u'_j} - \frac{1}{3} \overline{u'_k u'_k} \delta_{ij} = -2\nu_t \overline{S}_{ij}. \quad (2.14)$$

To derive the turbulent viscosity field, turbulent length and time scales characteristic of the turbulent mixing process are calculated. This can be done from simple algebraic relations such as Prandtl's mixing length hypothesis (Prandtl, 1925), to one equation models for the turbulent kinetic energy k (Kolmogorov, 1942), to two equations models such as $k - \varepsilon$ (Jones and Launder, 1972). The major flaw of these models resides in the eddy viscosity assumption which implies that the turbulent motion is in equilibrium with the mean flow. Turbulence is long lived and does not adjust rapidly to imposed mean straining in contrast to molecular motion which adjusts instantaneously to turbulent fluctuations. Turbulent structures are determined by the prior history of straining to which it has been subjected and not to the local mean strain rate. The assumption that the Reynolds stresses are locally determined by the mean rate of strain has no general validity (Pope, 2000). However for simple shear flows in which the local mean velocity gradient characterizes the history of the mean distortion to which the turbulence has been subjected, the eddy viscosity assumption is a reasonable approximation and turbulence models based upon it are known to perform well.

Reynolds stress models bring the modeling one step further by solving model transport equations for the individual Reynolds stresses and for the dissipation. Consequently no eddy viscosity is computed, removing a lot of empiricism compared to the eddy viscosity models based on Eq. (2.14). The solution of transport equations for each stress component makes it possible to reproduce accurately the stress field anisotropy and non-local or history effects that might be associated to it. This in turn makes it possible to reproduce effects of streamline curvature, rotation and swirl, secondary motion, and other effects encountered in complex flows, better than with an eddy-viscosity model (see Launder et al. (1975) or Speziale et al. (1991)). From an engineering point of view however, the improved physical content of this approach is often offset by the increased computational cost of solving seven equations (6 equations

for the Reynolds stresses and one equation for the rate of dissipation).

All RANS models presented so far are designed to work outside the viscous sublayer where viscous effects are negligible compared with inertial effects. In order to simulate wall flows, they are usually used in conjunction with a *wall function* approach. The role of a wall function is to return the correct wall shear stress corresponding to the known velocity at the wall nearest computational node. This approach requires an assumption to be made on how the instantaneous velocity varies within the bridged near-wall region. Usually a log-law approximation is used which assumes that the flow is at equilibrium and that the nearest wall node is in the log-law region, at $y^+ > 30$. In practice this constraint is quite difficult to ensure and the log-law approximation is known to fail for non-equilibrium flows with acceleration, separation or rotation (Wilcox, 1993).

In order to better take into account the near-wall effects in RANS models, low-Reynolds versions of existing high-Reynolds models have been derived. The model proposed by Launder and Sharma (1974) for instance is a popular adaptation of the original model of Jones and Launder (1972) to solve the equations down to the wall using a Van Driest (1956) like damping function. However, RANS models based on damping functions remain empirical and do not generally take into account the source of the turbulence reduction in the near wall region, but rather try to mimic it. Elliptic relaxation models (Durbin, 1991) have been derived to consider the wall effects in a somewhat more universal way, by modelling the non-local effects felt by the turbulence due to the presence of the wall.

RANS models have been very successfull in the industry mainly because of their cheap computational cost. Although in theory RANS and LES have similar resolution requirements (since both models should have a grid spacing proportional to the integral length scale), in practise RANS is significantly cheaper. The proportionality constant between RANS and LES resolution requirements may be of the order of 10 – 100 in each direction, for a total saving of three to six orders of magnitude for RANS over LES. Additionally, homogeneity in the mean flow leads to further reductions in the RANS resolution requirements. Two-dimensional grids are often used in RANS whereas grids used in LES must be three-dimensional due to the inherently three-dimensional nature of turbulent eddies.

RANS models have remained the mainstay in the industry for over three decades. Due to the increase in computing power however, they are now challenged by the development of LES and hybrid methods combining RANS and LES. The limitations of RANS models arise firstly from the empirical rationale that makes them unsuitable for predicting accurately genuinely new complex situations. For complex three-dimensional non-equilibrium flows away from walls, finely resolved LES can provide very accurate predictions over RANS models. Also, an inherent limitation of RANS is that it only provides an averaged picture of the flow. For applications where the focus is on structural and temporal details of the turbulent

motion, LES has already supplemented RANS as an engineering tool (see Peniguel et al. (2003) for instance) and this trend is set to continue. For a review of new RANS developments and a perspective of its future role in CFD methods, one is referred to Hanjalic (2005).

2.2.4 Hybrid RANS-LES

The recent interest of the scientific community in alternative approaches combining RANS and LES methods has been motivated by two observations:

1. LES is limited by its prohibitive cost to simulate wall flows at high Reynolds numbers; RANS models are designed to perform well for thin attached boundary layer flows,
2. RANS is limited by its empirical modelling assumptions which limits its accuracy in complex situations; LES is best designed for complex non-equilibrium flows away from walls.

Hybrid RANS-LES methods thus aim to bridge the gap between both approaches by simultaneously making LES less computationally demanding while improving the performance and range of applicability of RANS models. Since the 1990s intensive research has yielded a wide variety of methods such as the VLES (Very-Large Eddy Simulation) of Speziale (1998), the LNS (Limited-Numerical Scales) of Batten et al. (2004), the DES (Detached Eddy Simulation) of Spalart et al. (1997), the SAS (Scale Adaptative Simulation) of Menter and Egorov (2005), the SDM (Semi-Deterministic Model) of Kourta and Minh (1993), the Two-Layer wall function approach of Balaras et al. (1996), the Two-Velocities hybrid method of Uribe et al. (2007) or the PITM (Partially Integrated Transport Model) of Chaouat and Schiestel (2005) among many others. The wealth of formulations proposed only underlines the complexity of the problem both from a practical and a fundamental point of view: How to reconcile the RANS and the LES representation of turbulence, especially at the interface between the RANS and the LES where the two representations coincide.

The questions posed by the combination of RANS and LES strategies are shared by all the approaches listed above. For sake of simplicity, more details on these questions will only be provided in the framework of the DES of Spalart et al. (1997), which due to its ease of use and implementation is certainly the most popular hybrid method among CFD users. DES uses a single grid and the same set of RANS equations is solved across the whole flow, but the turbulent length-scale appearing in the RANS equations is switched to a LES like length-scale based on the grid spacing to ensure LES treatment in regions where the grid is fine enough. The length-scale l_{DES} used in the model thus reads

$$l_{DES} = \min(l_{RANS}, C_{DES}\Delta), \quad (2.15)$$

where l_{RANS} is the turbulent length-scale predicted by the RANS model, Δ is the filter width and C_{DES} is a numerical constant. Close to the wall, the DES works in a RANS mode, whereas further away from the wall (where the RANS length-scale can exceed the grid spacing) DES works in a LES mode. The model was originally designed for separated flows in which strong instabilities are present that cause the rapid formation of turbulent eddies.

However for thick boundary layers or relatively low Reynolds number flows, the interface between the RANS and the LES modes can be positioned inside an attached boundary layer. In this case there is no strong instability mechanism which could trigger the formation of turbulent eddies as in separated flows. Consequently there is a region around the interface (referred to as the *grey area*) where the large eddies are not yet generated but the RANS modelled contribution to the Reynolds stresses is already low (Nikitin et al., 2000). Forcing techniques using synthetic turbulence to convert the modelled energy of the RANS region into resolvable fluctuations for the LES region have been successfully used by Piomelli et al. (2003), Davidson and Dahlström (2005) or Keating and Piomelli (2006).

Another challenge for DES and hybrid methods (Spalart, 2004) is when the LES mode is intently activated inside the boundary layer by grid refinement, to predict separation for instance. This reduces the role of the empiricism present in the RANS region but a mature LES content must be generated before the separation is reached, and after as short a development length as possible, in order to limit the length of the grey area between the RANS mode and the LES mode. This challenge could again be addressed by the generation of synthetic turbulence, which will be reviewed in the next chapter.

Chapter 3

Generation of Inflow Boundary Conditions for LES and DNS

3.1 Introduction

The choice of an appropriate turbulence model in order to provide a good representation of the physical system one wants to simulate has been discussed in the previous section. Another issue of great importance is the specification of realistic boundary conditions and, especially, inlet boundary conditions. The prescribed inflow data at the inlet should be consistent with the turbulence model chosen for the simulation.

For RANS simulations, simple analytical or experimental profiles for the mean velocities and turbulent variables are usually imposed. This practice was justified by George and Davidson (2004) where it was shown that RANS models reach a universal asymptotic behavior irrespective of the initial boundary conditions, at least for simple shear flows.

For LES or DNS simulations where the flow at the inlet is turbulent, the specification of inflow data becomes more problematic. Usually the description of the inflow is limited to the knowledge of statistical quantities such as the mean mass flow rate or a mean velocity and turbulent kinetic energy profile. Instead inflow data for LES or DNS should consist of an unsteady turbulent velocity signal representative of the turbulence at the inlet. Ideally the simulation of the upstream flow entering the computational domain would provide realistic inlet conditions to the main simulation. For obvious reasons however, the computational domain cannot be extended upstream indefinitely, and so approximate turbulent inlet conditions must be specified. Exceptions include LES or DNS of transition processes, where the inlet boundary is located in a region where the flow is laminar (Rai and Moin (1993), Grinstein et al. (1996)). In this case,

random disturbances are superimposed on a laminar profile to trigger the transition process, and no turbulent fluctuations are required at the inlet. However, this method cannot be extended to inlet boundaries where the flow is turbulent, since simulating the whole transition process would be far too costly. In order to limit the computational cost of LES or DNS of spatially evolving flows, the boundaries have to be placed as close as possible to the region of interest. This in turn requires the approximate boundary conditions to be as accurate as possible in order to limit their effect on the flow inside the domain. Therefore, the length of the transition region (where the approximate inflow data generated at the inlet of the LES or DNS domain develops towards a more physical state) must be made as short as possible.

The influence of the inlet boundary conditions on the downstream flow not only depends on the accuracy of the inflow data, but also on the flow under consideration. As already mentioned, for free shear flows an inviscid instability mechanism amplifies exponentially the small perturbations, and the inlet boundary conditions is believed to be of small importance (Li et al., 2000) in the formation of turbulence downstream of the inlet. On the contrary, for attached flows (where instability mechanisms are not so powerful), the specification of accurate boundary conditions is necessary to reach a turbulent state in the downstream flow. In all cases, it was shown by George and Davidson (2004), that even simple shear flows (such as mixing layers or boundary layers) simulated with LES or DNS do not reach equilibrium states under different upstream conditions.

In the following, we review methods of generation of inflow boundary conditions for LES and DNS, principally in terms of their computational cost, the information that they require to operate, the turbulent flow field they provide and the impact they have on the downstream flow.

3.2 Recycling Methods

The most accurate method to specify turbulent fluctuations for a LES or DNS is to run a precursor simulation whose only role is to provide the main simulation with accurate boundary conditions. If the turbulence at the inlet of the main simulation can be considered as fully developed (which is often the case for internal flows such as ducts, channels or pipes), periodic boundary conditions in the mean flow direction can be applied to the precursor simulation. The flow at the outflow plane is then recycled and reintroduced at the inlet so that the simulation generates its own inflow data. As shown in Fig. 3.1, instantaneous velocity fluctuations in a plane at a fixed streamwise location are extracted from the precursor simulation and prescribed at the inlet of the main simulation at each time step. Although no explicit boundary conditions need to be imposed, special care has to be taken to initialize the flow field properly so that turbulence can be generated as the simulation evolves. In general, the flow is initialized with a

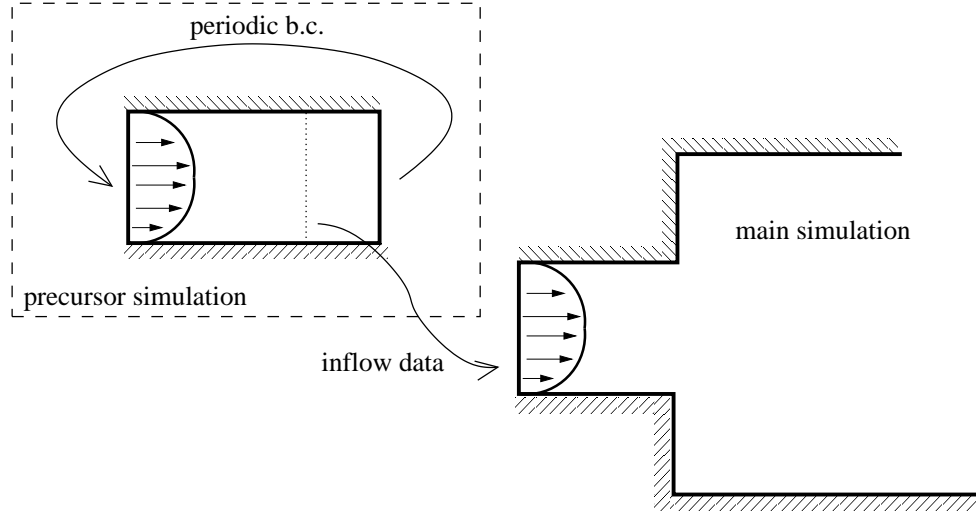


Figure 3.1: Sketch of a LES using a precursor simulation dedicated to the generation of the inflow data.

mean velocity profile plus a few unstable Fourier modes (Rogers and Moser (1992) or Kim et al. (1987)). As already mentioned, periodic boundary conditions can only be used to generate inflow conditions for flows which are homogeneous in the streamwise direction, which limits their applications to simple fully developed flows. This approach was adopted by Kaltenbach et al. (1999) and by Friedrich and Arnal (1990) who extracted velocity planes from a precursor periodic channel flow to generate inflow data for a LES of a plane diffuser and a LES of a backward-facing step respectively. Breuer and Rodi (2007) used a precursor simulation of a periodic square duct flow to generate inflow data for LES of a 180° bend. Akselvoll and Moin (1996) simulated two periodic coaxial pipe flows to generate inflow data for the inlet section of the LES of a coaxial jet combustor.

Spalart (1988) managed to simulate a zero-pressure gradient canonical spatially developing boundary layer by adding adequate source terms in the Navier-Stokes equations and using periodic boundary conditions in the streamwise directions. Spalart and Watmuff (1992) proposed a similar method for a boundary layer with adverse pressure gradient. Periodic boundary conditions were used in the streamwise direction and three zones were defined: one main zone in the middle of the domain and two fringe zones on each side. The first fringe zone is where the inlet conditions are generated while the second fringe zone is a buffer region at the exit of the domain. In the first fringe zone, source terms are added to the Navier-Stokes equations, while in the main zone the equations are not modified. There have been few attempts up to now to use these methods to generate inflow data, probably because the transformed equations require a dedicated flow solver which makes these methods complicated to program.

A more flexible technique to generate inlet conditions for a zero pressure gradient spatially developing

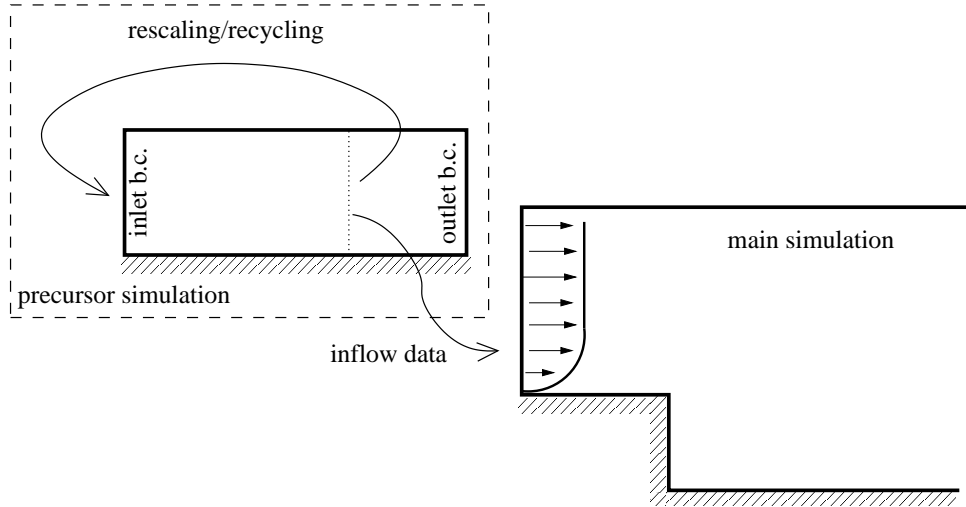


Figure 3.2: Sketch of the rescaling/recycling method of Lund et al. (1998) to generate inlet conditions for a zero pressure gradient boundary layer.

boundary layer is proposed by Lund et al. (1998). Fig. 3.2 shows a sketch of the computational set-up. The method uses the velocity in a plane located several boundary-layer thicknesses downstream of the inlet (the rescaling station) to evaluate the velocity signal at the inlet plane. The velocity field at the rescaling station is decomposed into its mean and fluctuating part; scaling is applied to the mean and the fluctuating parts in the inner and outer layers separately, to account for the different similarity laws that are observed in these two regions. The rescaled velocity is finally reintroduced as a boundary condition at the inlet. The procedure was shown by Lund et al. (1998) to result in a spatially evolving boundary layer simulation that generates its own inflow data. Planes of velocity data can then be saved from a precursor simulation using this procedure and used as inflow conditions for the main simulation. The method was used by Aider and Danet (2006) to generate inlet conditions for turbulent flow over a backward-facing step and by Wang and Moin (2000) to generate inlet conditions for a hydrofoil upstream of the trailing edge, in a region where the pressure gradient was minimal. The method has so far only been applied to equilibrium boundary layers, but Lund et al. (1998) mentioned that it can be extended to non-equilibrium accelerating or decelerating boundary layers by simply changing the rescaling procedure. It is reported that simulations using this modified version of the original procedure seemed to be promising but, to our knowledge, no results on the subject have since been published. An extension of the original method of Lund et al. (1998) to compressible turbulence was subsequently proposed by Sagaut et al. (2004). It uses rescaling and recycling of the pressure and temperature fluctuations in addition to the usual operations performed in the original method.

Ferrante and Elghobashi (2004) noticed that Lund's method was very sensitive to the initialization of the flow field. They were unable to generate fully developed turbulence from the initialization procedure recommended in Lund et al. (1998) (mean velocity profile superimposed with random uncorrelated fluctuations). They proposed a more robust variant of the original method of Lund, where the flow field is initialized using synthetic turbulence with a prescribed energy spectrum and shear stress profile. Recently Spalart et al. (2006) also proposed some modifications to the original method of Lund et al. (1998). They noticed that since the near-wall turbulence regenerates itself much faster than the outer-region turbulence, little damage is caused by applying the outer-scaling throughout. The recycling station is taken much closer to the inflow so that the computational cost of generating the inflow data is reduced. The recycling station is positioned 1δ downstream of the inlet compared to 8δ in the original method. In order to remove the spurious periodicity introduced by the recycling procedure, they recycled the structures introducing a spanwise shift to keep turbulence at the inlet and recycling station out of phase. In order to reduce further the computational cost of generating the inflow data, there is no precursor simulation. The recycling procedure is carried out in the main simulation domain so that it generates its own inflow data. With the approximations made to the original method, they noticed that the friction coefficient needed a downstream distance of about 4δ to stabilize.

Li et al. (2000) proposed another procedure to reduce the storage requirement and the computational cost of running a precursor simulation prior to the main simulation. A spatially developing turbulent mixing layer, originating from the mixing of a low- and high-speed boundary layer at the end of a splitter plate was simulated with LES. Instead of running the precursor boundary layer simulations with the mixing layer simulation, only a time series of instantaneous velocity planes with duration approximately equal to the integral time scale of the flow is extracted from the boundary layer simulation and saved on disk. This signal is converted into a periodic one using a classic windowing technique (see Li et al. (2000)) and is reused as many times as required to obtain converged statistics in the main simulation. This procedure is beneficial both from a computational and storage point of view since the precursor simulation is run only for a short duration and the data used to generate the inflow data corresponds only to a few integral time scales of the flow. In the case of the mixing layer, the periodicity involved by the inflow decays rapidly in about 25% of the domain. However Li et al. (2000) reported that the utilization of this procedure for wall-bounded flows where destabilizing effects are not so strong might require a longer transition region to weaken the periodicity involved by the inflow which might then interfere with low-frequency flow dynamics. In flows involving separation from a smooth surface for instance, Adams (1997) observed that the periodicity of the inflow signal can trigger the unsteady behavior of the detachment point.

Another method to generate inflow conditions for LES or DNS from a precursor simulation was proposed by Schlüter et al. (2004). A database containing instantaneous planes of velocity is created from a precursor LES using either periodic boundary conditions or the recycling and rescaling method of Lund et al. (1998). Turbulent velocity fluctuations are extracted from this database, and rescaled to have the required statistics,

$$u_{i,LES}(t) = \bar{u}_{i,RANS} + (u_{i,DB}(t) - \bar{u}_{i,DB}) \frac{\sqrt{u'^2}_{i,RANS}}{\sqrt{u'^2}_{i,DB}}, \quad (3.1)$$

where the subscripts LES, RANS and DB denote values for the rescaling LES inflow, the RANS target velocity field statistics and the stored database, respectively. One advantage of the method is that in the case of RANS-to-LES coupling, the database can be modified with the above equation to reproduce the RANS mean statistics which are not known *a priori* and to account for their possible unsteadiness. Keating et al. (2004) used the method to generate inlet boundary conditions for a channel flow at $Re = 6,900$, using a database from a channel flow at $Re = 2,280$. The correct phase information present in the inflow produced a shorter transition region than when using synthetic turbulence although the coefficient of friction and turbulent kinetic energy still required more than 10δ to recover. A major drawback of methods using rescaling of databases is that, although each database can easily be used to generate inflow conditions for higher Reynolds number flows than the one at which it was created, they are specific to one geometry and therefore lack generality.

3.3 Synthetic Turbulence

Methods which do not use a precursor simulation or rescaling of a database created from a precursor simulation synthesize inflow conditions using some kind of stochastic procedure. These stochastic procedures use random number generators to construct a random velocity signal which resembles turbulence. Such methods are referred to as synthetic turbulence generation methods. They are based on the underlying assumption that a turbulent flow can be approximated by reproducing a set of low order statistics. Typical statistics which can be specified by these methods include mean velocity, turbulent kinetic energy, Reynolds stresses, two-point and two-time correlations. However, the synthesized turbulence represents only a crude approximation of real turbulence. From a statistical point of view, higher order statistics such as the terms in the budget of the Reynolds stresses (the rate of dissipation, the turbulent transport or the pressure-strain term) are not usually reproduced. Additionally, the synthesized turbulence might have a structure sensibly different from the one of the real flow. As we have discussed, a turbulent flow is composed of a variety of eddies of different sizes whose shapes depend upon the flow under consid-

eration. If the structure of the turbulent eddies and their dynamics is not accurately reproduced, then it is expected that the synthetized turbulence undergoes a transition process before it redevelops towards a more physical state. There is a significant variety of synthetic turbulence generation methods which have been proposed in recent years. In order to classify them, we choose to separate methods working in physical space (referred to as algebraic methods) to methods working in Fourier space (referred to as spectral methods).

3.3.1 Algebraic methods

Algebraic methods use sets of random numbers and try to match the target statistics of turbulence by performing operations on them. The most straight forward approach to generate synthetic fluctuations is to generate a set of independent random numbers r_i taken from a normal distribution $\mathcal{N}(0, 1)$ of mean $\mu = 0$ and variance $\sigma = 1$ and rescale them such that the fluctuations have the correct turbulent kinetic energy k ; they are then added on to a mean velocity profile \mathbf{U} . The inflow signal thus reads

$$u_i = U_i + r_i \sqrt{\frac{2}{3}k} \quad (3.2)$$

where the r_i are taken from independent random variables for each velocity component at each point and at each time step. The procedure below generates a random signal which reproduces the target mean velocity and kinetic energy profiles. However all cross-correlations between the velocity components and the two-point and two-time correlations are zero.

An improvement to this method to correlate the components of the velocity was proposed in Appendix B of Lund et al. (1998). In the case of the Reynolds stress tensor being available, the Cholesky decomposition a_{ij} of the Reynolds stress tensor R_{ij} can be used to reconstruct a signal which matches the target Reynolds stress tensor,

$$u_i = U_i + r_j a_{ij} \quad (3.3)$$

where a_{ij} is

$$(a_{ij}) = \begin{pmatrix} \sqrt{R_{11}} & 0 & 0 \\ R_{21}/a_{11} & \sqrt{R_{22} - a_{21}^2} & 0 \\ R_{31}/a_{11} & (R_{32} - a_{21}a_{31})/a_{22} & \sqrt{R_{33} - a_{31}^2 - a_{32}^2} \end{pmatrix} \quad (3.4)$$

This procedure allows the basic random procedure to reproduce the target cross-correlations R_{ij} between velocity components i and j if the random data satisfy the necessary conditions $\langle r_i r_j \rangle = \delta_{ij}$ and $\langle r_i \rangle = 0$. This is the case when the r_i are independent random numbers taken from a normal distribution $\mathcal{N}(0, 1)$. In the following of the thesis, the procedure described above in Eq. (3.3) and Eq. (3.4) will be referred to as the random method.

The random methods presented above however still do not yield any correlations either in space or in time. In real turbulence, the cascade of energy from large scales to small scales is initiated in the large scales, which contain most of the energy. The above uncorrelated random fluctuations have energy uniformly spread over all wave numbers and thus contain an excess of energy in the small scales which dissipate very quickly. Lund et al. (1998) showed that inflow conditions for a spatially developing boundary layer generated from the above procedure lead to a laminarization of the flow up to a point where transition takes place and realistic turbulence starts to develop. It should however be noted that in their study, the boundary layer thickness never grew at the correct rate (the domain length was 48δ where δ is the inlet boundary layer thickness), and the friction coefficient never reached a fully developed value, although turbulence started to be produced at the wall. Klein et al. (2003) noted that the random method gave the same results as imposing a laminar profile at the inlet nozzle of a turbulent jet. Glaze and Frankel (2003) used the above random method to generate the flow in the inlet nozzle of a turbulent round jet, and reported that the random fluctuations were almost instantaneously dissipated downstream of the inlet. The turbulent jet was thus fed with an almost laminar inflow profile, which confirms the observations made by Klein et al. (2003). As a result the turbulent jet was transitional downstream of the nozzle exit, with the turbulence driven by a shear layer instability, leading to the shedding of large scale vortex rings not present in the reference experiment (or when more advanced methods of generation of inflow conditions are used). Schlüter et al. (2004) performed LES of confined swirling and non-swirling turbulent jets, testing the influence of the jet inflow. It was reported again that using the random method, fluctuations decay immediately downstream of the inlet, leading to quasi-laminar inflow. As a result the spreading rate near the nozzle exit is underestimated and the reattachment length is overestimated. Aider and Danet (2006) also reported an overestimation of the size of the recirculation bubble in the LES of a backward-facing step when inlet conditions were generated with the random method.

Klein et al. (2003) proposed a digital filtering procedure to remedy the lack of large-scale dominance in the inflow data generated by the random method. In one dimension the velocity signal $u'(j)$ at point j is defined by a convolution (or a digital linear non-recursive filter) as

$$u'(j) = \sum_{k=-N}^N b_k r(j+k) \quad (3.5)$$

where b_k are the filter coefficients, N is connected to the support of the filter and $r(j+k)$ is the random number generated at point $(j+k)$ following a normal distribution $\mathcal{N}(0,1)$. As a result the two-point correlations between points j and $(j+m)$ depend on the filter choice and read

$$\langle u'(j)u'(j+m) \rangle = \sum_{k=-N+m}^N b_k b_{k-m}. \quad (3.6)$$

This procedure is extended to the time-dependent generation of synthetic velocity field on a plane (Oyz) by generating a three-dimensional random field $r_m(i, j, k)$ for each velocity component m . The indices i , j , and k represent the time t , the direction y and the direction z respectively. A three-dimensional filter b_{ijk} is obtained by the convolution of three one-dimensional filters $b_{ijk} = b_i \cdot b_j \cdot b_k$. This is used to filter the random data $r_m(i, j, k)$ in the three directions t , y and z ,

$$u'_m(j, k) = \sum_{i'=-N_x}^{N_x} \sum_{j'=-N_y}^{N_y} \sum_{k'=-N_z}^{N_z} b_{i'j'k'} r_m(i', j + j', k + k'). \quad (3.7)$$

At each time step the random numbers are convected through the inlet plane using Taylor's frozen turbulence hypothesis $r_{i,j,k} \rightarrow r_{i+1,j,k}$ and new random numbers are generated on the plane $i = 1$. At the next time step, the new random field is filtered and so on. If there would only be the need to generate homogeneous turbulence the procedure would stop here. Since in general however this is not the case, the signal is reconstructed at each time step following Eq. (3.3) to reproduce target mean velocity and Reynolds stresses profiles.

In order to generate fluctuations that reproduce exactly the target two-point correlations $\langle u'(j)u'(j+m) \rangle$, the filter coefficients b_k should be computed by inverting Eq. (3.6). Since the two-point autocorrelation tensor is rarely available, Klein et al. (2003) assumed a Gaussian shape depending on one single parameter, the lengthscale L . The coefficients can then be computed analytically without inverting Eq. (3.6). Klein et al. (2003) were able with this procedure to test the influence of the length and time scales (uniform over the inlet plane) on the development of a plane jet and the primary break-up of a liquid jet. Veloudis et al. (2005) generated inlet conditions for a channel flow with a periodically repeating construction using the digital filtering method of Klein et al. (2003). They extracted the length scale L from a simulation with periodic boundary conditions in the streamwise direction and compared simulations using a uniform length scale with simulations using the exact length scale. Better agreements with the reference LES with periodic boundary conditions were obtained when the length-scale was allowed to vary in the filtering procedure.

Supposing the autocorrelations $\langle u'(j)u'(j+k) \rangle$ are known, di Mare et al. (2006) set the task to invert Eq. (3.6) in order to compute the filter coefficients b_k . The two-point two-time covariance tensor was extracted from a precursor spatially developing boundary layer simulation. The coefficients b_{ih} were decomposed as,

$$b_{ih} = \sqrt{\lambda_h} n_{ih} \quad (3.8)$$

where n_{ih} are the eigenvectors of the covariance tensor and λ_h are the corresponding eigenvalues. This representation of a random process is known as its Karunen-Loeve expansion (see Lumley (1970)). The

coefficients b_{ih} assume the physical meaning of characteristic eddies of the field under consideration, and are often referred to as Proper Orthogonal Decomposition (POD) modes. The inversion of Eq. (3.6) thus reduces to the computation of the eigenvalues and eigenvectors of the covariance tensor. Inlet conditions computing the coefficients from Eq. (3.8) were then generated for a spatially developing boundary layer and compared with (a) inlet conditions obtained from the recycling procedure of Lund et al. (1998) and (b) filtered random numbers with assumed Gaussian shape of the filter coefficients (as in Klein et al. (2003)). Results using the computed exact filter coefficients showed a slightly better agreement with the recycling inflow data simulation than when using the Gaussian shaped filter coefficients. It appears that questions still remain regarding the relevance of computing the exact filter coefficients in light of the major drawbacks the procedure entails. The two-point correlations are rarely available which makes the procedure of di Mare et al. (2006) not suitable for practical engineering applications where little is known about the inlet flow. Additionally, the deconvolution procedure by which the filter coefficients are obtained is computationally very costly and difficult to implement from a practical point of view.

The application of the method proposed by di Mare et al. (2006) to RANS-LES coupling is difficult because it requires very detailed statistics of the flow field. The same drawback is shared by the method proposed by Druault et al. (2004), designed in the first place to interface experimental data with LES or DNS of turbulence. The method combines Proper Orthogonal Decomposition (POD) with linear stochastic estimation in order to generate inlet conditions from measurements at a minimum number of locations in the experiment. Although the method uses stochastic tools of analysis, it requires the computation of complex statistics from a precursor numerical simulation or an experiment. Another method to generate inlet conditions using POD was proposed by Johansson and Andersson (2004). The Navier-Stokes equations are projected onto the (previously computed) POD modes of the signal at the inlet and the resulting dynamical system is solved only for the most energetic equations. The method was used to generate inlet conditions for channel flows at $Re_\tau = 180$ and $Re_\tau = 400$, and it was shown that the statistics require 1,500 wall units (about 4 channel half heights) downstream of the inlet to recover fully developed statistics. Although computational savings were achieved compared to performing a precursor simulation, the complexity of the implemented method and the necessity of the POD basis are major drawbacks for its implementation in an engineering framework.

3.3.2 Spectral methods

We will now study spectral methods which use a decomposition of the signal into Fourier modes. The first to use a Fourier decomposition to generate a synthetic flow field was Kraichnan (1969). The flow domain was initialized with a three-dimensional homogeneous and isotropic synthetic velocity field to

study the diffusion of a passive scalar. Since the signal is homogeneous in the three directions of space, it can be decomposed in Fourier space,

$$\mathbf{u}'(\mathbf{x}) = \sum_{\mathbf{k}} \hat{\mathbf{u}}_{\mathbf{k}} e^{-i \mathbf{k} \cdot \mathbf{x}}, \quad (3.9)$$

where \mathbf{k} is a three-dimensional wavenumber. Each complex Fourier coefficient $\hat{\mathbf{u}}_{\mathbf{k}}$ is given a defined amplitude calculated from a prescribed isotropic three-dimensional energy spectrum $E(|\mathbf{k}|)$ and a random phase $\theta_{\mathbf{k}}$, taken from a uniform distribution on the interval $[0, 2\pi]$. The synthesized velocity field reads,

$$\mathbf{u}'(\mathbf{x}) = \sum_{\mathbf{k}} \sqrt{E(|\mathbf{k}|)} e^{-i (\mathbf{k} \cdot \mathbf{x} + \theta_{\mathbf{k}})}. \quad (3.10)$$

This method has been used extensively to initialise velocity fields in the study of the temporal decay of homogeneous isotropic turbulence (Rogallo, 1981).

An adaptation of this method for generating inlet boundary conditions for the simulation of spatially evolving turbulent flows was proposed by Lee et al. (1992). Supposing that the flow is evolving in the x direction, the signal prescribed at the inlet is thus homogeneous in the transverse directions y and z and stationary in time. The signal can thus be decomposed into Fourier modes as in Eq. (3.9), with the Fourier coefficients calculated from an energy spectrum prescribed in terms of frequency and two transverse wave numbers,

$$\hat{\mathbf{u}}(k_y, k_z, \omega, t) = \sqrt{E(k_y, k_z, \omega)} \exp(i \phi(k_y, k_z, \omega, t)) \quad (3.11)$$

where the phases ϕ depend on time in order to avoid generating a periodic signal. They are shifted once in a given time interval T_r (typically proportional to the integral time scale of the flow) at a random time and from a random amount $\Delta\phi_r$ (where $|\Delta\phi_r|$ is typically bounded by $2\pi/20$). Because the phases have a random phase dependence the computed signal is not continuous and its spectrum differs from the target energy spectrum. The less dependent of time the phases are, the better the approximation of the target signal is but the more periodic the generated signal is. A three-dimensional energy spectrum $E(|\mathbf{k}|)$ is prescribed where $|\mathbf{k}| = \sqrt{k_x^2 + k_y^2 + k_z^2}$ and the streamwise wavenumber k_x is converted into frequency ω via $k_x = \omega/U_0$ (where U_0 is the mean convection velocity) to give an energy spectrum of the form $E(k_y, k_z, \omega)$. The velocity signal in physical space is obtained as in Kraichnan (1969) by performing a three-dimensional inverse Fourier transform in the y , z and t directions. This operation can be performed very effectively by using fast Fourier transform (see Press et al. (2007) for instance).

Le et al. (1997) generated velocity fluctuations with the spectral method of Lee et al. (1992), and then rescaled it following Eq. (3.3) so that the reconstructed fluctuations match a prescribed Reynolds stress tensor. This procedure was used to generate inlet conditions for the turbulent boundary layer upstream of a backward facing step. A number of conceptual and computational problems arose. First,

the inlet mesh is not homogeneous anymore, which precludes the use of a fast Fourier transform in the wall normal-direction. This makes the computation of the three-dimensional inverse Fourier transform much more expensive than in the original proposal of Lee et al. (1992). Additionally, a constant isotropic spectrum is used across the boundary layer, which is a very crude representation of the actual physics of the boundary layer. However it was noted that only 12 boundary layer thicknesses downstream of the inlet were necessary to recover the correct statistics of the boundary layer, which is significantly better than results obtained by Lund et al. (1998) with the random method.

The phase information in the Fourier decomposition is related to the structure and dynamics of the turbulence, therefore the method used by Le et al. (1997) in which phases are random is believed to have a lack of structural information which is assumed to be responsible for the lengthy transition region necessary to recover turbulence statistics noted by Le et al. (1997). In order to reduce the length of this transition region, Na and Moin (1998) convected through the inlet plane of their simulation (using Taylor's hypothesis) a frozen DNS field. The phase angle of the Fourier coefficients was unchanged while their amplitude factors were randomized. They were able to recover correct levels of friction coefficient C_f after only 3 boundary layer thicknesses. Another way of randomizing the Fourier coefficients previously calculated from a precursor database is to give them a random phase shift. This method was investigated by Handler et al. (1993) to generate inlet conditions for a plane channel flow. They observed a downstream reduction of the friction coefficient of 30% and a decay of the turbulence intensity in the near wall region. Similar methods of phase randomization or amplitude randomization have been investigated by Chung and Sung (1997) in the framework of inlet conditions for LES and lead to the same conclusions. Phase randomization generates a signal with the exact turbulence statistics but the flow turbulent structures are badly reproduced, which causes the friction coefficient to decay downstream of the inlet. On the contrary, with amplitude randomization, the correct structure of the flow is reproduced and the turbulence does not undergo any significant transient downstream of the inlet.

It should be noted that these methods of phase randomization or amplitude randomization require a precursor simulation to compute the Fourier decomposition of the flow. If no precursor simulation is available, these ideas could however be used to improve methods of generation of synthetic turbulence such as Le et al. (1997), by including more advanced models to correlate phase angles between Fourier modes so that the structure of turbulence is more accurately reproduced. A tentative solution was proposed by Sandham et al. (2003). He derived a method which introduces specific inner and outer layer disturbances in the form of Fourier harmonics with associated phase information. Disturbances in the inner layer are used to represent lifted streaks, with a peak at location $y^+ = 12$ while the outer region disturbances represent three-dimensional isotropic eddies. The method generates coherent turbulent structures characteristic

of turbulent boundary layers using one Fourier mode for the inner layer streaks and three Fourier modes for the outer layer isotropic eddies. The method seems to produce only a short transient downstream of the inlet before the friction coefficient recovers. Terracol (2005) used this procedure to generate inlet conditions for the LES of a blunted trailing edge and a NACA0012 airfoil. Although the inlet plane of the LES domain was positioned only a couple of boundary layer thicknesses upstream of the trailing edge in both cases, good predictions of the pressure spectrum at the trailing edge were obtained. The method of Sandham et al. (2003) however involves many empirical coefficients necessary to specify the boundary layer properties. Additionally the method is in the form presented in Sandham et al. (2003) restricted to the generation of inlet conditions for turbulent boundary layers, and its extension to non-equilibrium boundary layers or other types of flows is not discussed in the paper.

More advanced models of Fourier decomposition of the flow field reconstructing phase correlations are reviewed in Fung et al. (1992) or Eggers and Grossmann (1992) among others. These models are however restricted to the generation of isotropic turbulence, and their aim is more to improve the understanding of inertial subrange energy transfer processes rather than to generate inflow conditions for practical LES applications.

Modifications of the original method of Le et al. (1997) requiring only statistical information have been proposed in order to be able to synthesize non-homogeneous turbulence in a general industrial framework. Smirnov et al. (2001) used a Fourier decomposition with Fourier coefficients computed from different spectra at different locations across the flow based on local turbulent time and length scales. A limited number of modes drawn randomly from a normal distribution were used, resulting in a three-dimensional energy spectrum that behaved like $k^4 \exp(-k^2)$. The method proposed by Smirnov et al. (2001) did not make use of the Cholesky decomposition in Eq. (3.3) but required the explicit diagonalization of the Reynolds stress tensor R_{ij} , without proposing any route to achieve this task. Batten et al. (2004) modified the formulation proposed by Smirnov et al. (2001) so that the velocity signal to be computed can be explicitly specified in terms of input parameters of the method such as mean velocity U_i , Reynolds stress tensor R_{ij} and dissipation rate ϵ . Since the method of Batten et al. (2004) has been implemented during the course of this thesis, the basic equations are presented here. The synthesized signal reads

$$u'_i(x_1, x_2, x_3, t) = U_i + \sqrt{\frac{2}{N}} \sum_{n=1}^N [p_i^n \cos(\hat{d}_j^n \hat{x}_j^n + \omega^n \hat{t}) + q_i^n \sin(\hat{d}_j^n \hat{x}_j^n + \omega^n \hat{t})] \quad (3.12)$$

where $\hat{x}_j = 2\pi x_j / L_b$ and $\hat{t} = 2\pi t / \tau_b$ are spatial coordinates normalized by the local turbulent length $L_b = k^{3/2} / \epsilon$ and time scale $\tau_b = k / \epsilon$. The random frequencies ω^n are taken from a normal distribution with mean $\mu = 1$ and variance $\sigma^2 = 1$. The amplitudes are given by

$$\mathbf{p}^n = \boldsymbol{\gamma}^n \times \mathbf{d}^n, \quad \mathbf{q}^n = \boldsymbol{\xi}^n \times \mathbf{d}^n \quad (3.13)$$

where γ_i^n and ξ_i^n are taken from a normal distribution of variance 1 and $\hat{d}_j^n = d_j^n V_b / c^n$ are modified wavenumbers obtained by multiplying the wavenumbers d_i^n by the ratio of the velocity scale $V_b = L_b / \tau_b$ to c_n given by

$$c_n = \sqrt{\frac{3}{2} R_{lm} \frac{d_l^n d_m^n}{d_k^n d_k^n}} \quad (3.14)$$

The wavenumbers d_i^n are chosen from a normal distribution with zero mean and variance 1/2. Dividing the wavenumber by c_n elongates those wavenumbers that are most closely aligned with the largest component of the Reynolds-stress tensor, and contracts those aligned with the smaller components. This results in a more physically realistic spectrum of turbulence. The fluctuations are finally reconstructed following Eq. (3.3). Compared to the method proposed by Lee et al. (1992), the computational cost of the generation of the inflow data is reduced due to the limited number of modes simulated and non-homogeneous turbulence can be generated due to the rescaling of the spatial and temporal coordinates with the local length and time scales respectively. Keating et al. (2004) generated inlet conditions using the method of Batten et al. (2004) for LES of a plane channel flow at $Re_\tau = 400$. The statistics still required about 208 to reach equilibrium.

3.3.3 Mixed methods

The present review already highlights the large variety of methods of generation of synthetic turbulence currently available. The classification adopted appears too restrictive to present the wide range of methods proposed in the literature. Indeed some methods do not uniquely perform operations in Fourier space or in physical space, but in both at the same time. These methods are referred to here as mixed methods, and some of them are briefly presented in this subsection.

Davidson (2007a) proposed a method to generate inlet conditions for LES or DNS based on both Fourier decomposition and digital filters. At each time step m isotropic turbulent fluctuations $\tilde{u}_i(\mathbf{x})^{(m)}$ are synthetized using a procedure similar to the original proposal of Kraichnan (1969) and independently of the previously generated signals. In order to create correlations in time, the independent isotropic fluctuations synthetized at each time step m are filtered in time using an asymmetric time filter,

$$u_i(\mathbf{x})^{(m)} = a u_i(\mathbf{x})^{(m-1)} + b \tilde{u}_i(\mathbf{x})^{(m)} \quad (3.15)$$

where a and b are the filter coefficients. The generated fluctuations are then superimposed on a target mean velocity profile. This method has the advantage over the method of Le et al. (1997) that the Fourier transform is only performed in two dimensions and that no randomization of the phase angles is necessary to break the periodicity of the signal. As in the method of Le et al. (1997) however, the synthetized

turbulence is homogeneous. No scaling of the fluctuations is performed as it is argued that it would simply destroy the correlations created in the non-homogeneous directions. In order to reduce the fluctuations close to the wall and in the free stream edge the fluctuations are multiplied by a blending function. The method was applied to the generation of inlet conditions of a variety of recirculating flows including the flow over a three-dimensional hill, a diffuser flow and the flow over a curved wall in a square duct (Davidson, 2007b), using the hybrid RANS-LES approach of Davidson and Billson (2004). In all flows investigated the proposed procedure of generation of synthetic inlet boundary conditions was superior to steady inlet boundary conditions.

Another mixed formulation comes from the area of structural analysis, where it is often necessary to simulate physical loadings due to atmospheric turbulence, ocean waves or earthquakes. The weighted amplitude wave superposition (WAWS) spectral representation method is capable of simulating multivariate, multidimensional, non-homogeneous stochastic fields. The method was used with success by Glaze and Frankel (2003) to generate the inlet boundary conditions of a fully turbulent jet and by Kondo et al. (1997) to simulate spatial decay of isotropic turbulence. The velocity fluctuations are expressed as a sum over a range of Fourier frequencies at each grid point i of the inlet mesh. The correlation of the signal in space requires the summation over contributions from every neighbouring point m and the knowledge of the cross-spectral density matrix $C_{im}(\omega)$ between point i and m at frequency ω . Detailed cross-spectral density data are unavailable for most flows and thus models have to be used. A classical model consists of computing the cross spectral density matrix C_{im} between two spatially separated points i and m by

$$C_{im}(\omega_n) = \gamma_{im} \sqrt{C_{ii}(\omega_n) C_{mm}(\omega_n)} \quad (3.16)$$

where γ_{im} is the complex coherence function. Detailed empirical correlations exist for the coherence function for some turbulent flows, such as the atmospheric boundary layer. In Glaze and Frankel (2003) a simple exponential decay was used

$$\gamma_{im} = \exp[-A(r_{im} + Br_{im}^2)\omega_n/U_{im}] \quad (3.17)$$

where r_{im} is the distance between points i and m , U_{im} is the average mean velocity between the two points and the constants A and B are given values of 1 and 4, respectively. From a computational point of view the WAWS method is similar to the digital filtering technique of Klein et al. (2003) since it involves a summation over all the nodes of the inlet mesh and simulated frequencies to compute the signal at each grid point. From a conceptual point of view, it can be classified as a mixed method since it uses a Fourier decomposition in the frequency domain and a filtering approach in physical space. It has not been applied to the generation of inlet conditions for wall bounded flows.

3.4 Forcing Techniques

Since approximate inlet conditions require a transition region downstream of the inlet to reach equilibrium, some propositions have been made to accelerate the adjustment process towards equilibrium turbulence. Sergent (2002) proposed to control the turbulent kinetic energy profile in a control plane downstream of the inlet, with the goal to match a target profile obtained from the RANS simulation at this location. For simplicity, only the maximum value of the k profile was compared with the target profile maximum value. The turbulent kinetic energy of the synthetic turbulence generated at the inlet was then amplified so that the target maximum value is achieved at the control plane.

Spille and Kaltenbach (2001) proposed a similar method where the correction is not applied to the synthesized turbulence at the inlet plane but directly to the flow field through a body force acting in the wall-normal direction. The goal of the forcing technique is to amplify the wall-normal velocity fluctuations in a number of control planes downstream of the inlet to match a target profile of Reynolds shear stress. The synthetic method of Le et al. (1997) is used to prescribe inlet conditions to the LES domain, and the target Reynolds shear stress profiles are obtained from a precursor simulation using the recycling procedure of Lund et al. (1998). Better convergence of the friction coefficient was obtained than when synthetic turbulence without forcing was prescribed at the inlet.

The forcing technique of Spille and Kaltenbach (2001) was used by Keating et al. (2004) with inlet conditions generated using the method of Batten et al. (2004) in the case of a plane channel flow. Simulations using two and four control planes, as well as continuous forcing (see Keating et al. (2005)) were carried out. The simulations using a continuous forcing showed slightly faster recovery of the shear stress profiles. In all cases, the friction coefficient recovered its equilibrium value at around $x/\delta = 10$ compared to $x/\delta = 20$ when only unforced synthetic inlet conditions were prescribed.

In Keating et al. (2006) the same technique was used to couple an upstream RANS simulation with a downstream LES. The coupling methodology managed to provide accurate interface conditions for the hybrid simulation of turbulent boundary layer flows in zero, favorable and adverse pressure gradients. The target shear stress profiles were extracted from the RANS simulation so that a precursor simulation was not required. The forcing used shortened the transition region downstream of the RANS-to-LES interface to 1 – 2 boundary layer thicknesses; distances of 10 – 20 boundary layer thicknesses were necessary to recover correct flow statistics when only synthetic turbulence was used. However, the accuracy of the method was shown to be highly dependent on both the RANS solution and the location of the LES inlet, and results obtained for the adverse pressure gradient case did not match the ones obtained with the recycling procedure of Lund et al. (1998).

Chapter 4

The Synthetic Eddy Method

4.1 Introduction

We saw in Chapter 2 that there exists an overwhelming variety of methods available to generate inflow boundary conditions for LES. The main objective of the work carried out during the course of this thesis is to derive a method which generates inflow boundary conditions for industrial applications of LES and hybrid RANS-LES approaches. This places special constraints on the method:

- the computational cost of generating the inflow data should be only a small fraction of the overall computational cost,
- the method should be able to generate inflow data for any type of inlet mesh, geometry and flow without requiring any particular intervention from the user,
- the information about the inflow needed for the method to work should be kept as simple as possible (mean flow, turbulence intensity, RANS statistics, etc.),
- the approximate inflow boundary conditions imposed should have a minimal effect on the flow downstream of the inlet.

Recycling methods require a precursor simulation, thus they increase the overall computational cost of the simulation which is not acceptable in an industrial framework. As we saw previously, they are restricted to simple flows and their generalization to arbitrary inflow geometries is difficult. On the contrary, synthetic turbulence generation methods seem to be a good candidate to address all the constraints mentioned above, since they have both generality and cheap computational cost.

The idea followed in this thesis is to construct a synthetic velocity signal which can be written as a sum over a finite number of eddies with random intensities and positions. The approach is grounded

on the presence of large scale coherent structures in turbulent flows which carry most of the Reynolds stresses. Since in LES these large scale eddies are resolved, the synthetic velocity signal specified at the inflow should, ideally, represent the contribution of these eddies.

In the following sections, we describe the construction of a stochastic velocity signal using the Synthetic Eddy Method (SEM) (Section 4.2) before deriving some exact results concerning the statistical properties of the synthesized signal (Section 4.3). Instantaneous synthetic signals are then computed for homogeneous isotropic turbulence (Section 4.4). In order to validate our implementation of the SEM, time averaged statistics are extracted from these simulations and compared with the exact results derived previously. The influence of a change in the input parameters of the method on the generated signal is also studied as an illustrative example of the possibilities and limitations of the SEM.

4.2 Basic Equations of the Synthetic Eddy Method

We begin by taking a finite set $S \subset \mathbb{R}^3$ of points $S = \{\mathbf{x}_1, \mathbf{x}_2, \dots, \mathbf{x}_s\}$ on which we want to generate synthetic velocity fluctuations with the SEM. We assume for now that the mean velocity \mathbf{U} , the Reynolds stresses R_{ij} and a characteristic length scale of the flow σ are available for the set of points considered. Details of the estimation of these quantities in the case where only reduced information is available (for instance if the full Reynolds stress tensor or the length scale are not known) will be addressed later.

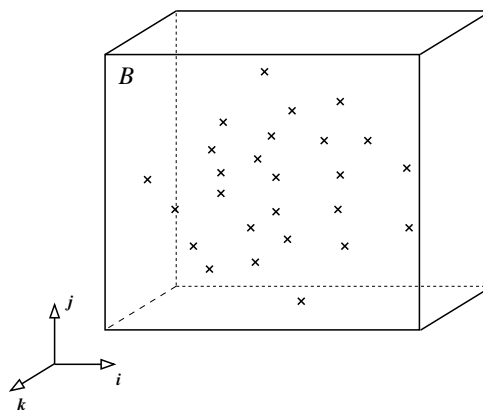


Figure 4.1: Set of points $S = \{\mathbf{x}_1, \mathbf{x}_2, \dots, \mathbf{x}_s\}$ on which the SEM signal is going to be computed and the surrounding box of eddies B .

The first step is to create a box of eddies B which contains the synthetic eddies. It is defined by

$$B = \{(x_1, x_2, x_3) \in \mathbb{R}^3 : x_{i,\min} < x_i < x_{i,\max}, i = \{1, 2, 3\}\} \quad (4.1)$$

where

$$x_{i,\min} = \min_{\mathbf{x} \in S} (x_i - \sigma(\mathbf{x})) \quad \text{and} \quad x_{i,\max} = \max_{\mathbf{x} \in S} (x_i + \sigma(\mathbf{x})) \quad (4.2)$$

The volume of the box of eddies is noted V_B . Fig. 4.1 shows the set of points on which the input information is available, and on which the signal will be computed, and its corresponding surrounding box of eddies B .

In the synthetic eddy method, the velocity signal generated by N eddies has the representation

$$\mathbf{u} = \mathbf{U} + \frac{1}{\sqrt{N}} \sum_{k=1}^N \mathbf{c}^k f_{\sigma(\mathbf{x})}(\mathbf{x} - \mathbf{x}^k). \quad (4.3)$$

where the \mathbf{x}^k are the locations of the N eddies and the \mathbf{c}^k are their respective intensities. $f_{\sigma(\mathbf{x})}(\mathbf{x} - \mathbf{x}^k)$ is the velocity distribution of the eddy located at \mathbf{x}^k . We assume that the differences in the distributions between the eddies depend only on the length scale σ and define f_σ by

$$f_\sigma(\mathbf{x} - \mathbf{x}_k) = \sqrt{V_B} \sigma^{-3} f\left(\frac{x - x_k}{\sigma}\right) f\left(\frac{y - y_k}{\sigma}\right) f\left(\frac{z - z_k}{\sigma}\right) \quad (4.4)$$

where the shape function f is common to all eddies. f has compact support $[-\sigma, \sigma]$ and has the normalization

$$\int_{\mathbb{R}} f^2(x) dx = 1 \quad \text{or only on its support} \quad \int_{-\sigma}^{+\sigma} f^2(x) dx = 1. \quad (4.5)$$

The issue of the choice of the shape function employed in our simulations and its impact on the computed signal will be addressed later.

The position of the eddies \mathbf{x}^k before the first time step are independent from each other and taken from a uniform distribution $\mathcal{U}(B)$ over the box of eddies B . The amplitudes \mathbf{c}^k are given by

$$c_i^k = a_{ij} \varepsilon_j^k \quad (4.6)$$

where a_{ij} is the Cholesky decomposition of the Reynolds stress tensor R_{ij} ,

$$\begin{pmatrix} \sqrt{R_{11}} & 0 & 0 \\ R_{21}/a_{11} & \sqrt{R_{22} - a_{21}^2} & 0 \\ R_{31}/a_{11} & (R_{32} - a_{21}a_{31})/a_{22} & \sqrt{R_{33} - a_{31}^2 - a_{32}^2} \end{pmatrix}, \quad (4.7)$$

and ε_j^k are independent random variables taken from any distribution with zero mean and unit variance (referred in the following as p_2). In all simulations carried out in this thesis we choose $\varepsilon_j^k \in \{-1, 1\}$ with equal probability to take one value or the other. This distribution is chosen because it has a lower flatness than any other distribution (see Chapter 14 of Press et al. (2007)). The advantages of this argument will become clearer later when some exact results concerning the intermittency of the signal are established in the following section.

The eddies are convected through the box of eddies B with a constant velocity \mathbf{U}_c characteristic of the flow. In our case it is straight forward to compute \mathbf{U}_c as the averaged mean velocity over the set of points S as,

$$\mathbf{U}_c = \int_S \mathbf{U}(\mathbf{x}) d\mathbf{x}. \quad (4.8)$$

At each iteration, the new position of eddy k is given by

$$\mathbf{x}^k(t + dt) = \mathbf{x}^k(t) + \mathbf{U}_c dt. \quad (4.9)$$

where dt is the time step of the simulation. If an eddy k is convected out of the box through face F of B , then it is immediately regenerated randomly on the inlet face of B facing F with a new independent random intensity vector ϵ_j^k still taken from the same distribution.

Finally the different steps in the generation of a velocity signal with the SEM can be summarized:

1. Estimate all the necessary input data (U_i , R_{ij} and σ) on the set of points S from the available information (from, say, RANS simulation, experience or analytical formulae).
2. Define the box of eddies B where the eddies will be generated from Eq. (4.1) and Eq. (4.2).
3. Generate for each eddy k two random vectors \mathbf{x}^k and ϵ_i^k for its location and its intensity, respectively.
4. Compute the velocity signal on the set of points S considered from Eq. (4.3).
5. Convect the eddies through B with velocity \mathbf{U}_c .
6. Generate new locations \mathbf{x}^k and intensities ϵ_i^k for eddies which were convected outside of B . Advance to next time step and go back to step 4.

4.3 Derivation of Exact Results

In what follows proofs of exact results concerning the statistical properties of the synthesized signal are derived.

4.3.1 A stationary ergodic process

At any location \mathbf{x} , the synthesized signal $\mathbf{u}(\mathbf{x}, t)$ can be seen as a random process of time. The recycling of the eddies ensures that the random variables ϵ_i^k and \mathbf{x}^k remain identically distributed during the simulation. At any given time t , the position of each eddy k follows a uniform distribution over B and its intensity is either 1 or -1 with equal probability. Since the synthetic signal computed from Eq. (4.3) is a function

of the random variables ε_i^k and x_i^k (which keep the same probability density function for all times), it is a stationary random process.

Moreover it is quite intuitive that the nature of the signal becomes completely independent of the initial population of eddies after a certain time has passed. Indeed the recycling process ensures that the position and intensity of each eddy before and after the recycling procedure are independent. Therefore the synthetic signal itself becomes independent of its previous states after a certain time has passed (namely after all eddies have been recycled at least once). A stationary random process which becomes independent of its previous state after a certain time is naturally ergodic (Lumley, 1970).

The signal generated by the SEM is thus a stationary ergodic random process. Hence the time average of the signal converges towards the mean as the length of the interval over which the time average is computed tends to infinity. In the following of the chapter, the statistical mean will be preferred to the time average to study the generated signal; this will greatly simplify the derivations. For a comprehensive review of tools and theorems of probability theory used in the following of the chapter, the reader is referred to Lumley (1970) or Chapter 3 of Pope (2000).

4.3.2 Mean flow and Reynolds stresses

The statistical properties of the synthesized signal are now going to be studied. We start by studying the mean value of the velocity signal given by Eq. (4.3). By linearity of the statistical mean, we obtain

$$\langle u_i \rangle = U_i + \frac{1}{\sqrt{N}} \sum_{k=1}^N \langle a_{ij} \varepsilon_j^k f_{\sigma(\mathbf{x})}(\mathbf{x} - \mathbf{x}^k) \rangle \quad (4.10)$$

The random variables x_j^k and ε_j^k involved in the mean $\langle a_{ij} \varepsilon_j^k f_{\sigma(\mathbf{x})}(\mathbf{x} - \mathbf{x}^k) \rangle$ are independent thus

$$\langle a_{ij} \varepsilon_j^k f_{\sigma(\mathbf{x})}(\mathbf{x} - \mathbf{x}^k) \rangle = \langle a_{ij} \varepsilon_j^k \rangle \langle f_{\sigma(\mathbf{x})}(\mathbf{x} - \mathbf{x}^k) \rangle \quad (4.11)$$

The term $\langle a_{ij} \varepsilon_j^k \rangle$ simplifies further to $\langle a_{ij} \varepsilon_j^k \rangle = a_{ij} \langle \varepsilon_j^k \rangle = 0$ since the intensities of the eddies is either 1 or -1 with equal probability. Substituting these relations into Eq. (4.10), the mean of the velocity signal u_i is simply the input mean velocity U_i ,

$$\langle u_i \rangle = U_i \quad (4.12)$$

and the fluctuations u'_i around the mean velocity are

$$u'_i = \frac{1}{\sqrt{N}} \sum_{k=1}^N a_{ij} \varepsilon_j^k f_{\sigma(\mathbf{x})}(\mathbf{x} - \mathbf{x}^k). \quad (4.13)$$

We now calculate the Reynolds stresses $\langle u'_i u'_j \rangle$ of the synthesized signal. Using the above expression and the linearity of the statistical mean, we obtain

$$\langle u'_i u'_j \rangle = \frac{1}{N} \sum_{k=1}^N \sum_{l=1}^N a_{im} a_{jn} \langle \varepsilon_m^k \varepsilon_n^l f_{\sigma}(\mathbf{x} - \mathbf{x}^k) f_{\sigma}(\mathbf{x} - \mathbf{x}^l) \rangle. \quad (4.14)$$

Using again the independence between the positions x_j^k and the intensities ϵ_j^k of the eddies, Eq. (4.14) becomes

$$\langle u'_i u'_j \rangle = \frac{1}{N} \sum_{k=1}^N \sum_{l=1}^N a_{im} a_{jn} \langle \epsilon_m^k \epsilon_n^l \rangle \langle f_\sigma(\mathbf{x} - \mathbf{x}^k) f_\sigma(\mathbf{x} - \mathbf{x}^l) \rangle. \quad (4.15)$$

If $k \neq l$ or $m \neq n$ the random variables ϵ_m^k and ϵ_n^l are independent and hence $\langle \epsilon_m^k \epsilon_n^l \rangle = \langle \epsilon_m^k \rangle \langle \epsilon_n^l \rangle = 0$. If $k = l$ and $m = n$, then $\langle \epsilon_m^k \epsilon_n^l \rangle = \langle (\epsilon_m^k)^2 \rangle = 1$ by definition of the intensities of the eddies. Hence we can write,

$$\langle \epsilon_m^k \epsilon_n^l \rangle = \delta_{kl} \delta_{mn}. \quad (4.16)$$

Using the above result, Eq. (4.14) simplifies to

$$\langle u'_i u'_j \rangle = \frac{1}{N} \sum_{k=1}^N a_{im} a_{jn} \underbrace{\langle f_\sigma^2(\mathbf{x} - \mathbf{x}^k) \rangle}_{I_1}. \quad (4.17)$$

The Probability Density Function (PDF) of \mathbf{x}^k is needed in order compute the term I_1 . \mathbf{x}^k follows a uniform distribution over B hence by definition its probability density function writes

$$p_1(\mathbf{x}) = \begin{cases} \frac{1}{V_B}, & \text{if } \mathbf{x} \in B \\ 0, & \text{otherwise} \end{cases} \quad (4.18)$$

Hence we have

$$I_1 = \int_{\mathbb{R}^3} p(\mathbf{y}) f_\sigma^2(\mathbf{x} - \mathbf{y}) d\mathbf{y} = \frac{1}{V_B} \int_B f_\sigma^2(\mathbf{x} - \mathbf{y}) d\mathbf{y} \quad (4.19)$$

Besides by definition of B ,

$$\mathbf{x} \in S, \quad \mathbf{y} \notin B \quad \Rightarrow \quad (\mathbf{x} - \mathbf{y}) \notin \text{supp}(f_\sigma) \quad (4.20)$$

Hence the integral over B on Eq. (4.19) can be replaced by an integral over \mathbb{R}^3 . Using the definition of f_σ and the normalization of f , I_1 rewrites

$$I_1 = \frac{1}{V_B} \int_{\mathbb{R}^3} f_\sigma^2(\mathbf{x} - \mathbf{y}) d\mathbf{y} = 1. \quad (4.21)$$

Finally using the above result into Eq. (4.17) the cross correlation tensor writes

$$\langle u'_i u'_j \rangle = a_{im} a_{jn} = R_{ij} \quad (4.22)$$

since a_{ij} is the Cholesky decomposition of R_{ij} . Hence the Reynolds stresses of the velocity fluctuations generated by the SEM reproduce exactly the input Reynolds stresses R_{ij} .

4.3.3 Two-point and two-time correlations

We now study the two-point cross-correlation of the velocity fluctuations

$$R_{ij}(\mathbf{x}, \mathbf{r}) = \langle u'_i(\mathbf{x}, t) u'_j(\mathbf{x} + \mathbf{r}, t) \rangle, \quad (4.23)$$

where $\mathbf{r} = (r_1, r_2, r_3)$ is a vector defining the relative positions between the two points at which the velocity correlations are computed. Using Eq. (4.3) and the linearity of the statistical mean, we write

$$R_{ij}(\mathbf{x}, \mathbf{r}) = \frac{1}{N} \sum_{k=1}^N \sum_{l=1}^N a_{im} a_{jn} \langle \varepsilon_m^k \varepsilon_n^l f_{\sigma(\mathbf{x})}(\mathbf{x} - \mathbf{x}^k) f_{\sigma(\mathbf{x}+\mathbf{r})}(\mathbf{x} + \mathbf{r} - \mathbf{x}^l) \rangle \quad (4.24)$$

Using again the independence between the positions x_j^k and the intensities ε_j^k of the eddies, together with the result derived in Eq. (4.16), the above expression can be rewritten as

$$R_{ij}(\mathbf{x}, \mathbf{r}) = \frac{1}{N} \sum_{k=1}^N a_{im} a_{jm} \underbrace{\langle f_{\sigma(\mathbf{x})}(\mathbf{x} - \mathbf{x}^k) f_{\sigma(\mathbf{x}+\mathbf{r})}(\mathbf{x} + \mathbf{r} - \mathbf{x}^k) \rangle}_{I_2} \quad (4.25)$$

By definition of the Cholesky decomposition, $a_{im} a_{jm} = R_{ij}$. The term I_2 is computed using the PDF of \mathbf{x}^k defined previously in Eq. (4.18);

$$\langle f_{\sigma(\mathbf{x})}(\mathbf{x} - \mathbf{x}^k) f_{\sigma(\mathbf{x}+\mathbf{r})}(\mathbf{x} + \mathbf{r} - \mathbf{x}^k) \rangle = \frac{1}{V_B} \int_B f_{\sigma(\mathbf{x})}(\mathbf{x} - \mathbf{y}) f_{\sigma(\mathbf{x}+\mathbf{r})}(\mathbf{x} + \mathbf{r} - \mathbf{y}) d\mathbf{y} \quad (4.26)$$

Using the result derived in Eq. (4.20), the above integral over B can be extended to an integral over \mathbb{R}^3 . Using the expression for f_σ , Eq. (4.25) becomes

$$R_{ij}(\mathbf{x}, \mathbf{r}) = R_{ij} \cdot \prod_{l=1}^3 [f_{\sigma(\mathbf{x})} * f_{\sigma(\mathbf{x}+\mathbf{r})}] (r_l) \quad (4.27)$$

where $*$ denotes the convolution product. In the case where $\mathbf{r} = \mathbf{0}$, the above expression simplifies greatly since the cross-correlation product is simply the norm of f_σ and we retrieve the results derived for the Reynolds stresses at the previous section.

For homogeneous turbulence, $\sigma(\mathbf{x} + \mathbf{r}) = \sigma(\mathbf{x}) = \sigma$ is constant and the two-point cross-correlation tensor $R_{ij}(\mathbf{x}, \mathbf{r})$ only depends on \mathbf{r} . The above expression simplifies to

$$R_{ij}(\mathbf{r}) = R_{ij} \cdot \prod_{l=1}^3 [f * f] \left(\frac{r_l}{\sigma} \right) \quad (4.28)$$

The integral length scale is defined as the integral of the two-point correlation and is thus proportional to σ . By integrating Eq. (4.28) it can be proved that in every direction $L = C_f \sigma$, where $C_f = (\int_{\mathbb{R}} f)^2$ is close to unity and only depends on the choice of f . Fourier analysis can also be used to study the signal. The velocity spectrum tensor $\phi_{ij}(\mathbf{k})$ is the Fourier transform of the two-point correlation tensor (Pope, 2000),

$$\phi_{ij}(\mathbf{k}) = \mathcal{F}_{\mathbf{k}} \{ R_{ij}(\mathbf{r}) \}. \quad (4.29)$$

The convolution theorem for cross-correlation states that

$$\mathcal{F}_{\mathbf{k}} \{f \star f\} = (\mathcal{F}_{\mathbf{k}} \{f\})^* \cdot \mathcal{F}_{\mathbf{k}} \{f\} = |\mathcal{F}_{\mathbf{k}} \{f\}|^2. \quad (4.30)$$

Hence the spatial velocity spectrum tensor is written as

$$\phi_{ij}(\mathbf{k}) = R_{ij} \sigma^3 \cdot \prod_{l=1}^3 |\mathcal{F}_{k_l \sigma} \{f\}|^2. \quad (4.31)$$

where $\mathbf{k} = (k_1, k_2, k_3)$. More specifically for instance, the one-dimensional spectra in the x direction is

$$E_{ij}(k) = 2R_{ij} \sigma^3 \cdot |\mathcal{F}_{k \sigma} \{f\}|^2. \quad (4.32)$$

Thus the one-dimensional spectrum of the signal at wavenumber k is proportional to the spectrum of the shape function f at wavenumber $k\sigma$.

We study now the time correlations of the signal. The two-time covariance tensor of the velocity signal $R_{ij}(\mathbf{x}, \tau)$ is the correlation between the process at times t and $t + \tau$. Since the process is stationary, it does not depend upon t ,

$$R_{ij}(\mathbf{x}, \tau) = \langle u'_i(\mathbf{x}, t) u'_j(\mathbf{x}, t + \tau) \rangle. \quad (4.33)$$

Using the definition of $u'_i(\mathbf{x}, t)$ in Eq. (7.2) and the linearity of the statistical mean, we have

$$R_{ij}(\mathbf{x}, \tau) = \frac{1}{N} \sum_{k=1}^N \sum_{l=1}^N a_{im} a_{jn} \langle \epsilon_m^k(t) \epsilon_n^l(t + \tau) f_{\sigma(\mathbf{x})}(\mathbf{x} - \mathbf{x}^k(t)) f_{\sigma(\mathbf{x})}(\mathbf{x} - \mathbf{x}^l(t + \tau)) \rangle. \quad (4.34)$$

The position and intensity of different eddies are independent, so for $k \neq l$ the statistical mean in the above equation can be split as follows,

$$\langle \epsilon_m^k(t) \rangle \langle \epsilon_n^l(t + \tau) \rangle \langle f_{\sigma(\mathbf{x})}(\mathbf{x} - \mathbf{x}^k(t)) \rangle \langle f_{\sigma(\mathbf{x})}(\mathbf{x} - \mathbf{x}^l(t + \tau)) \rangle = 0. \quad (4.35)$$

Thus Eq. (4.34) becomes

$$R_{ij}(\mathbf{x}, \tau) = \frac{1}{N} \sum_{k=1}^N a_{im} a_{jn} \underbrace{\langle \epsilon_m^k(t) \epsilon_n^k(t + \tau) f_{\sigma(\mathbf{x})}(\mathbf{x} - \mathbf{x}^k(t)) f_{\sigma(\mathbf{x})}(\mathbf{x} - \mathbf{x}^k(t + \tau)) \rangle}_{I_3}. \quad (4.36)$$

The random variables involved in the above expression are no longer independent. Indeed, both the position and the intensity of an eddy at a given time depend on its previous states. The term I_3 cannot be split into the product of means as in previous derivations but needs to be computed using the joint probability distribution function of $\mathbf{x}^k(t)$, $\mathbf{x}^k(t + \tau)$, $\epsilon_m^k(t)$ and $\epsilon_n^k(t + \tau)$. I_3 is thus an integral in a four-dimensional space over the above variables. Before computing I_3 we first define $B_\tau \subset B$ such that all eddies present in B_τ at time t will be convected far enough so that they will be recycled at least once before time $t + \tau$:

$$B_\tau = \{\mathbf{x} \in B, (\mathbf{x} + \tau \mathbf{U}_c) \notin B\}. \quad (4.37)$$

If $\mathbf{x}^k(t) \in B_\tau$, then it is going to be recycled between time t and $t + \tau$ and hence both $\mathbf{x}^k(t + \tau)$ and $\varepsilon_n^k(t + \tau)$ will be independent of their previous values. The contribution of the region where $\mathbf{x}^k(t) \in B_\tau$ to the integral in I_3 is thus zero. On the contrary if $\mathbf{x}^k(t) \notin B_\tau$ it will remain inside of the box at time $t + \tau$ and hence $\varepsilon_n^k(t + \tau) = \varepsilon_n^k(t)$ and $\mathbf{x}^k(t + \tau) = \mathbf{x}^k(t) + \tau \mathbf{U}_c$. Therefore both $\mathbf{x}^k(t + \tau)$ and $\varepsilon_n^k(t + \tau)$ depend on the previous position $\mathbf{x}^k(t)$ of eddy k relative to B_τ . For $\mathbf{x}^k(t) \notin B_\tau$, the joint probability density function can thus be written

$$p_1(\mathbf{x}^k(t))\delta(\mathbf{x}^k(t + \tau) - (\mathbf{x}^k(t) + \tau \mathbf{U}_c))p_2(\varepsilon_n^k(t))\delta(\varepsilon_n^k(t + \tau) - \varepsilon_n^k(t)). \quad (4.38)$$

Using the above joint probability density function, the term I_3 in Eq. (4.36) can be computed and the derivation is straight forward. It leads to

$$R_{ij}(\mathbf{x}, \tau) = R_{ij} \int_{B \setminus B_\tau} f_{\sigma(\mathbf{x})}(\mathbf{x} - \mathbf{y})f_{\sigma(\mathbf{x})}(\mathbf{x} - (\mathbf{y} + \tau \mathbf{U}_c))d\mathbf{y} \quad (4.39)$$

Since $\mathbf{y} \in B_\tau \Rightarrow (\mathbf{y} + \tau \mathbf{U}_c) \notin B \Rightarrow f(\mathbf{x} - (\mathbf{y} + \tau \mathbf{U}_c)) = 0$, the integral over $(B \setminus B_\tau)$ in the above expression can be extended to an integral over B . Besides $\mathbf{y} \notin B \Rightarrow f_\sigma(\mathbf{x} - \mathbf{y}) = 0$ as previously demonstrated on Eq. (4.20) therefore the integral in the above expression can be further extended to an integral over \mathbb{R}^3 . Using the definition of f_σ rewrites

$$R_{ij}(\mathbf{x}, \tau) = R_{ij} \cdot \prod_{l=1}^3 [f * f] \left(\frac{\tau U_{c,l}}{\sigma} \right) \quad (4.40)$$

In the case where the convective velocity is in the x -direction only $\mathbf{U}_c = (U_c, 0, 0)$, it rewrites

$$R_{ij}(\mathbf{x}, \tau) = R_{ij} [f * f] \left(\frac{\tau U_c}{\sigma} \right). \quad (4.41)$$

Thus the two-time correlation of the signal at time τ is simply the autocorrelation function of f at separation distance $\tau U_c / \sigma$. By integrating the above equation it can be proved that the integral time scale of the signal writes $T = \sigma / U_c C_f$ where $C_f = (\int_{\mathbb{R}} f)^2$ is close to one and only depends on the choice of f . Thus σ controls both the length-scale and the time-scale of the synthetic signal. Having one single parameter to control both the time and length scales of the signal is not really a problem since most of the time quick motions are generated by small structures and inversely. In order to have a better physical model for our synthetic turbulence, we could have used a local convective velocity \mathbf{U}_c for each eddy (computed at its centre for instance) instead of one constant velocity for all eddies. However this would mean some regions are populated with faster moving eddies than others, therefore spending less time than others inside the box which is impossible. In all our derivations we required that the distribution of eddies for all times remain uniform over B which is ensured by taking a constant convective \mathbf{U}_c velocity for all eddies.

Since the signal is stationary, the information the two-time cross-correlation tensor $R_{ij}(\mathbf{x}, \tau)$ contains can be re-expressed in terms of the wavenumber velocity spectrum tensor,

$$\phi_{ij}(\mathbf{x}, \omega) = \mathcal{F}_\omega \{ R_{ij}(\mathbf{x}, \tau) \}. \quad (4.42)$$

Using again the convolution theorem as expressed, the above expression simplifies to

$$\phi_{ij}(\mathbf{x}, \omega) = R_{ij} \frac{\sigma}{|U_c|} |\mathcal{F}_{\omega\sigma/|U_c|}\{f\}|^2. \quad (4.43)$$

The temporal spectrum of the signal is simply the spectrum of the shape function f rescaled by the time-scale $\sigma/|U_c|$.

4.3.4 Probability density function and higher order statistics

Another way of expressing the SEM velocity fluctuations by rearranging Eq. (4.3) is,

$$u'_i(\mathbf{x}, t) = \frac{1}{\sqrt{N}} \sum_{k=1}^N X_i^{(k)} \quad \text{with} \quad X_i^{(k)} = a_{ij} \varepsilon_j^k f_\sigma(\mathbf{x} - \mathbf{x}^k). \quad (4.44)$$

$X_i^{(k)}$ are independent random variables which follow the same distribution, and therefore the central limit theorem can apply. This states that when N tends towards infinity, the probability density function of $u'_i(\mathbf{x}, t)$ tends towards a Normal distribution $N(\mu_i, \sigma_i^2)$ of mean $\mu_i = \langle X_i^{(k)} \rangle$ and of variance $\sigma_i^2 = \langle (X_i^{(k)})^2 \rangle$ (it was shown previously that $\mu_i = 0$ and $\sigma_i^2 = R_{ii}$). In other words, as the number of eddies N tends towards infinity, the signature of each eddy in the final synthetic signal becomes more faint and the final signal tends toward a universal Gaussian state. Higher order moments of the signal (i.e. the skewness and flatness) can be computed in order to better understand the behaviour of the signal and characterize its probability density function when a reduced number of eddies is used.

Using Eq. (4.44), the skewness of the velocity signal writes,

$$S_{u_i} = \frac{\langle u_i'^3 \rangle}{\langle u_i'^2 \rangle^{3/2}} = \frac{1}{(NR_{ii})^{3/2}} \left\langle \left(\sum_{k=1}^N X_i^{(k)} \right)^3 \right\rangle. \quad (4.45)$$

The multinomial theorem will help us expand the above sum. It states that for any positive integer m and any non-negative integer n ,

$$(x_1 + x_2 + \cdots + x_m)^n = \sum_{k_1, k_2, \dots, k_m} \frac{n!}{k_1! k_2! \cdots k_m!} x_1^{k_1} x_2^{k_2} \cdots x_m^{k_m} \quad (4.46)$$

where the above sum is taken over the non-negative integers k_i such that $\sum_{i=1}^m k_i = n$. Applied to Eq. (4.45), using again the linearity of the statistical mean and the independence between the \mathbf{X}^k , we obtain

$$S_{u_i} = \frac{1}{(NR_{ii})^{3/2}} \sum_{k_1, k_2, \dots, k_N} \frac{n!}{k_1! k_2! \cdots k_N!} \left\langle \left(X_i^{(1)} \right)^{k_1} \right\rangle \left\langle \left(X_i^{(2)} \right)^{k_2} \right\rangle \cdots \left\langle \left(X_i^{(N)} \right)^{k_N} \right\rangle. \quad (4.47)$$

Since we must have $\sum_{p=1}^N k_p = 3$, the only possible solutions are for all k_p to be zero except for three, which must satisfy either $3+0+0=3$ or $2+1+0=3$ or $1+1+1=3$. Since the average fluctuations generated by each eddy is zero, it follows that $\langle (X_i^p)^{k_p} \rangle = 0$ if $k_p = 1$; the multiplicative nature of Eq.

(4.47) implies a nondegenerate sum only if the contributions to k_p of the form $3 + 0 + 0$ are employed. Using the independence of position and intensities, the third order moment of X_i^P is given by

$$\langle (X_i^P)^3 \rangle = \left\langle (a_{ij}\epsilon_j^k)^3 \right\rangle \left\langle (f_\sigma(\mathbf{x} - \mathbf{x}^k))^3 \right\rangle. \quad (4.48)$$

Using the multinomial theorem again, the term $\left\langle (a_{ij}\epsilon_j^k)^3 \right\rangle$ is expanded into

$$\left\langle (a_{ij}\epsilon_j^k)^3 \right\rangle = \sum_{k_1, k_2, k_3} \frac{3!}{k_1! k_2! k_3!} \left(a_{i1}\epsilon_1^k \right)^{k_1} \left(a_{i2}\epsilon_2^k \right)^{k_2} \left(a_{i3}\epsilon_3^k \right)^{k_3} \quad (4.49)$$

with $k_1 + k_2 + k_3 = 3$. By definition, $\langle \epsilon_j^k \rangle = 0$ and $\langle (\epsilon_j^k)^3 \rangle = 0$ since the intensities are taken from a non-skewed distribution. The multiplicative nature of Eq. (4.49) implies that all the terms in the sum are zero. As a result the third order moment of X_i^P is zero and all the terms in the sum on Eq. (4.47) are zero. Consequently the skewness of the velocity signal is zero,

$$S_{u_i} = 0. \quad (4.50)$$

We now calculate the flatness of the signal which, using Eq. (4.44), develops into

$$F_{u_i} = \frac{\langle u_i'^4 \rangle}{\langle u_i'^2 \rangle^2} = \frac{1}{N^2 R_{ii}^2} \left\langle \left(\sum_{k=1}^N X_i^k \right)^4 \right\rangle. \quad (4.51)$$

Using again the multinomial theorem plus the linearity of the statistical mean and the independence of the \mathbf{X}^k the above expression expands into

$$F_{u_i} = \frac{1}{(NR_{ii})^2} \sum_{k_1, k_2, \dots, k_N} \frac{n!}{k_1! k_2! \dots k_N!} \left\langle (X_i^1)^{k_1} \right\rangle \left\langle (X_i^2)^{k_2} \right\rangle \dots \left\langle (X_i^N)^{k_N} \right\rangle. \quad (4.52)$$

with $\sum_{p=1}^N k_p = 4$. The above sum involves first, second, third and fourth order moments of X_i^k . We have already seen that the first and third order moments of X_i^k are zero and that the second order moment of X_i^k is R_{ii} . We now compute the fourth order moment of X_i^k , which is written as

$$\left\langle (X_i^k)^4 \right\rangle = \left\langle (a_{ij}\epsilon_j^k f_\sigma(\mathbf{x} - \mathbf{x}^k))^4 \right\rangle = \left\langle (a_{ij}\epsilon_j^k)^4 \right\rangle \left\langle (f_\sigma(\mathbf{x} - \mathbf{x}^k))^4 \right\rangle \quad (4.53)$$

using the independence between position and intensity of the eddies. The term $\langle (a_{ij}\epsilon_j^k)^4 \rangle$ is somewhat complicated to compute, because of the off-diagonal terms of the Cholesky decomposition a_{ij} of the Reynolds stress tensor. Additionally these off-diagonal terms are relatively unimportant for the final expression of the flatness we are going to derive. To simplify the derivations we then first restrict ourselves to the case where only the normal stresses of the Reynolds stress tensor R_{ij} are prescribed. The Cholesky decomposition a_{ij} of the Reynolds stress tensor is then a diagonal matrix $a_{ii} = \sqrt{R_{ii}}$ and consequently

the term $\langle (a_{ij}\varepsilon_j^k)^4 \rangle$ simplifies to $R_{ii}^2 F_\varepsilon$, where F_ε is the flatness of the PDF of ε_j^k . The second term on Eq. (4.53) is computed using the probability density function of \mathbf{x}^k and the definition of f_σ ,

$$\left\langle (f_\sigma(\mathbf{x} - \mathbf{x}^k))^4 \right\rangle = \frac{1}{V_B} \int_B f_\sigma(\mathbf{x} - \mathbf{y})^4 d\mathbf{y} = \frac{V_B F_f^3}{\sigma^3} \quad (4.54)$$

where F_f is the flatness of the shape function f . Finally using the above results, Eq. (4.53) rewrites

$$\left\langle (X_i^k)^4 \right\rangle = R_{ii}^2 F_\varepsilon \frac{V_B F_f^3}{\sigma^3} \quad (4.55)$$

Using the expression for the second and fourth order moments of (X_i^k) into Eq. (4.52) we finally obtain

$$F_{u_i} = \frac{1}{(NR_{ii})^2} \left(4N \frac{R_{ii}^2 F_\varepsilon V_B F_f^3}{\sigma^3} + \frac{6N(N-1)}{2} R_{ii}^2 \right) \quad (4.56)$$

which further simplifies in

$$F_{u_j} = 3 + \frac{1}{N} \left(4F_f^3 F_\varepsilon \frac{V_B}{\sigma^3} - 3 \right) \quad (4.57)$$

An important result is that the flatness of the velocity fluctuations tends towards its Gaussian value of 3 as $\frac{1}{N}$. For a fixed value of N , the flatness can be significantly larger than 3 if the ratio $\frac{V_B}{\sigma^3}$ is large. This corresponds to the case where the box of eddies is insufficiently filled with eddies because either B is too large or the eddies are too small. The expression derived on Eq. (4.57) is only valid when the Reynolds stress tensor is diagonal. In the general case where the shear stresses are also prescribed we mentioned previously that expression of the flatness was similar. This is indeed the case and in the general case we can write

$$F_{u_j} = 3 + \frac{1}{N} \left(A \frac{V_B}{\sigma^3} + B \right), \quad (4.58)$$

where A and B are relatively close to unity and only depend on the flatness of f and ε and the Reynolds stress tensor. The expression for the flatness in the general case is thus very similar to Eq. (4.57), the main dependence being on the number of eddies N , and the ratio $\frac{V_B}{\sigma^3}$.

4.4 Simulation of Instantaneous Signals

The SEM as described in Section 4.2 has been implemented. Synthetic isotropic turbulence is now simulated using the SEM in order to illustrate the possibilities of the method with practical examples. To check the validity of our particular implementation of the SEM, time averaged statistics extracted from our simulation are compared with exact results derived in the previous section.

Isotropic synthetic fluctuations are generated on a two-dimensional (Oyz) plane with the SEM. The dimensions of the plane are $2\pi \times 2\pi$. There is a mean flow $U_0 = 10 \text{ m/s}$ in the x -direction normal to the

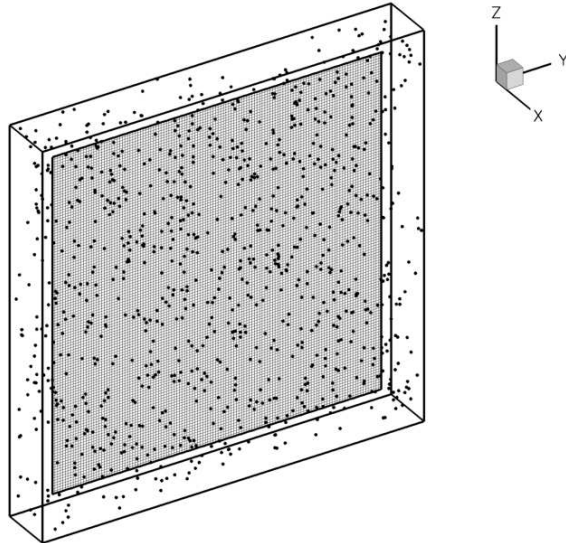


Figure 4.2: 128×128 two-dimensional grid, box of eddies and initial population of eddies. Simulation of isotropic turbulence with the SEM.

plane and the rms velocity is $u'_0 = 1 \text{ m/s}$. In wind-tunnel experiments, this situation is approached by passing a uniform stream through a grid.

The velocity fluctuations generated by each eddy are described by the shape function f ,

$$f(x) = \begin{cases} \sqrt{\frac{3}{2}} (1 - |x|), & \text{if } x < 1 \\ 0, & \text{otherwise} \end{cases} \quad (4.59)$$

The radius of each eddy is taken to be constant $\sigma = 0.5 \text{ m}$ and the number of eddies is $N = 1,000$. The velocity fluctuations generated by the SEM are evaluated on a discrete grid with 128 cells in each direction ($\Delta y = \Delta z \approx 0.1\sigma$) every $dt = 0.1 \sigma/U_0$. Fig. 4.2 shows the grid, the box of eddies surrounding it and the initial population of eddies before the first time step.

Fig. 4.3 shows the time history of u , v and w recorded at point $(x,y) = (\pi,\pi)$ and instantaneous contours of u , v and w on the two-dimensional plane after 1,000 iterations. The signal is stationary in time and homogeneous and isotropic in space as expected. Fig. 4.4 shows the convergence history of the time averaged mean velocity, Reynolds stresses, skewness and flatness of the signal at point $(x,y) = (\pi,\pi)$. The statistics (in the sense of the statistical mean using results of the previous section) of the generated signal are

$$\langle u \rangle = U_0, \quad \langle u_i u_j \rangle = u'_0 \delta_{ij}, \quad S_{u_i} = 0, \quad F_{u_i} = 3 + \frac{1}{N} \left(4F_f^3 F_\varepsilon \frac{V_B}{\sigma^3} - 3 \right). \quad (4.60)$$

In our case, $F_\varepsilon = 1$, $F_f = 0.9$, $V_B \approx 50 \text{ m}^3$ and $\sigma = 0.5 \text{ m}$ therefore the target flatness is around 4.1. All the time averages of the various moments shown in Fig. 4.4 converge to their target statistical mean

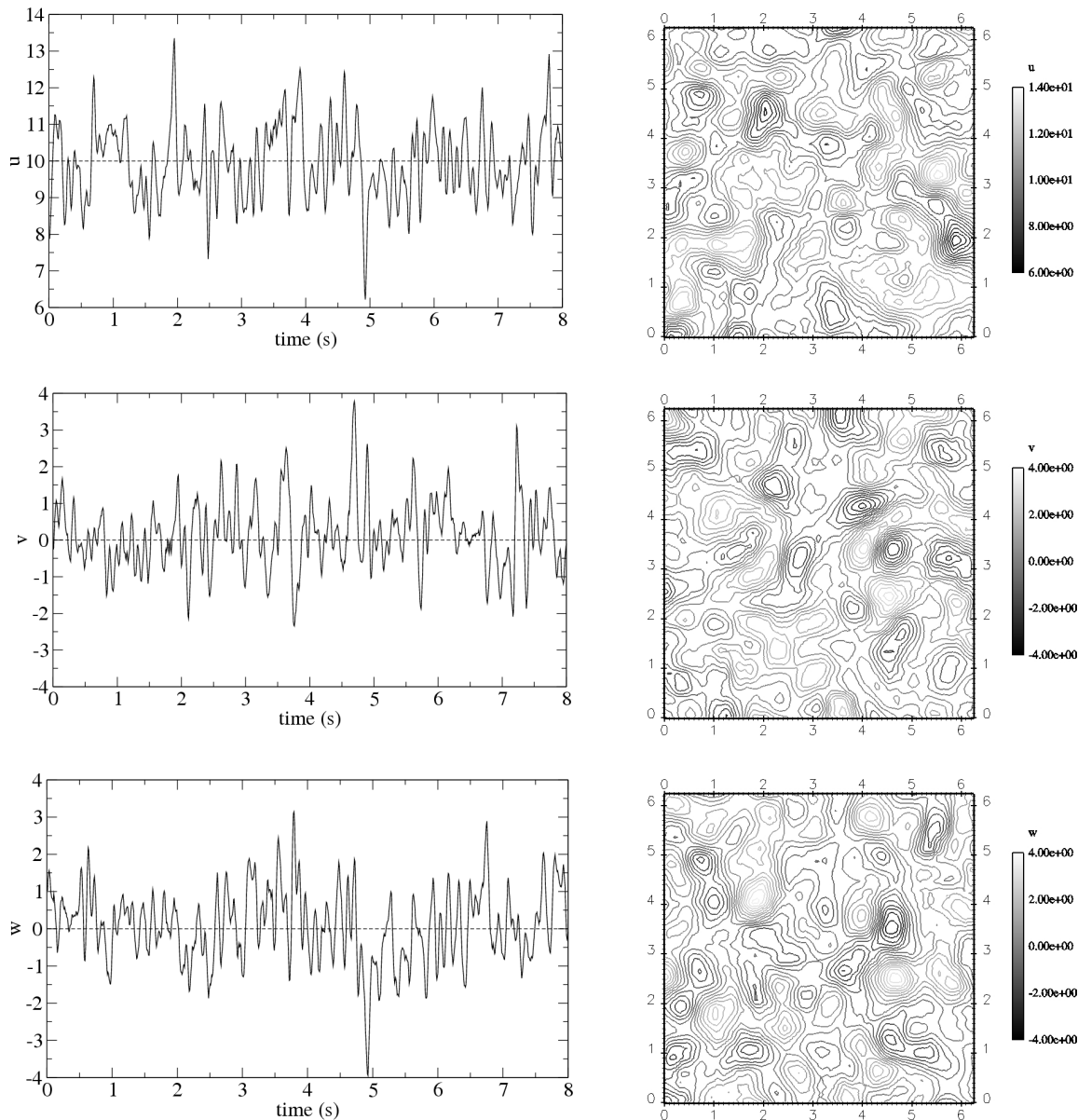


Figure 4.3: Time history and velocity field of u , v and w from top to bottom. Simulation of isotropic turbulence with the SEM.

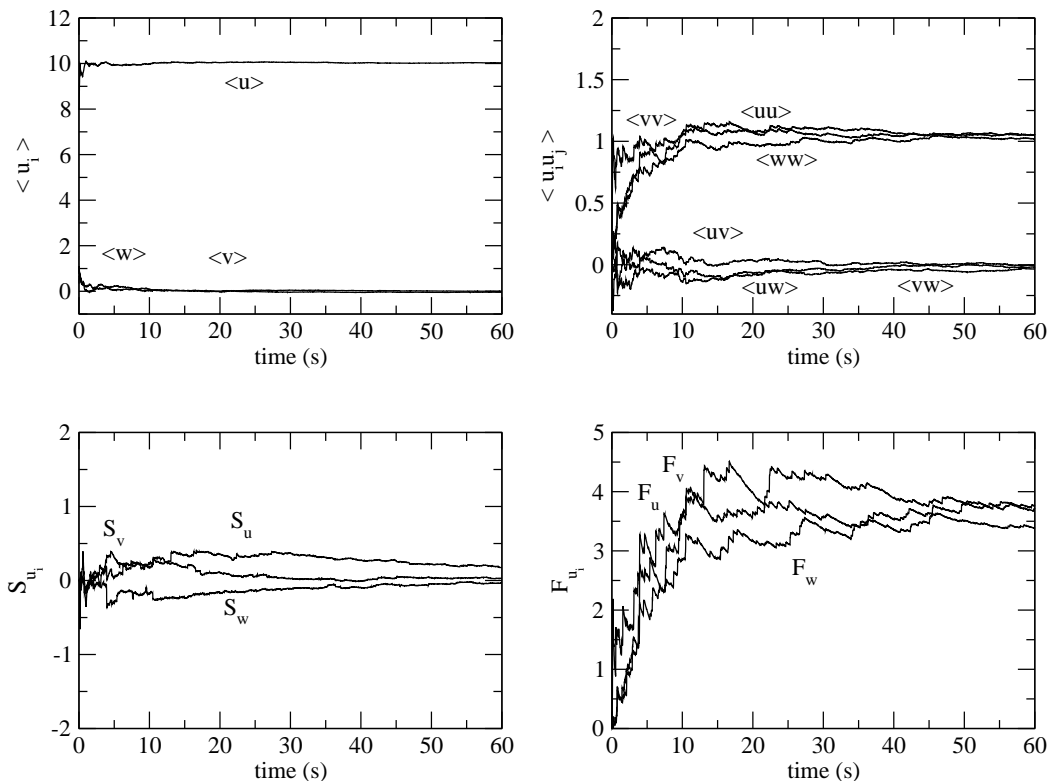


Figure 4.4: Time history of time averaged u_i (top left), $u'_i u'_j$ (top right), skewness (bottom left) and flatness (bottom right) at point $(x, y) = (\pi, \pi)$. Simulation of isotropic turbulence with the SEM.

Run	U_0 ($m s^{-1}$)	u'_0 ($m s^{-1}$)	N	σ (m)	f
DIT A	10	1	1,000	0.5	tent function
DIT B	10	1	10	0.5	tent function
DIT C	10	1	100	0.5	tent function
DIT D	10	1	10,000	0.5	tent function
DIT E	10	1	1,000	0.5	step function
DIT F	10	1	1,000	0.5	gaussian function
DIT G	10	1	1,000	0.25	tent function
DIT H	10	1	1,000	1.0	tent function

Table 4.1: Parameter settings used in the simulation of isotropic turbulence with the SEM.

values, even though skewness and flatness require further averaging to be fully converged. The time averaged two-point correlations and one-dimensional energy spectra in the y -direction of the three velocity components are shown in Fig. 4.5. The expected two-point correlations and one-dimensional spectra have been computed from Eq. (4.28) and Eq. (4.32) derived in the previous section. The time averaged correlations and spectra agree very well with their expected values, except for the spectra at very high wave numbers where discrepancies can be observed. Errors between the computed and theoretical spectra can be attributed to the non-periodicity of the SEM signal in the direction where the spectra are computed. This could have been corrected by ensuring that the signal is periodic, for instance by creating ghost vortices at the boundaries where periodic boundary conditions should apply (see Sergent (2002)). However it is noted in Keating et al. (2004) that no difference in the development of turbulence in a channel downstream of the inlet is observed when the inflow data is made periodic in the spanwise direction. Additionally, from an engineering point of view, a special treatment at the boundary where periodic boundary conditions should apply would make the method less portable and would complicate greatly its implementation. To conclude, all comparisons made between the signal generated by our implementation of the SEM and exact results derived in the previous section agree very well. This validates our implementation.

We will now investigate the effect on the synthesized signal of a change in the input parameters of the method. Table 4.1 provides the details of the different simulations carried out. We study first the influence of the number of eddies. The previous reference run (DIT A) with 1,000 eddies is reproduced with $N = 10$ (DIT B), $N = 100$ (DIT C) and $N = 10,000$ eddies (DIT D). Results are compared in Fig. 4.6. The time history of v on the left column clearly shows that the less eddies there are present, the more intermittent the signal is. The run with $N = 10$ eddies shows whole regions empty of any fluctuations

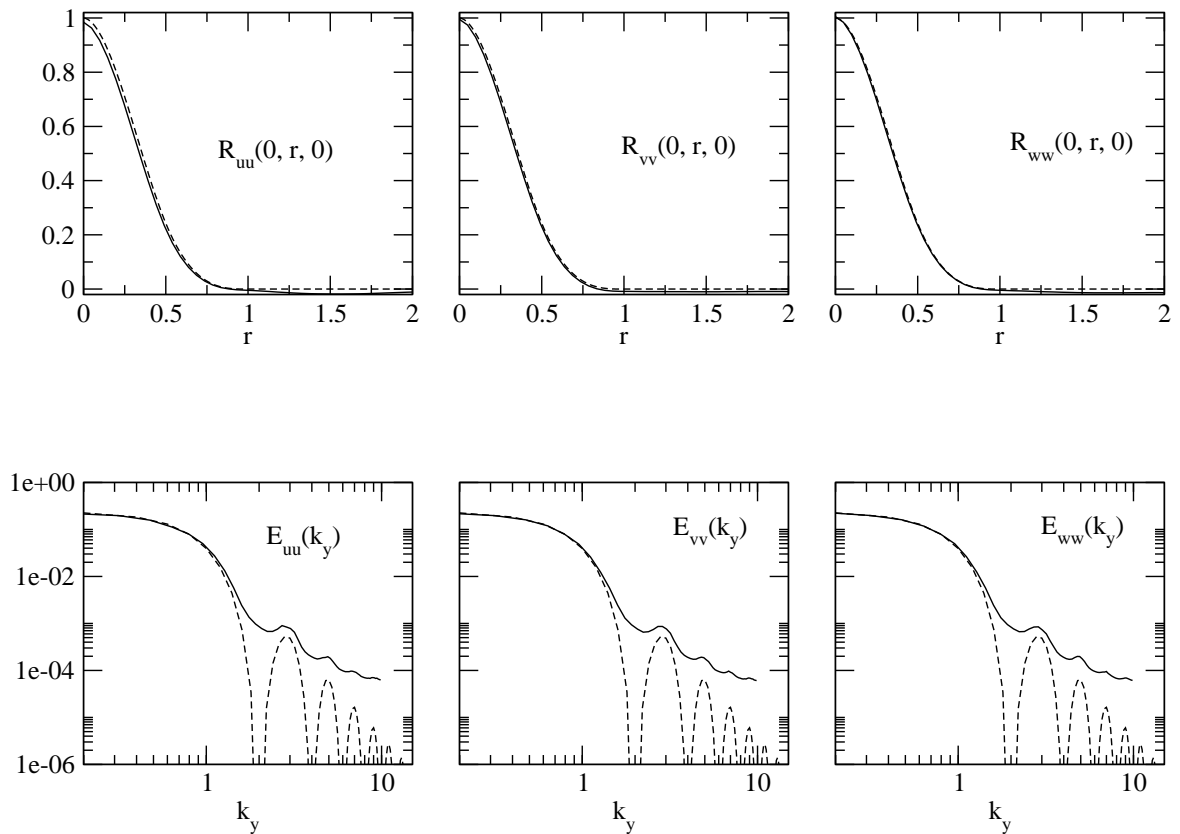


Figure 4.5: Two-point correlations (top) and one dimensional energy spectra (bottom) in the y direction for the velocity components of the simulated SEM signal: dashed lines represent the expected values as calculated in the previous section.

in between some very intense eddies. Since the energy of the signal does not depend on the number of eddies, the less eddies are present, the more energy each eddy carries. These conclusions are confirmed by the probability density function of v . The less eddies there are present, the more peaked around zero the probability density function is (values around zero are very likely) and the longer the tails are (very large fluctuations are more frequent). For the run with $N = 10,000$, the PDF is very close to a normal distribution which is simply an illustration of the central limit theorem. The tails of the probability density function in the case with $N = 10,000$ are not well averaged because they correspond to very improbable events, and have not been observed enough in the limited time sample over which the averages have been accumulated.

We study now the influence of the shape function f of the eddies. The previous reference run (DIT A) using a tent function is reproduced using instead a step function (DIT E),

$$f(x) = \begin{cases} \frac{1}{\sqrt{2}}, & \text{if } x < 1 \\ 0, & \text{otherwise,} \end{cases} \quad (4.61)$$

and a truncated Gaussian function (DIT F),

$$f(x) = \begin{cases} Ce^{-9x^2/2}, & \text{if } x < 1 \\ 0, & \text{otherwise.} \end{cases} \quad (4.62)$$

where the constant C is tuned to ensure that the truncated Gaussian has the normalization of Eq. (4.5). Fig. 4.7 shows the different shape functions f used and time averaged one-dimensional energy spectra and instantaneous contours of v . Theoretical one-dimensional energy spectra obtained from Eq. (4.32) are included for comparisons (dashed lines). The signal using a step function contains more energy at high frequencies than the two other signals. The signal using the tent function and the signal using the truncated Gaussian function cannot really be differentiated by mere observation of the instantaneous fields. The signal using the truncated Gaussian should be much less energetic than the tent function signal in its small scales, however due to the non-periodicity of the SEM signal, errors dominate the high frequency part of the spectra making both spectra undistinguishable at high frequencies.

Finally, we investigate the influence of the size of the eddies σ . The reference run (DIT A) is reproduced with $\sigma = 0.25m$ (DIT G) and $\sigma = 1m$ (DIT H). The time history, the PDF and the instantaneous contours of v are shown in Fig. 4.8. As expected the bigger σ is, the larger the length and time scales of the signal are. However σ does not only control the length scale of the synthesized signal but also its probability density function. The smaller the eddies are, the more peaked around zero the probability density function is. Indeed if one reduces the size of the eddies without adding more eddies inside of

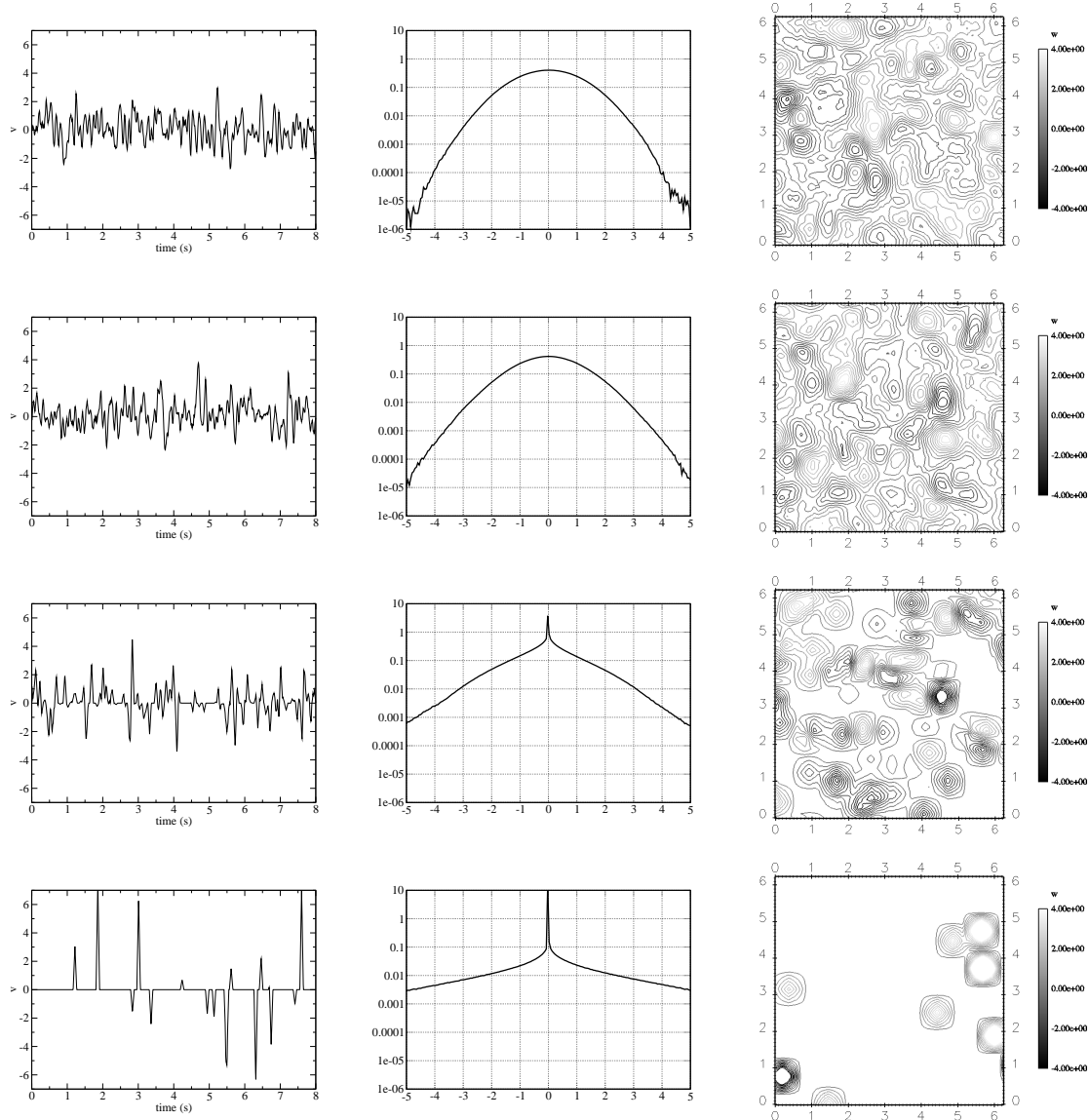


Figure 4.6: Simulation of isotropic turbulence with the SEM using different number of eddies. From top to bottom: $N = 10,000$, $N = 1,000$, $N = 100$ and $N = 10$; From left to right: Time history of v , probability density function of v and instantaneous contours of w .

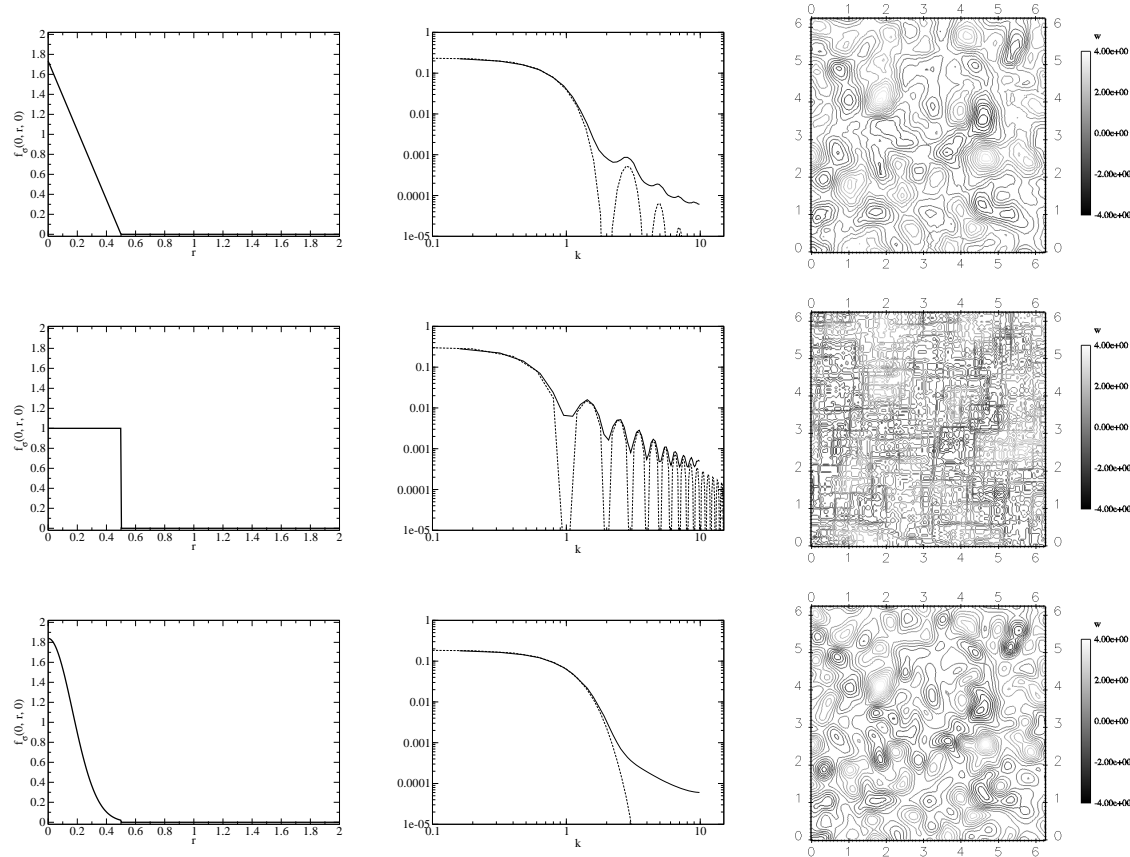


Figure 4.7: Simulation of isotropic turbulence with the SEM using different shape functions. From top to bottom: f is a tent function, a step function and a truncated gaussian function; From left to right: Shape function f , one-dimensional energy spectrum of v in the y -direction and instantaneous contours of w .

the box then the size of the region influenced by the eddies will decrease and the turbulent signal will become more patchy and intermittent. As expected from Eq. (4.57) obtained in the previous section for the flatness,

$$F_{u_i} \approx 3 + \frac{1}{N} \left(4F_f F_\epsilon \frac{V_B}{\sigma^3} - 3 \right), \quad (4.63)$$

we should adapt the number of eddies N to the size of the eddies σ if we want to limit the flatness of the signal. The limiting case is for N tending towards infinity where the second term in the above expression becomes so small that the flatness is seemingly independent of σ . However in practical applications, N should be kept as small as possible in order to limit the cost of generating the inflow data. In Chapter 7, a formulae to set N without any user intervention, solely from the input data of the SEM will be derived.

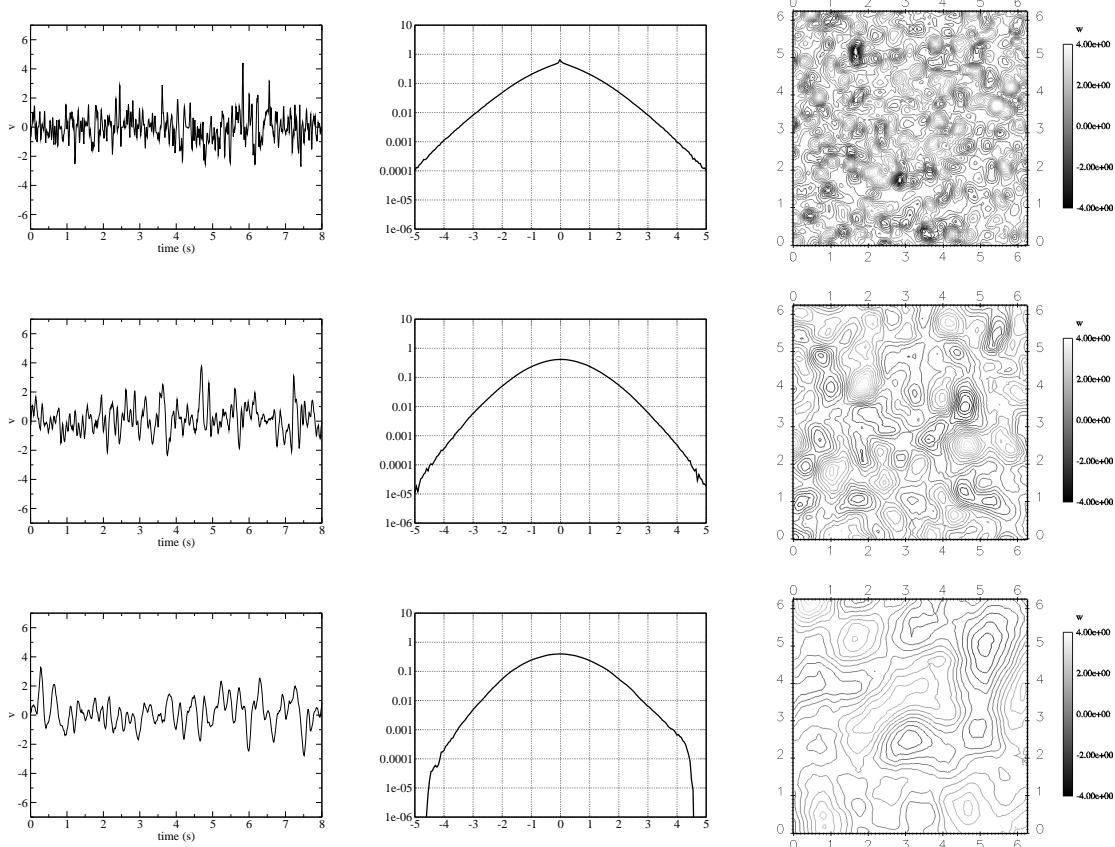


Figure 4.8: Simulation of isotropic turbulence with the SEM using different values of σ . From top to bottom: $\sigma = 0.25m$ (DIT G), $\sigma = 0.5m$ (DIT A) and $\sigma = 1m$ (DIT H); From left to right: Time history of v , probability density function of v and instantaneous contours of w .

Chapter 5

Computational Techniques

5.1 Introduction

In the following sections, we describe the equations governing the motion of the flows considered in this thesis. In Section 5.2, the RANS and LES governing equations for averaged and filtered quantities are derived and details of the turbulence models used to close the equations are provided. The CFD code, *Code_Saturne* (Archambeau et al., 2004), is used to solve the equations and is presented in Section 5.3 with specific emphasis on the capabilities of the code used in this thesis. Aspects of the fractional-step method and time-advancing scheme, spatial discretization and boundary conditions are described in detail.

5.2 Governing Equations

We restrict ourselves to the simulation of incompressible flows where the mass density ρ and the dynamic viscosity μ are constant. In this case, the equations governing the evolution of the velocity \mathbf{u} and pressure p of the fluid reads

$$\rho \frac{\partial \mathbf{u}}{\partial t} + \nabla \cdot (\rho \mathbf{u} \otimes \mathbf{u}) = -\nabla p + \nabla \cdot \underline{\underline{\sigma}}, \quad (5.1)$$

$$\nabla \cdot \mathbf{u} = 0. \quad (5.2)$$

For a Newtonian fluid the viscous stress tensor σ is given by $\underline{\underline{\sigma}} = 2\mu \underline{\underline{S}}$ where

$$\underline{\underline{S}} = \frac{1}{2}(\nabla \mathbf{u} + (\nabla \mathbf{u})^T) \quad (5.3)$$

is the strain tensor. Eq. (5.1) and (5.2) are referred to as the Navier-Stokes equations.

We saw in Chapter 2 that the direct numerical simulation of the above Navier-Stokes equations was computationally extremely costly due to the many different scales involved. In order to reduce the complexity of the system to be simulated, a smoothing operator has to be applied to the exact solution \mathbf{u} of the Navier-Stokes equations. Labourasse and Sagaut (2002) defined the RANS averaging operator (see Eq. (2.13) on page 48) and the LES spatial filtering operator (see Eq. (2.10) on page 46) in the general framework of multilevel methods relying on different scale separation operators. The RANS and the LES representations of the flow field are seen as two lower levels of description of the exact solution \mathbf{u} of the Navier-Stokes equations. In the following of the section, the RANS and LES averaging operators will both be denoted by $\bar{\mathbf{u}}$, and governing equations for the filtered/averaged quantities $\bar{\mathbf{u}}$ and \bar{p} will be derived. By applying either the RANS or the LES scale separation operator to the Navier-Stokes equations, and assuming that the LES spatial filter and the derivative operators commute, we obtain

$$\rho \frac{\partial \bar{\mathbf{u}}}{\partial t} + \nabla \cdot (\rho \bar{\mathbf{u}} \otimes \bar{\mathbf{u}}) = -\nabla \bar{p} + \nabla \cdot (\bar{\underline{\sigma}} + \underline{\underline{\tau}}), \quad (5.4)$$

$$\nabla \cdot \bar{\mathbf{u}} = 0, \quad (5.5)$$

where $\underline{\underline{\tau}} = -\rho(\bar{\mathbf{u}} \otimes \bar{\mathbf{u}} - \bar{\mathbf{u}} \otimes \bar{\mathbf{u}})$. It represents the Reynolds stress tensor in RANS and the subgrid-scale stress tensor in LES. In order for the above set of equations to be closed, τ needs to be modelled as a function of known quantities. In both models, an eddy viscosity model is used:

$$\underline{\underline{\tau}} + \frac{1}{3} \text{tr}(\underline{\underline{\tau}}) \underline{\underline{Id}} = 2\mu_t \bar{\underline{\underline{S}}} \quad (5.6)$$

where Id is the identity matrix and $\text{tr}(A)$ is the trace of matrix A . Thus Eq. (5.4) can be rewritten as

$$\rho \frac{\partial \bar{\mathbf{u}}}{\partial t} = -\nabla \bar{p} + \nabla \cdot \underline{\underline{F}}(\bar{\mathbf{u}}) \quad (5.7)$$

where the operator $\underline{\underline{F}}$ represents the sum of the convection and diffusion fluxes.

$$\underline{\underline{F}}(\bar{\mathbf{u}}) = -\rho \bar{\mathbf{u}} \otimes \bar{\mathbf{u}} + (\mu + \mu_t)(\nabla \bar{\mathbf{u}} + (\nabla \bar{\mathbf{u}})^T). \quad (5.8)$$

Based on the eddy viscosity hypothesis, the closure problem of modelling a 3×3 second order tensor $\underline{\underline{\tau}}$ is changed to modelling only one scalar μ_t . Eq. (5.7) is used both in RANS and in LES regions of the flow. The different nature of the solution in the RANS and LES regions depends solely on the computation of the eddy viscosity μ_t which is going to be detailed herein.

The SST two-equation model of Menter (1994) is the only RANS model used in this thesis therefore it will be detailed herein. In addition to the RANS equations above, the SST model solves two transport

equations for the turbulent kinetic energy k and the rate of dissipation per unit of kinetic energy ω ,

$$\frac{\partial k}{\partial t} + \nabla \cdot (\bar{u}k) = P_k - \beta^* k \omega + \nabla \cdot \left[\left(v + \frac{v_t}{\sigma_k} \right) \nabla k \right], \quad (5.9)$$

$$\frac{\partial \omega}{\partial t} + \nabla \cdot (\bar{u}\omega) = \alpha \frac{\omega}{k} P_k - \beta \omega^2 + \nabla \cdot \left[\left(v + \frac{v_t}{\sigma_\omega} \right) \nabla \omega \right] + 2 \frac{(1 - F_1)}{\sigma_{\omega 2}} \frac{1}{\omega} \nabla k \cdot \nabla \omega, \quad (5.10)$$

where $P_k = 2v_t S_{ij} S_{ij}$ is the production of turbulent kinetic energy in closed form. The turbulent viscosity v_t is given by

$$v_t = \frac{a_1 k}{\max(a_1 \omega; \sqrt{2S_{ij} S_{ij}} F_2)}. \quad (5.11)$$

The blending functions F_1 and F_2 appearing in Eq. (5.10) and Eq. (5.11) are given by

$$F_1 = \tanh(arg_1^4), \quad (5.12)$$

$$arg_1 = \min \left[\max \left(\frac{\sqrt{k}}{0.09\omega y}; \frac{500v}{y^2\omega} \right); \frac{4\rho k}{\sigma_{\omega 2} CD_{k\omega} y^2} \right], \quad (5.13)$$

$$CD_{k\omega} = \max \left(2\rho \frac{1}{\sigma_{\omega 2} \omega} \nabla k \cdot \nabla \omega; 10^{-20} \right), \quad (5.14)$$

and

$$F_2 = \tanh(arg_2^2), \quad (5.15)$$

$$arg_2^2 = \max \left(\frac{2\sqrt{k}}{0.09\omega y}; \frac{500v}{y^2\omega} \right). \quad (5.16)$$

Here, y represents the distance from the wall. The model uses a value of any coefficient c computed from

$$c = F_1 c_1 + (1 - F_1) c_2, \quad (5.17)$$

where c_1 and c_2 are the closure coefficients for the SST model shown in Table 5.1. Additional constants used by the model are $C_\mu = 0.09$, $a_1 = 0.31$ and $\kappa = 0.41$. This model has been chosen here for its robustness and good performance over a wide range of flows (Menter, 1994).

α_1	β_1	σ_{k1}	$\sigma_{\omega 1}$
$\beta_1/\beta^* - \kappa^2/(\sigma_{\omega 1} \sqrt{\beta^*})$	0.075	1.176	2
α_2	β_2	σ_{k2}	$\sigma_{\omega 2}$
$\beta_2/\beta^* - \kappa^2/(\sigma_{\omega 2} \sqrt{\beta^*})$	0.0828	1.0	1.1682

Table 5.1: Coefficients of the SST model.

In LES regions of the flow, the standard Smagorinsky model is used (Smagorinsky, 1963). The eddy viscosity is computed from

$$v_t = (C_s \bar{\Delta})^2 \sqrt{2S_{ij}S_{ij}}, \quad (5.18)$$

where $C_s = 0.065$ is the Smagorinsky constant typically used in the simulation of wall-bounded flows (Deardorff, 1970) and the filter width $\bar{\Delta}$ is twice the cubic root of the cell volume. A Van Driest (1956) damping function is used to reduce the Smagorinsky constant close to the wall as,

$$C_s(1 - e^{-y^+/A^+}) \quad \text{with} \quad A^+ = 26, \quad (5.19)$$

where y represents the distance from the wall.

5.3 Numerical Method

The finite volume code, *Code_Saturne*, is used to solve the above set of equations. *Code_Saturne* is an industrial CFD code developed at Electricité de France (EDF) over the past 10 years. It was released for external use in 2001 and was made open source in 2007. It has been used in various applications such as nuclear flow problems, process engineering, heating and ventilation, dispersion and combustion, pollutant prediction in gas turbines and thermal shock in a pressure water reactor vessel. In this section, we describe the spatial and temporal discretization of the transport equations presented above. The reader is referred to Archambeau et al. (2004) for further information on all of the capabilities of *Code_Saturne*.

5.3.1 Time discretization

In *Code_Saturne*, the filtered Navier-Stokes equations Eq. (5.4) and Eq. (5.5) are integrated in time using a fractional step technique that can be associated with the SIMPLEC method of Van Doormal and Taithby (1984). The first step consists in a prediction of the velocity by solving the momentum equation with an explicit pressure gradient. After this prediction step a new velocity field \mathbf{u}^* is obtained which is usually not divergence free. The second step consists of calculating the pressure gradient in order to correct the predicted velocity. The reader is referred to Ferziger and Perić (1999) for further details on this fractional step technique. In the following, we describe the time discretization of the equations between time-steps n and $n + 1$.

In order to linearize the momentum equation Eq. (5.7), the operator $\underline{\underline{F}}$ is approximated by $\underline{\underline{F}}_l$ as follows

$$\underline{\underline{F}}_l(\mathbf{u}) = \mathbf{Q}^e \otimes \mathbf{u} + (\mu + \mu_t)(\nabla \mathbf{u} + \nabla^T \mathbf{u}) \quad (5.20)$$

where $\mathbf{Q}^e = \rho \mathbf{u}^e$ is the momentum computed using an explicit Euler method in the RANS regions and an explicit Adams-Bashforth method in the LES regions. The diffusion term and the remaining part of the convection term in $\underline{\underline{F}}_l$ are discretized using an implicit second order Crank-Nicolson method in the LES regions, and an implicit first order Euler scheme in the RANS regions. Thus the first step (prediction step) of the fractional step advancement scheme used in *Code_Saturne* can be written as follows

$$\frac{\rho \mathbf{u}^* - \rho \mathbf{u}^n}{\Delta t} + \theta \nabla \cdot \underline{\underline{F}}_l(\mathbf{u}^*) = (1 - \theta) \nabla \cdot \underline{\underline{F}}_l(\mathbf{u}^n) - \nabla p^n \quad (5.21)$$

In the LES regions, $\theta = 0.5$ and in the RANS regions, $\theta = 1$.

The second step consists in solving a Poisson equation for the pressure increment δp ,

$$\nabla \cdot (\Delta t \nabla (\delta p)) = \nabla (\rho \mathbf{u}^*) \quad (5.22)$$

The velocity and the pressure are then updated as,

$$\rho \mathbf{u}^{n+1} = \rho \mathbf{u}^* - \Delta t \nabla (\delta p) \quad \text{and} \quad p^{n+1} = p^n + \delta p \quad (5.23)$$

When the SST model is used, the equations for the turbulent variables are solved at the end of each iteration after the velocity and pressure have been updated. Details concerning the resolution of the $k - \varepsilon$ equations in *Code_Saturne* (whose treatment is very similar to the SST equations) can be found in Section 12 of Archambeau et al. (2004).

5.3.2 Space discretization

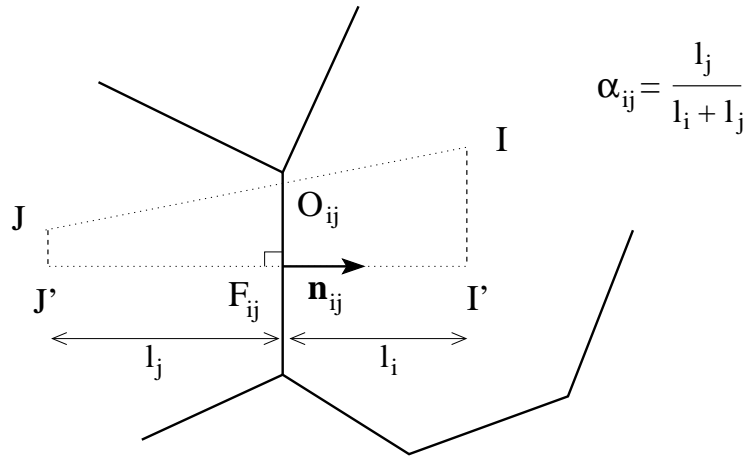


Figure 5.1: Notations for the spatial discretization of an internal face. For clarity, the representation is two-dimensional even though *Code_Saturne* is three-dimensional.

Discretization in space is achieved using a finite volume approach for a collocated arrangement of all variables. The computational domain is divided into control volumes (or cells) and the value of each

variable is stored at the mass centre of these cells. Fig. 5.1 represents entities related to an interior face (i, j) , between neighbouring cells i and j . Capital letters I and J refer to the centre of cells i and j respectively. F_{ij} is the mass centre of face (i, j) and O_{ij} is defined as the intersection of the face (i, j) and the straight line (IJ) . I' and J' are the projections of I and J , respectively onto the line normal to the face (i, j) and containing F_{ij} . The volume of cell i is denoted Ω_i and the surface of face (i, j) is $\partial\Omega_{ij}$.

The set of equations resulting from the discretization in time (Eq. (5.21) - (5.23)) are then integrated over each control volume i . Before proceeding to the integration in space - and to simplify the final expressions - some discrete operators that will be used later are defined here. $G_i(\phi)$ is the discrete operator providing the gradient of a variable ϕ at cell i . $G_{n,ij}(\phi)$ is the discrete operator providing the normal gradient of variable ϕ at face (i, j) . Details of the space discretization for the momentum equation Eq. (5.21), the Poisson equation Eq. (5.22) and (5.23) are given below.

Discretization in space of the momentum equation

Using Gauss divergence theorem, the momentum equation (Eq. (5.21)) is integrated over cell i as follows,

$$\frac{|\Omega_i|}{\Delta t} (\rho \mathbf{u}_i^* - \rho \mathbf{u}_i^n) + \theta \sum_{j \in \aleph(i)} (\underline{\underline{F}}_l(\mathbf{u}^*) \cdot \mathbf{n})_{F_{ij}} |\partial\Omega_{ij}| = (1 - \theta) \sum_{j \in \aleph(i)} (\underline{\underline{F}}_l(\mathbf{u}^n) \cdot \mathbf{n})_{F_{ij}} |\partial\Omega_{ij}| - G_i(p^n). \quad (5.24)$$

where $\aleph(i)$ refers to the neighbouring cells of cell i . In Eq. (5.24) the volume and face integrals have been approximated using the midpoint rule by

$$\int_{\Omega} \phi d\Omega \simeq \phi_i |\Omega_i| \quad \text{and} \quad \int_{\partial\Omega_{ij}} \phi dS \simeq \phi_{F_{ij}} |\partial\Omega_{ij}|, \quad (5.25)$$

which yields a second order approximation. The evaluation of the flux operator F at the face centre F_{ij} requires the evaluation of the convective $(\mathbf{u}^* (\mathbf{Q}^e \cdot \mathbf{n}))_{F_{ij}}$ and diffusive $(\nabla \mathbf{u}^* \cdot \mathbf{n})_{F_{ij}}$ fluxes.

The convective fluxes are approximated by

$$(\mathbf{u}^* (\mathbf{Q}^e \cdot \mathbf{n}))_{F_{ij}} = (\mathbf{u}^*)_{F_{ij}} (\mathbf{Q}^e \cdot \mathbf{n})_{F_{ij}} \quad (5.26)$$

Face values for the mass fluxes $(\mathbf{Q}^e \cdot \mathbf{n})_{F_{ij}}$ are obtained from the previous correction step; their discretization will be detailed later (see Eq. (5.42)). Several convection schemes are available for the computation of the face value for the velocity $(\mathbf{u}^*)_{F_{ij}}$. In all of the simulations carried out in this thesis, a fully centered scheme is used. The value at the face for any transported variable ϕ is then computed using a Taylor series expansion to obtain:

$$\phi_{F_{ij}} = \alpha_{ij} \phi_I + (1 - \alpha_{ij}) \phi_J + \frac{1}{2} (G_i(\phi) + G_j(\phi)) \cdot \mathbf{O}_{ij} \mathbf{F}_{ij} \quad (5.27)$$

The last term in Eq. (5.27) is added for non-orthogonal grids, where the centre of the face does not lie at the midpoint between the cell centres.

The diffusion term $((\mu + \mu_t) \nabla \mathbf{u}^* \cdot \mathbf{n})_{F_{ij}}$ is decomposed as follows,

$$((\mu + \mu_t) \nabla \mathbf{u}^* \cdot \mathbf{n})_{F_{ij}} = (\mu + (\mu_t)_{F_{ij}})(\nabla \mathbf{u}^* \cdot \mathbf{n})_{F_{ij}}. \quad (5.28)$$

The face gradient $(\nabla \phi \cdot \mathbf{n})_{F_{ij}}$ of any variable ϕ is then evaluated by the difference of two Taylor series expansions as,

$$(\nabla \phi \cdot \mathbf{n})_{F_{ij}} = G_{\mathbf{n},ij}(\phi) = \frac{\phi_{J'} - \phi_{I'}}{I'J'} \quad (5.29)$$

$$= \frac{\phi_J - \phi_I}{I'J'} + \frac{1}{I'J'}(G_j(\phi) \cdot \mathbf{J}' \mathbf{J} - G_i(\phi) \cdot \mathbf{I}' \mathbf{I}) \quad (5.30)$$

The eddy viscosity comes from

$$(\mu_t)_{F_{ij}} = \alpha_{ij}\mu_{t,i} + (1 - \alpha_{ij})\mu_{t,j}. \quad (5.31)$$

Gradient reconstruction

The calculation of the cell gradients $G_i(\phi)$ of any variable ϕ is achieved by an iterative solver (see Muzaferija and Gosman (1997)). Starting from the definition of the cell gradient

$$G_i(\phi) = \frac{1}{|\Omega_i|} \int_{\Omega_i} \nabla \phi d\Omega \quad (5.32)$$

Gauss divergence theorem implies

$$G_i(\phi) = \frac{1}{|\Omega_i|} \sum_{j \in \mathfrak{K}(i)} \int_{\partial\Omega_{ij}} \phi \mathbf{n}_{ij} dS. \quad (5.33)$$

Using the mid point rule and assuming \mathbf{n}_{ij} is constant over the interface (ij) Eq. (5.33) yields

$$G_i(\phi) = \frac{1}{|\Omega_i|} \sum_{j \in \mathfrak{K}(i)} \phi_{F_{ij}} \mathbf{n}_{ij} |\partial\Omega_{ij}|. \quad (5.34)$$

Using the value of $\phi_{F_{ij}}$ computed in Eq. (5.27), Eq. (5.34) becomes

$$|\Omega_i| G_i(\phi) = \sum_{j \in \mathfrak{K}(i)} \left\{ \alpha_{ij} \phi_I + (1 - \alpha_{ij}) \phi_J + \frac{1}{2} \mathbf{O}_{ij} \mathbf{F}_{ij} \cdot (G_i(\phi) + G_j(\phi)) \right\} |\partial\Omega_{ij}| \mathbf{n}_{ij} \quad (5.35)$$

The above system with the unknowns $G_i(\phi)$ is solved with an iterative algorithm which can be written as

$$|\Omega_i| G_i(\phi)^{k+1} = \sum_{j \in \mathfrak{K}(i)} \left\{ \alpha_{ij} \phi_I + (1 - \alpha_{ij}) \phi_J + \frac{1}{2} \mathbf{O}_{ij} \mathbf{F}_{ij} \cdot (G_i(\phi)^{k+1} + G_j(\phi)^k) \right\} |\partial\Omega_{ij}| \mathbf{n}_{ij} \quad (5.36)$$

with the initial term in the loop over k being the cell gradient without any reconstruction terms,

$$G_i(\phi)^0 = \sum_{j \in \mathfrak{K}(i)} \left\{ \alpha_{ij} \phi_I + (1 - \alpha_{ij}) \phi_J \right\} |\partial\Omega_{ij}| \mathbf{n}_{ij}. \quad (5.37)$$

Discretization in space of the pressure correction

The Poisson equation (Eq. (5.22)) for the pressure correction δp is integrated over cell i as follows:

$$\Delta t \sum_{j \in \mathfrak{F}(i)} (\nabla(\delta p) \cdot \mathbf{n})_{F_{ij}} |\partial\Omega_{ij}| = \sum_{j \in \mathfrak{F}(i)} (\rho \mathbf{u}^* \cdot \mathbf{n})_{F_{ij}} |\partial\Omega_{ij}| \quad (5.38)$$

The normal gradient on the left hand side is evaluated as follows

$$(\nabla(\delta p) \cdot \mathbf{n})_{F_{ij}} = \mathcal{G}_{\mathbf{n},ij}(\delta p) \quad (5.39)$$

In order to avoid checker-board oscillations of the pressure in cases with homogeneous distribution of cells, a Rhie-Chow interpolation (Rhie and Chow, 1983) is used to compute the right hand side of Eq. (5.38). $\mathbf{Q}^{*,P}$ is the solution of the momentum equation without pressure gradient;

$$\mathbf{Q}_i^{*,P} = \rho \mathbf{u}_i^* + \Delta t G_i(p^n) \quad (5.40)$$

With this notation the Rhie-Chow interpolation consists of evaluating the right hand side of Eq. (5.38) as

$$\sum_{j \in \mathfrak{F}(i)} (\rho \mathbf{u}^* \cdot \mathbf{n})_{F_{ij}} |\partial\Omega_{ij}| = \sum_{j \in \mathfrak{F}(i)} ((\mathbf{Q}^{*,P})_{F_{ij}} - \Delta t \mathcal{G}_{\mathbf{n},ij}(p^n)) |\partial\Omega_{ij}|. \quad (5.41)$$

The mass fluxes through each face are updated at this point using the predicted velocity and the face gradient of the pressure increment δp ;

$$(\mathbf{Q}^{n+1} \cdot \mathbf{n})_{F_{ij}} = (\mathbf{Q}^* \cdot \mathbf{n})_{F_{ij}} - \Delta t \mathcal{G}_{\mathbf{n},ij}(\delta p). \quad (5.42)$$

Finally the velocities are corrected using

$$\rho \mathbf{u}_i^{n+1} = \rho \mathbf{u}_i^* - \Delta t G_i(\delta p) \quad (5.43)$$

and the pressure is updated with the pressure increment

$$p_i^{n+1} = p_i^n + \delta p_i. \quad (5.44)$$

5.3.3 Boundary Conditions

Fig. 5.2 represents entities related to a boundary face. In the discretized momentum equation Eq. (5.24), boundary conditions must be specified for the convective fluxes, the diffusive fluxes and the pressure gradient term. In the correction step, boundary conditions must be specified for the terms of the discretized Poisson equation Eq. (5.38) and the pressure gradient term in the correction of the velocity Eq. (5.43). Two main kinds of boundary conditions can be applied:

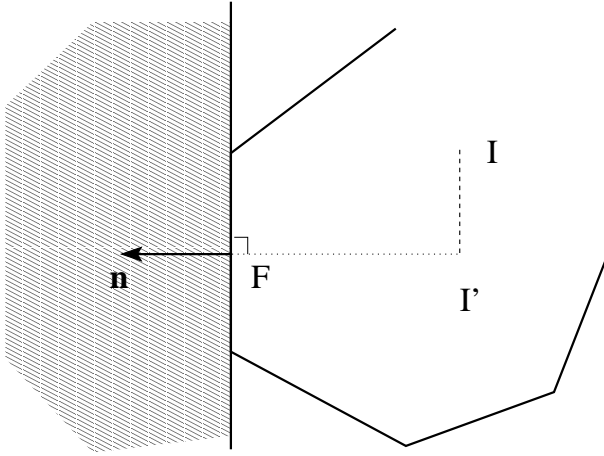


Figure 5.2: Notations for the spatial discretization of a boundary face. For clarity, the representation is two-dimensional even though *Code_Saturne* is three-dimensional.

- Dirichlet boundary conditions: the value of the variable is fixed at the boundary face centre
 $\phi_F = \phi^{dir}$.
- Neumann boundary conditions: the normal gradient of the variable at the boundary face is fixed
 $\phi_F = \phi_{I'} + (\nabla\phi^{neu}) \cdot \mathbf{I}'\mathbf{F}$.

Periodic boundary conditions can also be used in the directions of homogeneity of the flow but are not included in the previous list as they are not actually treated as strict boundaries. Instead, a layer of “ghost cells” is created on the side of the boundary face that is located outside of the computational domain. These “ghost cells” are the translated images of actual cells of the domain. Hence a periodic face is considered as an internal face and the simulation is coupled to itself which alleviates the need to specify boundary conditions.

Depending on the nature of the flow on the domain boundary, different pre-defined sets of Dirichlet and Neumann boundary conditions can be imposed for the velocity, pressure and turbulent variables:

- inlet boundary conditions: a Dirichlet condition is prescribed for all transport variables (velocity \mathbf{u} and turbulent variables k and ω if necessary). A homogeneous Neumann condition ($\nabla p \cdot \mathbf{n} = 0$) is imposed on the pressure.
- outlet boundary conditions: a homogeneous Neumann condition is imposed on all transport variables. For the pressure, a Dirichlet condition is used. The value of the pressure is computed by setting the pressure to zero at an arbitrary outlet face and by supposing that the pressure profile across outlet reproduces the pressure obtained upstream at the previous time step.

- wall boundary conditions: a Dirichlet condition is imposed on all transport variables at the wall. The velocity and k are set to zero while ω is set to $10 \frac{6v}{\beta y^2}$ where y is the distance from the centre of the cell to the wall as recommended by Menter (1994). A homogeneous Neumann condition is used on the pressure.
- symmetry conditions: a homogeneous Neumann condition is imposed on the tangential velocity, the pressure, k and ω . The normal velocity is set to zero with a Dirichlet boundary condition.

Chapter 6

Periodic Channel Flow Computations

6.1 Introduction

Fully developed turbulent channel flow is the most studied configuration of engineering interest in CFD research (Deardorff (1970), Kim et al. (1987), Piomelli et al. (2003) among others). The homogeneity of the flow in the streamwise and spanwise directions allows for simple periodic boundary conditions to be used. The simulation generates its own inflow data and will thus be considered as a baseline to assess simulations described in Chapter 7 with inlet and outlet boundary conditions. The simplicity of the geometry makes the channel flow an ideal test case for investigating the near wall behavior of turbulence.

In this chapter, different Reynolds numbers are considered in the range $Re_\tau = 180 - 950$. The test cases simulated are summarized in Section 6.2. The influence of the grid density for the case $Re_\tau = 395$ will be investigated in Section 6.3. A meshing strategy applied throughout this thesis both to wall bounded flows is then proposed and tested at different Reynolds numbers in Section 6.4. Finally, Section 6.5 summarizes the conclusions drawn from the simulations performed in this chapter.

6.2 Simulations Performed

Fig. 6.1 shows a sketch of the flow configuration. The distance between the two-parallel walls of the channel is 2δ where δ is referred to as the channel half width. If the flow is fully developed, there is a constant mean pressure gradient in the streamwise direction which is directly related to the friction velocity u_τ at the wall by (Pope, 2000)

$$\frac{dP}{dx} = \frac{u_\tau^2}{2\delta}. \quad (6.1)$$

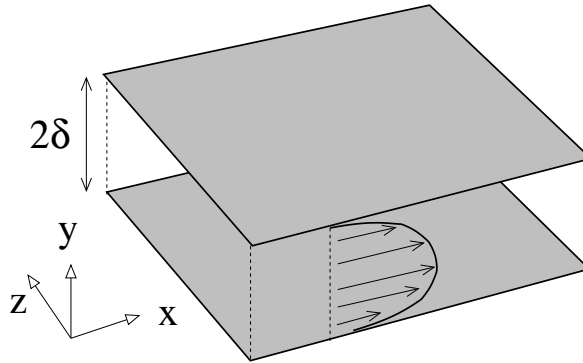


Figure 6.1: Sketch of a channel flow and the coordinate system adopted.

In all our simulations we impose a constant pressure gradient which, through Eq. (6.1) fixes the friction velocity u_τ . The friction Reynolds number Re_τ , already defined in Eq. (2.7), is thus imposed, and the Reynolds number Re , defined in Eq. (2.8), is part of the output of the simulation. Four different periodic channel flows at four Reynolds numbers have been investigated. Reference data are taken from the DNS of Hoyas and Jimenez (2006) for the cases at $Re_\tau = 180$ and $Re_\tau = 950$, from the DNS of Iwamoto et al. (2002) for the case at $Re_\tau = 395$, and from the DNS of Moser et al. (1999) for the case at $Re_\tau = 590$.

The dimensions of the computational domain are $2\pi\delta \times 2\delta \times \pi\delta$ for all Reynolds numbers in the streamwise, wall-normal and spanwise directions, respectively. This is sufficient to resolve the largest structures of the flow at $Re_\tau = 395$ and higher Reynolds numbers (Moser et al., 1999), although a larger domain is usually used for the lowest Reynolds number $Re_\tau = 180$ (Kim et al., 1987). A simulation on a larger domain of $3\pi\delta$ in the streamwise direction however did not show any influence of the domain length on the mean velocity and Reynolds stresses profiles. Periodic boundary conditions were applied in the streamwise and spanwise directions, whereas no-slip boundary conditions were imposed at the walls. For all simulations, the time step Δt was adjusted so that the maximum Courant-Friedrichs-Lowy (CFL) number remains lower than unity. The Smagorinsky model with Van Driest damping at the wall was used. The different Reynolds numbers and grids investigated are summarized in Table 6.1.

6.3 Tests of Mesh Refinement

Simulations considered in this section aim to investigate the influence of grid refinement on the LES solution. As already mentioned in Chapter 2, current subgrid-scale stress models do not represent accurately the energy carrying turbulent structures in the near-wall region. Thus the grid at the wall must be fine enough so that most of the Reynolds stresses are carried by the resolved motion.

In order to control the computational cost of our LES, we need to understand the dependence of the

Run	Re_τ	$N_x \times N_y \times N_z$	Δx^+	Δz^+	Δy_{\min}^+	Δy_{\max}^+
A	395	$32 \times 32 \times 24$	77	51	2.0	62
B	395	$48 \times 48 \times 32$	52	39	1.7	39
C	395	$64 \times 64 \times 64$	39	19	1.6	27
D	395	$96 \times 96 \times 96$	26	13	0.9	19
E	395	$128 \times 128 \times 128$	20	10	0.7	14
F	180	$38 \times 38 \times 32$	30	18	1.8	17
G	395	$50 \times 46 \times 82$	50	15	1.9	39
H	590	$92 \times 52 \times 124$	40	15	1.7	56
I	950	$120 \times 56 \times 198$	50	15	1.9	94

Table 6.1: Parameter settings used in the LES computations of the fully developed turbulent channel flow. The parameters not listed here are kept constant for all simulations.

results on the mesh refinement. The grid refinement in LES of wall-bounded flows is usually expressed in wall units. This gives an indication about the number of grid points used to discretize the smallest structures of the flow, since as we saw in Chapter 2, the size of these structures scales in wall units. It is known that for channel flows the minimum resolution requirement depends on the specific numerical method and turbulence model employed.

Despite its simplicity, the Smagorinsky model with near-wall Van-Driest damping was shown by Temmerman (2004) to produce similar predictions to the more advanced models presented in Chapter 2. No major computational savings would thus be achievable by using a more advanced modelling methodology.

As regards the numerical method, spectral methods can produce accurate results with refinements of the order of $\Delta x^+ = 100$ and $\Delta z^+ = 30$ (Piomelli, 1991) while second order finite differences require the grid spacing to be reduced by a factor of two to achieve similar accuracy (Lund and Kaltenbach, 1995).

For a given mesh refinement we need to evaluate the level of accuracy that can be expected in the solution with the computational technique employed so that our results can be assessed critically. We start by investigating the effect of the grid refinement on the flow statistics at $Re_\tau = 395$. Given a chosen level of accuracy we wish to have (say 10% error in the friction coefficient), we will then be able to estimate some minimum grid spacing in wall units to achieve this accuracy at different Reynolds numbers.

Simulations A, B, C, D, E and F whose details are provided on Table 6.1 are considered in this section. The grid resolution is homogeneous in the streamwise and spanwise directions, but there is a clustering of cells in the wall-normal direction at both walls. The coarser mesh exploited in run A used $32 \times 32 \times 24$

Run	$Re_\tau = u_\tau \delta / v$	$Re = 2U_b \delta / v$	$C_f \cdot 10^3$	U_c / U_b
DNS	395 (-)	13,898 (-)	6.47 (-)	1.14 (-)
A	394 (-0.4%)	17,531 (+26.1%)	4.04 (+37.6%)	1.12 (-1.9%)
B	392 (-0.7%)	16,753 (+20.5%)	4.39 (+32.2%)	1.12 (-2.3%)
C	395 (-0.2%)	14,713 (+5.8%)	5.76 (+11.0%)	1.12 (-1.9%)
D	396 (+0.1%)	14,255 (+2.5%)	6.17 (+4.8%)	1.13 (-1.0%)
E	395 (-0.1%)	14,144 (+1.7%)	6.23 (+3.7%)	1.14 (-0.2%)

Table 6.2: Mean flow properties obtained from LES computations of the periodic channel flow at $Re_\tau = 395$ and reference DNS of Iwamoto et al. (2002).

cells in the streamwise, wall-normal and spanwise directions, respectively, whereas the finer mesh used $128 \times 128 \times 128$ cells. In wall units, this translates into $\Delta x^+ = 77$ and $\Delta z^+ = 51$ for the coarser mesh down to $\Delta x^+ = 20$ and $\Delta z^+ = 10$ for the finer mesh. For comparison, the DNS of Moser et al. (1999) uses a grid of $256 \times 193 \times 192$ nodes on the same domain, which translates into $\Delta x^+ = 10$, $\Delta z^+ = 6.5$ and $\Delta y_{\max}^+ = 6.5$.

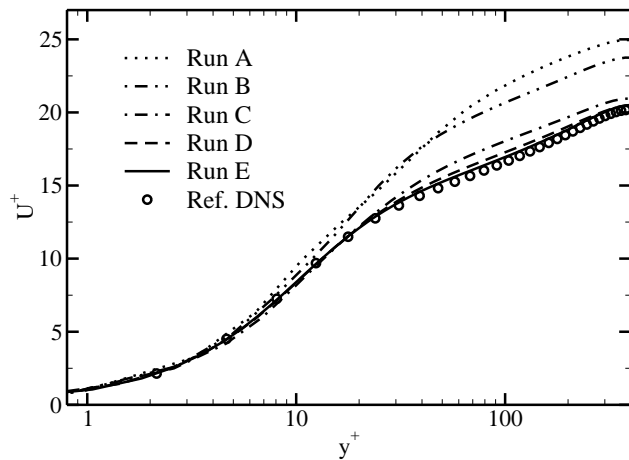


Figure 6.2: Periodic channel flow simulations at $Re_\tau = 395$. Profiles of the mean streamwise velocity.

Fig. 6.2 compares the mean velocity profiles for runs A, B, C, D and E. It can be seen from Fig. 6.2 (a) that the coarser the mesh is, the thicker the viscous sublayer and the higher the intercept with the logarithmic layer. As a result, the bulk velocity U_b and the centreline velocity U_c are overestimated and the friction coefficient is underestimated. Table 6.2 summarizes the mean flow properties computed from the five LES runs and the associated errors relative to the reference DNS data of Iwamoto et al. (2002).

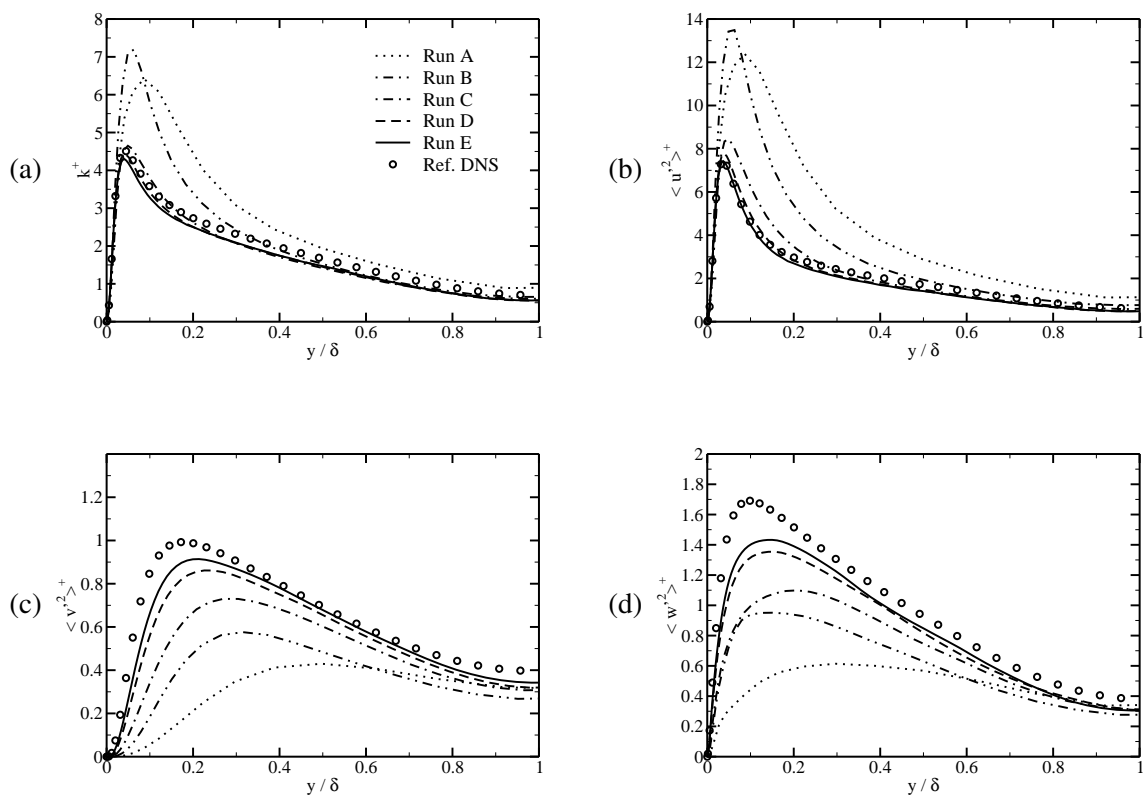


Figure 6.3: Periodic channel flow simulations at $Re_\tau = 395$. Profiles of (a) the turbulent kinetic energy k and the three normal Reynolds stresses (b) $\langle u'^2 \rangle$, (c) $\langle v'^2 \rangle$ and (d) $\langle w'^2 \rangle$.

Fig. 6.3 shows profiles of the turbulent kinetic energy and of the normal Reynolds stresses in wall units. The two coarsest grids used in run A and run B overpredict the levels of turbulent kinetic energy, especially the near-wall peak. On the contrary one would expect the turbulent kinetic energy to be low in coarse LES, since the contributions of the smaller eddies are neglected. Although this is a common feature of under-resolved LES, there is no widely accepted explanation, at this point, for such a phenomenon (see Appendix B of Celik et al. (2005) for a discussion on this issue). The k profiles obtained with the three finer meshes used in run C, run D and run E show very good agreement with the DNS profile. However the normal Reynolds stresses profiles (Fig. 6.3 (b), (c) and (d)) show an overestimation of the streamwise fluctuations and an underestimation of the wall-normal and spanwise fluctuations close to the wall that persist for all runs. This indicates that the near-wall structures are not correctly resolved and again, it is a common feature of under-resolved LES (Celik et al., 2005). Another observation from these profiles is that the peaks of turbulent kinetic energy and Reynolds stress are shifted towards the centre of the channel as the mesh becomes coarser. This clearly supports the conclusion made from the observation of the mean flow profiles, that coarse resolution leads to an overly thick viscous sublayer.

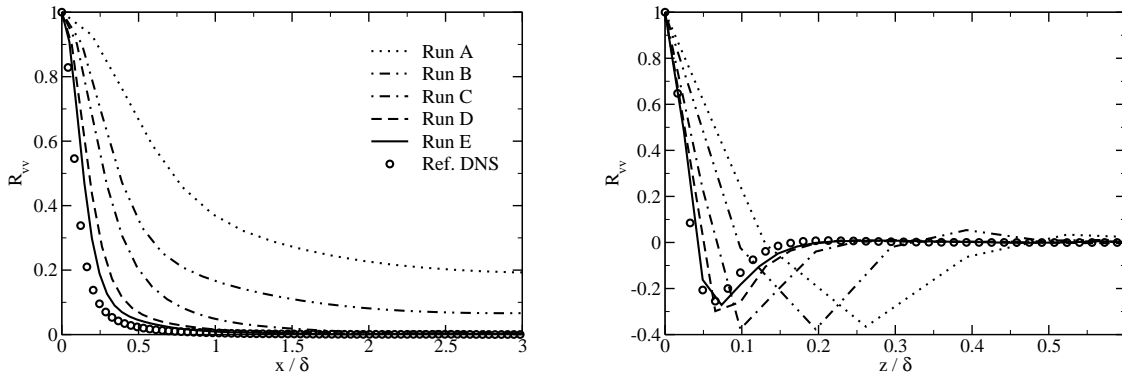


Figure 6.4: Two-point correlations of the wall-normal velocity fluctuations at $y^+ = 5$ in channel flow at $Re_\tau = 395$. Streamwise separations (left), and spanwise separations (right).

In order to understand better the effect of the mesh resolution on the structure of the near wall turbulence, the two-point correlations of the wall-normal velocity fluctuations as a function of streamwise and spanwise separations at $y^+ = 5$ are shown in Fig. 6.4. In the streamwise direction, the coarsening of the mesh leads to high correlations of velocity over large separation distances. This is an indicator of the presence of overly elongated streaks in the streamwise direction, often referred to as super streaks (Piomelli et al. (2003)), which is a common feature of the near-wall region of under-resolved LES. In the spanwise direction, the negative peak in the two-point correlations of the wall-normal fluctuations is an

indicator of the presence of counter-rotating vortices aligned in the streamwise direction. The coarsest grids used in run A, run B and run C do not allow for the discretization of these structures. However the negative peak is still present, although its position is dependent on the spanwise grid resolution. This feature of the two-point correlations is due to the presence of the non-physical super-streaks, whose size scales with the near-wall grid spacing Δz rather than with the viscous length-scale v/u_τ . The overly thick viscous sublayer observed in the mean velocity and Reynolds stresses profiles for runs A, B and C can also be accounted for by the presence of these overly large non-physical structures in the near wall region.

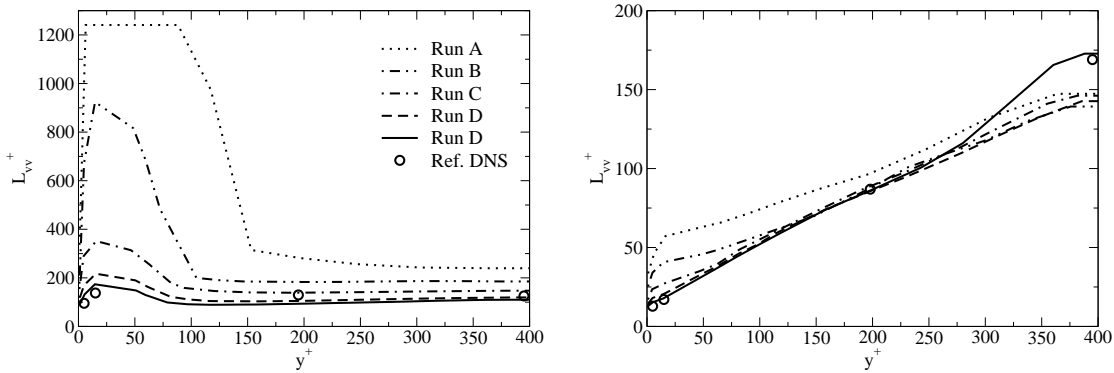


Figure 6.5: Integral length scale of the wall-normal velocity in the streamwise (left) and in the spanwise (right) directions in channel flow $Re_\tau = 395$.

In order to analyze the structure of the turbulence not only in the near-wall region but across the whole channel, Fig. 6.5 shows the integral lengthscales of the wall-normal fluctuations in the streamwise and spanwise directions as a function of the distance from the wall. The integral length scale is computed as the distance at which the two-point correlations drop to 0.1. This has the double advantage that errors due to oscillations of the tail of the two-point correlations and negative contributions due to two-dimensional vortices can be avoided. This definition of the integral length scale has already been used by Keating et al. (2004) with a coefficient of correlation of 0.2 instead of 0.1 used in the present study. The signature of the super-streaks can be observed via the excessively large length scale in both the streamwise and spanwise directions computed close to the wall for the coarsest grids. As the grid resolution increases, the integral length scale becomes independent of further grid refinement indicating sufficient resolution of the energy containing structures. It can be seen that for the finest mesh, the length scale in the spanwise direction increases away from the wall. In the streamwise direction however, the length scale is maximum at the wall due to the presence of the elongated rolls and decays towards the centre of the channel. This is likely to be a low Reynolds number effect which can be accounted for by the lack of clear separation

between the size of the near wall structures (which scales with the viscous length scale ν/u_τ) and the size of the structures in the centre of the channel (which scales with the geometrical length scale δ) at the low Reynolds number Re_τ simulated. At higher Reynolds number, the streamwise length scale in the near-wall region will decay as the inverse of the Reynolds number Re_τ , and become eventually smaller than in the core of the channel.

Fig. 6.6 represents planes of instantaneous streamwise velocity fluctuations at $y^+ = 15$. The super streaks can clearly be observed at the lowest grid resolution (runs A and B). These are streamwise velocity fluctuations whose magnitude is in good agreement with the magnitude of the streaks observed at the highest resolution, but whose size is significantly larger both in the streamwise and spanwise directions.

Finally we wish to investigate the presence of strong vortical structures in our LES solution. A natural candidate to identify coherent vortices is a high modulus of the vorticity field. The presence of a wall however creates a mean shear which is usually higher than the vorticity of the near wall eddies. A more advanced criterion to identify coherent vortices and distinguish them from the mean shear is to visualize positive regions of Q (Dubief and Delcayre, 2000), the second invariant of the velocity gradient tensor $\nabla\mathbf{u}$, defined as

$$Q = \frac{1}{2}(\Omega_{ij}\Omega_{ij} - S_{ij}S_{ij}) \quad (6.2)$$

where Ω_{ij} and S_{ij} are respectively the antisymmetric and the symmetric components of $\nabla\mathbf{u}$. Fig. 6.7 shows isosurfaces of $Q = 250 (u_\tau/\delta)^2$ for runs A, B, C, D and E. This threshold of Q corresponds to standards thresholds of $Q \approx 0.5 - 0.8 (U_b/\delta)^2$ (depending on the value of the bulk velocity in the calculation considered) recommended for eduction of near-wall vortices in Dubief and Delcayre (2000). Fig. 6.7 shows that the vortical activity is strongly influenced by the mesh refinement. No coherent vortices are visible at the lowest resolutions (runs A and B) whereas the turbulent kinetic energy is overestimated, as shown on Fig. 6.3 (a). For finer resolutions such as in runs C, D and E, the characteristic size of the coherent vortices seem to be constant, and more small scales can be resolved as the grid is refined.

6.4 Meshing Strategy

Results of the LES simulations presented in the previous section were shown to be highly dependent on the grid resolution. The failure to predict the correct mean velocity and Reynolds stresses profiles for the coarsest grids was traced back to the existence of super streaks in the near wall region, whose size scales roughly with the grid spacing. It appeared that these spurious structures were not present in simulations performed on grids which were able to discretize accurately the real near wall structures, and consequently accurate predictions for the mean velocity and Reynolds stress profiles could be obtained.

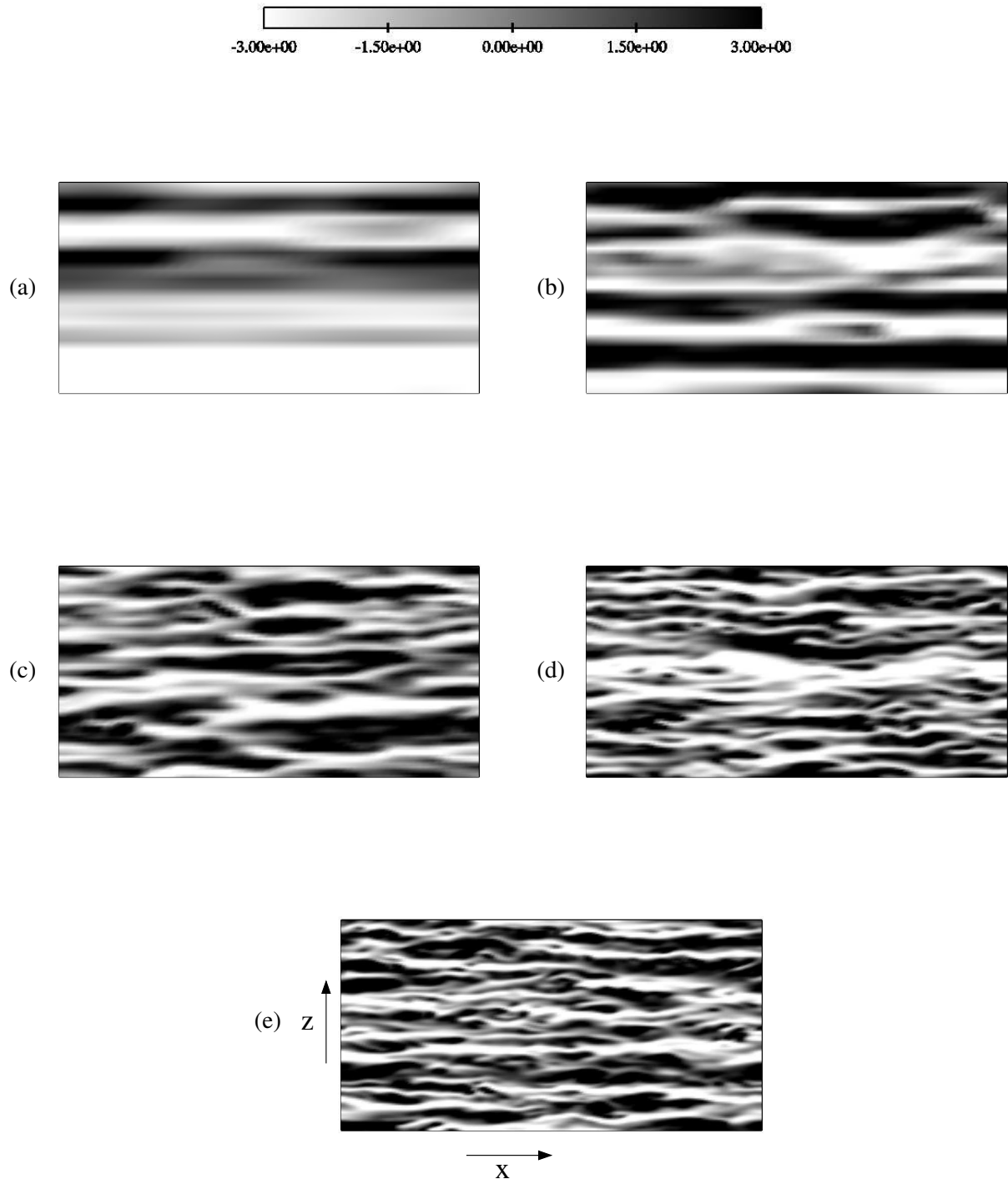


Figure 6.6: Streamwise velocity fluctuations on a plane parallel to the wall at $y^+ = 15$ in channel flow $Re_\tau = 395$: (a) run A; (b) run B; (c) run C; (d) run D and (e) run E.

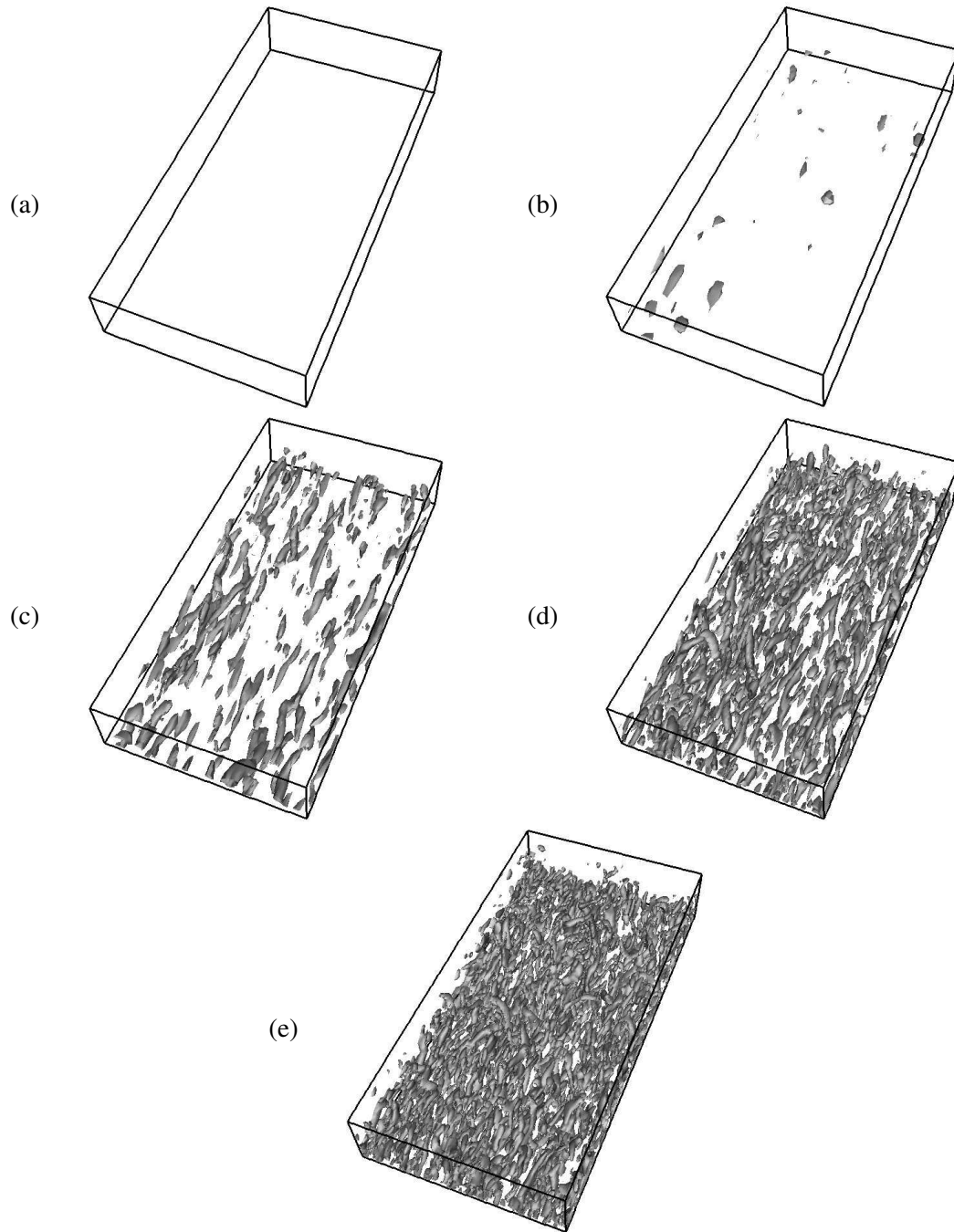


Figure 6.7: Isosurfaces of $Q = 250 (u_\tau/\delta)^2$ in channel flow $Re_\tau = 395$: (a) run A; (b) run B; (c) run C; (d) run D and (e) run E.

Run	$Re_\tau = u_\tau \delta / v$	$Re = 2U_b \delta / v$	$C_f \cdot 10^3$	U_c / U_b
F	180 (-1.7%)	6,172 (+9.1%)	6.80 (-18.9%)	1.16 (-0.9%)
G	395 (+0.0%)	14,519 (+4.5%)	5.93 (-8.3%)	1.12 (-2.3%)
H	588 (-0.3%)	22,907 (+3.2%)	5.27 (-6.9%)	1.13 (-0.6%)
I	934 (-0.8%)	38,920 (+3.3%)	4.61 (-7.9%)	1.13 (-0.2%)

Table 6.3: Mean flow properties obtained from LES computations of fully developed channel flow at Re_τ between 180 and 950. Reference data are taken from the DNS of Hoyas and Jimenez (2006) for run F and I, from the DNS of Iwamoto et al. (2002) for run G, and from the DNS of Moser et al. (1999) for run H.

Since the near wall structures scale with the viscous length scale v/u_τ , and since we saw previously that these need to be resolved by the grid for LES predictions to be accurate, it seems natural to derive a quality criteria based on this length scale. In order to resolve accurately the near wall structures in the streamwise and spanwise directions, we decide to impose the following constraint on the grid spacing:

$$\Delta x^+ \leq 50 \quad \text{and} \quad \Delta z^+ \leq 15. \quad (6.3)$$

In order to resolve steep gradients in the mean velocity profile near the wall, we impose:

$$\Delta y^+ \approx 2 \text{ at the wall} \quad \text{and} \quad \Delta y \approx 0.1\delta \text{ in the centre.} \quad (6.4)$$

The resolution requirement in the centre of the channel scales with the geometrical length scale δ since the size of the dominant eddies in this region also scale with δ . These criteria were derived to obtain the best results possible with the minimum number of cells, and were chosen to favour the spanwise grid resolution over the streamwise and wall-normal resolution. The arguments to do so are based on best practise guidelines found in the literature (Lund and Kaltenbach (1995), Lund et al. (1998), Temmerman et al. (2003) among others), and tests on other grids which are not going to be presented in this manuscript.

Four cases at different Reynolds numbers in the range $Re_\tau = 180 - 950$ are considered. They correspond to runs F, G, H and I whose details are provided in Table 6.1. All grids considered follow the resolution requirements derived in Eq. (6.3) and Eq. (6.4). As the Reynolds number increases, the grid resolution increases in order to discretize accurately the near-wall eddies. The simulation at $Re_\tau = 180$ uses 46,208 cells, while the simulation at $Re_\tau = 950$ uses about 1.3M cells.

Fig. 6.8 shows the mean velocity profiles for runs F, G, H and I. The discrepancies between the LES predictions and the reference data are relatively small for all Reynolds numbers. As shown in Table 6.3, the error in the Reynolds number Re is lower than 10% for all simulations. On Fig. 6.8, it can be

observed that the mean velocity profiles in the logarithmic layer and in the core of the channel become more accurate as the Reynolds number increases. The Smagorinsky model is designed to dissipate energy coming from motions in the inertial range. In the lower Reynolds number case (run F), there is no clear separation between large scales and small scales, and hence no inertial cascade neither in the logarithmic region nor in the core of the channel. On the contrary, the higher Reynolds number cases (runs H and I) exhibit a substantial inertial range where the Smagorinsky model can operate correctly.

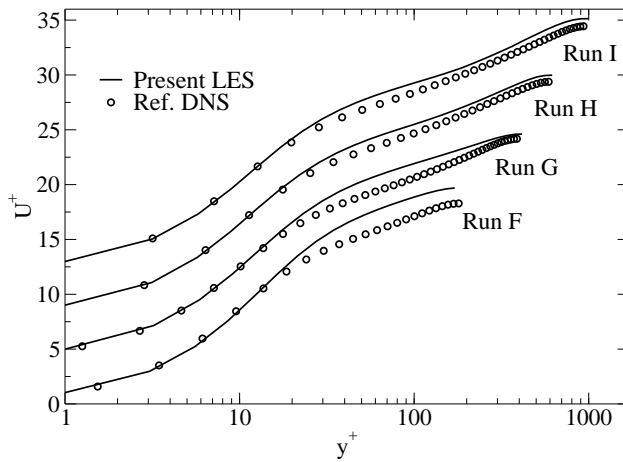


Figure 6.8: Periodic channel flow simulations at different Reynolds numbers Re_τ . Profiles of the mean velocity for runs F, G, H and I. Individual profiles are separated with a vertical offset of 4.

Fig. 6.9 shows the turbulent kinetic energy and Reynolds stresses profiles for runs F, G, H and I. The kinetic energy profiles are in very good agreement with the reference data for all Reynolds numbers and again the results seem to become more accurate as the Reynolds number increases. The normal Reynolds stresses in the near-wall region exhibit the same features as in the previous runs at $Re_\tau = 395$: the streamwise fluctuations are overestimated while the wall-normal and spanwise fluctuations are underestimated. The discrepancies observed seem again to be independent of the Reynolds number due to the efficient meshing strategy adopted. Further away from the wall in the logarithmic region ($y^+ \approx 200$), the cases at $Re_\tau = 590$ and $Re_\tau = 950$ seem to show the inverse trend: the streamwise fluctuations are underestimated while the other normal stresses are overestimated. There are no explanations at this point for such a phenomenon. However these discrepancies are quite small and localized around $y^+ = 200$. In the core of the channel, the agreement with the reference data is very good for all Reynolds stresses at all Reynolds numbers.

The two-point correlations in the spanwise direction at $y^+ = 5$ are shown on Fig. 6.10 as a function of

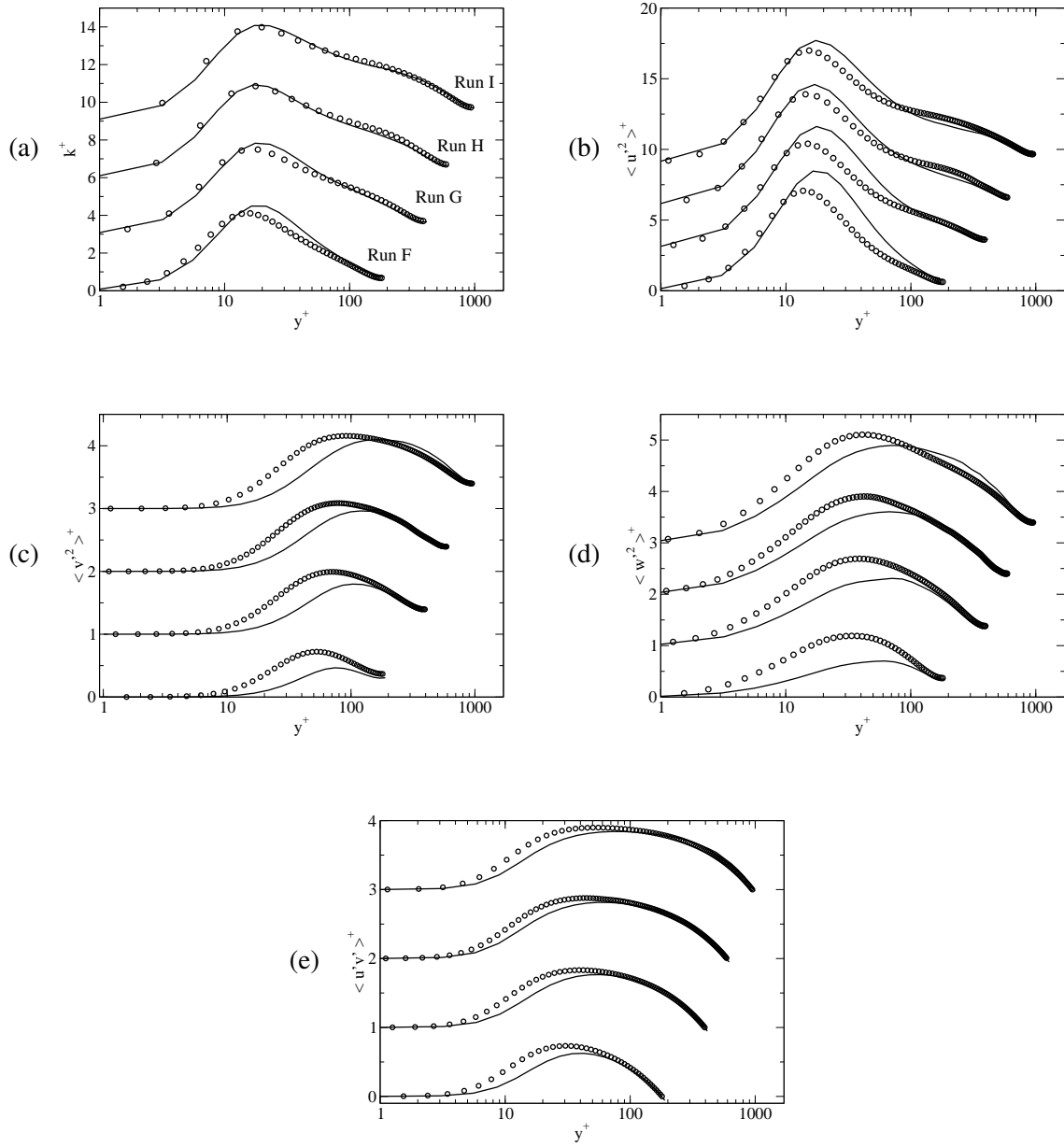


Figure 6.9: Periodic channel flow simulations at different Reynolds numbers Re_τ . Profiles of (a) the turbulent kinetic energy k , (b) $\langle u'^2 \rangle$, (c) $\langle v'^2 \rangle$, (d) $\langle w'^2 \rangle$ and (e) $\langle u'v' \rangle$.

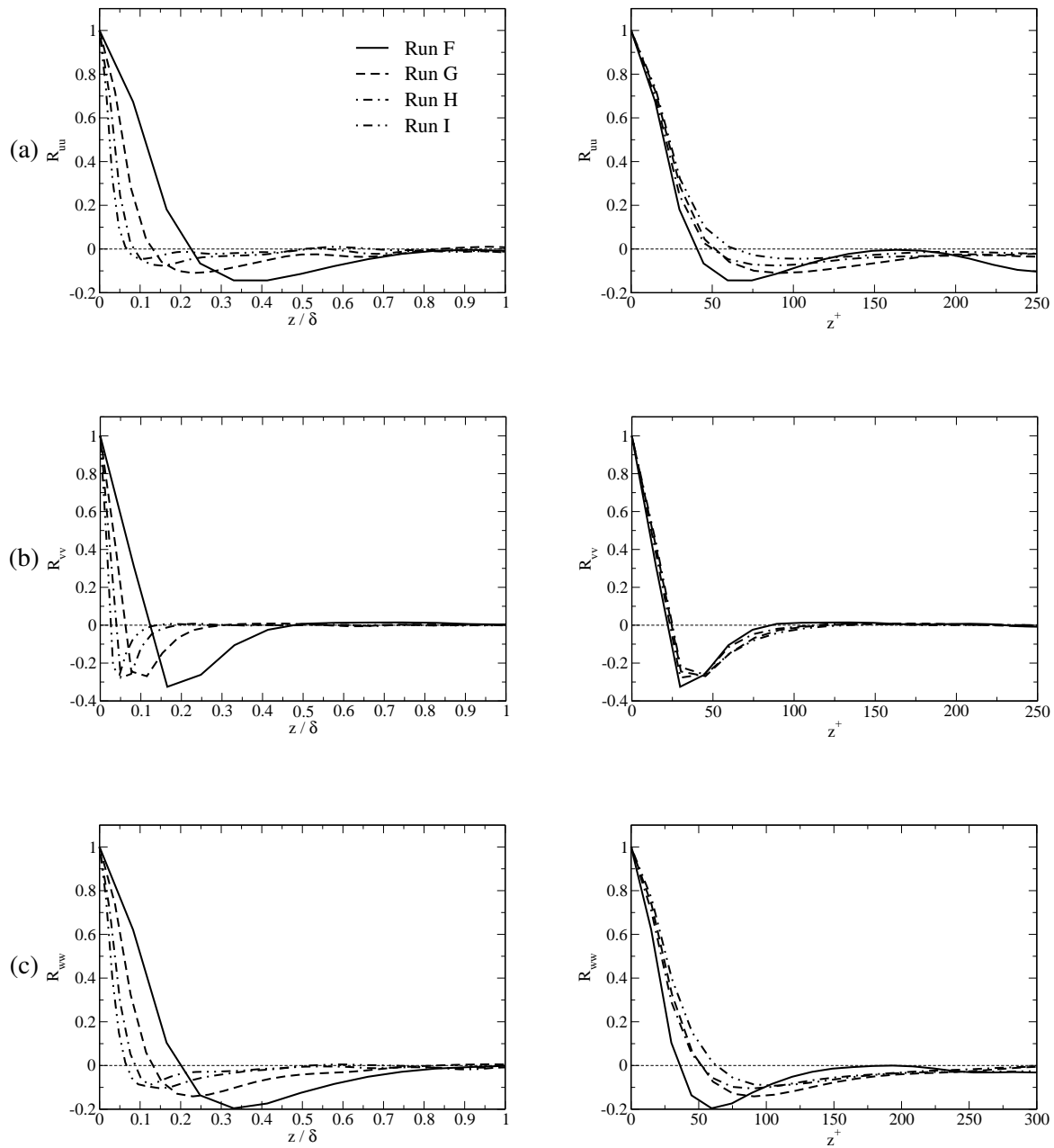


Figure 6.10: Periodic channel flow simulations at different Reynolds numbers Re_τ . Two-point correlations of the three velocity components in the spanwise direction at $y^+ = 5$. Spanwise separation distance z is normalized by δ on the left and by $\delta_v = v/u_\tau$ on the right. Correlations of (a) the streamwise fluctuations, (b) the wall-normal fluctuations and (c) the spanwise fluctuations.

the spanwise separation distance z normalized in outer layer units z/δ and in wall units z^+ . As expected in the viscous sublayer the two-point correlations tend to collapse on one single curve when normalized in wall units. This is especially the case for the wall-normal fluctuations; in contrast, the spanwise and streamwise fluctuations do not collapse so well. The cause of this scaling failure was recently explained in Hoyas and Jimenez (2006) by the presence of ridge modes which do not scale in wall units. These structures are inactive in the sense of Townsend (1976) i.e. they do not carry any Reynolds shear stress and do not affect the wall-normal fluctuations. Their role is to link the near-wall streaks with the global modes further away from the wall. On the other hand the near-wall streaks and counter rotating vortices scale well in wall units (Hoyas and Jimenez, 2006) as can be seen on Fig. 6.10 (b).

Fig. 6.11 shows the integral length scale in the spanwise direction as a function of the distance from the wall for the three components of the velocity. All length scales are normalized by δ on the left handside and by $\delta_v = v/u_\tau$ on the right handside. The length scale seems roughly to be constant when normalized in wall units for $y^+ < 20$ for all cases. This constant scaling in wall units conforms to previous DNS (Iwamoto et al., 2002) and experimental (den Toonder and Nieuwstadt, 1997) studies and proves that our meshing strategy allows for accurate discretization of the near wall structures of the channel flow at all Reynolds number. Further away from the wall, the integral length scales grow. It can be observed in particular that away from the wall, the length scale of the wall-normal fluctuations follow closely the mixing length $L = \kappa y$. In the core of the channel, the integral lengthscales are roughly constant and equal to 0.5δ for all Reynolds number investigated. Agreement with the reference DNS data at $Re_\tau = 395$ is very satisfactory for run G.

6.5 Concluding Remarks

A grid refinement study for LES of fully developed turbulent plane channel flow has been performed. The effect of insufficient near-wall refinement on the statistics and near-wall structures has been studied. As already observed in the literature, a coarse LES grid leads to the formation of unphysical near-wall structures whose size scales with the grid spacing, and to the underestimation of the coefficient of friction. A grid refinement of $\Delta z^+ \leq 15$ and $\Delta x^+ \leq 50$ was shown to be sufficient to obtain satisfactory results at several Reynolds numbers in the range $Re_\tau = 180 - 950$. In order to resolve the mean velocity profile in the viscous sublayer, several points have to be placed below $y^+ < 5$. In the present case, a wall-normal grid spacing of $\Delta y^+ \approx 2$ yielded good results. These guidelines are going to be applied in the following chapters for the meshing of other types of wall bounded flows. The behavior of turbulence in duct flows or in the near-wall region of boundary layer flows is essentially the same as that in channel flows, hence

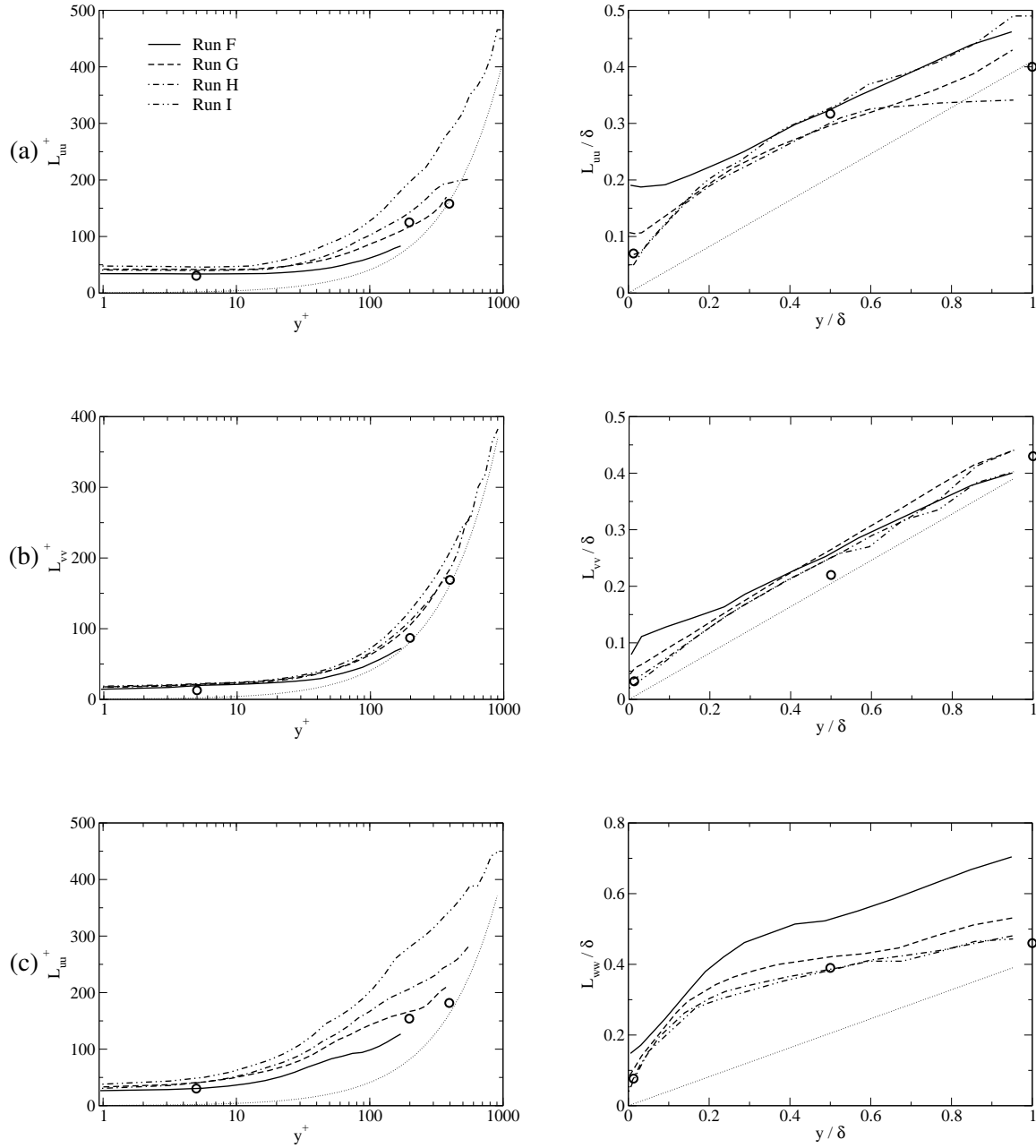


Figure 6.11: Periodic channel flow simulations at different Reynolds numbers Re_τ . Integral lengthscales in the spanwise direction for the three velocity components. Lengthscales are normalized by δ_v on the left hand side and by δ on the right hand side. Integral spanwise lengthscale (a) of the streamwise velocity fluctuations, (b) wall-normal velocity fluctuations and (c) spanwise velocity fluctuations. Symbols represent reference DNS data at $Re_\tau = 395$. Thin dashed line represents the mixing length $L = \kappa y$

accurate results are expected to be obtained with the grid refinement requirements introduced in this chapter. For more complicated flows studied in Chapter 9 involving boundary layer acceleration and separation, a specific grid refinement study should be performed. This has not been carried out due to the limited amount of time and computer resources available. In the following chapters, the same resolution requirements derived here in the case of fully developed turbulence in a channel flow will be used. For a discussion on the effect of grid resolution in LES or DNS of boundary layer flows with separation, the reader is referred to Le et al. (1997), Kaltenbach et al. (1999) or Wang (1997).

Chapter 7

Synthetic Inlet Conditions for Spatially Developing Channel Flow Computations

7.1 Introduction

In this chapter, the SEM is used to generate inlet conditions for LES of turbulent plane channel flow at $Re_\tau = 395$. The SEM is slightly modified compared to the version presented in Chapter 4, in order to generate non-isotropic eddies to reproduce the non-isotropic nature of the turbulence in the near-wall region. The statistics required to calculate the properties of the synthetic eddies are extracted from the LES of a fully developed turbulent channel flow with periodic streamwise boundary conditions performed in the previous chapter (run G). This simulation will also serve as a basis for comparisons with all simulations using inlet and outlet boundary conditions.

The present chapter is organized as follows. After the present introduction (Section 7.1), details are provided on the modification to the SEM in Section 7.2. In Section 7.3, a simulation with inlet conditions prescribed using the modified SEM is studied in detail, and compared with the reference LES. The influence of the synthetic inlet boundary conditions on the statistical and instantaneous structural properties of the flow downstream of the inlet is studied. In Section 7.4, we investigate the effect of an error in the specification of one of the optimal parameters extracted from the periodic LES (mean velocity, Reynolds stresses, length scales and time scales) on the evolution of the synthetic turbulence downstream of the inlet, in order to demonstrate the robustness of the SEM. Finally, Section 7.5 summarizes the observations presented in this chapter, and provides guidelines on the use of the SEM when reduced information on the flow statistics is available.

7.2 Synthesized Turbulence with a Modified SEM

7.2.1 Description of the modified SEM

A slightly modified version of the SEM was used in this chapter. In its original form the SEM assumes that the lengthscale σ is the same for all velocity components and for all directions. It was shown in the simulations of channel flows in the previous chapter that this is not the case. Instead of isotropic structures, the near-wall region for instance is dominated by streamwise elongated coherent structures. In order to provide the SEM with more information on the spatial structure of the turbulence, a different length scale σ_{ij} is used for each velocity component i in each direction j . Using these new lengthscales, the SEM is modified as follows:

1. The box of eddies B is defined by

$$x_{j,\min} = \min_{\mathbf{x} \in S, i \in 1,2,3} (x_j - \sigma_{ij}(\mathbf{x})) \quad \text{and} \quad x_{j,\max} = \max_{\mathbf{x} \in S, i \in 1,2,3} (x_j + \sigma_{ij}(\mathbf{x})). \quad (7.1)$$

2. The velocity signal generated by N eddies has the representation,

$$u_i = U_i + \frac{1}{\sqrt{N}} \sum_{k=1}^N c_i^k f_{\sigma_{ij}}(\mathbf{x} - \mathbf{x}^k), \quad (7.2)$$

where the shape function $f_{\sigma_{ij}}(\mathbf{x} - \mathbf{x}^k)$ of the eddies on component i is given by

$$f_{\sigma_{ij}}(\mathbf{x} - \mathbf{x}_k) = \sqrt{V_B} \cdot \frac{1}{\sigma_{i1}} f\left(\frac{x_1 - x_1^k}{\sigma_{i1}}\right) \cdot \frac{1}{\sigma_{i2}} f\left(\frac{x_2 - x_2^k}{\sigma_{i2}}\right) \cdot \frac{1}{\sigma_{i3}} f\left(\frac{x_3 - x_3^k}{\sigma_{i3}}\right). \quad (7.3)$$

For each velocity component i , there is a three-dimensional length scale σ_{ij} which defines the structure of the turbulent eddies in each spatial direction j . The modified SEM can thus generate non-isotropic velocity fluctuations which reproduce more realistically the elongated structures present in the near-wall region of fully developed channel flows.

The input statistics (mean velocity \mathbf{U} , Reynolds stresses R_{ij} and length scales σ_{ij}) required by the modified SEM are extracted from the periodic LES run G (see Table 6.1 on page 125) presented in the previous chapter. The length scales in the wall normal direction σ_{i2} are assumed to be equal to the length scales in the spanwise direction σ_{i3} . The spanwise lengthscales of the eddies σ_{i3} are taken as the integral length scales calculated from run G. As in the previous chapter, the integral length scales are defined as the distance at which the two-point correlations drop to 0.1. The streamwise length scales of the eddies σ_{i1} are related to the characteristic integral timescale T_i of the signal by $\sigma_{i1} = U_c T_i$ as shown in Chapter 4. The integral timescales T_i are calculated from run G as the distance at which the two-time correlations are 0.1 (consistent with the definition of the spanwise length scales). A tent function is used for the

shape function of the eddies and the number of eddies is first set to 10,000 in order to ensure a Gaussian behaviour of the probability density function of the generated signal.

7.2.2 Validation of the modified SEM

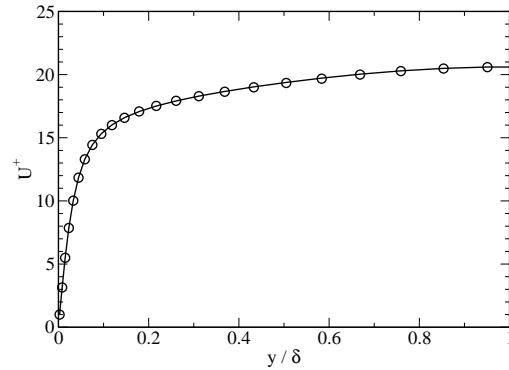


Figure 7.1: Profiles of the mean streamwise velocity of the modified SEM signal (—) and of the reference periodic LES (○○○).

The modified SEM is used to synthesize instantaneous velocity fluctuations on the plane $x = 0$ of the computational grid used in run G. The time step is $0.0025 \delta/u_\tau$, and statistics are computed over a time interval corresponding to 4,000 iterations. Fig. 7.1 and Fig. 7.2 compare mean velocity and Reynolds stresses profiles computed from the modified SEM signal and from the reference periodic LES. As expected from the exact results derived in Chapter 4, first and second order one-point statistics are well reproduced by the modified SEM. Fig. 7.3 shows the integral length scale in the spanwise direction for the three components of the velocity. It can be seen that the SEM finely reproduces the integral length scale distribution of the periodic LES for the components of the velocity. More specifically the small spanwise length scale of the near-wall eddies is accurately reproduced. The integral time scales for the three components of the velocity are shown on Fig. 7.4. In the near-wall region in particular, the long time scales associated with the near-wall streaks are accurately reproduced by the modified SEM. This would not have been possible if only one single length scale had been used in all spatial directions.

Although important one-point and two-point statistics of the flow are accurately reproduced by the modified SEM, the synthesized signal does not completely reproduce all the turbulent structures and their dynamics that can be found in the real flow. These limitations of methods of generation of synthetic turbulence are briefly presented here. Fig. 7.5 shows two-point correlations of the wall-normal velocity in the spanwise direction for the modified SEM signal and the periodic LES. Although eddies with correct

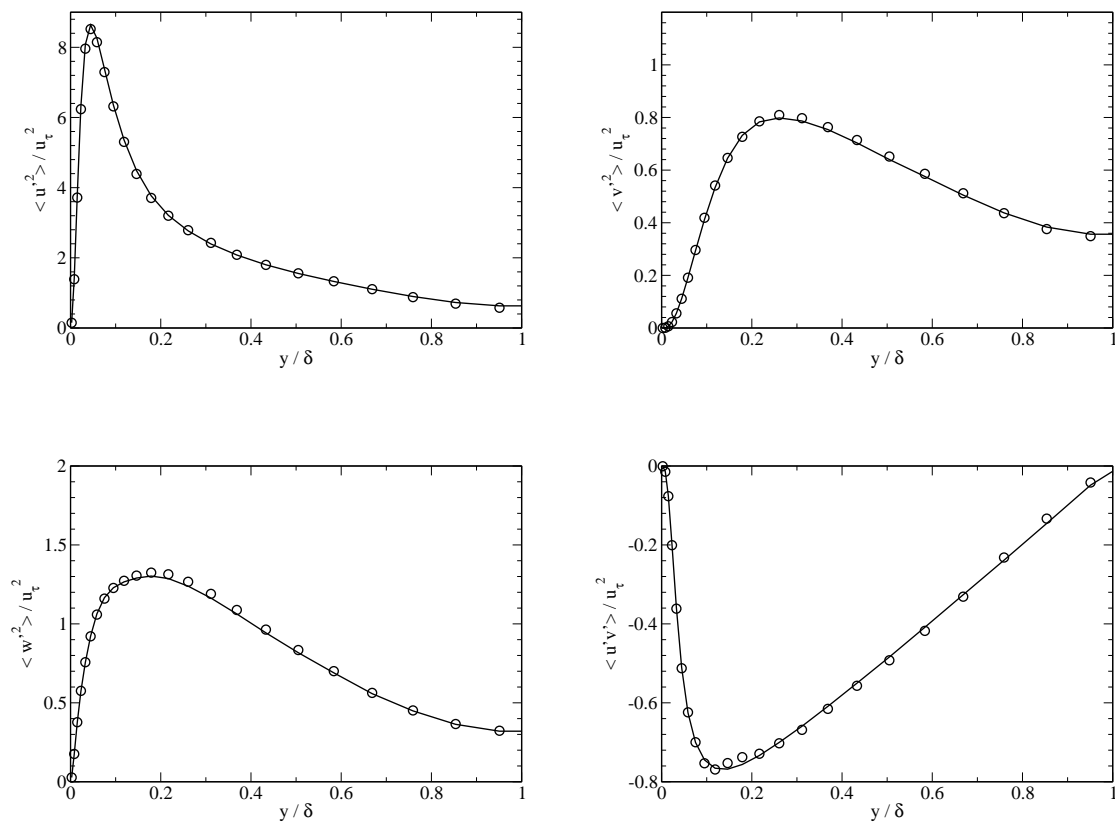


Figure 7.2: Profiles of the Reynolds stresses of the modified SEM signal (—) and the reference periodic LES (○○○).

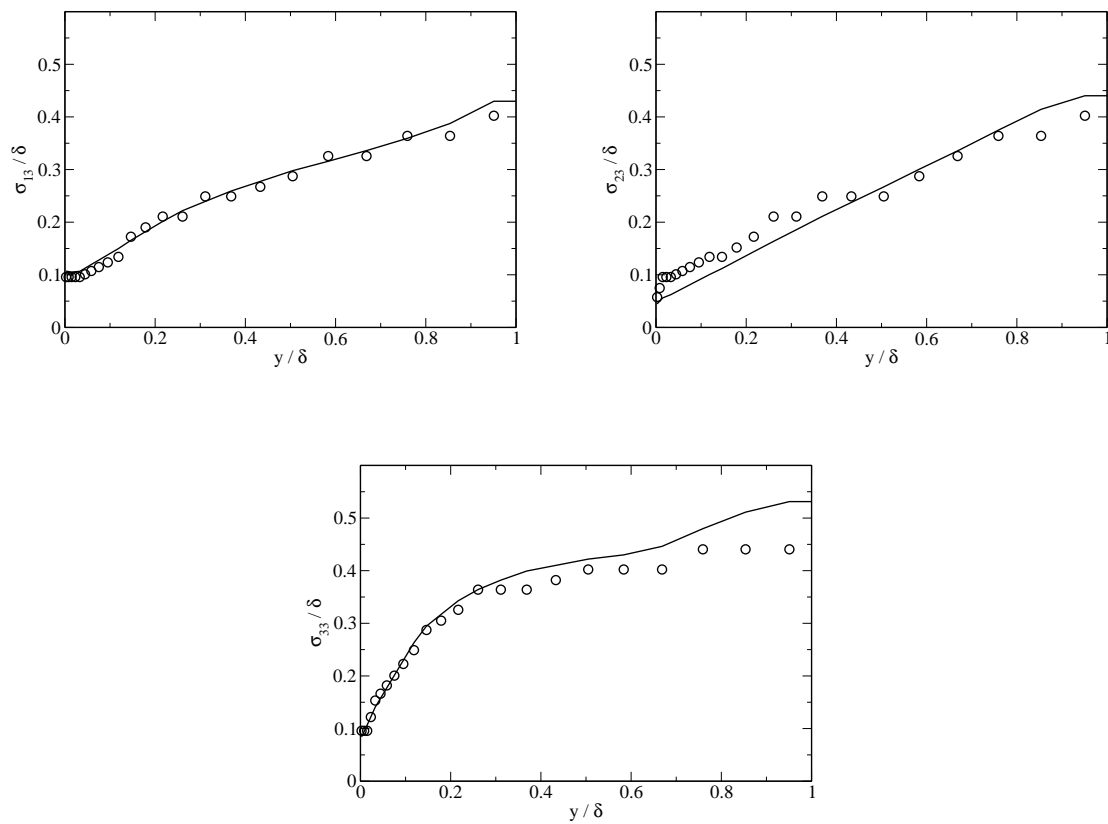


Figure 7.3: Profiles of the integral length scales of the three velocity components of the modified SEM signal (—) and the reference periodic LES (○○○).

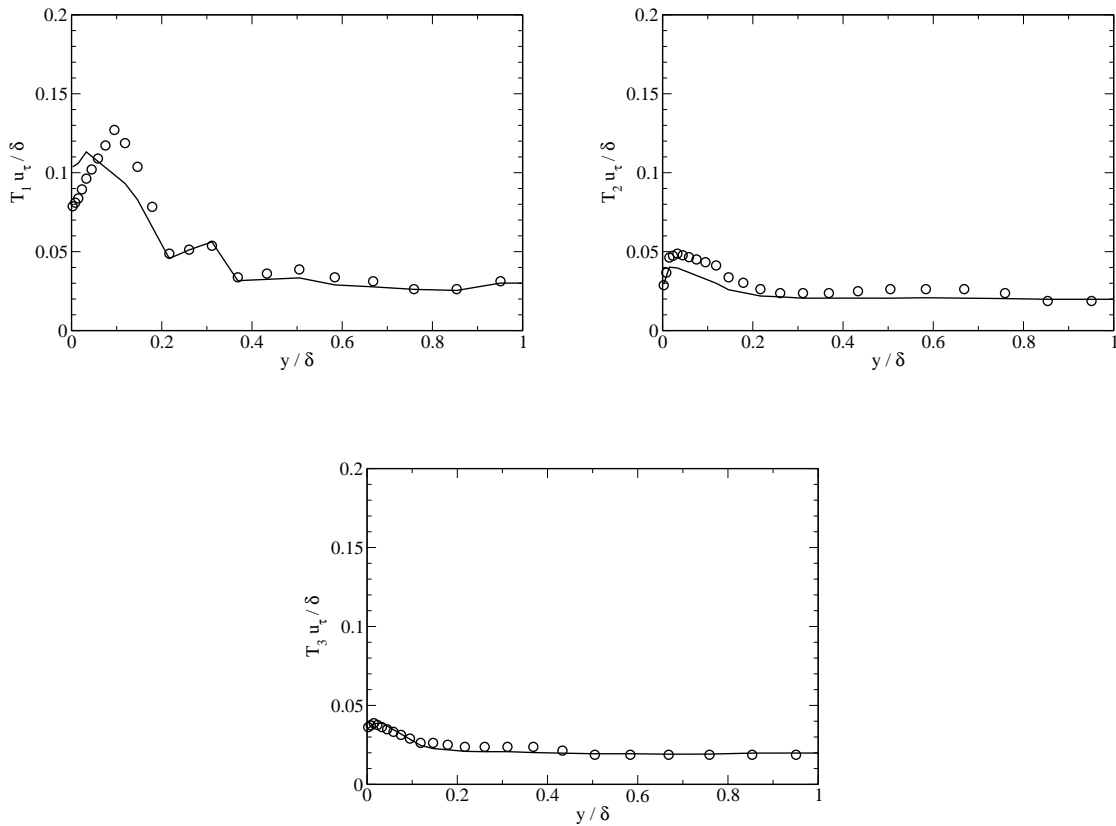


Figure 7.4: Profiles of the integral time scales of the three velocity components of the modified SEM signal (—) and the reference periodic LES (○○○).

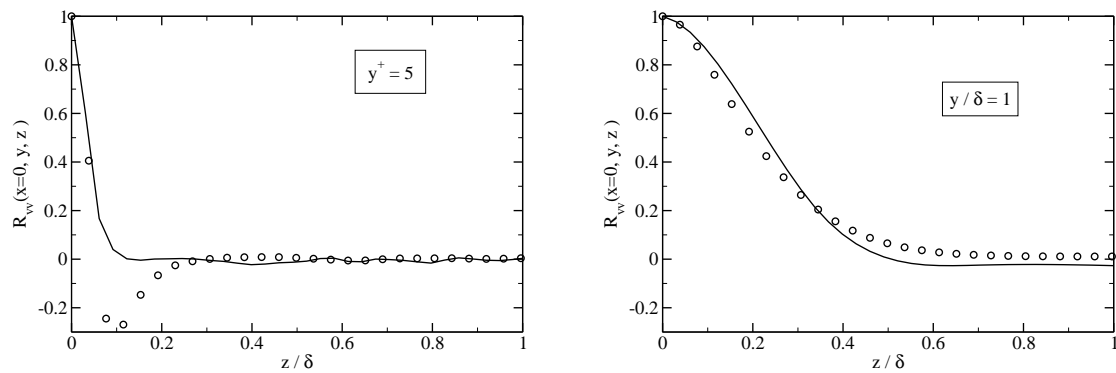


Figure 7.5: Two-point v correlations in the spanwise direction for the modified SEM signal (—) and the reference periodic LES (○○○) near the wall (left) and in the centre of the channel (right).

integral length-scales are produced across the whole flow (as already shown in Fig. 7.3), the SEM does not generate near-wall counter-rotating streamwise vortices, and thus does not reproduce the negative peak of the v' correlations at $y^+ = 5$. Fig. 7.6 shows one-dimensional spanwise energy spectra of the

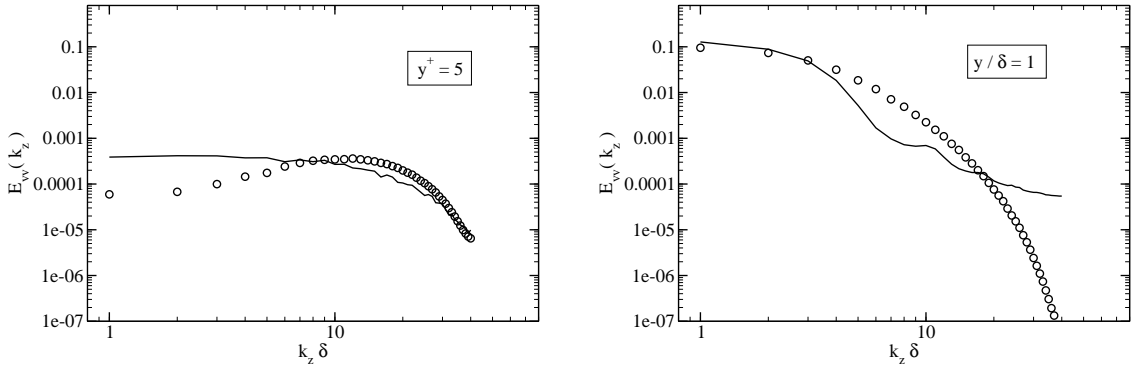


Figure 7.6: One-dimensional spanwise energy spectra of the wall-normal fluctuations for the modified SEM signal (—) and the reference periodic LES (○○○) near the wall (left) and in the centre of the channel (right).

wall-normal fluctuations. As already mentioned in the previous chapter (see Eq. (4.32)), the spectrum of the fluctuations is simply the spectrum of the shape function f . The discrepancies between the modified SEM signal and the periodic LES are the most significant in the middle of the channel. The modified SEM signal cannot generate an energy cascade from large to small eddies, since it locally generates only one type of eddies with one single characteristic length-scale.

A comparison of instantaneous velocity planes of the modified SEM and periodic LES signals is shown on Fig. 7.7. More small scale structures are observed in the LES signal than in the modified SEM signal, especially in the core of the channel. Although the SEM generates eddies of different sizes in different regions of the inlet plane, at a given location only eddies of a single length scale are prescribed. In the periodic LES, the core of the channel is populated with near-wall structures which have been ejected from the wall, and the energy cascade transfers energy from the large scale motion towards the small scale motion. All these phenomena cannot be fully accounted for by the SEM, and these are responsible for the richer nature of the periodic LES signal in the middle of the channel. Close to the wall, the vortical structures present in the synthetic signal do not seem as intense and distorted as in the LES field. Again this can be accounted for by the phenomena of sweep and ejection which are not taken into account in the modified SEM.

To conclude, although the eddy structure in the modified LES signal is still different from the one in

the periodic LES signal, both synthetic and LES signals are identical from a statistical point of view (only comparing low order statistics). The development of the synthetic fluctuations downstream of the inlet towards a more physical state inside of the computational domain will now be studied.

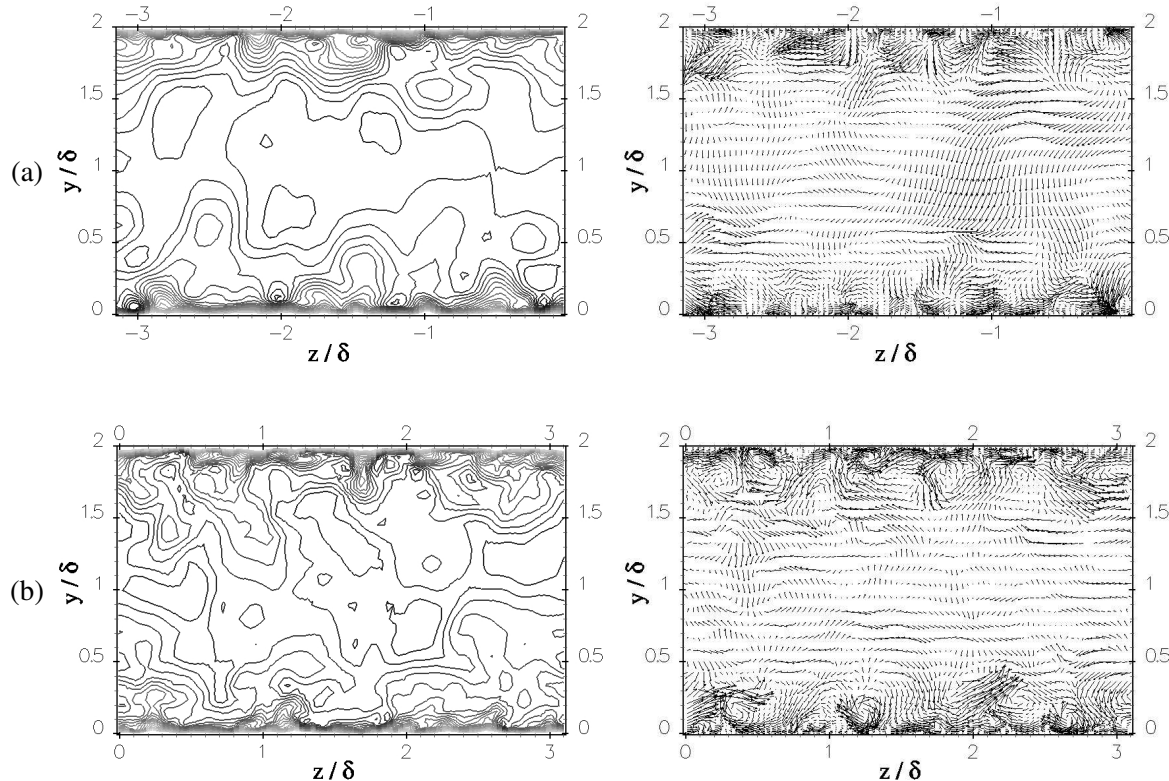


Figure 7.7: Instantaneous streamwise velocity contours (left) and velocity vectors (right) of (a) the modified SEM signal and (b) the periodic LES signal. Streamwise velocity contours are evenly spaced at 0, 2, 4, ..., 22. Velocity vectors are projected onto the (Oxy) plane.

7.3 Spatially Developing Channel Flow Simulation with Optimal SEM Inlet Parameters

Channel flow simulations with synthetic inlet boundary conditions were carried out in a computational domain of dimensions $20\pi\delta \times 2\delta \times \pi\delta$ in the streamwise, wall-normal and spanwise directions, respectively. The numerical method, turbulence model and grid resolution are the same as in the periodic LES run G. This results in a grid of $250 \times 46 \times 82$ cells in the streamwise, wall-normal and spanwise directions, respectively. The Smagorinsky model (with a constant $C_S = 0.065$) and Van-Driest damping at the wall is used.

Inlet conditions were generated at each time step using the modified SEM presented in the previous section. The mean velocity profile calculated from run G was prescribed at the inlet which fixed the Reynolds number, $Re = 14,516$ ($Re_\tau = 395$). At the exit plane, the standard outlet boundary condition implemented in *Code_Saturne* (see page 97 in Chapter 5) was used. Periodic boundary conditions were applied in the spanwise directions, whereas no-slip boundary conditions were imposed at the walls.

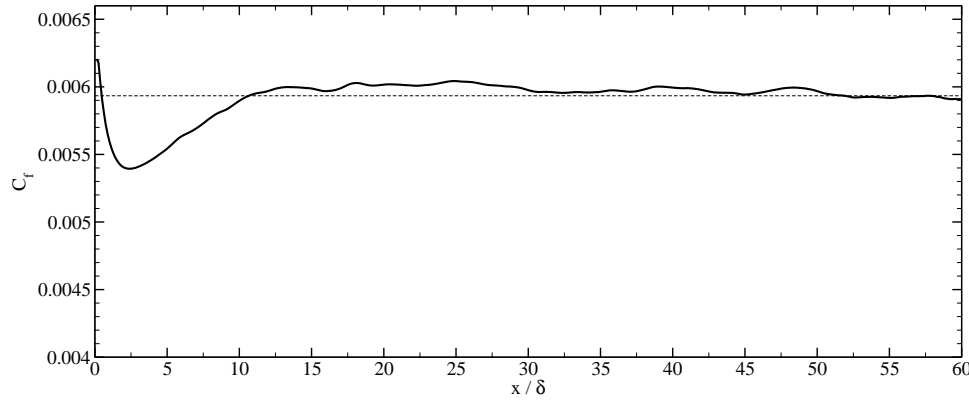


Figure 7.8: Downstream development of the coefficient of friction C_f . Channel flow at $Re_\tau = 395$ with SEM inlet conditions. ——, Periodic LES target value.

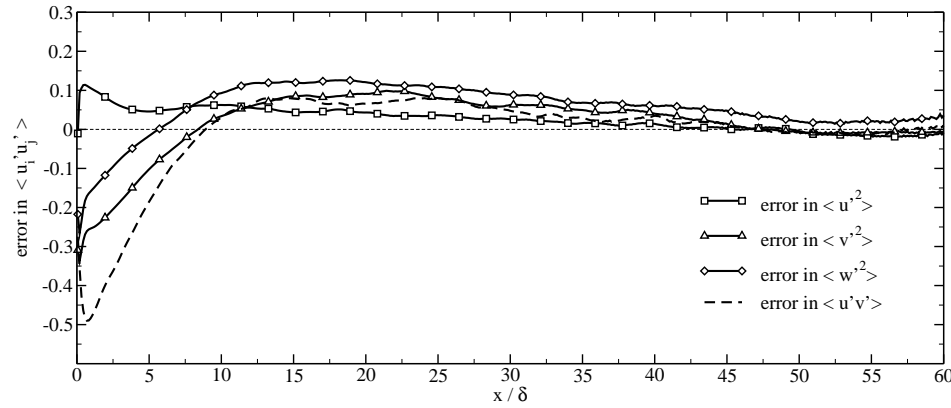


Figure 7.9: Downstream development of the error in the Reynolds stresses. Channel flow at $Re_\tau = 395$ with SEM inlet conditions. ——, Periodic LES target value.

Since synthetic velocity fluctuations are prescribed at the inlet by the modified SEM, a transition region - during which the flow statistics will differ from their fully developed values - is expected downstream of the inlet. In order to measure the development of the synthetic fluctuations downstream of the

inlet, we define the error in the profile of a variable a (a will be either the Reynolds stresses or the kinetic energy) as,

$$e_a(x) = \frac{\int_0^{2\delta} (|a| - |a^{\text{perio}}|) dy}{\int_0^{2\delta} |a^{\text{perio}}| dy} \quad (7.4)$$

where a^{perio} is calculated from the periodic LES and a is calculated from the spatially developing simulation. If the turbulent kinetic energy is studied for instance, a positive value of e_k indicates a higher turbulent activity than in the fully developed flow whereas a negative value of e_k indicates a lower turbulent activity. The coefficient of friction,

$$C_f = \frac{\tau_w}{\frac{1}{2}\rho U_b^2}$$

, will be preferred to an error function to study the development of the mean velocity profile. For all of the simulations presented in this chapter, the statistics are obtained over a time period $184 \delta/U_b$, and are averaged in space over the spanwise direction as well as over the lower and upper halves of the channel.

Fig. 7.8 shows the evolution of the coefficient of friction downstream of the inlet. For comparisons, the horizontal dashed line represent the coefficient of friction in the periodic LES. When the SEM is used, the friction coefficient decreases downstream of the inlet to reach a minimum around 3δ , before converging towards the periodic LES value around 15δ downstream of the inlet.

The decrease of C_f immediately downstream of the inlet indicates that the flow undergoes a short laminarization process. The development of the error in the Reynolds stresses is shown on Fig. 7.9. The laminarization of the flow is initiated by a sudden decay of all the Reynolds stresses downstream of the inlet. The Reynolds shear stress is the most affected, losing about 50% of its intensity immediately downstream of the inlet. Although the SEM generates fluctuations with realistic length and time scales, the complex structures and dynamics of near-wall turbulence are not reproduced which causes the decay of the Reynolds stresses downstream of the inlet. However the flow does not laminarize and starts redeveloping Reynolds stresses immediately after the initial drop downstream of the inlet. By $x/\delta = 10$ the error in all the Reynolds stresses is within 10% of fully developed values. Further downstream there is a region where the intensity of all the Reynolds stresses is slightly overestimated (of about 10%). This region extends up to $x = 40\delta$ where the Reynolds stresses recover fully developed values. To the author's knowledge, this excess of turbulent activity following the initial decay of the prescribed synthetic fluctuations has never been documented before.

Fig. 7.10 shows the downstream development of the error in the Reynolds shear stress profiles in the near-wall region ($y^+ < 50$) and in the core of the channel ($y/\delta > 0.5$). In the near-wall region, there is a severe initial decay of the Reynolds shear stress downstream of the inlet, but for $x/\delta > 10$, the error is very small and the Reynolds shear stress profile can be considered as fully developed. In the core of

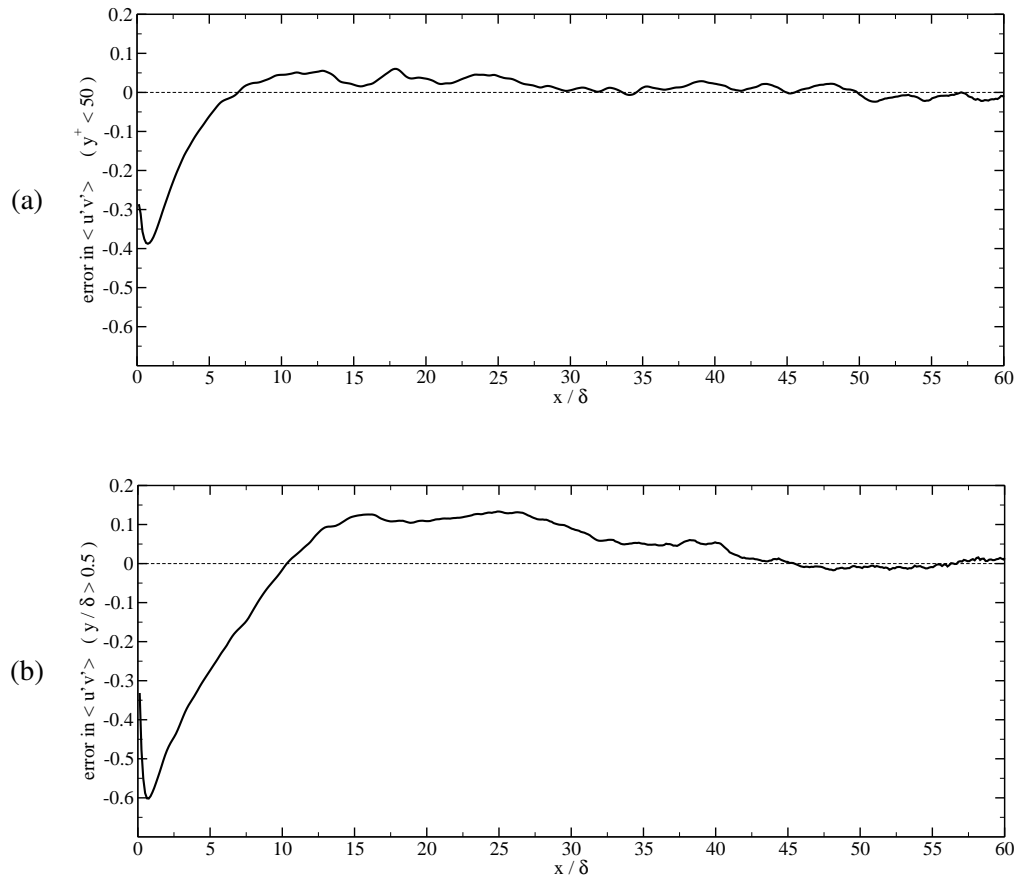


Figure 7.10: Downstream development of the error in the Reynolds shear stress profile: (a) integration of the error for $y^+ < 50$ and (b) integration of the error for $y/\delta > 0.5$. Grey lines represent streamwise extended domain solution.

the channel, the Reynolds shear stress also decays immediately downstream of the inlet before increasing until about 20δ downstream of the inlet, where it is overestimated by almost 15%. This excess of energy is then slowly dissipated, and the Reynolds shear stress slowly decreases towards fully developed levels. To conclude, the transient in the centre of the channel is much longer than in the near-wall region: for $x/\delta > 10$, the near-wall Reynolds stress profiles and the coefficient of friction are recovered, whereas errors of up to 20% remain in the core of the channel up to about $x = 20\delta$.

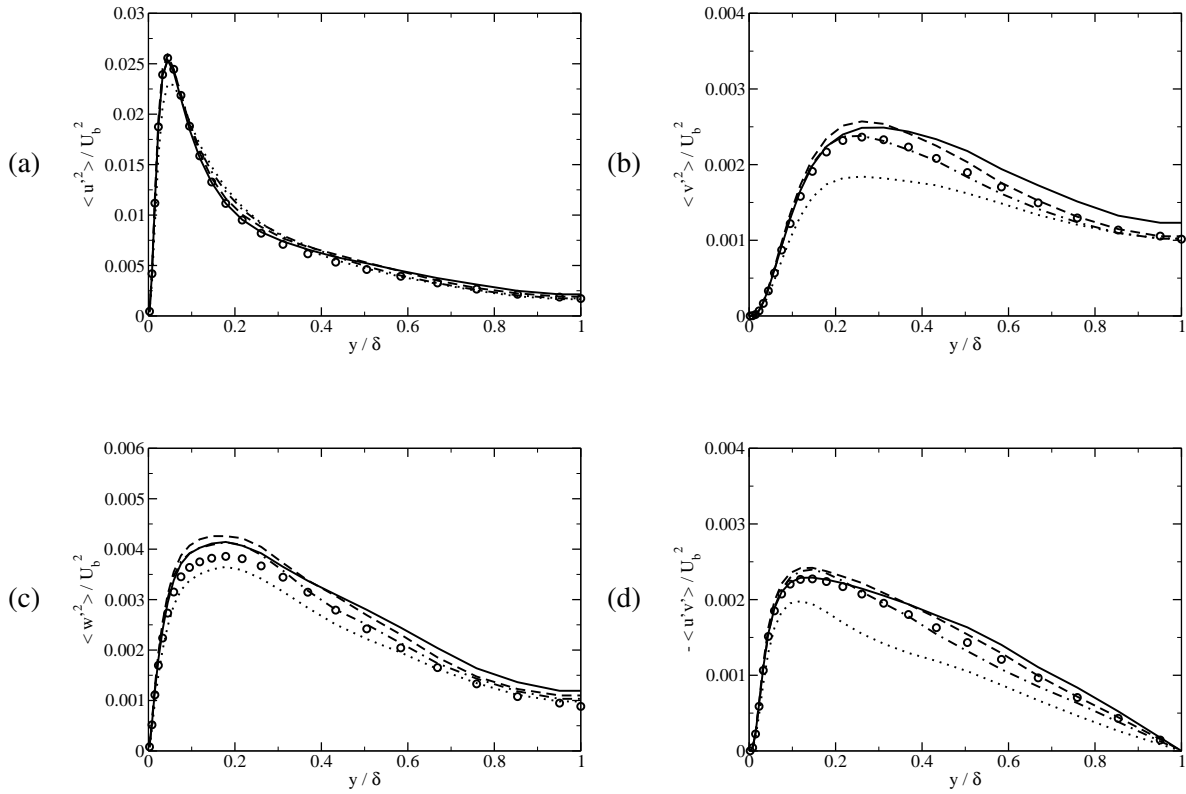


Figure 7.11: Spatially developing channel flow at $Re_\tau = 395$. Profiles of the Reynolds shear stress at various streamwise locations. , $x/\delta = 5$; -·-, $x/\delta = 10$; -·-, $x/\delta = 15$; —, $x/\delta = 25$; ○○○, reference periodic LES.

Profiles of the Reynolds stresses at several streamwise locations are shown on Fig. 7.11 to illustrate more clearly the observations made above. All of the Reynolds stresses (apart from the streamwise fluctuations $\langle u'^2 \rangle$) decay downstream of the inlet, the wall-normal fluctuations $\langle v'^2 \rangle$ being particularly reduced at the first location $x/\delta = 5$. Further downstream of the inlet, realistic correlations and turbulent structures redevelop and the correct profiles are recovered. As mentioned previously, the levels of fluctuations in the centre of the channel remain slightly higher than in the periodic LES, even by the end of the short

domain at $x/\delta = 25$.

In order to analyse more in depth the structure of the turbulence in the channel, Fig. 7.12 shows one-dimensional spectra in the spanwise direction at several streamwise locations in the near-wall region and in the centre of the channel. The collapse of the spectra at $y^+ = 5$ is excellent and in very good agreement with the periodic LES spectra for $x > 3\delta$. In the centre of the channel, the collapse of the large scales is relatively good whereas the small scales undergo a strong transient. The modified SEM only generates eddies whose characteristic size is the local integral length scale, resulting in a lack of small scale eddies in the inertial and dissipative ranges. As the flow is convected downstream, the inertial range of the spectrum is fed with small scales cascaded from the low wave number part of the spectrum, or generated at the wall and convected in the wall-normal direction towards the centre. It should be noted that the high levels of energy at the highest wavenumbers in the first plane $x/\delta = 0.1$ are only due to the non-periodicity of the inflow signal in the spanwise direction and do not affect (according to Keating et al. (2004)) the development of the turbulence.

Fig. 7.13 shows instantaneous streamwise velocity fluctuations in three planes parallel to the wall located in the viscous sublayer ($y^+ = 5$), in the logarithmic region ($y^+ = 100$) and in the centre of the channel ($y/\delta = 1$). High and low speed streaks are clearly visible in the viscous sublayer immediately downstream of the inlet. Further away from the wall, on the planes at $y^+ = 100$ and $y/\delta = 1$, the signal undergoes a small transient mostly in its small scales. This can be accounted for by the ejection of small scale structures from the wall towards the centre and the establishment of the inertial energy cascade, which after a certain distance leads to a velocity signal richer in small scales in the centre of the channel downstream of the inlet. Fig. 7.14 shows contours of spanwise velocity fluctuations on the plane $z = 2\delta$. One can notice the rapid alignment at angles of $30^\circ - 45^\circ$ to the wall (which is a signature of the presence of hairpin vortices) of the large-scale structures prescribed at the inlet. This shows that the velocity fluctuations prescribed by the modified SEM (although they do not have a correct structure) rapidly trigger the mechanisms of production of near-wall turbulence. Finally Fig. 7.15 shows isosurfaces of Q . The vortical activity is quite intense everywhere on the domain and the visual agreement with the periodic LES is very good.

7.4 Sensitivity Analysis of the SEM to its Input Parameters

The simulation with inflow data generated by the modified SEM with optimal parameters extracted from a periodic LES has been analyzed in the previous section. In the present section, inlet conditions are prescribed using the modified SEM with different input parameters. In order to increase the number of

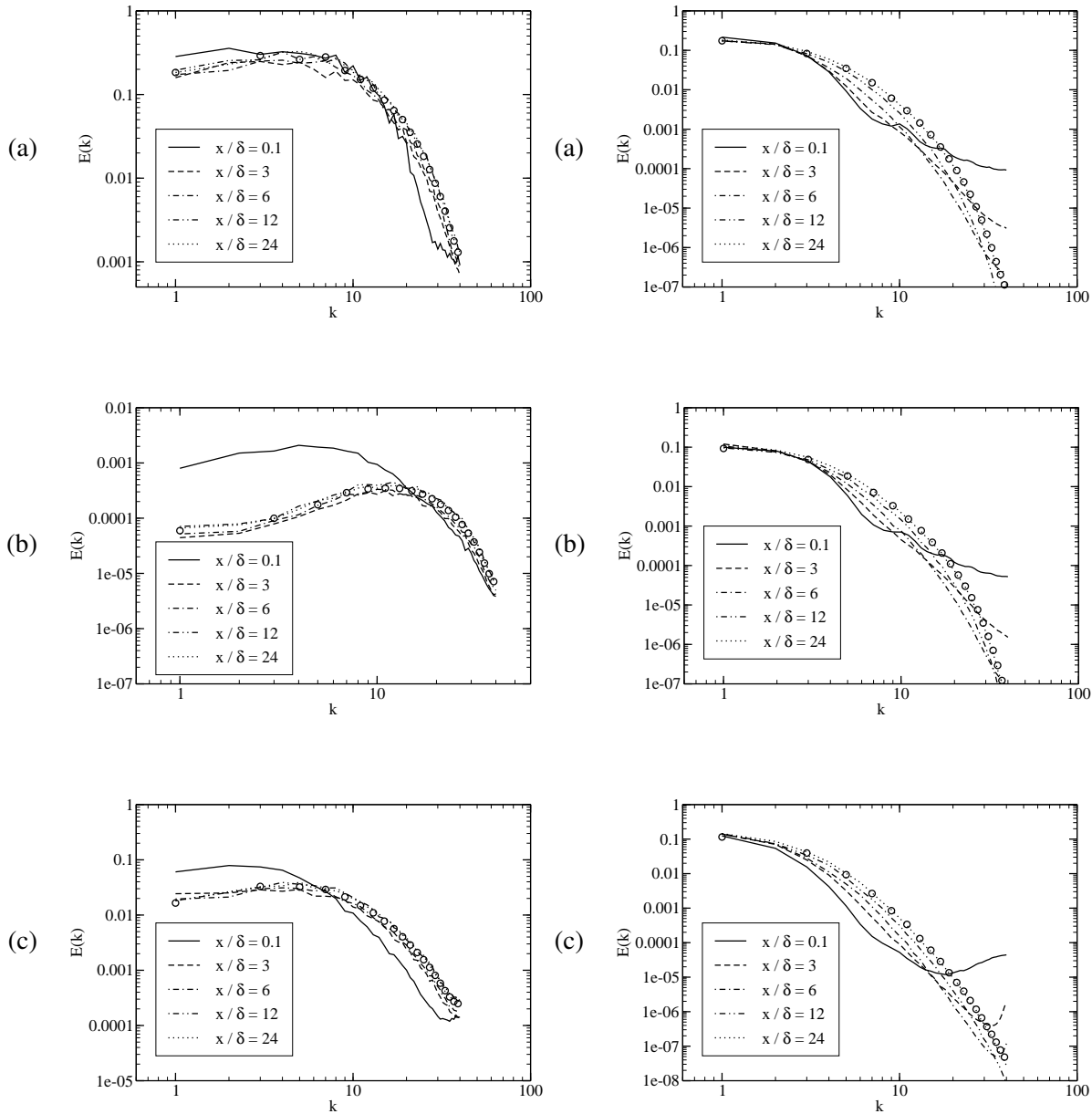


Figure 7.12: Spatially developing channel flow at $Re_\tau = 395$. One-dimensional spanwise energy spectra (a) E_{uu} , (b) E_{vv} and (c) E_{ww} at various streamwise locations at $y^+ = 5$ (left) and at $y/\delta = 1$ (right): Lines represent spatially developing simulation with the SEM at different locations; $\circ\circ\circ$ represent reference periodic LES.

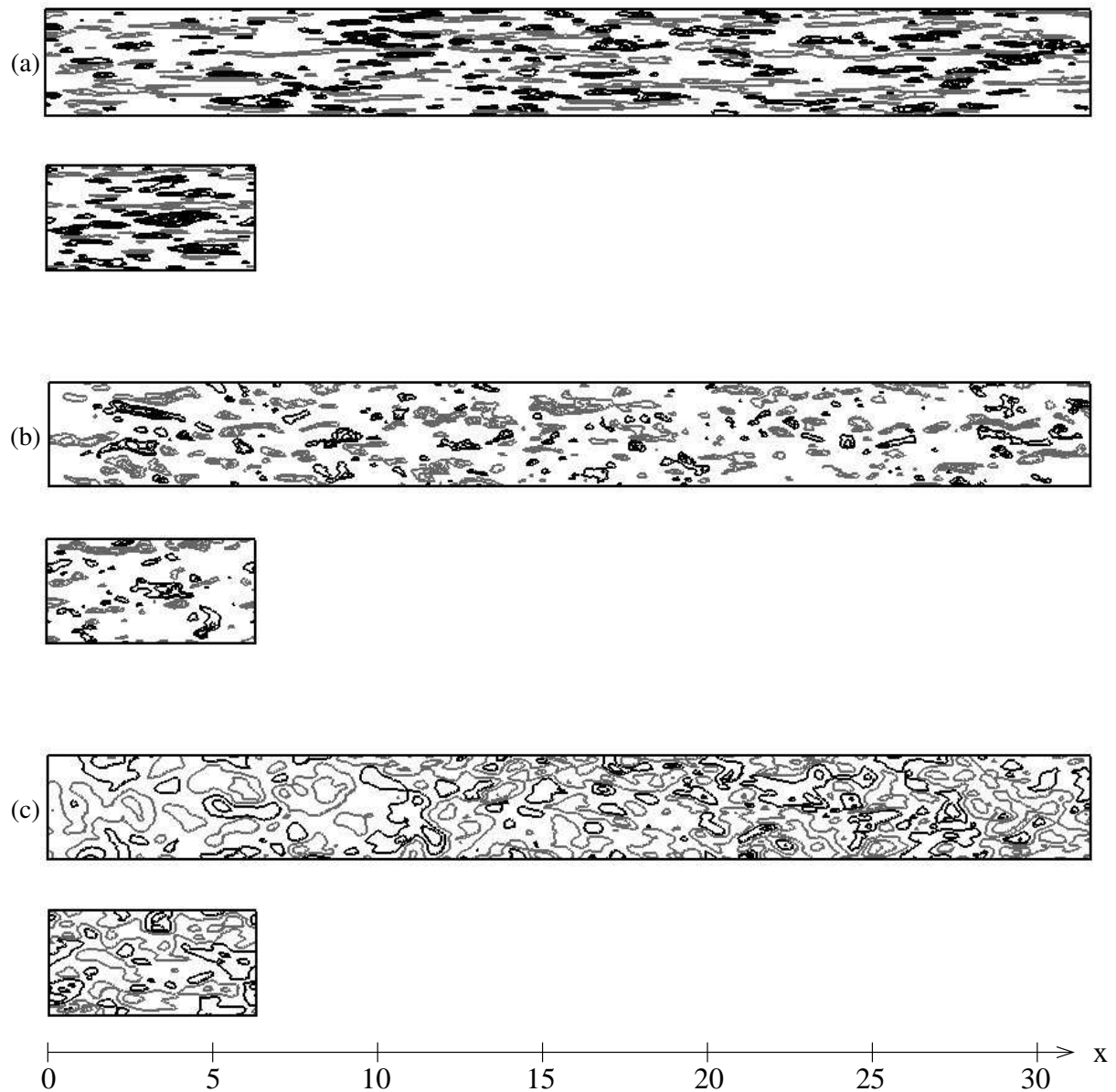


Figure 7.13: Spatially developing channel flow at $Re_\tau = 395$. Streamwise velocity fluctuations at different y locations. (a) Plane $y^+ = 5$, (b) plane $y^+ = 100$ and (c) plane $y/\delta = 1$. Velocity planes at the same y location for the periodic LES (run G) are provided for comparisons. Contour lines are evenly spaced at $\pm 0.5, \pm 1.5, \pm 2.5, \pm 3.5$ and ± 4.5 for the planes at $y/\delta = 1$ and at $\pm 2, \pm 3, \pm 4, \pm 5$ and ± 6 for the planes at $y^+ = 5$ and $y^+ = 100$. Grey lines indicate negative value contours.

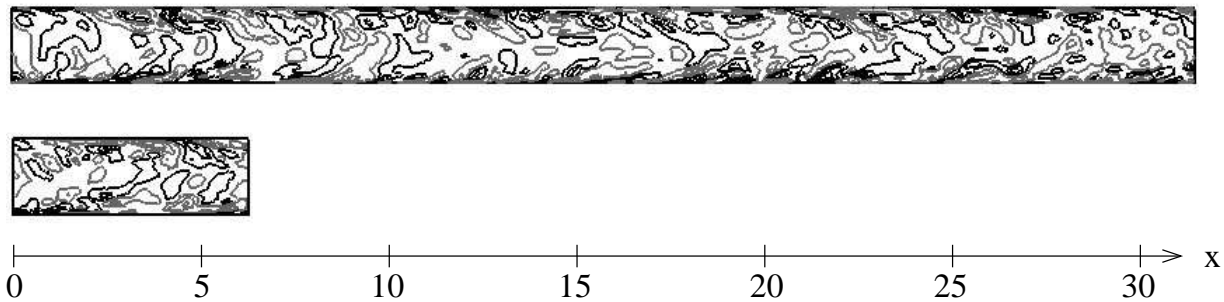


Figure 7.14: Spanwise velocity fluctuations on a plane of constant in the spatially developing (top) and in the periodic LES (bottom) of channel flow at $Re_\tau = 395$. Contour lines are evenly spaced at ± 0.5 , ± 1.5 , ± 2.5 , ± 3.5 and ± 4.5 . Grey lines indicate negative value contours.

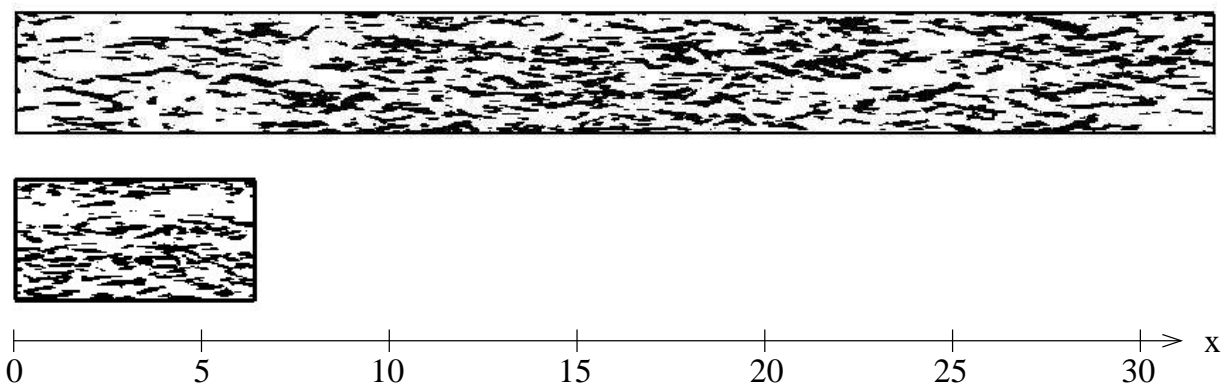


Figure 7.15: Instantaneous isosurfaces of $Q = 250 (u_\tau^2 / \delta)^2$ in the lower half of the channel in the spatially developing (top) and in the periodic LES (bottom) case.

tests that can be performed the size of the computational domain in the streamwise direction was reduced from $20\pi\delta$ to $10\pi\delta$. The influence of modifications to the target inlet mean velocity, Reynolds stress tensor and length and time scales profiles on the development of the flow downstream of the inlet is studied.

7.4.1 Influence of the prescribed mean velocity profile

The previous simulation used at the inlet the mean velocity profile extracted from the periodic LES. In this subsection, the mean inflow velocity profile is prescribed as,

$$U = \alpha U^{\text{test}} + (1 - \alpha) U^{\text{perio}} \quad (7.5)$$

where U^{perio} is the mean optimal velocity profile extracted from the periodic LES and U^{test} corresponds either to a flat velocity profile,

$$U^{\text{test}} = U_b,$$

or to a laminar velocity profile,

$$U^{\text{test}} = \frac{3U_b}{2}(2\delta - y)y.$$

α is a weighting coefficient which characterizes how far the prescribed inlet velocity profile is from the optimal velocity profile U^{perio} . The simulation with $\alpha = 0$ corresponds to the simulation presented in the previous section with a mean velocity profile calculated from the periodic LES. Four simulations with different values of α and U^{test} are performed to test a wide range of inlet profiles. The first two simulations performed use a flat profile for U^{test} and $\alpha = 0.1$ (run UT10) or $\alpha = 0.25$ (run UT25). Fig. 7.16 shows the corresponding inlet velocity profiles. It can be seen that the slope of the velocity profile is overestimated in the near wall region and underestimated in the centre of the channel. The two last simulations are performed with a laminar profile for U^{test} and $\alpha = 0.1$ (run UL10) or $\alpha = 0.25$ (run UL25). The slope of the velocity profile is then underestimated in the near-wall region and overestimated in the centre of the channel.

The coefficient of friction and the error in the turbulent kinetic energy profile downstream of the inlet shown in Fig. 7.17 are both strongly affected by the inflow velocity profile. In order to analyse this phenomenon, Fig. 7.18 shows mean velocity and turbulent kinetic energy profiles at different streamwise locations downstream of the inlet for run UL25. The inlet velocity profile prescribed at the inlet in UL25 (Fig. 7.18 (a)) underestimates the coefficient of friction but overestimates the shear in the centre of the channel. This high shear then interacts with the turbulent fluctuations prescribed at the inlet to produce overly high levels of turbulent kinetic energy downstream of the inlet, as shown on Fig. 7.18 (b). In the

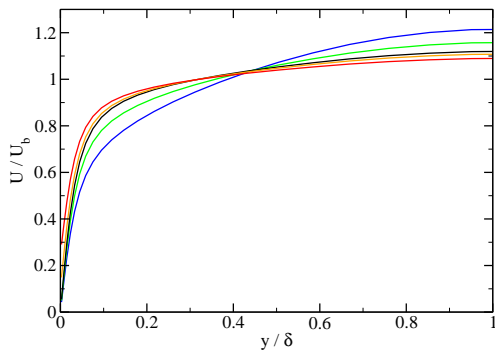


Figure 7.16: Comparisons of different prescribed inlet velocity profiles: Run UL25 — ; Run UL10 — ; periodic LES mean velocity profile — ; Run UT10 — ; Run UT25 — .

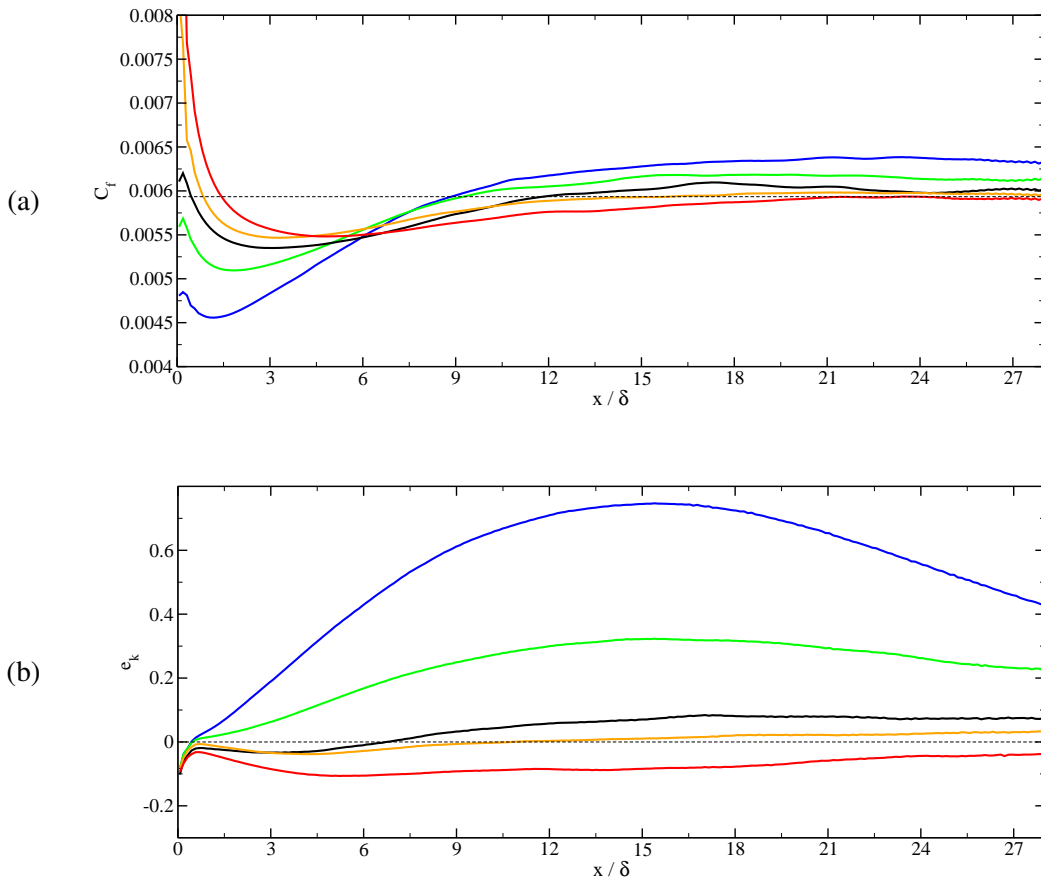


Figure 7.17: Downstream development of (a) the coefficient of friction and (b) the error in the turbulent kinetic energy profile for the modified SEM inlet conditions with different prescribed mean velocity profiles. Same legend as in Fig. 7.16.

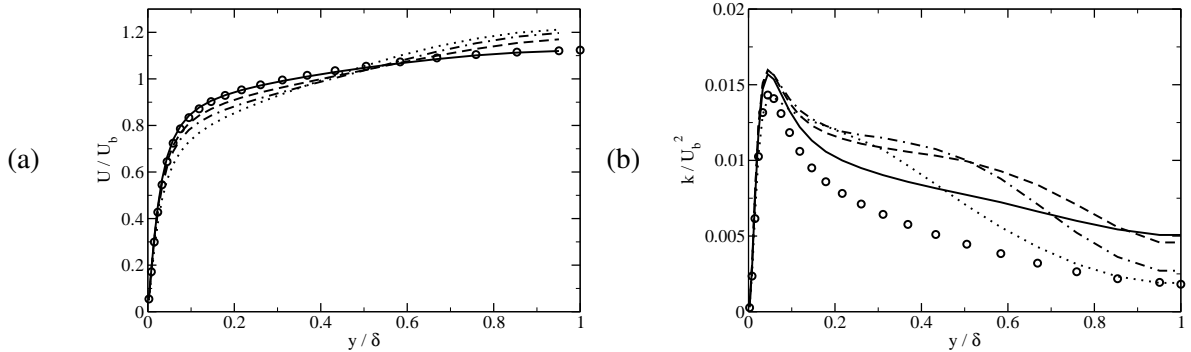


Figure 7.18: Profiles of (a) mean velocity and (b) turbulent kinetic energy. Modified SEM inflow with a different inflow mean velocity profile, run UL25: , $x/\delta = 5$; - - - , $x/\delta = 10$; - - - - , $x/\delta = 15$; —, $x/\delta = 30$; ○○○, reference periodic LES.

near-wall region however, both the mean velocity and the turbulent kinetic energy profiles are in good agreement with the fully developed profiles. Fig. 7.19 shows the production term in the Reynolds shear stress budget for fully developed turbulence,

$$P_{\langle u'v' \rangle} = -\langle v'^2 \rangle \frac{\partial U}{\partial y}. \quad (7.6)$$

for run UL25 and the reference simulation with exact inflow mean velocity profile. Because of the high shear in the centre of the channel for UL25, the isocontours of $P_{\langle u'v' \rangle}$ bend towards the core of the channel around $x/\delta = 10 - 15$ generating an excess of Reynolds shear stress. The same analysis can be performed for run UT25 to account for the reduced levels of turbulent kinetic energy and coefficient of friction on Fig. 7.17. Since the slope of the prescribed inflow profile is underpredicted at the inlet, the production of Reynolds shear stress and kinetic energy downstream of the inlet is underpredicted downstream of the inlet and the recovery is a very slow process.

7.4.2 Influence of the prescribed Reynolds stress tensor

Influence of the inflow turbulent kinetic energy profile

Simulations were first performed by only modifying the inlet turbulent kinetic energy k . The optimal profiles of the three normal stresses $\langle u'^2 \rangle$, $\langle v'^2 \rangle$ and $\langle w'^2 \rangle$ were multiplied by a constant factor r . Seven calculations with different values of r in the range $r = 0.25 - 1.5$ were performed.

Fig. 7.20 shows the downstream development of the coefficient of friction and the errors in the the turbulent kinetic energy and Reynolds shear stress profiles. The recovery of a fully developed k profile is a

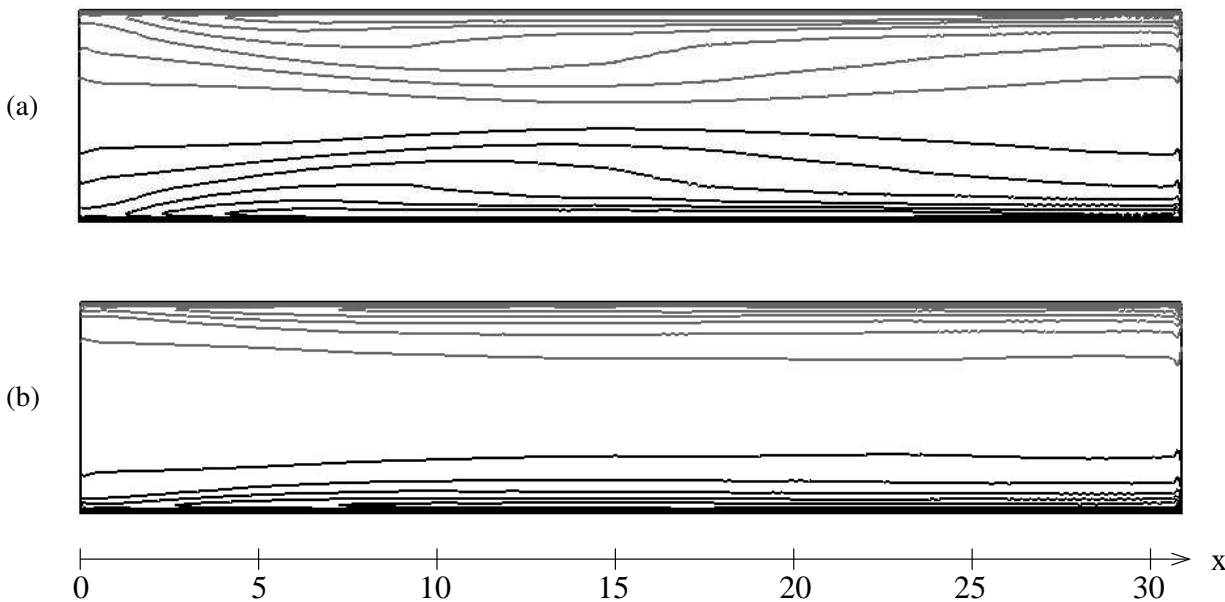


Figure 7.19: Production of Reynolds shear stress $P_{\langle u'v' \rangle}$. Modified SEM inflow: (a) run UL25 and (b) reference simulation with the exact mean inflow velocity profile. Contour lines of are evenly spaced at $\pm 4, \pm 8, \pm 12, \pm 16$ and ± 20 . Grey lines indicate negative value contours.

fairly slow process regardless of whether the prescribed inflow turbulent kinetic energy is overestimated or underestimated. An overprediction of k however limits the initial drop of the coefficient of friction downstream of the inlet as shown on Fig. 7.20 (a). However the Reynolds shear stress (see Fig. 7.20 (c)) drops in all cases by almost 50% immediately downstream of the inlet, indicating that the higher coefficient of friction observed for the simulations with an overprediction of k downstream of the inlet is not maintained by the Reynolds shear stress, but by the artificially high levels of turbulence intensity imposed at the inlet. In the case where the inflow k profile is underestimated, there is a significant drop of the coefficient of friction downstream of the inlet. In the most extreme case simulated where only 75% of the fully developed turbulent kinetic energy profile is prescribed at the inlet, the friction coefficient decays by almost 30% at $x = 6\delta$ and recovers correct values only after about 25δ .

Fig. 7.21 shows the downstream development of the error in the turbulent kinetic energy profile in the near wall region ($y^+ < 50$) and in the core of the channel ($y/\delta > 0.5$). As expected the return to equilibrium is much slower in the core of the channel than in the near wall region. Close to the wall, the excess of energy is quickly dissipated and the flow redevelops turbulence quickly downstream of the inlet. As shown on Fig. 7.21 (a), all simulations exhibit errors in the k profile in the near-wall region lower than 5% after $x/\delta = 10$. In the core of the flow however, a fairly long transition region is necessary both to dissipate the excess of energy (in the case of an overestimation of the inlet turbulent intensity) or

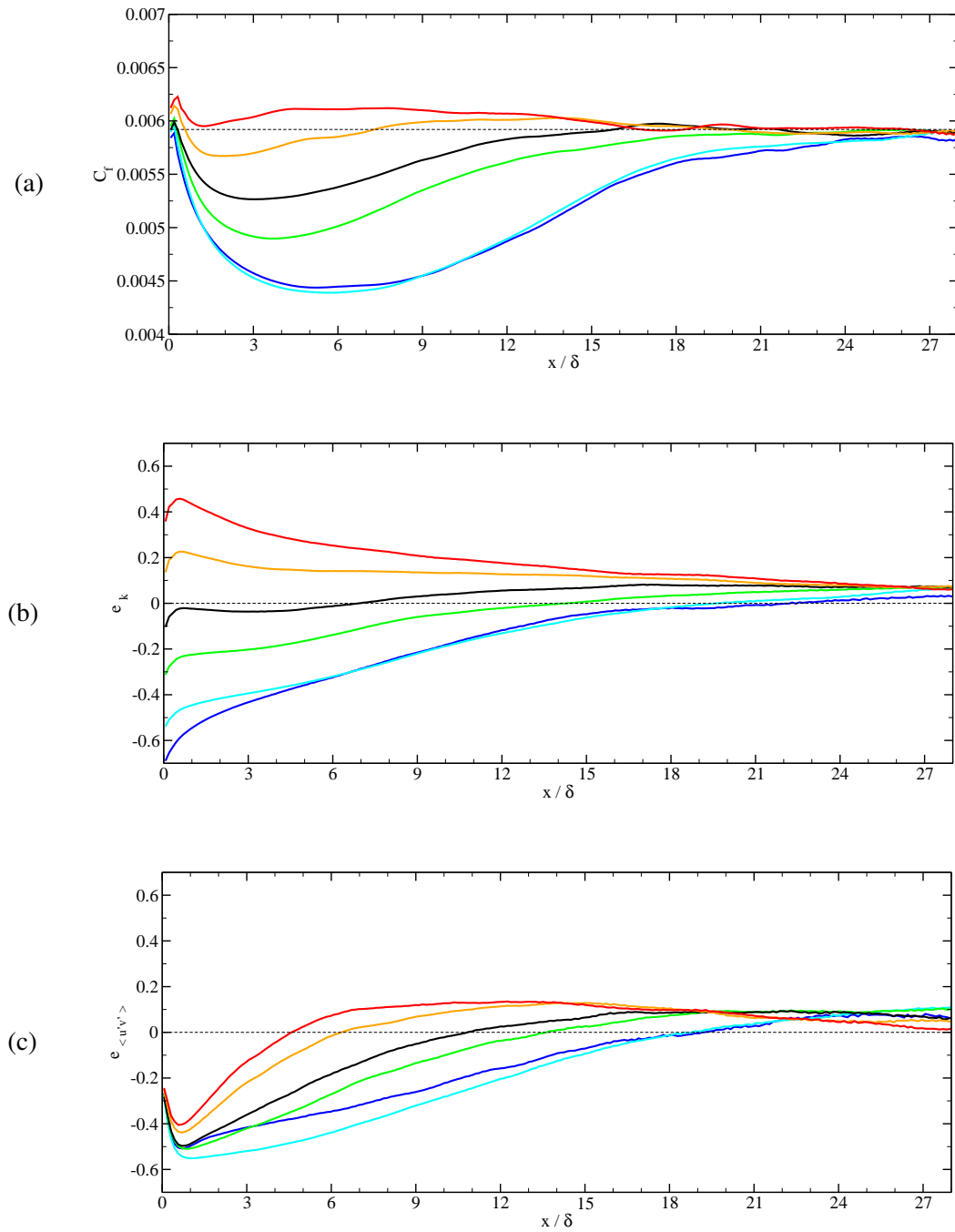


Figure 7.20: Downstream development of (a) the coefficient of friction and the errors in (b) the turbulent kinetic energy, and (c) the Reynolds shear stress profiles. Modified SEM inflow with -75% —; -50% —; -25% —; exact —; +25% —; and +50% — of optimal target k profile at the inlet.

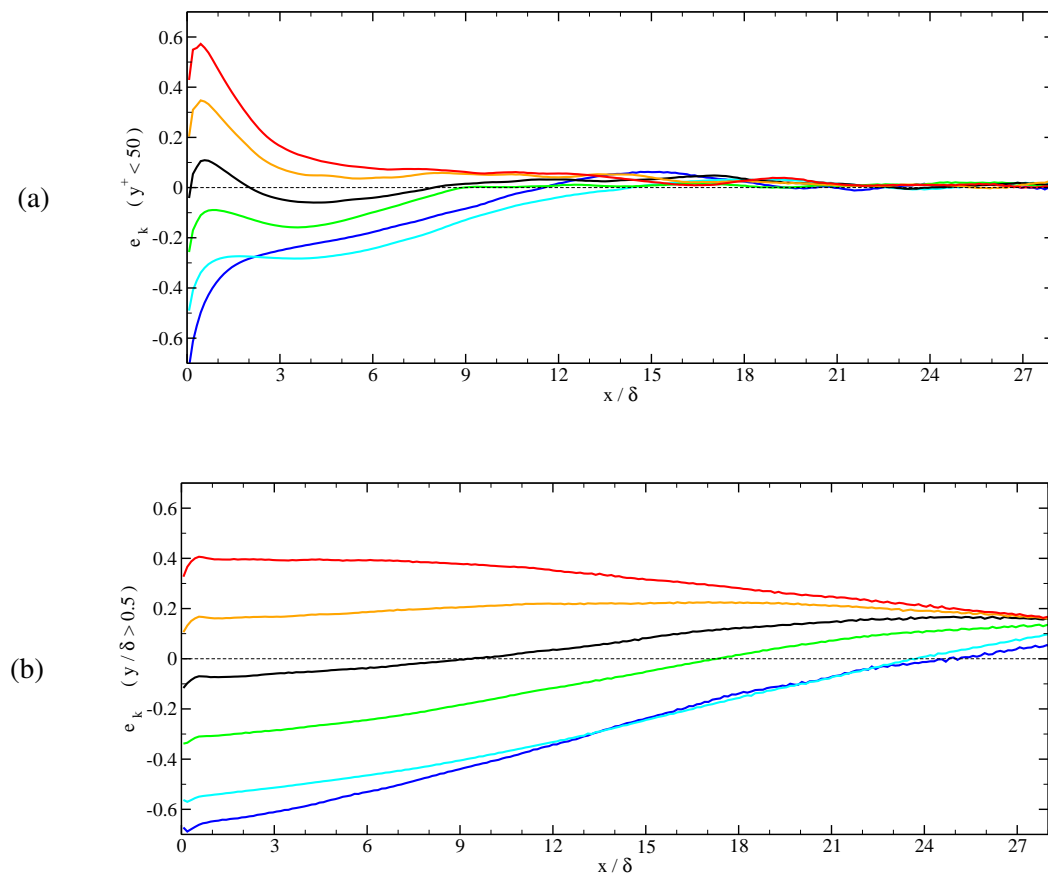


Figure 7.21: Downstream development of the error in the turbulent kinetic energy profile: (a) integration of the error for $y^+ < 50$ and (b) integration of the error for $y/\delta > 0.5$. Same legend as in Fig. 7.20.

to convect the turbulence generated at the wall towards the centre (in the case of an underestimation of the inlet turbulent intensity). This longer development time of the core of the flow to the prescribed inlet conditions can be explained by the different characteristics of the flow in these two regions. In the near-wall region the turbulent fluctuations are highly influenced by the mean shear and it is there that most of the energy is produced and dissipated. Any transient will thus be rapidly corrected so that the turbulence is in equilibrium with the mean shear. In the core of the flow on the other hand, inviscid processes dominate. The turbulent structures are remnants of upstream structures which have been convected downstream, or wall eddies which have been ejected towards the centre of the channel. This stresses the importance of imposing inflow data which not only triggers the near wall turbulence regeneration cycle more quickly, but also has the correct outer layer properties.

Influence of the Reynolds shear stress and of the normal Reynolds stresses distribution

Finally, two simulations are performed using the kind of reduced information typically available from a RANS simulation, rather than the full Reynolds stress tensor that was used in the calculations described above. In the first simulation we assume that only the normal stresses are known and set the shear stress to zero $\langle u'v' \rangle = 0$ whereas in the second simulation, we assume that the normal stresses are isotropic and equal to $2/3k$. Results are compared with the baseline simulation using the modified SEM where the full Reynolds stress tensor is prescribed. These tests have significant applications to RANS-LES coupling when the full Reynolds stress tensor cannot be extracted from the RANS solution.

Fig. 7.22 shows the downstream development of the coefficient of friction, and the errors in the turbulent kinetic energy, and the Reynolds shear stress profiles. The simulations with and without Reynolds shear stress in the prescribed inflow fluctuations show similar evolution of the coefficient of friction and turbulent kinetic energy profile. The redevelopment of the Reynolds shear stress in the case where it is not prescribed at the inlet is extremely fast (see Fig. 7.22 (c)). By the end of the domain, the simulation with no Reynolds shear stress prescribed in the inflow data has similar (and even slightly higher) levels of Reynolds shear stress as the reference simulation with the exact inlet Reynolds shear stress profile. This clearly shows that the artificial Reynolds shear stress prescribed at the inlet by the SEM has little effect on the redevelopment of Reynolds shear stress producing events inside of the LES domain. The simulation with isotropic normal stresses $R_{ii} = 2/3k$ gave surprisingly very good results in terms of the development of the coefficient of friction (see Fig. 7.22 (a)). There is an increase in the coefficient of friction immediately downstream of the inlet which recovers its fully developed value at $x/\delta = 3$. The levels of errors are significantly lower than in the two other cases both in terms of coefficient of friction and Reynolds shear stress throughout the domain. This behavior can be understood by studying the development of the

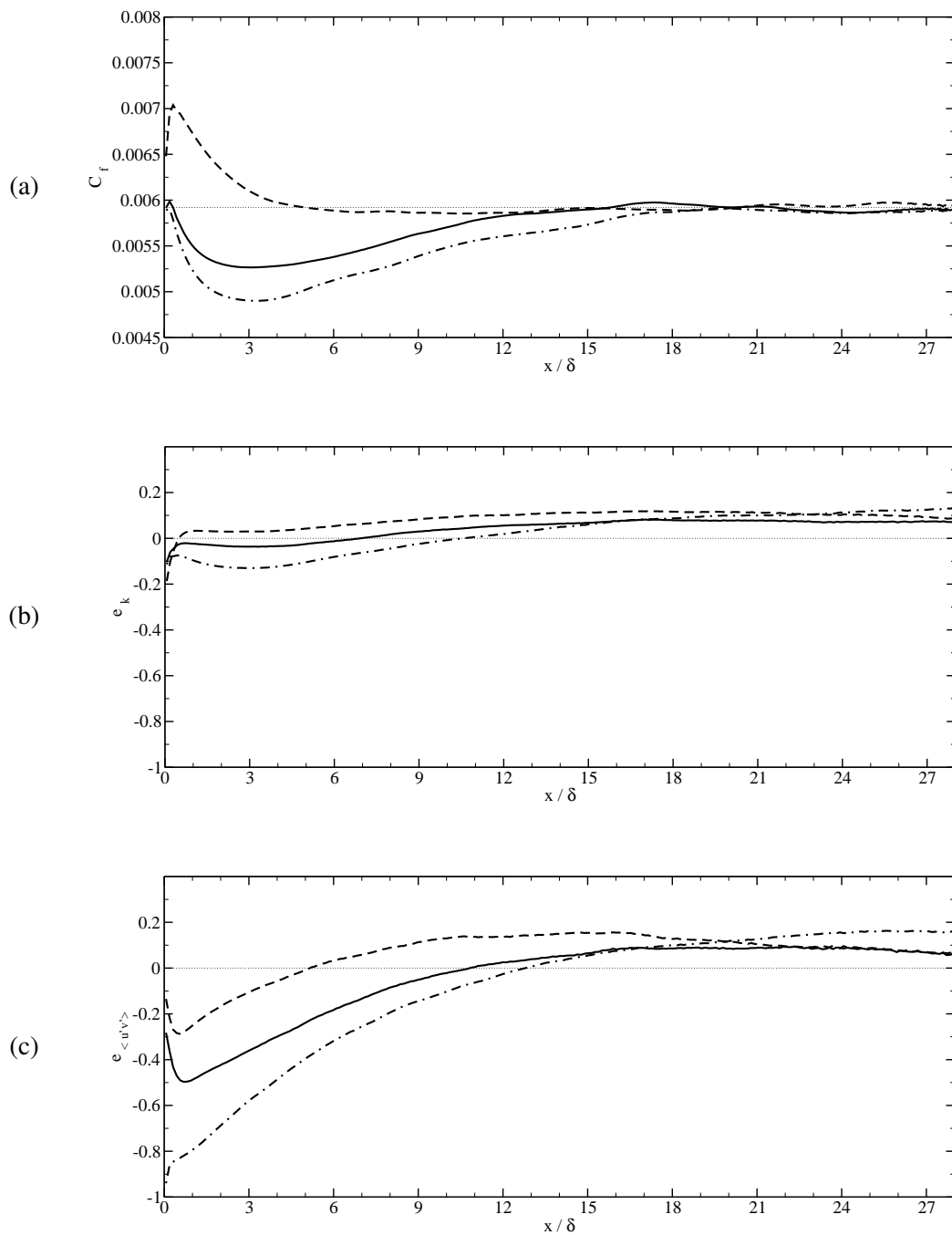


Figure 7.22: Downstream development of (a) the coefficient of friction and the errors in (b) the turbulent kinetic energy, and (c) the Reynolds shear stress profiles. Modified SEM inflow with exact R_{ij} profiles — ; with $2/3k$ in the normal stresses and exact other R_{ij} profiles --- ; with exact normal stresses and zero shear stress

error in the wall-normal fluctuations in the near wall-region (see Fig. 7.23 (a)). The imposed wall-normal

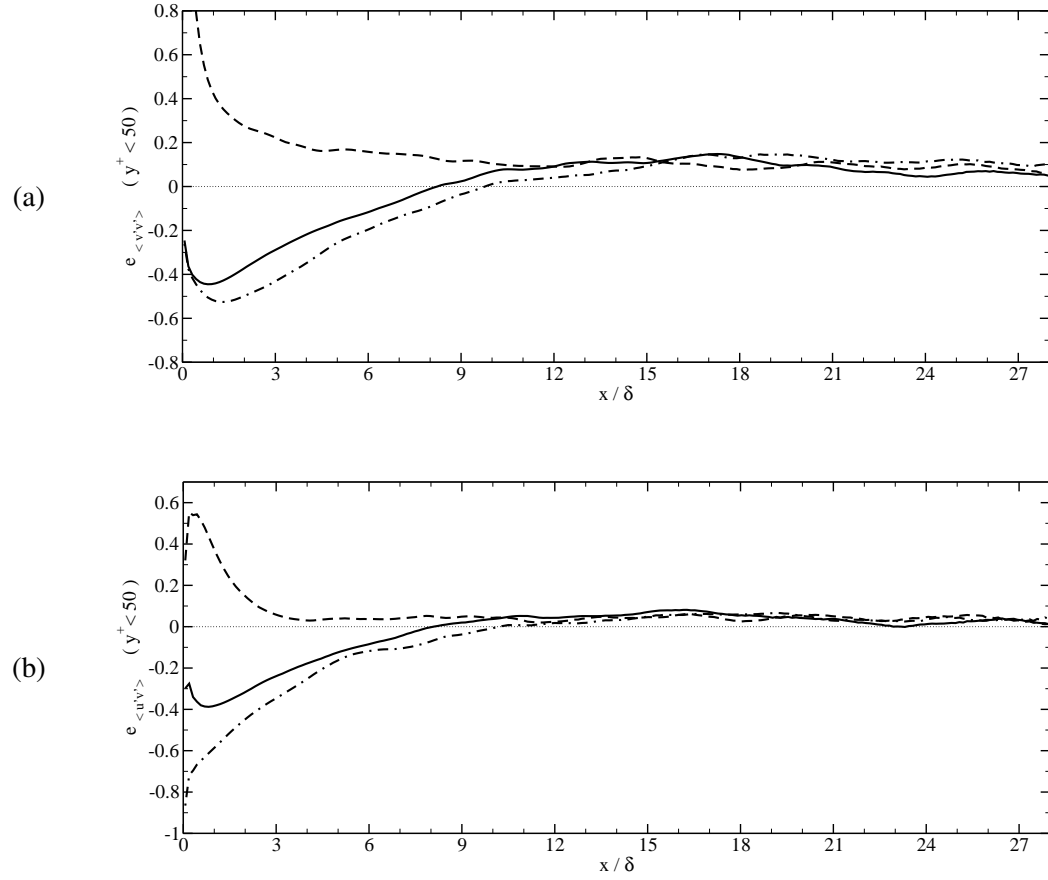


Figure 7.23: Downstream development of the error (integrated for $y^+ < 50$) in (a) the wall-normal fluctuations and in (b) the Reynolds shear stress profiles. Same legend as in Fig. 7.22.

fluctuations are severely overestimated, especially in the near wall region where the y^4 behavior of the $\langle v'^2 \rangle$ profile is replaced by a y^2 behavior (the leading term in the Taylor series expansion of $2/3k$ at the wall is in y^2). The error in $\langle v'^2 \rangle$ in the near wall region reaches +250% in the first cell downstream of the inlet. This excess of wall normal fluctuations is actually beneficial to the development of the Reynolds shear stress as can be seen on Fig. 7.23 (b). Indeed the production term $P_{\langle u'v' \rangle}$ in the Reynolds shear stress budget for fully developed turbulence (see Eq. (7.6)) strongly depends on the intensity of the wall normal fluctuations. The initial overestimation of $\langle v'^2 \rangle$ triggers more quickly the production of shear stress and thus the establishment of the correct near-wall dynamics. This has already been observed by Keating et al. (2004) (also in the case of the channel flow) using other methods to generate the synthetic turbulence (Batten et al., 2004).

7.4.3 Influence of the prescribed length and time scales

Influence of the length scale

Simulations were first performed by modifying the target length scale of the inflow data while keeping the time scale to its optimal value. The three spanwise σ_{i3} and wall-normal σ_{i2} length scales were multiplied by a factor r . Seven calculations with different values of r in the range $r = 0.25 - 2.0$ were performed.

Fig. 7.20 shows the downstream development of the coefficient of friction and the errors in the turbulent kinetic energy and Reynolds shear stress profiles. The development region downstream of the inlet is again characterized by a decay in the coefficient of friction and in the Reynolds shear stress for all calculations. In the case of an overestimation of the inflow length scale, the flow however redevelops Reynolds shear stress right away which makes the recovery process of the coefficient of friction relatively fast irrespective of the overestimation of the inflow length scale. However once the near-wall cycle of production of turbulence has re-established, the overly large turbulent eddies prescribed at the inflow entail an excess of turbulent kinetic energy (Fig. 7.20 (b)) and Reynolds shear stress (Fig. 7.20 (c)) at around $x/\delta = 20$. This can be explained by the persisting presence of long lived large scale structures whose contribution to the turbulent kinetic energy and Reynolds shear stress add to the contribution of the real eddies newly generated at the wall. Significant errors (around 20%) remain in the turbulent kinetic energy profiles by the end of the domain for the case with the highest inflow length scale. In the case of an underestimation of the inflow length scale, the recovery of the correct Reynolds shear stress and coefficient of friction is much slower. In the case where the inflow length scale is underestimated by -75% , the flow does not redevelop Reynolds shear stress before $x/\delta = 6$ and the coefficient of friction decays until $x/\delta = 12$, before converging very slowly towards its fully developed value which is not yet reached by the end of the domain.

Fig. 7.25 shows the downstream development of the error in the Reynolds shear stress profile in the near-wall region ($y^+ < 50$) and in the core of the channel ($y/\delta > 0.5$). Again the near-wall equilibrium value is reached relatively quickly (around $x/\delta = 10$) for simulations where the underestimation of the inflow length scale is not too severe. It should be noted that the intensity of the Reynolds shear stress, even in the near wall layer, is slightly overestimated if the inflow length scale is overestimated. This could be attributed to large scale fluctuations originating from the core of the channel and stimulating more strongly the near wall cycle of turbulence production. In the centre of the channel, a fully developed state is far from being reached by the end of the domain for most simulations (Fig. 7.25 (b)).

The effect of the inflow length scale on the instantaneous features of the flow is now studied. Fig. 7.26 and Fig. 7.27 show streamwise velocity fluctuations at $y^+ = 5$ and $y/\delta = 1$, respectively. Fig. 7.28 shows

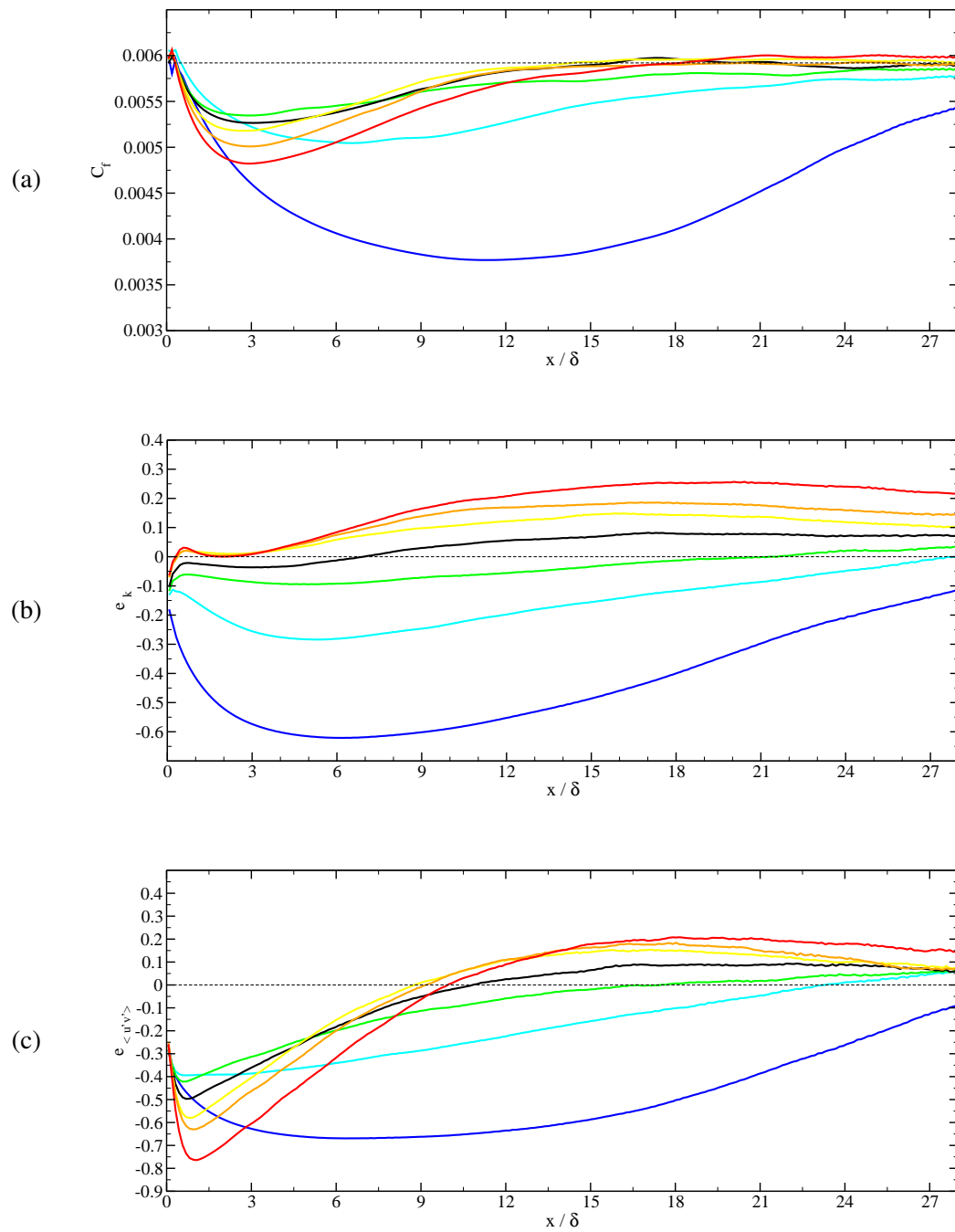


Figure 7.24: Downstream development of (a) the coefficient of friction and the errors in (b) the turbulent kinetic energy, and (c) the Reynolds shear stress profiles. Modified SEM inflow with -75% —; -50% —; -25% —; exact —; +25% —; +50% — and +100% — of optimal input spanwise length scales profiles.

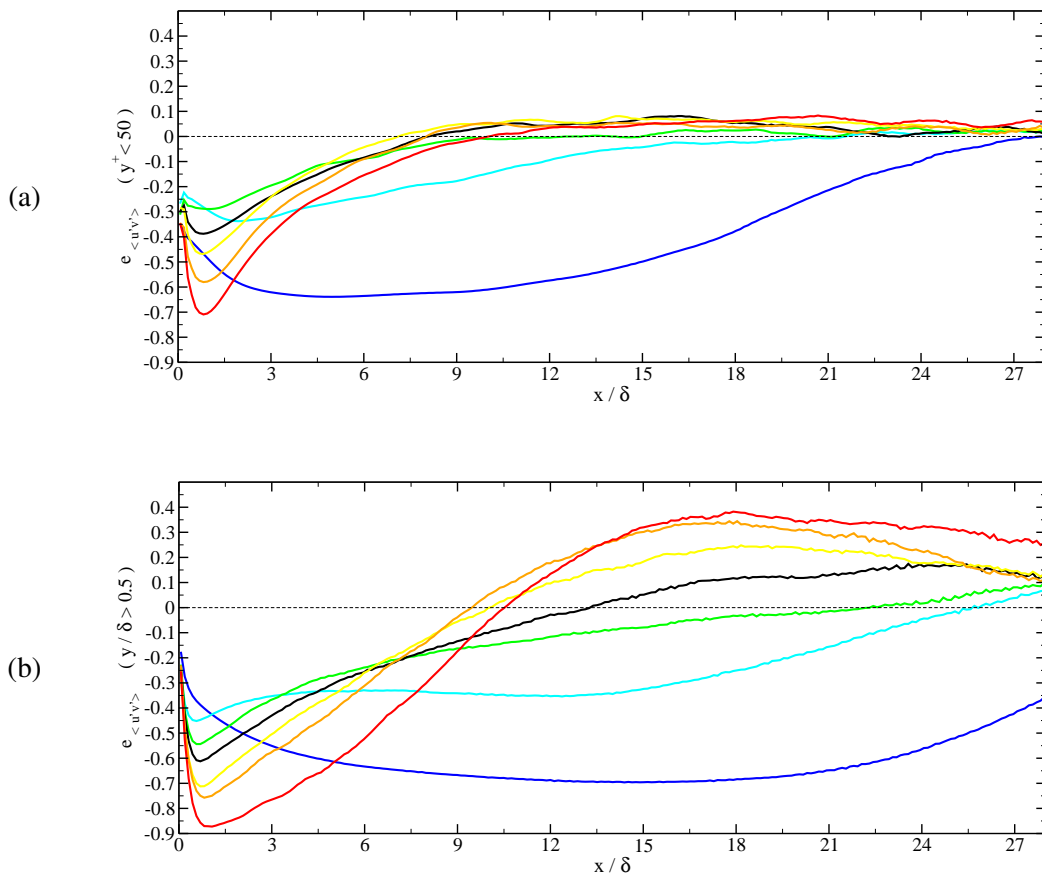


Figure 7.25: Downstream development of the error in the Reynolds shear stress profile: (a) integration of the error for $y^+ < 50$ and (b) integration of the error for $y/\delta > 0.5$. Same legend as in Fig. 7.24.

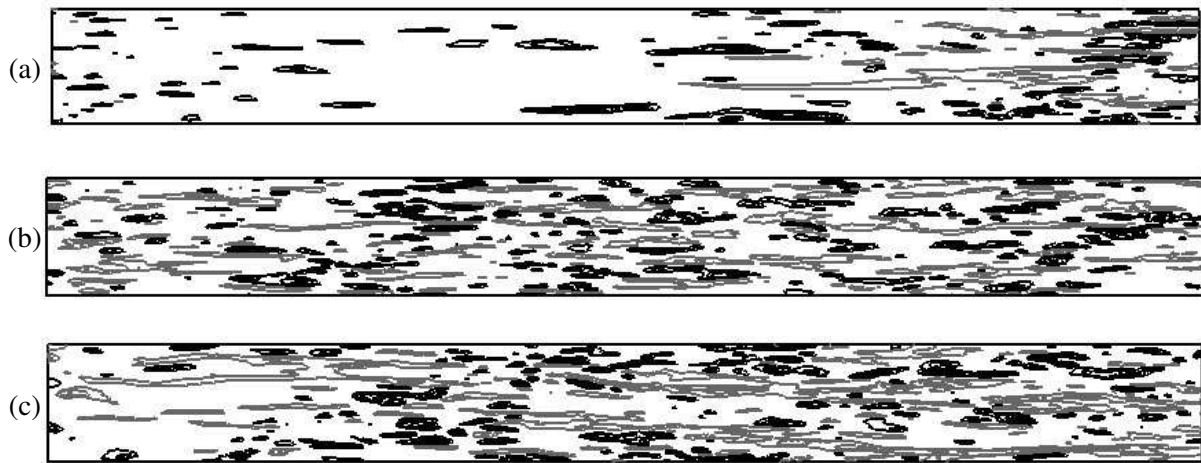


Figure 7.26: Contours of streamwise velocity fluctuations u^+ at $y^+ = 5$: Modified SEM with (a) -75% , (b) exact, and (c) $+100\%$ of optimal inflow length scale. Contour lines are evenly spaced at $\pm 2, \pm 3, \pm 4, \pm 5$ and ± 6 . Grey lines indicate negative value contours.

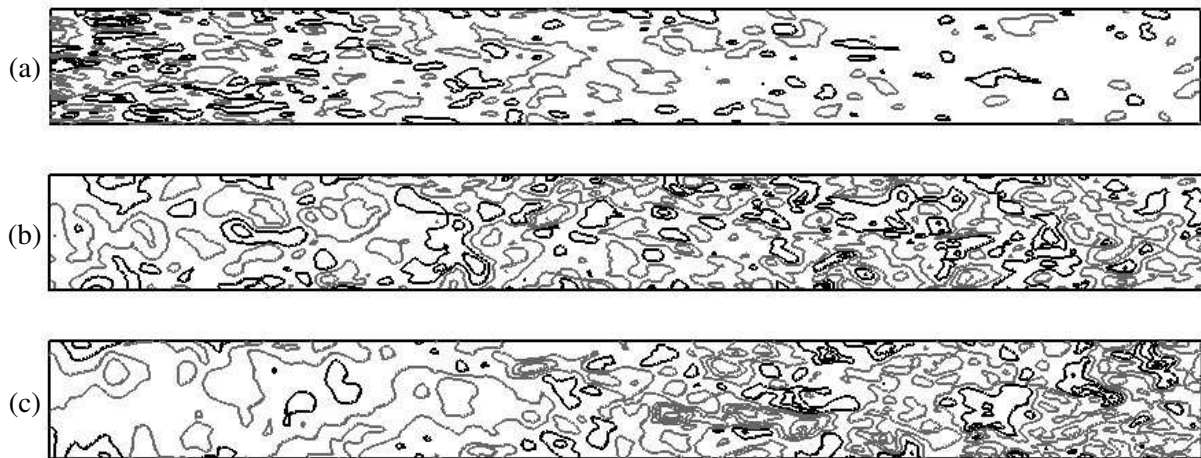


Figure 7.27: Contours of spanwise velocity fluctuations u^+ at $y/\delta = 1$: Modified SEM with (a) -75% , (b) exact, and (c) $+100\%$ of optimal inflow length scale. Contour lines are evenly spaced at $\pm 0.5, \pm 1.5, \pm 2.5, \pm 3.5$ and ± 4.5 . Grey lines indicate negative value contours.

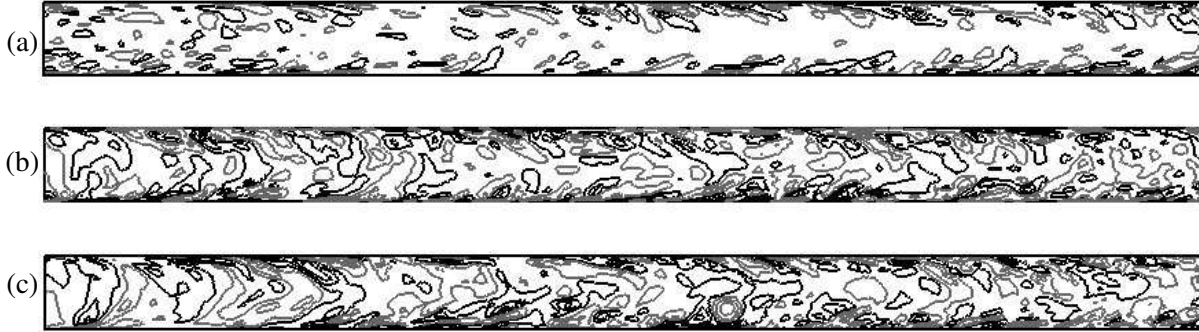


Figure 7.28: Contours of streamwise velocity fluctuations u^+ at $y/\delta = 1$: Modified SEM with (a) -75% , (b) exact, and (c) $+100\%$ of optimal inflow length scale. Contour lines are evenly spaced at ± 0.5 , ± 1.5 , ± 2.5 , ± 3.5 and ± 4.5 . Grey lines indicate negative value contours.

contours of spanwise velocity fluctuations in a z cross section. Only the cases where the underestimation or overestimation of the inflow length scale is the most severe and the baseline simulation with optimal length scale are represented. As expected, the near-wall fluctuations are rapidly dissipated in the case where the inflow length scale is underestimated by 75% (see Fig. 7.26 (a)). As a result, no energy is produced in the near-wall region and the fluctuations in the core of the channel also decay (see Fig. 7.28 (a)). By the end of the channel, the near-wall mechanisms of production of turbulence re-establish but no turbulent fluctuations has yet been convected towards the centre of the channel (see Fig. 7.27 (a)). On the contrary when the inflow length scale is overestimated, the near-wall production of turbulence is triggered relatively quickly around $x/\delta = 15$ (see Fig. 7.26 (b)), and consequently the transient in the centre of the channel is less severe (see Fig. 7.27 (c) and Fig. 7.28 (c)).

Influence of the time scale

We wish now to investigate the effect of a change in the time scales of the inflow turbulence. The spanwise σ_{i3} and wall normal σ_{i2} length scales are kept constant and equal to the optimal spanwise length scales calculated from the periodic LES. The three streamwise length scales σ_{i1} are multiplied by a factor r , which affects proportionally the time scales. Seven calculations with r in the range $r = 0.25 - 2.0$ were carried out.

The downstream development of the coefficient of friction and the errors in the turbulent kinetic energy, and the Reynolds shear stress profiles is shown on Fig. 7.29. Similar conclusions as in the previous tests on the effect on the inflow length scales can be drawn. The overestimation of the time scales at the inlet leads to an excess of turbulent kinetic energy at around $x/\delta = 20$, due to the presence

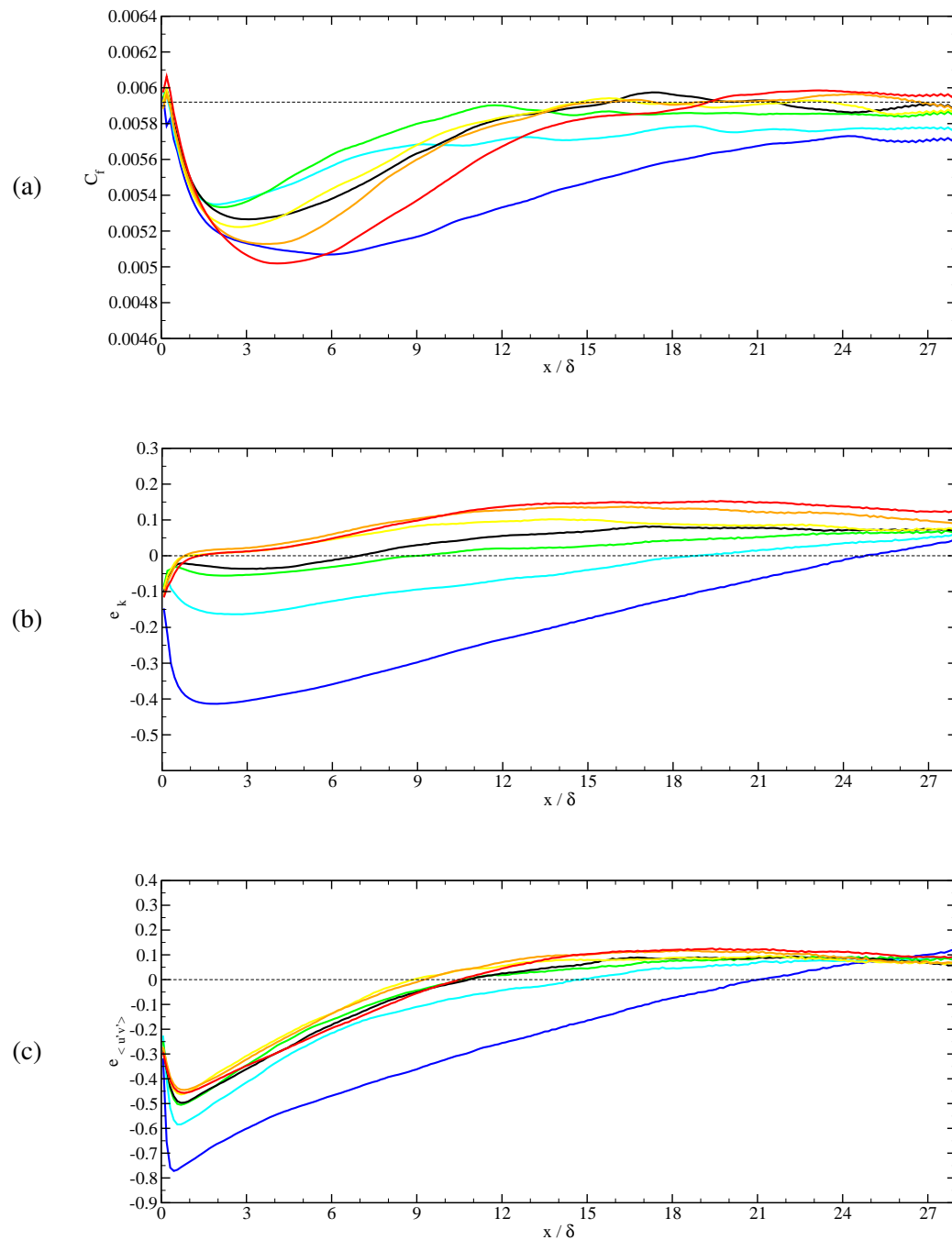


Figure 7.29: Downstream development of (a) the coefficient of friction and the error in (b) the turbulent kinetic energy profile and in (c) the Reynolds shear stress profile. Modified SEM inflow with -75% — ; -50% — ; -25% — ; exact — ; +25% — ; +50% — and +100% — of optimal input time scales profiles.

of overly large eddies in the core of the channel. The overestimation of the inflow time scale however does not significantly affect the development of the coefficient of friction and the Reynolds shear stress. On the contrary, underestimating the inflow time scales leads to a severe decay of the turbulent kinetic energy and Reynolds shear stress downstream of the inlet, followed by a very slow recovery.

Influence of a simultaneous change in the length and time scales

Finally the combined effect of a change in the length and time scales of the inflow turbulence is investigated. All the length scales σ_{ij} of the synthetic eddies are simultaneously multiplied by the same factor r in the range $0.25 - 1.5$. Five calculations with r in the range $r = 0.25 - 2.0$ are performed.

Fig. 7.30 shows the downstream development of the coefficient of friction and the errors in the turbulent kinetic energy, and the Reynolds shear stress profiles. The same conclusions as in the case where the length and time scales were modified separately can be drawn. In the case of an overestimation of the inflow length and time scales, the eddies prescribed at the inlet (although larger than real fully developed turbulence eddies) are effective in triggering the near-wall cycle of turbulence production. Thus an overestimation of both the length and time scales of the inflow fluctuations does not significantly affect the distance (about 10δ) after which the coefficient of friction recovers fully developed values. However these overly large inlet eddies produce an excess of turbulent kinetic energy further downstream of the inlet, especially in the core of the flow. On the contrary, in the case of an underestimation of the inflow length and time scales, the initial drops in the coefficient of friction and Reynolds stresses are severe, and their recovery is very slow. For the simulation with a 75% underspecified inflow length and time scale, the coefficient of friction decays until $x = 20 - 25\delta$ and does not recover its fully developed value by the end of the domain.

Fig. 7.31 and Fig. 7.32 showing streamwise velocity fluctuations at $y^+ = 5$ and $y/\delta = 1$, respectively, confirm conclusions drawn from the analysis of the statistics. If the length and time scales are too severely underestimated, the fluctuations prescribed at the inlet are rapidly dissipated both in the near-wall region (see Fig. 7.31 (a)) and in the core of the channel (see Fig. 7.32 (b)). On the contrary, overestimating the size of the eddies prescribed at the inlet leads to a shorter transient because the near-wall mechanism of production of turbulence is triggered more rapidly (see Fig. 7.31 (c)).

7.5 Concluding Remarks

In its original form presented in Chapter 4, the eddies generated by the SEM were only characterized by one length scale, and the structures generated were thus isotropic. In the present chapter, the SEM was

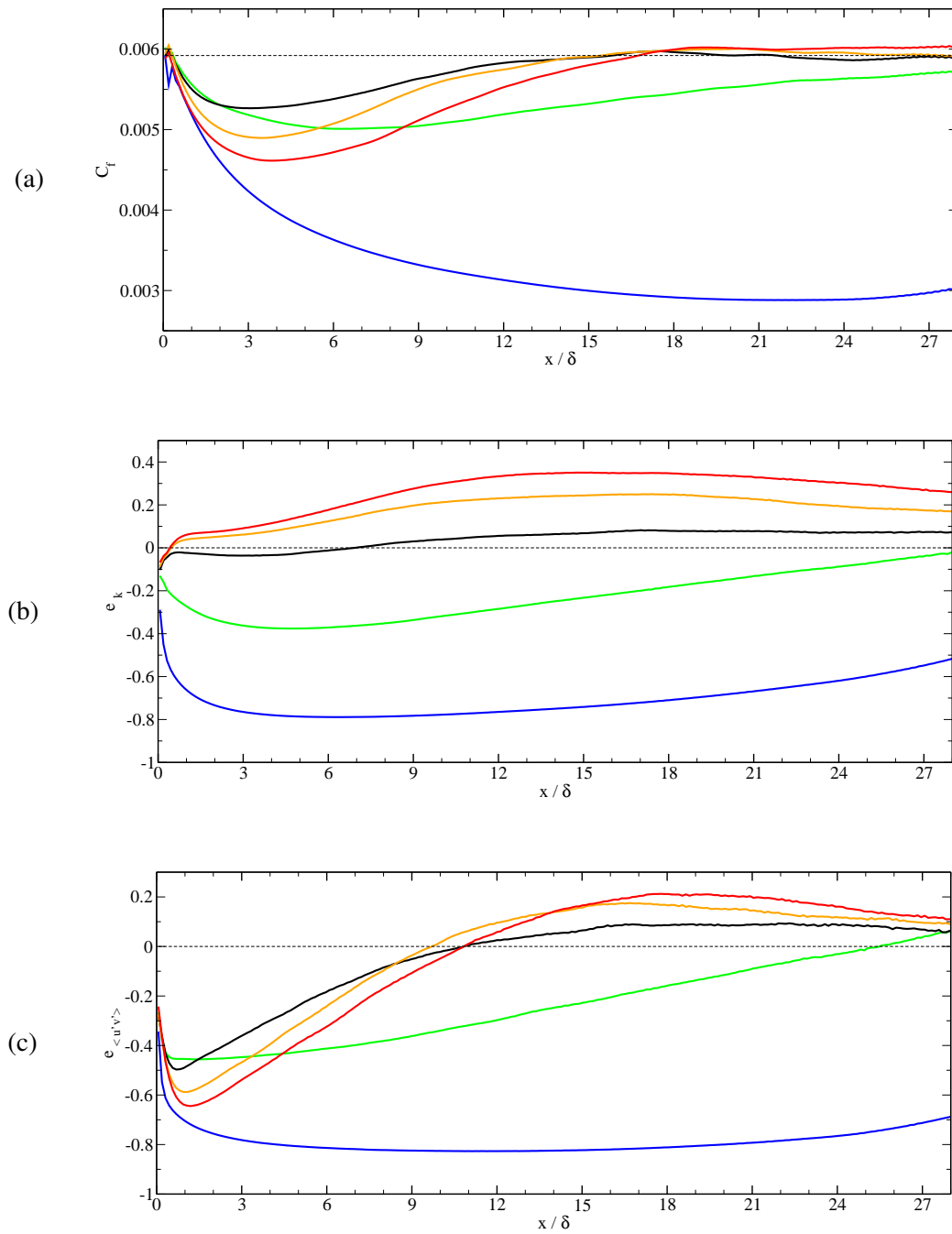


Figure 7.30: Downstream development of (a) the coefficient of friction and the errors in (b) the turbulent kinetic energy, and (c) the Reynolds shear stress profiles. Modified SEM inflow with -75% — ; -50% — ; exact — ; +50% — ; and +100% — ; of optimal input length and time scales profiles.

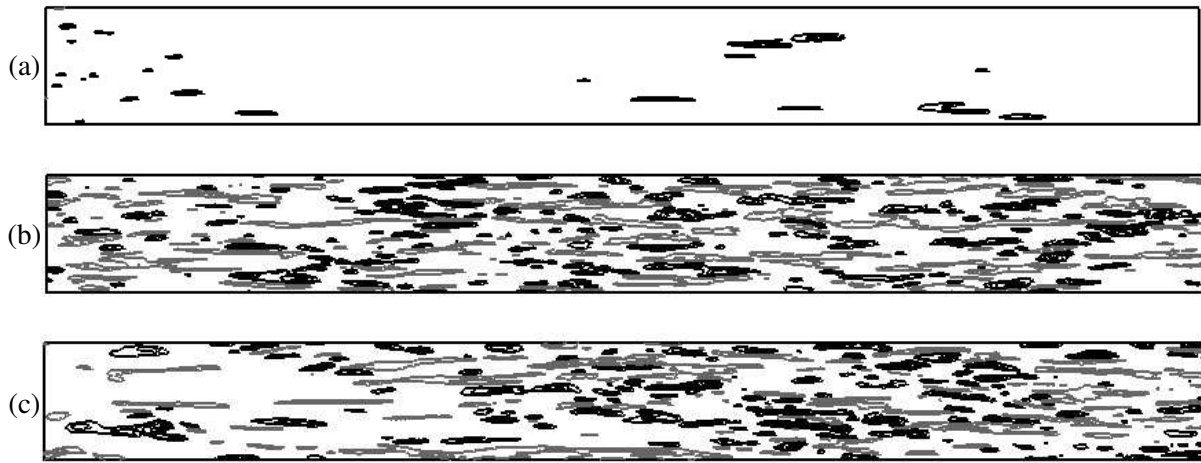


Figure 7.31: Contours of streamwise velocity fluctuations u^+ at $y^+ = 5$: Modified SEM with (a) -75% , (b) exact, and (c) $+100\%$ of optimal inflow length and time scales. Contour lines are evenly spaced at $\pm 2, \pm 3, \pm 4, \pm 5$ and ± 6 . Grey lines indicate negative value contours.

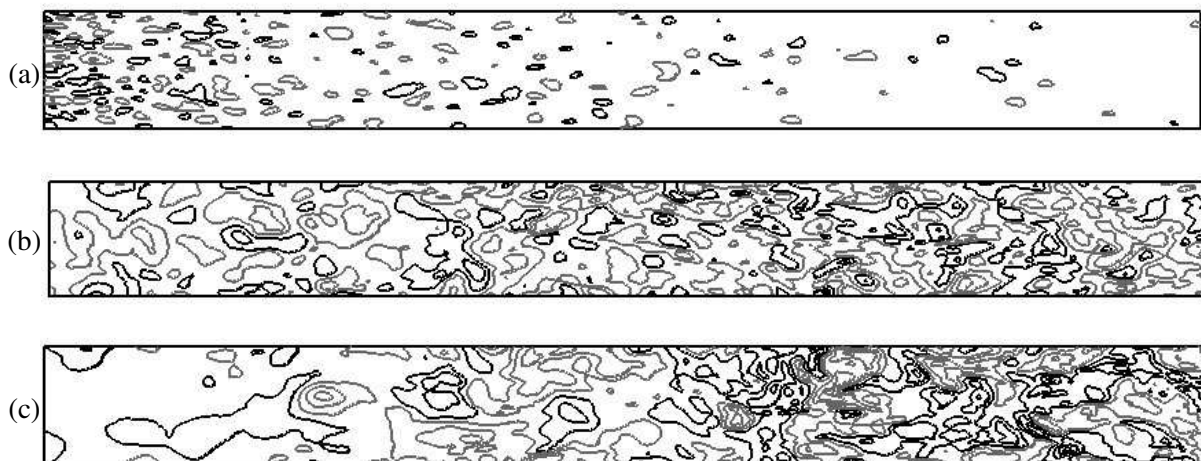


Figure 7.32: Contours of streamwise velocity fluctuations u^+ at $y/\delta = 1$: Modified SEM with (a) -75% , (b) exact, and (c) $+100\%$ of optimal inflow length and time scales. Contour lines are evenly spaced at $\pm 2, \pm 3, \pm 4, \pm 5$ and ± 6 . Grey lines indicate negative value contours.

slightly modified to generate non-isotropic eddies, so that the synthetic signal generated can reproduce both the correct integral length and time scales.

The modified SEM has been used to generate inlet conditions for a LES of a spatially developing turbulent plane channel flow at $Re_\tau = 395$. Input statistics for the SEM were extracted from a periodic LES of fully developed turbulence at the same Reynolds number and with the same numerical methodology. The prescribed inlet conditions were shown to produce a transient characterized by a decay of the coefficient of friction and the Reynolds stresses up to $x/\delta = 3$, followed by a recovery towards fully developed values. By around $x/\delta = 15$, the coefficient of friction recovered its fully developed value, and the Reynolds stresses were within 10% of their fully developed value.

The effect of a modification of the physical parameters extracted from the periodic LES was then investigated. It was shown that the mean velocity profiles, the turbulent kinetic energy, the integral length and time scales all have a great influence on the development of the turbulence downstream of the inlet. Therefore the correct estimation of these physical quantities at the inlet is of paramount importance to provide LES with accurate boundary conditions. In the following chapters, we will use the SEM to couple an upstream RANS simulation with an embedded LES. The sensitivity analysis performed in this chapter will be used to set the input parameters of the SEM in such situations where only the reduced information typically available from a RANS simulation is provided.

Chapter 8

Interface Conditions for RANS-to-LES Coupling of Simple Wall Flows

8.1 Introduction

In the present chapter, the SEM is used to generate inlet conditions for a LES, using only information available from an upstream RANS simulation. Compared to simulations performed in the previous chapter, the exact full Reynolds stress tensor, and the length and time scales are not directly available (from a precursor periodic LES), and each are computed from the upstream RANS solution.

In Section 8.2, equations to compute all of the input parameters of the SEM from simple RANS statistics are proposed. The rationale behind the approach is strongly linked to the sensitivity of the SEM to its input parameters studied in the previous chapter.

In Section 8.3, the SEM is used to generate inlet conditions for the LES of channel flow, only using information extracted from an upstream steady SST solution. The present RANS-LES coupling strategy is tested at different Reynolds number, and is compared to other existing methods of generation of inlet conditions for LES.

Results for other simple fully developed wall bounded flows are then presented. This includes boundary layer flows, where the thickness of the boundary layer grows as the flow develops (Section 8.4) and square duct flows, where the presence of the secondary motion is not predicted by the upstream RANS solution (Section 8.5).

Finally, Section 8.6 summarizes the conclusions drawn from the simulations performed in this chapter.

8.2 SEM Parametrization for RANS-to-LES Coupling

The SEM requires information on the upstream flow conditions such as the mean velocity U_i , the Reynolds stress tensor R_{ij} and the length-scale of the eddies σ . Additionally, the number of eddies N and the shape function f of the eddies are other numerical parameters required by the SEM. In this section, all the physical and numerical free parameters of the SEM are set, based only on information obtained from a RANS simulation using the SST model of Menter (1994), in order to limit the requirement for user intervention.

8.2.1 Physical parameters

The mean velocity U_i and Reynolds stress tensor R_{ij} are directly extracted from the RANS solution. In this work, the SST model is used such that the Reynolds stress tensor is given by,

$$R_{ij} = -2v_t S_{ij} + \frac{2}{3}k\delta_{ij}. \quad (8.1)$$

However in the case where the full Reynolds stress tensor is not available (in the case where v_t or S_{ij} are not computed for instance), only the available information can be provided. As was shown on Fig. 7.22 of Chapter 7, the absence of Reynolds shear stress in the synthesized signal has very little effect on the redevelopment of the downstream turbulence. In the case where only the turbulent kinetic energy is available (when eddy viscosity models are used), it was shown in Fig. 7.22 of Chapter 7 that the imposition of an isotropic stress $2/3k$ in all the normal stresses actually had beneficial effect on the development of the downstream flow due to the enhancement of the wall normal fluctuations.

The estimation of the length scale of the eddies σ is quite problematic because the variety of eddies present in a channel flow and their structure cannot be represented by a single length scale. Additionally, it was shown in Chapter 7 that an inaccurate estimation (especially an underestimation) of the inflow length and time scales strongly increases the transition region downstream of the inlet. In the SST model, the length scale is given by,

$$L = \frac{k^{\frac{3}{2}}}{\epsilon} \quad (8.2)$$

where $\epsilon = C_\mu k \omega$. For a fully developed channel flow in the log-law region, L grows proportionally to the wall distance (Pope, 2000). The spanwise integral length scale computed from periodic LES at three different Reynolds number shows a similar trend as shown in Chapter 6 in Fig. 6.11. Closer to the wall for $y^+ < 50$ however, the RANS length scale L tends towards zero whereas the LES length scale is constant (see Fig. 6.11). Several RANS length scales characteristic of the near-wall region could be defined to clip L in the near-wall region. The Kolmogorov length scale $(v^3/\epsilon)^{1/4}$ or the viscous length scale v/u_τ appear

to be reasonable choices since it was shown in Chapter 2 that the Kolmogorov length scale, the viscous length scale and the integral length scale were virtually the same in the viscous sublayer. Neither of these two solutions was adopted for robustness reasons, because the correct estimate of the SEM inflow length scale σ is too critical an issue to leave entirely to the RANS model. In fully developed turbulence, the Kolmogorov and viscous length scales provide a good estimate of the integral length scale in the near wall region, but in the general case, there is no guarantee that they have any physical relevance. In the case of a free shear flow, or at the reattachment point of a detached flow for instance, v/u_τ is infinite. Instead we chose to limit the length scale L by the local grid spacing Δ on the LES domain, based on the argument that the LES grid refinement is conditioned by the size of the near wall structures. The length scale of the eddies is then given by,

$$\sigma = \max\left(\frac{k^{\frac{3}{2}}}{\varepsilon}, \Delta\right) \quad \text{where} \quad \Delta = \max(\Delta x, \Delta y, \Delta z). \quad (8.3)$$

The above criteria has the extra advantage of guaranteeing that the synthetized structures can be accurately discretized on the LES grid. Another region of an attached boundary layer where RANS predictions become less accurate is the free stream edge. σ was thus limited by an additional geometrical length scale δ characteristic of the flow under consideration. The final length scale σ used by the SEM is then computed from,

$$\sigma = \max\left(\min\left(\frac{k^{\frac{3}{2}}}{\varepsilon}, \kappa\delta\right), \Delta\right), \quad (8.4)$$

where $\kappa = 0.41$.

8.2.2 Numerical parameters

All the input physical parameters required by the SEM have now been set. However, there are still several numerical parameters (such as the shape function f or the number of eddies N) which appear in the formulation of the SEM given in Chapter 4, and that need to be set.

An equation to estimate the number of eddies N is derived here. Our aim is to have a LES solution that is not influenced by the specific number of eddies prescribed at the inlet. The number of eddies mainly control the intermittency of the synthetized signal, for which the flatness,

$$F_{u'_i} = \frac{\langle u_i'^4 \rangle}{\langle u_i'^2 \rangle^2}$$

is a good indicator. It was shown in Chapter 4 that the flatness of the signal is given by,

$$F = 3 + \frac{1}{N} \left(A \frac{V_B}{\sigma^3} + B \right) \quad (8.5)$$

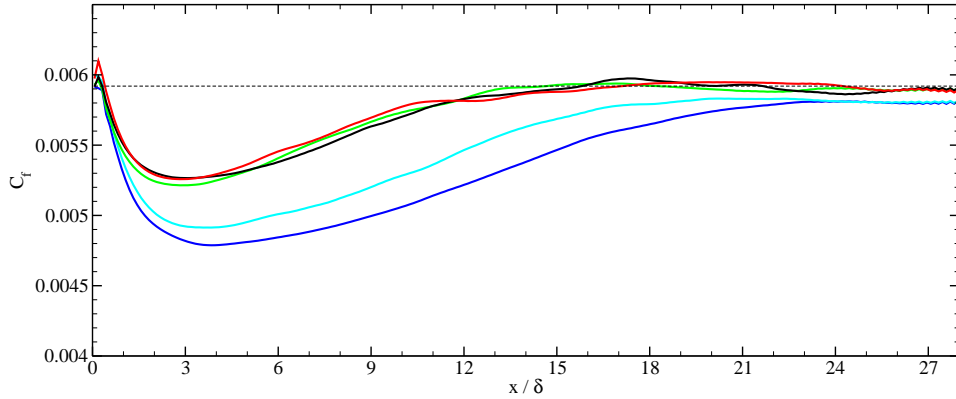


Figure 8.1: Downstream development of the coefficient of friction. Modified SEM with optimal parameters and different number of eddies. $N = 50$, — ; $N = 100$, — ; $N = 1,000$, — ; $N = 10,000$, — ; and $N = 100,000$, — .

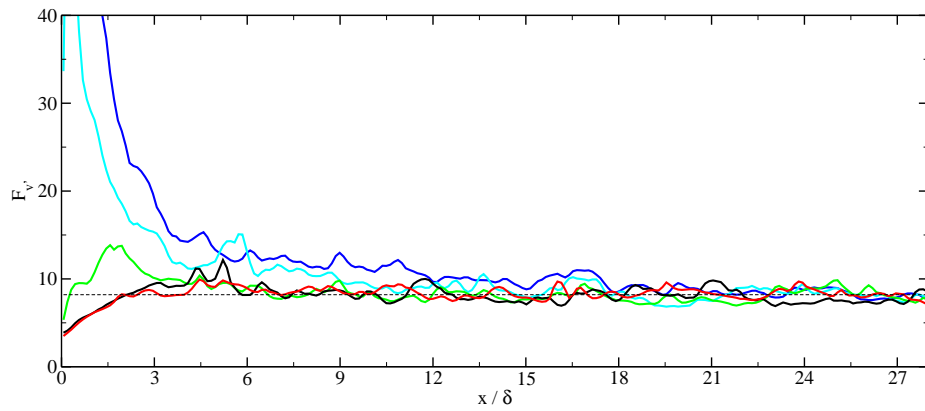


Figure 8.2: Downstream development of the flatness of the wall-normal fluctuations at $y^+ = 5$. Modified SEM with optimal parameters and different number of eddies. Same legend as in Fig. 8.1.

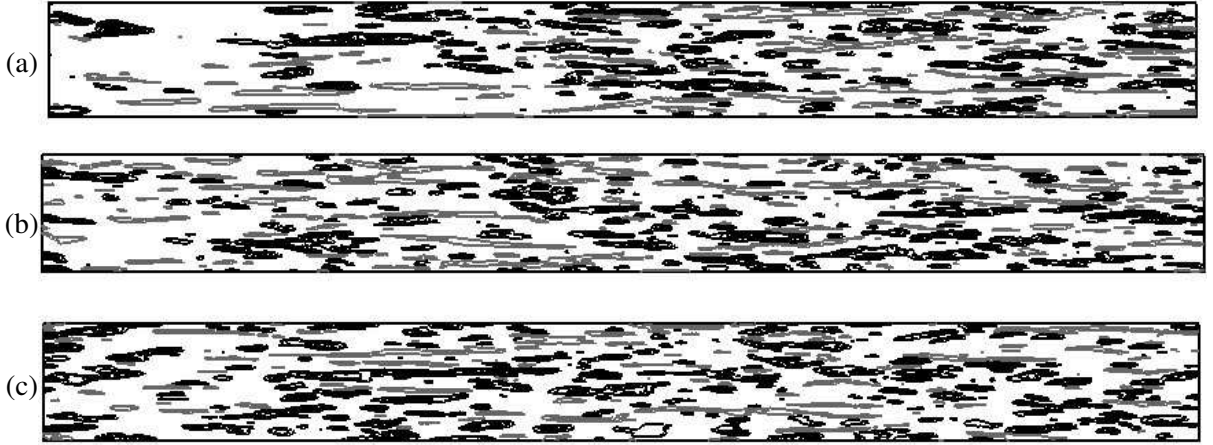


Figure 8.3: Contours of streamwise velocity fluctuations u^+ at $y^+ = 5$: Modified SEM with (a) $N = 50$, (b) $N = 1,000$ and (c) $N = 100,000$. Contour lines are evenly spaced at $\pm 2, \pm 3, \pm 4, \pm 5$ and ± 6 . Grey lines indicate negative value contours.

where A and B are constants. In order to have a constant flatness in the SEM signal, and hence a LES solution independent of N , the ratio $\frac{V_B}{N\sigma^3}$ should be constant. The number of eddies N should then be proportional to $\frac{V_B}{\sigma^3}$. For non-homogeneous distributions of σ , this ratio is also non-homogeneous in space, and the number of eddies can be computed as,

$$N = C \max_{\mathbf{x} \in B} \left(\frac{V_B}{\sigma} \right)$$

where C is a proportionality coefficient to be estimated. This equation ensures that in different situations, the density of eddies in the inflow, or say the intermittency of the signal is controlled. Now in a given situation, we wish to compute the minimum value of C which gives rise to a solution independent of N with further addition of eddies. In order to calibrate C , the baseline simulation of the previous chapter which used 10,000 eddies (corresponding to $C = 5$) is run with different values of C (and hence different values of N). Five other simulations with $C = 0.025$ ($N \approx 50$), $C = 0.05$ ($N \approx 100$), $C = 0.5$ ($N \approx 1,000$) and $C = 50$ ($N \approx 100,000$) are performed. Fig. 8.1 shows the downstream development of the coefficient of friction. As expected, the results become independent of the number of eddies present in the inflow for large values of N ($N = 1,000$ in the present case). When a lower value of N is chosen, the length of the transition region is slightly extended. On Fig. 8.2, the development of the flatness of the wall-normal velocity fluctuations $F_{v'}$ at $y^+ = 5$ is shown. Although it can be seen that large values of the flatness are prescribed at the inlet for the cases with $N = 50$ and $N = 100$, the recovery towards a fully developed value is very fast. Fig. 8.3 shows contours of streamwise velocity fluctuations at $y^+ = 5$. It can be seen that the structure of the turbulence in the cases with $N = 1,000$ ($C = 0.5$) and $N = 100,000$ ($C = 50$)

is identical after only a few δ . From the analysis of the development of the coefficient of friction and fluctuations in the near-wall region, we conclude that the solution reaches a converged state in terms of number of eddies for $N = 1,000$ ($C = 0.5$). Therefore we choose in all our RANS-LES simulations to take $C = 1$ such that N is given by,

$$N = \max_{\mathbf{x} \in B} \left(\frac{V_B}{\sigma} \right). \quad (8.6)$$

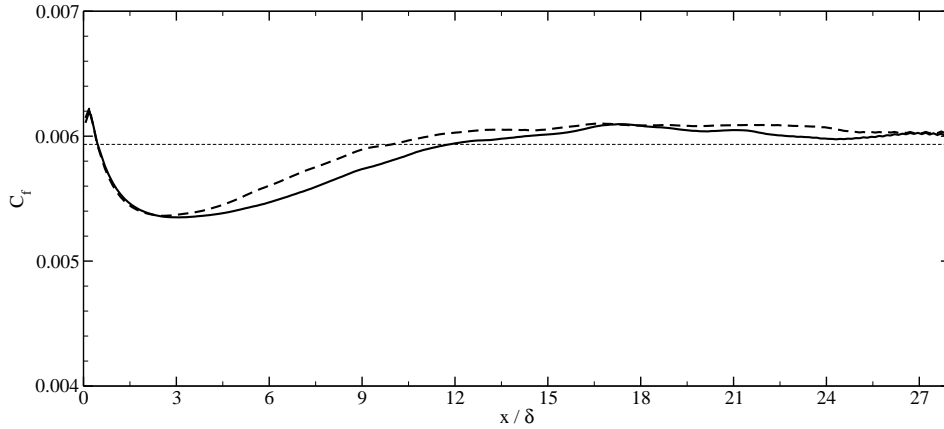


Figure 8.4: Downstream development of the coefficient of friction. Modified SEM with optimal parameters and different shape functions f : Tent function, — ; Truncated Gaussian function, - - - .

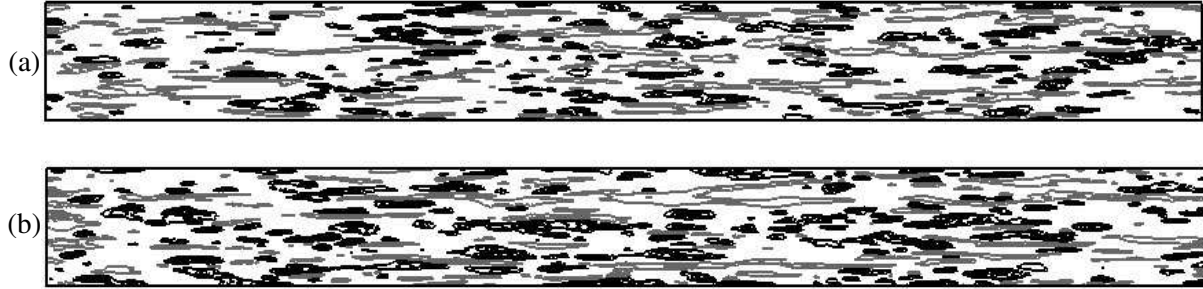


Figure 8.5: Contours of streamwise velocity fluctuations u^+ at $y^+ = 5$: Modified SEM with (a) tent function, and (b) truncated Gaussian function. Contour lines are evenly spaced at $\pm 2, \pm 3, \pm 4, \pm 5$ and ± 6 . Grey lines indicate negative value contours.

The specific form of the shape function f determines the spectral content of the inflow data, as shown in Chapter 4. In the preceding chapter, a tent function was used in all calculations. Fig. 8.4 shows that the differences in the development of the coefficient of friction between a simulation using a tent function and a simulation using a truncated Gaussian function (Eq. (4.62)) are small. Fig. 8.5 shows that velocity fluctuations on a plane at $y^+ = 5$ are not influenced by the specific form of the shape function. The two

shape functions investigated are thus similar in terms of the quality of inflow data generated. In terms of computational cost however, the tent function is computed using only a couple of multiplications and additions, which makes it much faster to compute than the Gaussian function. Therefore in all subsequent calculations, f is a tent function, as defined on Eq. (4.59).

8.3 Channel Flow Results

8.3.1 Presentation of the case

Three cases at three different Reynolds number Re based on the bulk velocity are investigated. The Reynolds numbers simulated are $Re = 14,519$, $Re = 22,907$ and $Re = 38,920$. Three periodic LES (runs G, H and I presented in Chapter 6) have already been performed at these three Reynolds numbers. They will be used as a comparison point for all spatially developing hybrid RANS-LES simulations performed in this chapter. The corresponding friction Reynolds numbers are $Re_\tau = 395$, $Re_\tau = 590$ and $Re_\tau = 950$ for run G, run H and run I, respectively.

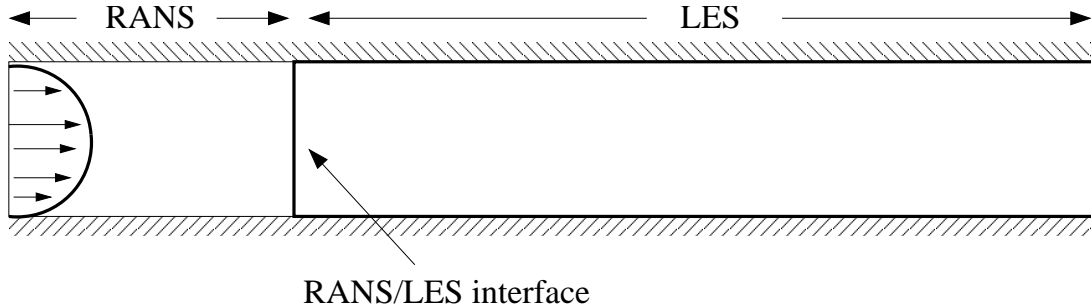


Figure 8.6: Sketch of the hybrid RANS/LES channel flows configuration.

The computational configuration is shown in Fig. 8.6. The RANS equations are solved using the SST model in a domain with dimensions $\delta \times 2\delta \times \pi\delta$ in the streamwise, wall-normal and spanwise directions, respectively. The RANS domain extends between $x/\delta = -1$ and $x/\delta = 0$. Periodic boundary conditions are applied in the streamwise and spanwise directions, whereas a no-slip boundary condition is applied at both walls.

At $x/\delta = 0$ the LES domain, of dimensions $L_D \times 2\delta \times \pi\delta$ begins. The streamwise length L_D of the computational domain is different for the different Reynolds numbers considered. Since the length of the transition region will decrease with increasing Reynolds number, we take L_D equal to $10\pi\delta$, $8\pi\delta$ and $6\pi\delta$ for the low, medium and high Reynolds number cases, respectively.

Run	Reynolds Re	Inflow method	Input statistics	LES domain length
S1	14,519	Synthetic Eddy Method	SST solution	$10\pi\delta$
S2	22,907	Synthetic Eddy Method	SST solution	$8\pi\delta$
S3	38,920	Synthetic Eddy Method	SST solution	$6\pi\delta$
B1	14,519	Batten et al. (2004)	SST solution	$10\pi\delta$
R1	14,519	Random Method	SST solution	$10\pi\delta$
P1	14,519	Precursor simulation	×	$10\pi\delta$

Table 8.1: Parameter settings used in the hybrid RANS-LES simulations of the channel flow. The parameters not listed here are kept constant for all simulations.

Periodic boundary conditions are applied in the spanwise direction and a no-slip boundary condition is applied at both walls. Different methods are used to generate the inflow data of the LES region, and the required input statistics are extracted from the upstream RANS simulation. At the exit plane, the standard outlet boundary condition implemented in *Code_Saturne* (see page 97 in Chapter 5) was used.

The same grid resolution as in the corresponding periodic simulations presented in Chapter 6 is used in the three cases. This results in grids of $250 \times 46 \times 82$, $368 \times 52 \times 124$ and $360 \times 56 \times 198$ cells for the low, medium and high Reynolds number cases, respectively. For all simulations, the time step Δt was adjusted so that the maximum CFL number remains lower than unity.

The RANS grid only uses one cell in the streamwise and spanwise directions and the wall-normal grid resolution is the same as in the downstream LES to avoid interpolation of the RANS data onto the LES grid. The RANS simulation is run prior to the LES and the statistics necessary for the generation of the inflow data for the LES domain are stored on disk.

The Smagorinsky model (with $C_S = 0.065$) and Van-Driest damping at the wall is used in the LES region, whereas the SST model of Menter (1994) is used in the RANS region. The different hybrid RANS-LES simulations performed on the channel flow case are summarized in Table 8.1.

8.3.2 Influence of the Reynolds number

The performance of the SEM parametrization proposed in Section 8.2 is tested at the three Reynolds number $Re = 14,519$ (run S1), $Re = 22,907$ (run S2) and $Re = 38,920$ (run S3).

Synthetized turbulence

Fig. 8.7 and Fig. 8.8 show the input statistics for the SEM extracted from the upstream SST solution. It can be seen that the SST model does not reproduce the near wall peak of the turbulent kinetic energy profiles observed in the real flow (see Fig. 8.7). As shown in Fig. 8.8, the two limiters introduced in Eq. (8.4) are effective in clipping the SST length scale to physical values in the near wall region and in the core of the channel. It should be noted however that the input time scale of the SEM does not reproduce correctly the large time scales near the wall associated with the streamwise elongated streaks. The number of eddies N was computed using Eq. (8.4) which yielded $N = 3,640$, $N = 21,615$ and $N = 47,392$ for the low, medium and high Reynolds number case, respectively. Although this might seem large, the CPU time required to generate the inflow data at each iteration did not exceed 1% of the total CPU time per iteration of the LES simulation.

Results and discussions

We study first the behavior of the flow in the near-wall region ($y^+ < 50$) for the three Reynolds number considered. Fig. 8.9 shows the downstream development of the error in the turbulent kinetic energy profile for $y^+ < 50$. The kinetic energy at the inlet is underestimated by about 70%, due to the error in the input k profile extracted from the SST. However this initial error in the prescribed inflow kinetic energy profile is rapidly corrected, and the transition region necessary to recover a fully developed k profile decreases as the Reynolds number increases. However, when the streamwise coordinate x is expressed in wall units (Fig. 8.9 (b)), the error curves collapse onto a single curve, independent of the Reynolds number. The length of the transition region necessary to recover the correct levels of turbulent kinetic energy in the near wall-region (to within, say, 10% of the error on the integrated profile) thus scales in wall units as $x^+ \approx 3,000$. As we have seen previously, the size of the turbulent eddies that carry the Reynolds stresses in the near-wall region scales in wall units. It seems natural then that the length of the transition region necessary to recover the correct levels of Reynolds stresses also scales with the size of the eddies that carry them. The length of a streak is around 1,000 wall units, so the length of the transition region corresponds approximately to the length of 3 near-wall streaks. A similar conclusion can be reached for the development of all Reynolds stresses. Fig. 8.10 shows for instance the downstream development of the error in the Reynolds shear stress in the near-wall region. Clearly the length of the transition region decreases as the Reynolds number increases and the error curves collapse when rescaled in wall units. Fig. 8.11 also shows that the development of the coefficient of friction downstream of the inlet is the same for the three Reynolds numbers considered when expressed as a function of x/δ_v . From

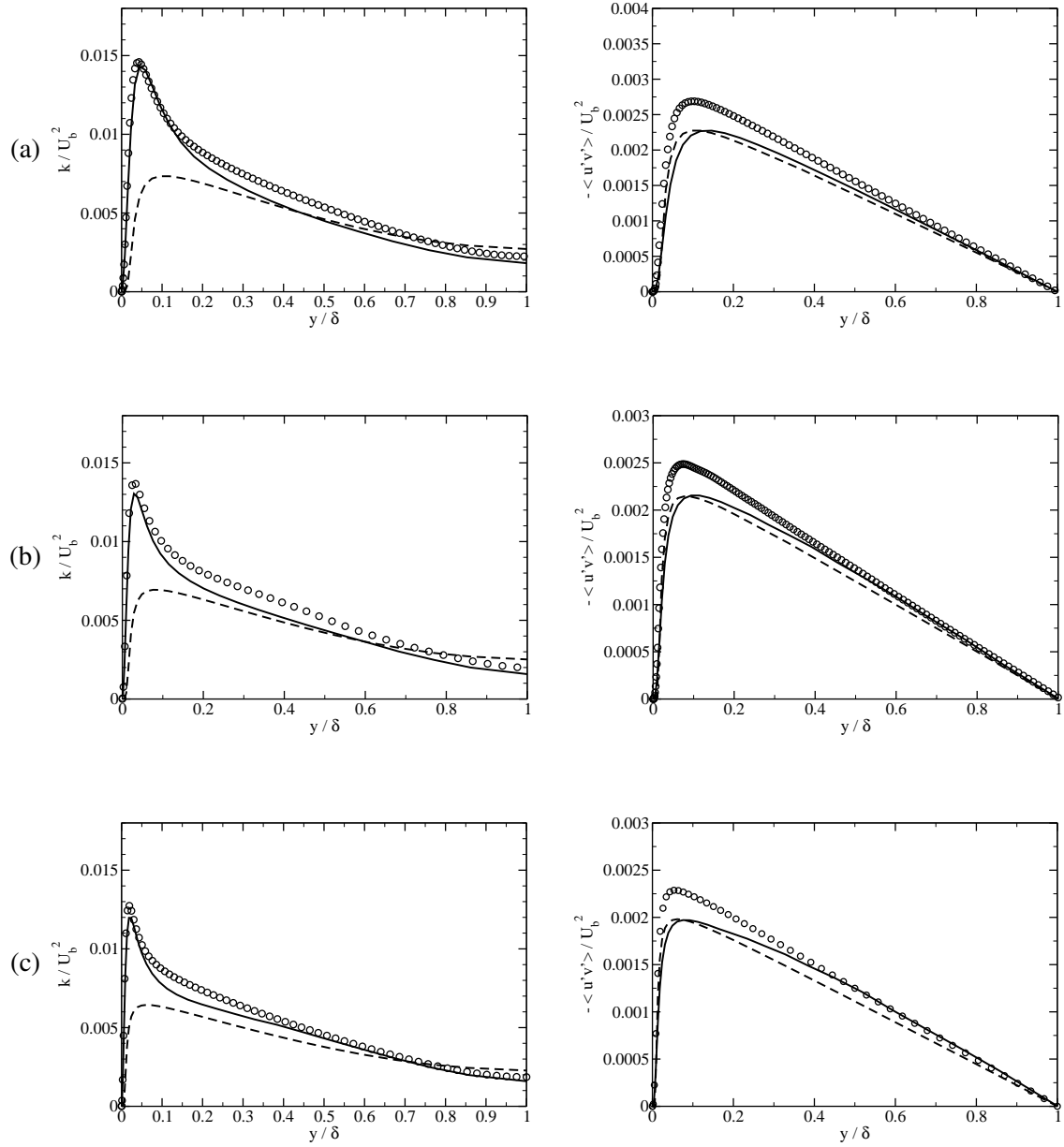


Figure 8.7: SEM turbulent kinetic energy and Reynolds shear stress profiles extracted from the SST simulation of plane channel flow at (a) $Re_\tau = 395$, (b) $Re_\tau = 590$ and (c) $Re_\tau = 950$. Turbulent kinetic energy profiles are plotted on the left hand side while while Reynolds shear stress profiles are plotted on the right hand side. ——, SEM input statistics; —, periodic LES data; ○○○, reference DNS data.

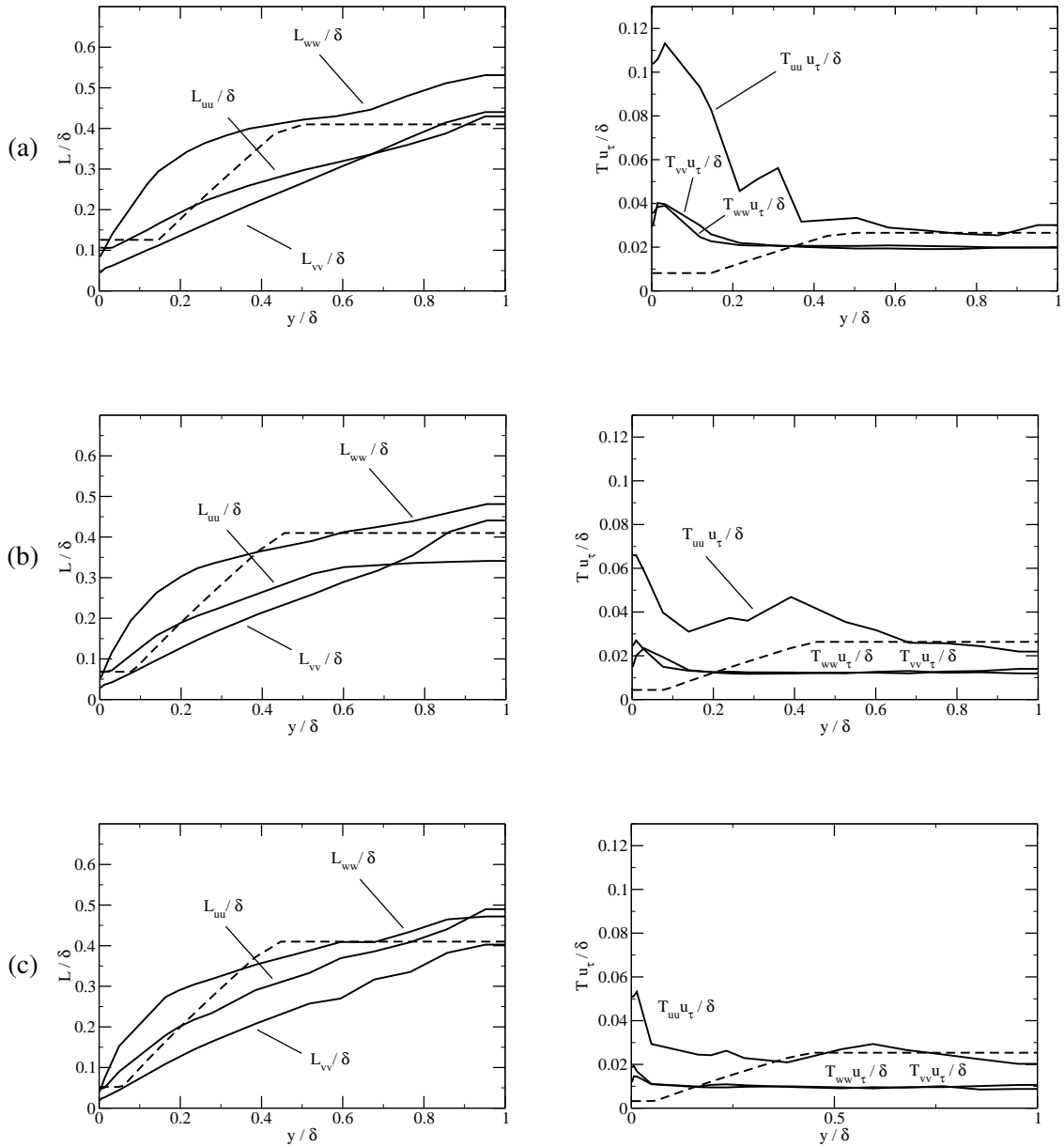


Figure 8.8: SEM input length and time scales extracted from the SST simulation of plane channel flow at (a) $Re_\tau = 395$, (b) $Re_\tau = 590$ and (c) $Re_\tau = 950$. Spanwise length scales (left) and time scales (right).
 ---, SEM input statistics; —, periodic LES data.

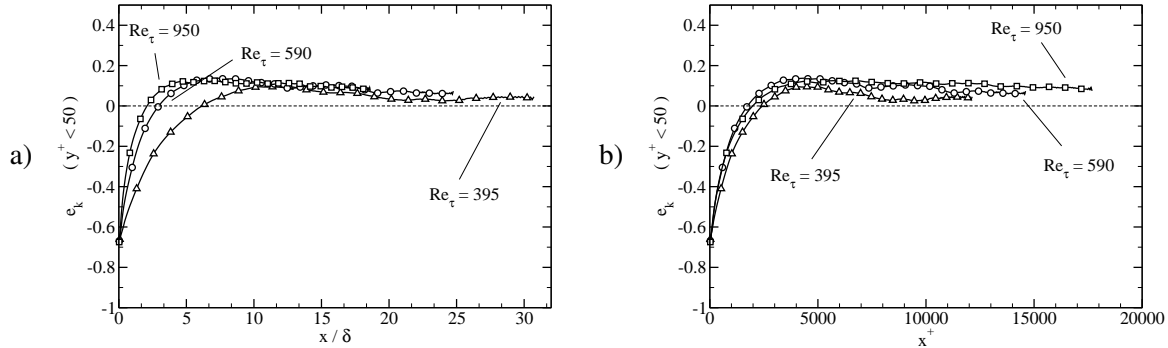


Figure 8.9: Channel flow at $Re_\tau = 395$ (\triangle), $Re_\tau = 590$ (\circ) and $Re_\tau = 950$ (\square). Downstream development of the error in the turbulent kinetic energy profiles for $y^+ < 50$ as a function of (a) x/δ and (b) x^+ .

the present analysis, it can be inferred that in the near-wall region, the error in all the statistics is reduced to reasonable levels after a transition region whose length scales as $x^+ \approx 3,000$. The behavior of the flow in the core of the flow for $y/\delta > 0.5$ will now be studied.

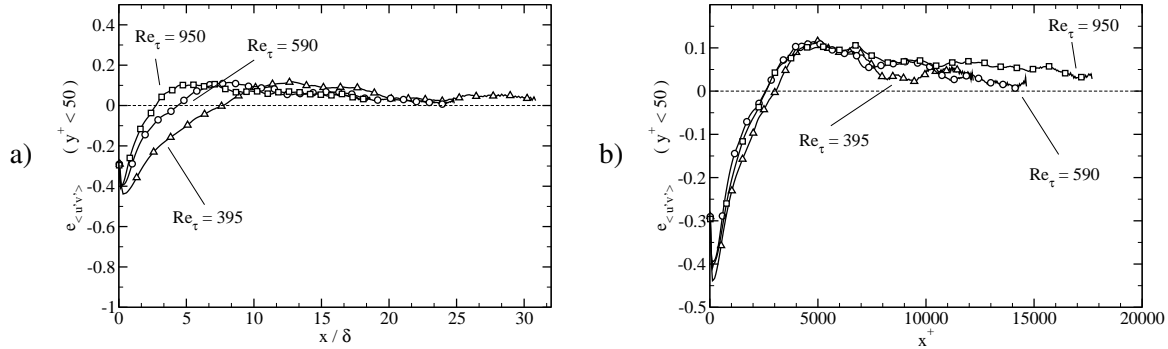


Figure 8.10: Channel flow at $Re_\tau = 395$ (\triangle), $Re_\tau = 590$ (\circ) and $Re_\tau = 950$ (\square). Downstream development of the error in the Reynolds shear stress profiles for $y^+ < 50$ as a function of (a) x/δ and (b) x^+ .

Fig. 8.12 and Fig. 8.13 compare the evolution of the error in the turbulent kinetic energy and Reynolds shear stress profiles in the near wall region for $y^+ < 50$ and in the core of the channel for $y/\delta > 0.5$. The recovery of low levels of error in the profiles is slower in the core of the channel than in the near-wall region. The turbulent kinetic energy and Reynolds shear stress profiles can be considered as fully developed in the near-wall region for $x \geq 5\delta$. On the contrary, in the core of the channel, the error

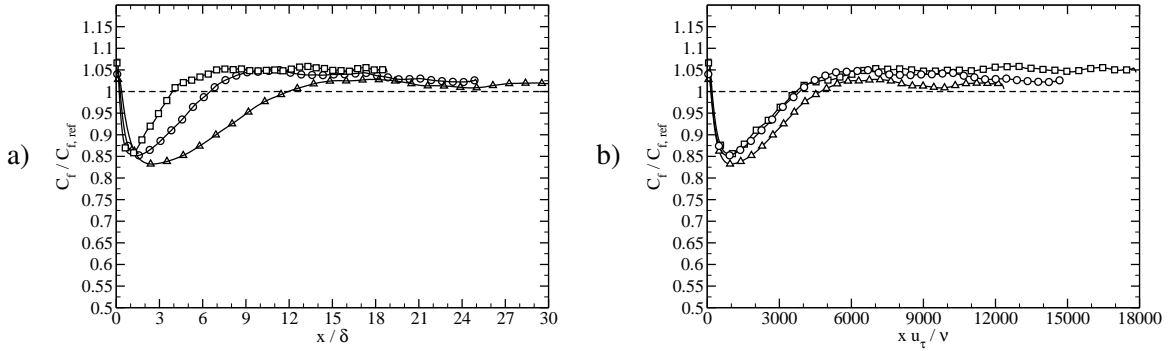


Figure 8.11: Channel flow at $Re_\tau = 395$ (\triangle), $Re_\tau = 590$ (\circ) and $Re_\tau = 950$ (\square). Downstream development of $C_f/C_{f,ref}$ as a function of (a) x/δ and (b) x^+ . $C_{f,ref}$ denotes the friction coefficient of the periodic LES simulation at the corresponding Reynolds number.

curves for the turbulent kinetic energy (see Fig. 8.12 (b)) and Reynolds shear stress (see Fig. 8.13 (b)) reach a maximum of 30 – 40% about 15δ downstream of the inlet. A higher level of errors in the core of the channel than in the near-wall region were also observed in the previous chapter. However, they were of the order of 5 – 10% compared to nearly 40% in the case of the present hybrid RANS-LES simulations. Several causes can be proposed to account for this phenomenon. The SST mean velocity profile is different from the LES mean velocity profile. We showed in the previous chapter that an error in the prescribed mean velocity profile can produce higher levels of turbulence in the core of the channel further downstream of the inlet. Another source of error could be the overestimation of the inflow integral time scale, especially in the core of the channel (see Fig. 8.8) which, as shown in the previous chapter, also yields higher levels of turbulence in the core of the channel.

The instantaneous features of the flow downstream of the inlet for the three Reynolds number considered are now studied. Streamwise velocity fluctuations at $y^+ = 5$ are shown in Fig. 8.14. A weak decay of the intensity of the streaks can be observed downstream of the inlet for all Reynolds numbers and, as expected, the length of this transient decreases with an increase in the Reynolds number. This confirms conclusions drawn from the analysis of statistical quantities: the near-wall region turbulence reaches a fully developed state after a short transition region whose length scales in wall units. Spanwise velocity fluctuations across the channel are shown in Fig. 8.15. As expected, the transient in the instantaneous flow structures in the core of the channel is longer than in the near-wall region. An analysis of the error in the turbulent kinetic energy profile reveals an increase of the turbulent activity in the core of the channel up to 15δ downstream of the inlet. It was indicated that the reason for this phenomenon was the overly

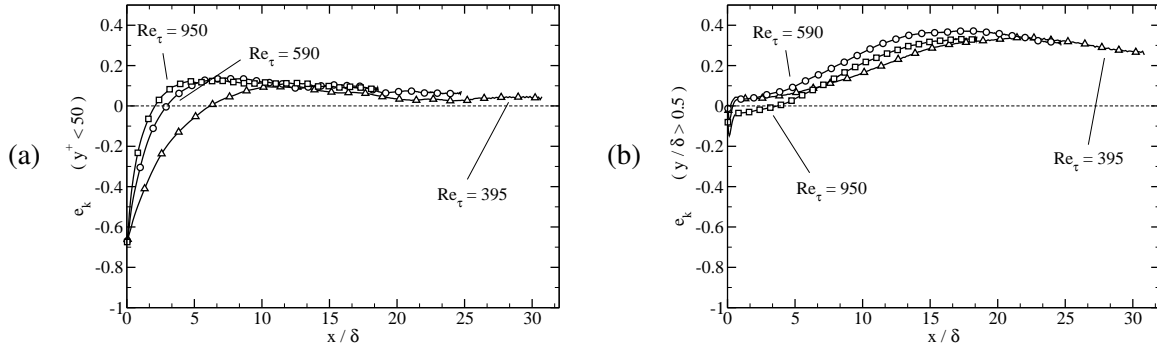


Figure 8.12: Channel flow at $Re_\tau = 395$ (\triangle), $Re_\tau = 590$ (\circ) and $Re_\tau = 950$ (\square). Downstream development of the error in the turbulent kinetic energy profiles (a) for $y^+ < 50$ and (b) for $y/\delta > 0.5$.

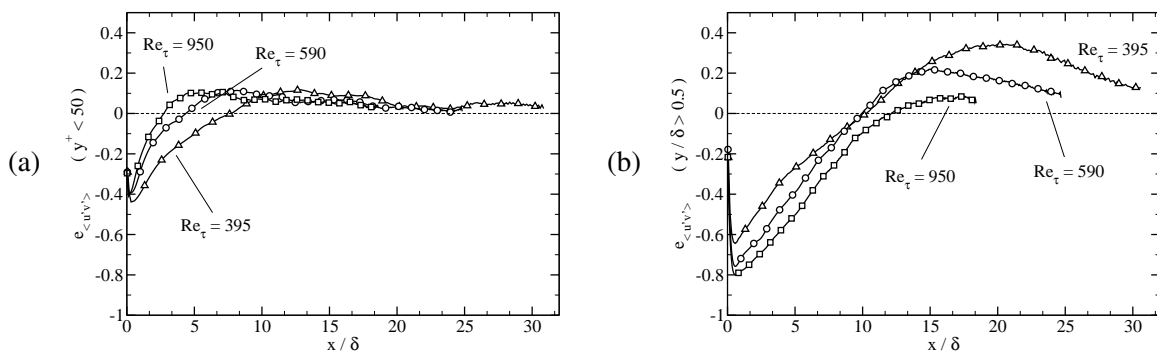


Figure 8.13: Channel flow at $Re_\tau = 395$ (\triangle), $Re_\tau = 590$ (\circ) and $Re_\tau = 950$ (\square). Downstream development of the error in the Reynolds shear stress profiles (a) for $y^+ < 50$ and (b) for $y/\delta > 0.5$.

large time scale prescribed at the inlet. Observation of the spanwise velocity fluctuations in Fig. 8.15 confirms this hypothesis. The core of the channel is populated with large scale structures prescribed at the inflow up to 15δ downstream of the inlet, and only further downstream small scales structures ejected from the wall destroy this initial large scale dominance.

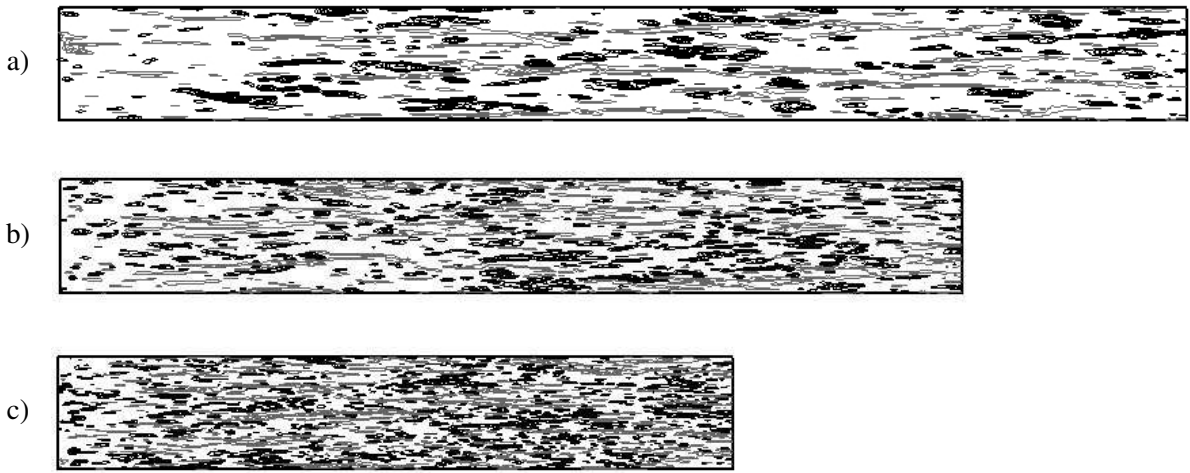


Figure 8.14: Channel flows at (a) $Re_\tau = 395$, (b) $Re_\tau = 590$ and (c) $Re_\tau = 950$. Contours of streamwise velocity fluctuations u^+ at $y^+ = 5$. Contour lines are evenly spaced at $\pm 2, \pm 3, \pm 4, \pm 5$ and ± 6 . Grey lines indicate negative value contours.

8.3.3 Comparisons of methods of generation of inlet conditions for LES

In this section, the SEM is compared to four other existing methods of generation of inlet conditions for LES. In all the simulations performed, the Reynolds number is $Re = 22,907$ (corresponding to $Re_\tau = 395$ in the periodic LES), and data from the upstream RANS simulation was used for the generation of inflow data for the LES region.

Synthesized turbulence

A baseline simulation was performed as a comparison point for all other cases (run P1). Time series of instantaneous velocity planes were extracted from a periodic LES (run G of the previous chapter) and imposed at the inlet of the LES domain. The mass flow rates of the upstream SST simulation and of the periodic LES (run G) are identical.

In all other simulations, alternative methods of generation of synthetic turbulence are used to prescribe inlet conditions for the LES region. Three hybrid calculations were conducted, using the SEM with the

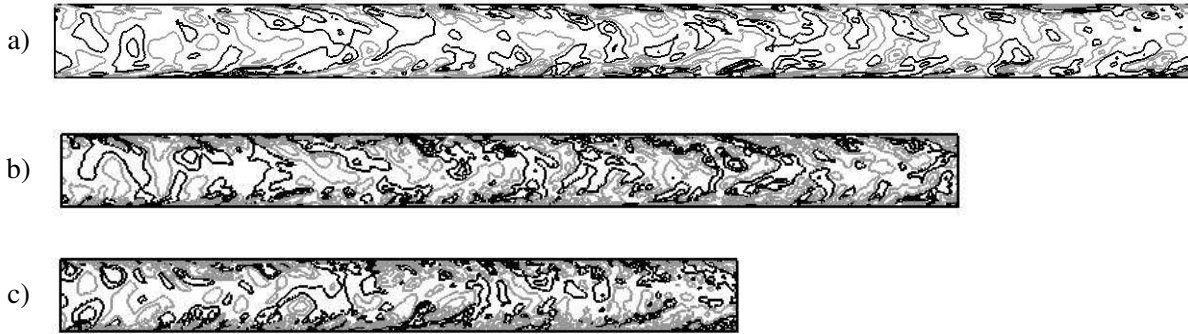


Figure 8.15: Channel flows at (a) $Re_\tau = 395$, (b) $Re_\tau = 590$ and (c) $Re_\tau = 950$. Contours of spanwise velocity fluctuations w^+ on a plane of constant z . Contour lines are evenly spaced at $\pm 0.5, \pm 1.5, \pm 2.5, \pm 3.5$ and ± 4.5 . Grey lines indicate negative value contours.

parametrization presented in the previous section (run S1), the spectral method of Batten et al. (2004) using $N = 5,000$ modes (run B1) and uncorrelated random numbers using the transformation presented in Eq. (3.3) to match the prescribed RANS Reynolds stress tensor (run R1).

Fig. 8.16 shows instantaneous velocity fluctuations prescribed at the inlet of the LES domain for run P1, S1, B1 and R1. Two-point correlations of the wall-normal velocity fluctuations are shown in Fig. 8.17.

The differences between the SEM and the periodic LES signal have already been discussed in Chapter 4. The SEM does not reproduce completely the complex structure of the near-wall turbulence (no ejection of near-wall streaks for instance) and the core of the channel exhibits a lack of small scale structures. These discrepancies are acceptable since the SEM is not designed to reproduce these fine features of the flow. However the length scale and intensity of the periodic LES fluctuations are well reproduced by the SEM (see Fig. 8.16 (b)).

Fig. 8.16 (d) shows the velocity fluctuations generated by the random method. As expected, the signal does not exhibit any spatial correlations.

The velocity fluctuations generated using the method of Batten et al. (2004) in Fig. 8.16 (c) exhibit surprising features. In the near-wall region, the fluctuations seem to be decorrelated in space. In the centre of the channel, the fluctuations are correlated in the spanwise direction but seem decorrelated in the wall-normal direction. Fig. 8.17 confirms that the signal exhibits spatial correlations in the spanwise direction, but not in the wall-normal direction. The reason for these phenomena is the decomposition into Fourier modes used in Batten's method (see Eq. (3.12) of Chapter 3). The signal is decomposed as a sum of cosine and sine functions, and the frequencies and wavelengths of these cosine and sine functions

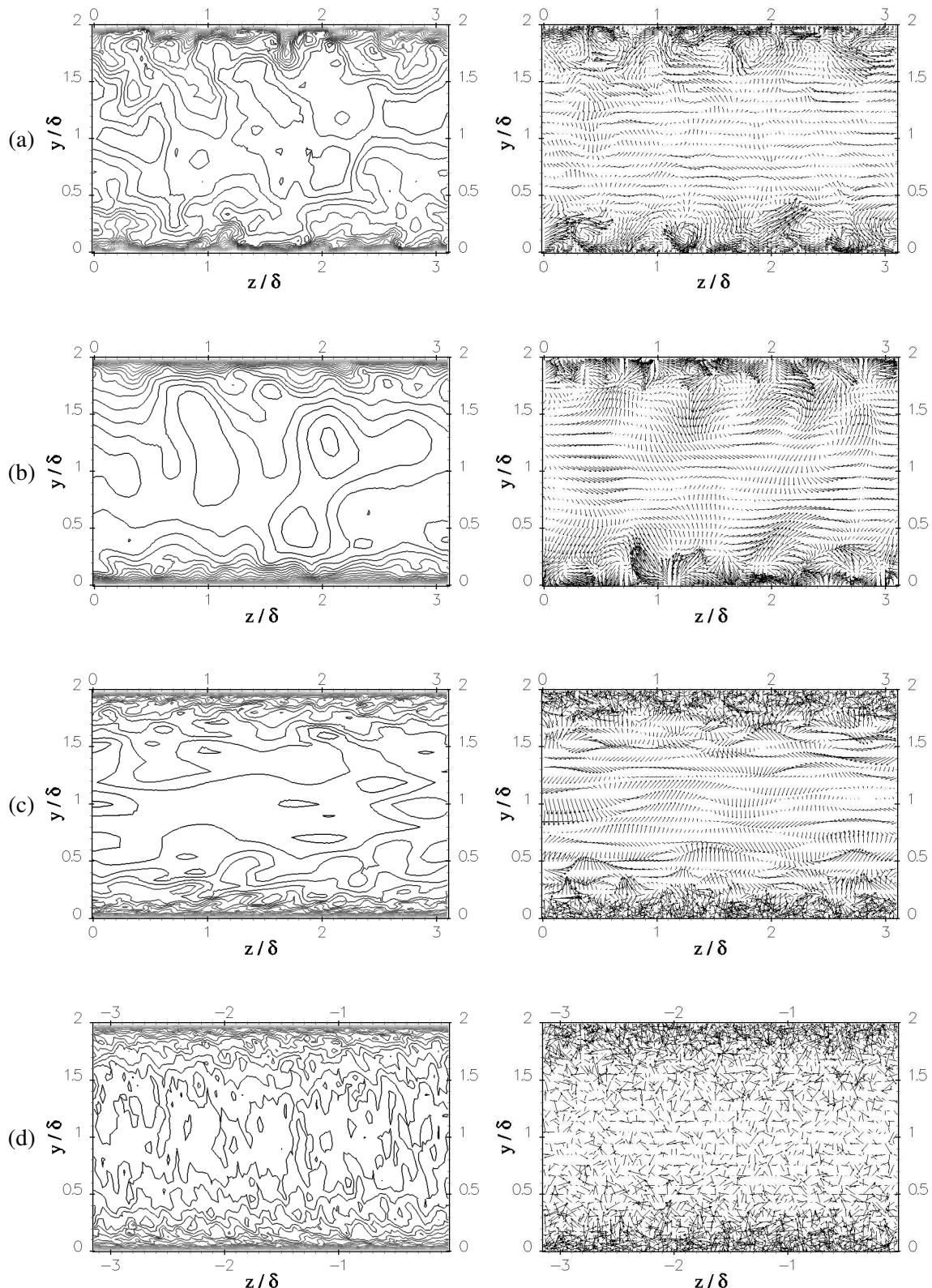


Figure 8.16: Inlet conditions for hybrid RANS-LES simulation. Streamwise velocity contours (left) and velocity vectors (right) for (a) run P1, (b) S1, (c) B1, and (d) R1.

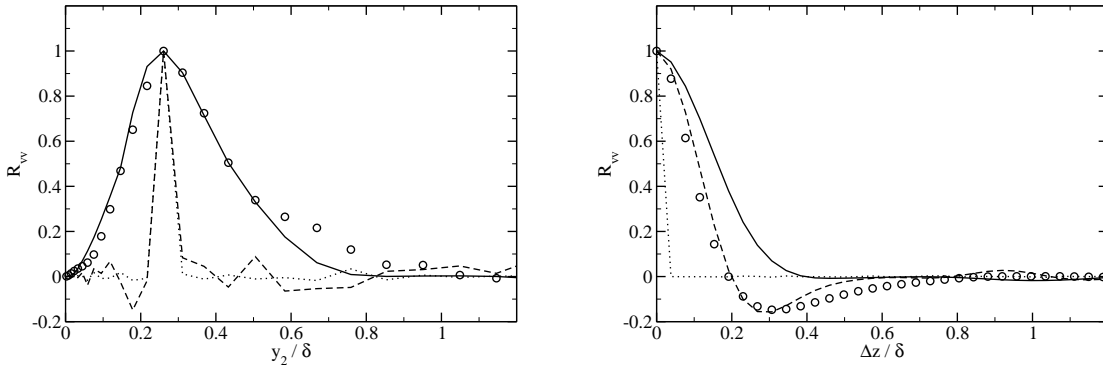


Figure 8.17: Two-point correlations $R_{vv}(y_1, y_2, \Delta z)$ of the wall-normal velocity fluctuations at $y_1/\delta = 0.25$ as a function of wall-normal distance y_2/δ (left), and as a function of spanwise separation Δz (right):
 random method inlet conditions (run R1); --- Batten et al. (2004) inlet conditions (run B1);
 — SEM inlet conditions (run S1); ○○○ precursor LES inlet conditions (run P1).

are allowed to vary in the direction of non-homogeneity of the flow (in the present case the wall-normal direction). The velocities at two points separated even by an infinitesimal distance in the wall-normal direction will thus oscillate at different frequencies, and therefore be completely decorrelated from each other. In the direction of homogeneity of the flow however (the spanwise direction in the present case), this problem does not occur since the frequencies and wavelengths are constant. Thus although the method of Batten et al. (2004) might appear to be capable of generating non-homogeneous turbulence by allowing the wavelengths to vary in space, it does so at the expense of destroying the spatial correlations in the non-homogeneous directions.

Results and discussions

The development of the prescribed fluctuations downstream of the inlet for runs S1, P1, B1 and R1 will now be studied. Fig. 8.18 shows the downstream development of the coefficient of friction. The horizontal dashed line represents the value of the coefficient of friction in the periodic LES and will be used as a reference point for the present RANS-LES simulations. Run P1 has a coefficient of friction in very good agreement with the periodic LES over the whole domain. All three of the other simulations using synthetic turbulence exhibit a transient downstream of the inlet. When only uncorrelated numbers are used (run R1), the coefficient of friction drops continuously downstream of the inlet which indicates that the flow laminarizes. The decay of the coefficient of friction is also quite important downstream of the inlet when the method of Batten et al. (2004) is used. However the coefficient of friction reaches

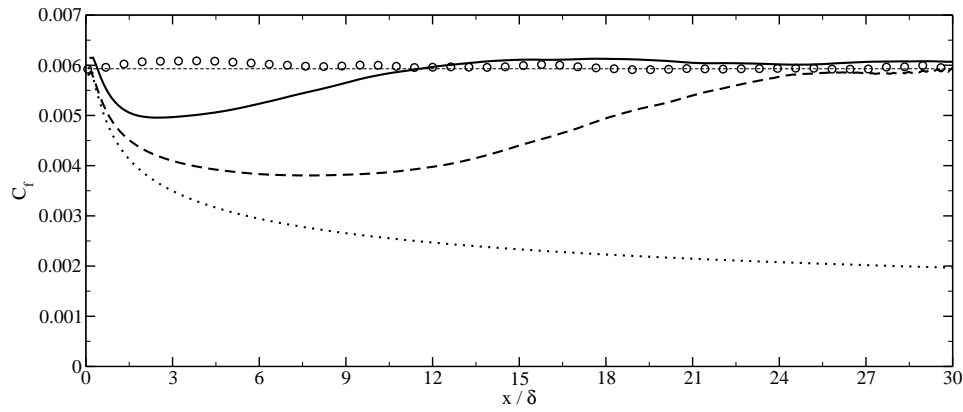


Figure 8.18: Hybrid RANS-LES simulation of channel flow at $Re_\tau = 395$. Downstream development of the coefficient of friction. random method inlet conditions; - - - Batten et al. (2004) inlet conditions; — SEM inlet conditions; ○○○, precursor LES inlet conditions.

a minimum after about 8δ (where it has lost about 35% of its initial value), before slowly recovering towards its fully developed value about 25δ downstream of the inlet. With the SEM, the coefficient of friction decays downstream of the inlet to reach a minimum about 3δ downstream of the inlet (where it has only lost 15% of its initial value), and recovers its fully developed value only after 10δ downstream of the inlet.

Fig. 8.19 compares the mean velocity profiles at different streamwise locations downstream of the inlet. When uncorrelated random numbers are prescribed at the inlet (see Fig. 8.19 (d)), the wall shear stress decreases and the centreline velocity increases which confirms that the flow tends to laminarize. The velocity profiles for run P1 collapse onto one single curve which indicates that the flow is fully developed over the whole computational domain (see Fig. 8.19 (a)). The collapse of the velocity profiles occur at location $x/\delta = 10$ when the SEM is used (see Fig. 8.19 (b)), whereas when Batten's method is used, the collapse only occurs at the last station $x/\delta = 30$ (see Fig. 8.19 (c)).

The downstream development of the turbulent fluctuations prescribed at the inlet is now studied. Profiles of turbulent kinetic energy and Reynolds shear stress at different streamwise locations are shown on Fig. 8.20 and Fig. 8.21, respectively. Again the profiles of the simulation using a precursor simulation collapse onto the periodic LES profiles at all stations. The fluctuations prescribed using the random method have been almost completely dissipated at the first station ($x/\delta = 5$), and no sign of regeneration of turbulence is visible before the end of the domain. This confirms the conclusions drawn from the observation of the mean velocity profiles: the flow has become essentially laminar. The turbulent fluctuations

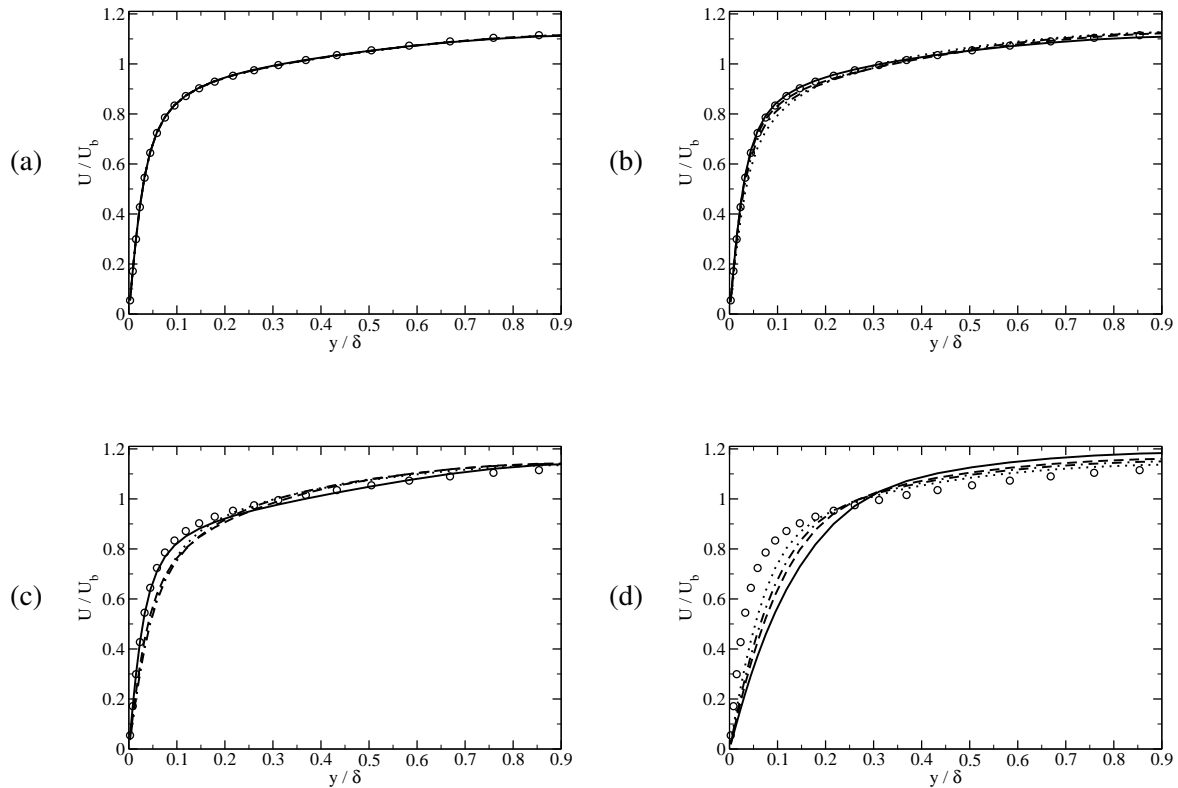


Figure 8.19: Hybrid RANS-LES simulation of channel flow at $Re_\tau = 395$. Profiles of the mean velocity at various streamwise locations: (a) Precursor simulation, (b) SEM, (c) Batten's method, and (d) random method inlet conditions. \cdots , $x / \delta = 5$; $\cdots\cdots$, $x / \delta = 10$; $-$, $x / \delta = 15$; $-$, $x / \delta = 15$; $-$, $x / \delta = 30$; $\circ\circ\circ$, reference periodic LES.

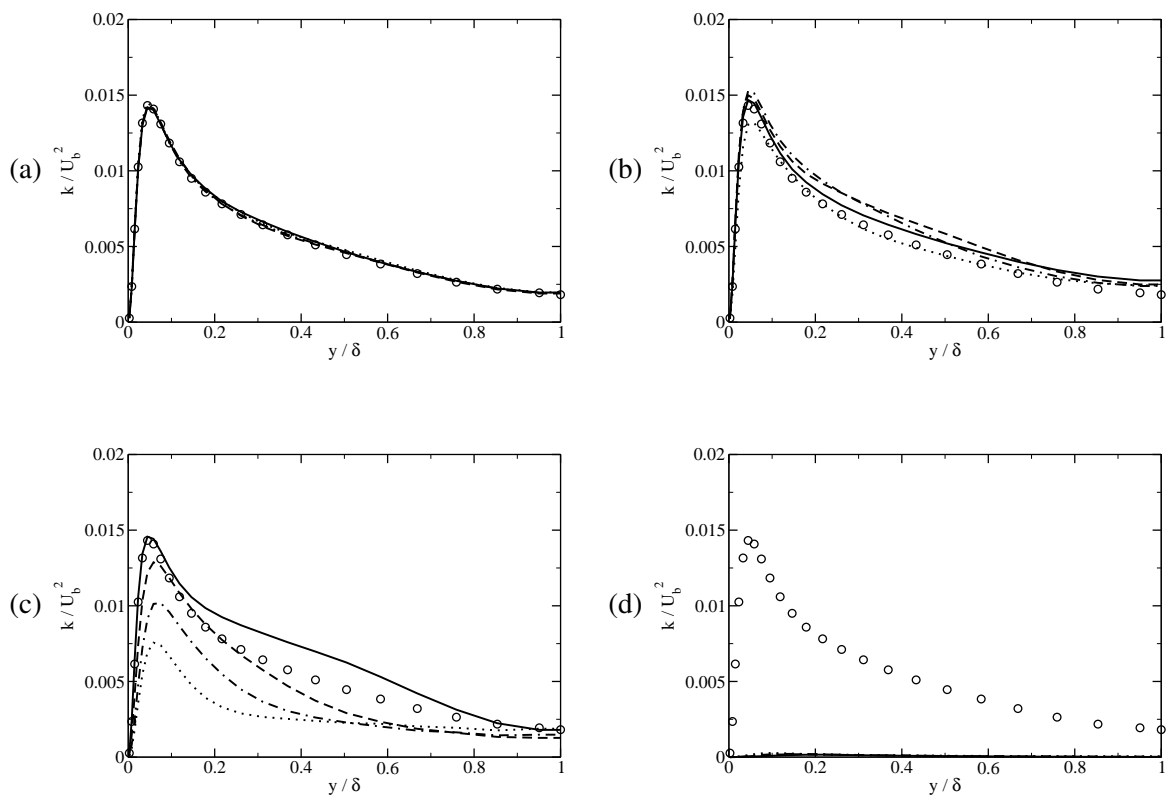


Figure 8.20: Hybrid RANS-LES simulation of channel flow at $Re_\tau = 395$. Profiles of the turbulent kinetic energy at various streamwise locations: (a) Precursor simulation, (b) SEM, (c) Batten's method, and (d) random method inlet conditions. Same legend as in Fig. 8.19.

and the Reynolds shear stress prescribed using Batten's method both decay significantly downstream of the inlet (as expected from Keating et al. (2004)) before being slowly regenerated. However the regeneration of turbulent kinetic energy and Reynolds shear stress is slow and by the last plane the profiles have not converged towards the fully developed profiles. At the last station, the error in the profiles seem to be localized in the core of the channel, which can be attributed to an overly large time scale of the inflow data in this region. The profiles obtained using the SEM only undergo a weak transient downstream of the inlet and at $x/\delta = 5$ the levels of turbulent kinetic energy and Reynolds shear stress are both in very good agreement with the periodic LES levels. As we have seen in the previous section, there is also an excess of turbulent kinetic energy and Reynolds shear stress in the core of the channel following the transient immediately downstream of the inlet, but the overall agreement with the fully developed profiles is good at all streamwise locations presented.

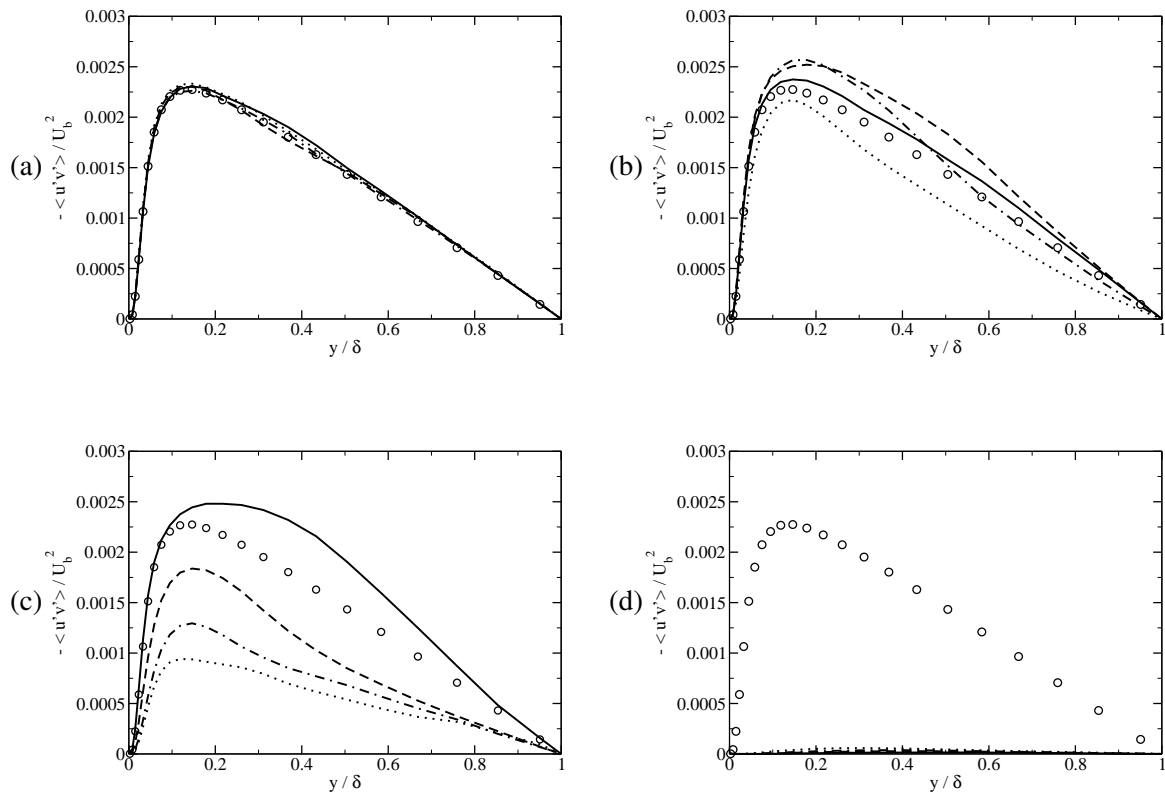


Figure 8.21: Hybrid RANS-LES simulation of channel flow at $Re_\tau = 395$. Profiles of the Reynolds shear stress at various streamwise locations: (a) Precursor simulation, (b) SEM, (c) Batten's method, and (d) random method inlet conditions. Same legend as in Fig. 8.19.

Contours of streamwise velocity fluctuations at $y^+ = 5$ are shown in Fig. 8.22. The streaky structure

characteristic of near-wall turbulence is fully developed at the inlet for run P1. On the contrary, no near-wall fluctuations can be observed in run R1. Both observations are consistent with conclusions drawn from the statistical analysis. When the SEM is used, the correct near-wall structure is established after $x/\delta \approx 5$, whereas with Batten's method, it is not established before $x/\delta \approx 20$. This is again consistent with results of the statistical analysis.

Fig. 8.23 shows contours of spanwise velocity fluctuations on a z cross section. The random method fluctuations are dissipated immediately downstream of the inlet across the whole channel. With Batten's method, the lack of turbulence production in the near-wall region entails a lack of turbulent fluctuations in the centre of the channel until $x/\delta = 25$ where the correct near-wall dynamics re-establishes. With the SEM, the fluctuations in the centre of the channel develop more quickly since the correct near-wall structures are established after only $x/\delta \approx 5$.

Finally Fig. 8.24 shows isosurfaces of Q for the four cases, and it confirms the conclusions drawn from the statistical and instantaneous flow features analysis.

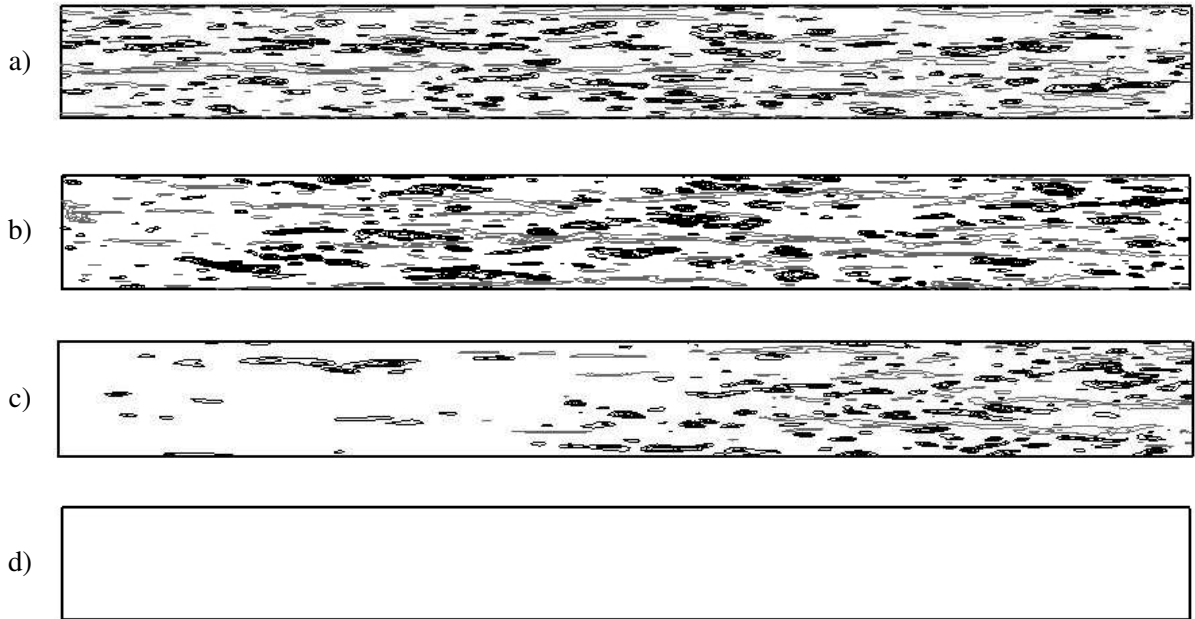


Figure 8.22: Hybrid RANS-LES simulation of channel flow at $Re_\tau = 395$. Contours of streamwise velocity fluctuations u^+ at $y^+ = 5$: (a) precursor simulation inlet conditions, (b) SEM inlet conditions, (c) Batten et al. (2004) inlet conditions and (d) random method inlet conditions. Contour lines are evenly spaced at $\pm 2, \pm 3, \pm 4, \pm 5$ and ± 6 . Grey lines indicate negative value contours.

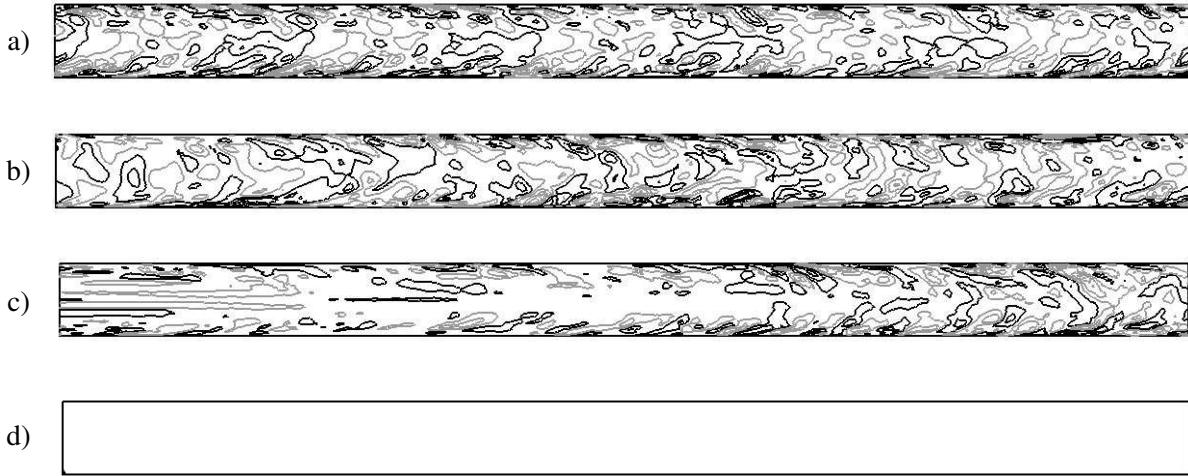


Figure 8.23: Hybrid RANS-LES simulation of channel flow at $Re_\tau = 395$. Contours of spanwise velocity fluctuations w^+ on a plane of constant z : (a) precursor simulation inlet conditions, (b) SEM inlet conditions, (c) Batten et al. (2004) inlet conditions and (d) random method inlet conditions. Contour lines are evenly spaced at $\pm 0.5, \pm 1.5, \pm 2.5, \pm 3.5$ and ± 4.5 . Grey lines indicate negative value contours.

8.4 Boundary Layer Flow Results

8.4.1 Presentation of the case

A zero-pressure gradient turbulent boundary layer over a flat plate is simulated. The difference between this flow and the channel flow is the presence of a free-stream edge at the top of the boundary layer where a turbulent flow mixes with a laminar flow. As a result, and in the absence of a pressure gradient, the thickness of the boundary layer increases as the boundary layer develops. Several quantities can be used to measure the thickness of the boundary layer. The boundary layer thickness δ denotes the distance from the wall at which the velocity profile reaches 99% of the free stream edge velocity U_∞ . However it is not a well conditioned quantity and we often prefer to use the displacement thickness defined as,

$$\delta^* = \int_0^\infty \left(1 - \frac{U}{U_\infty}\right) dy, \quad (8.7)$$

or the momentum thickness θ defined as,

$$\theta = \int_0^\infty \frac{U}{U_\infty} \left(1 - \frac{U}{U_\infty}\right) dy. \quad (8.8)$$

In the near-wall region, the boundary layer flow is essentially the same as in a plane channel flow: the turbulent structures are in equilibrium with the mean flow and there is an inner layer close to the wall in which mean velocity and Reynolds stresses scale in wall units.

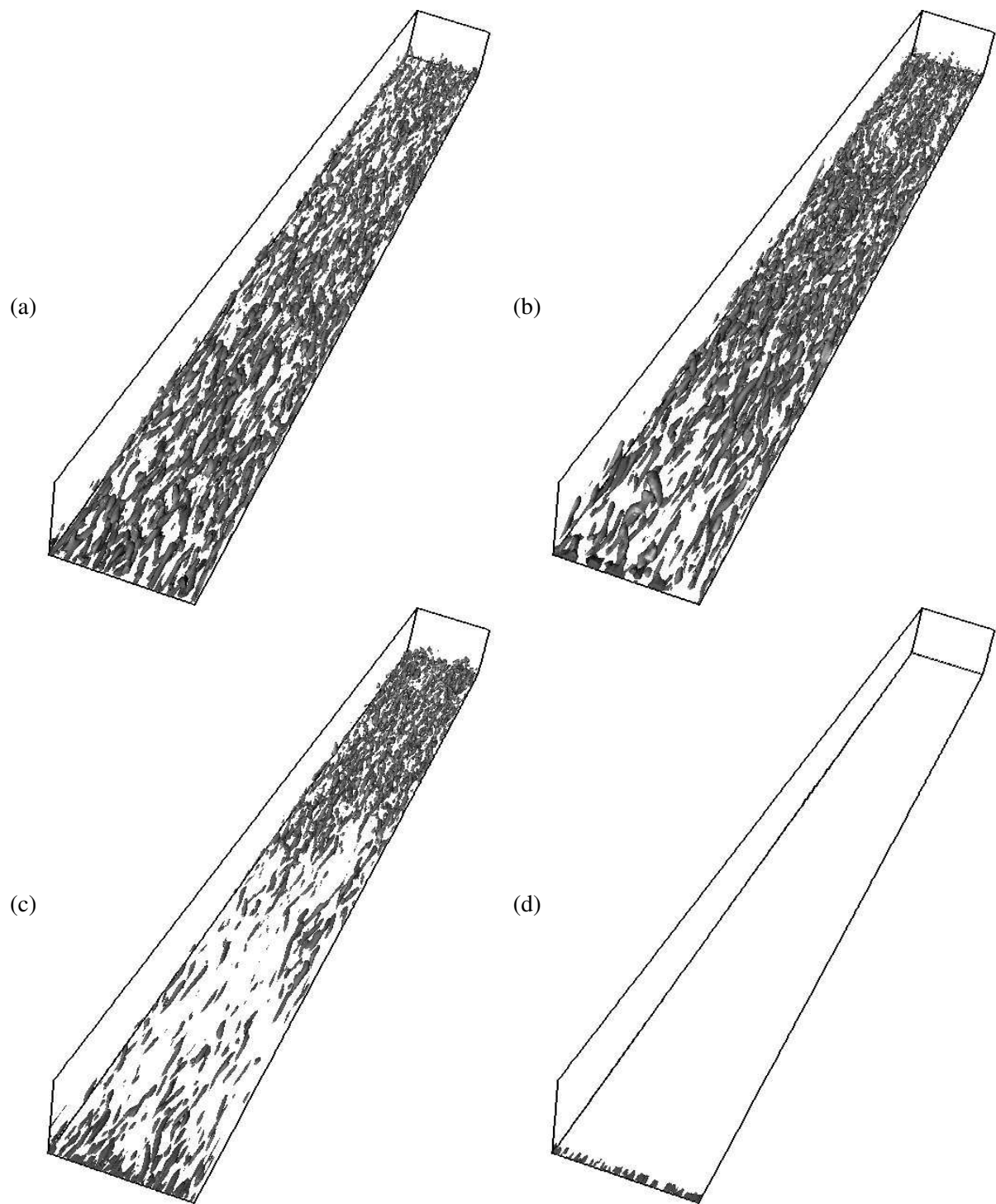


Figure 8.24: Hybrid RANS-LES simulation of channel flow at $Re_\tau = 395$. Instantaneous isosurfaces of $Q = 300$: (a) precursor simulation inlet conditions, (b) SEM inlet conditions, (c) Batten et al. (2004) inlet conditions and (d) random method inlet conditions.

Four simulations of a zero-pressure gradient turbulent boundary layer are performed: a reference LES solution and three hybrid RANS-LES calculations. The reference LES is performed on a domain of dimensions $35\delta_0 \times 4\delta_0 \times 3\delta_0$ (δ_0 is the boundary layer thickness at the inflow) in the streamwise, wall-normal and spanwise directions, respectively. In the hybrid simulations, the RANS equations are solved in a domain of dimensions $35\delta_0 \times 4\delta_0 \times 3\delta_0$, and at $x = 10\delta_0$ the LES domain of dimensions $35\delta_0 \times 4\delta_0 \times 3\delta_0$ begins. A sketch of the computational configurations of the reference LES and the hybrid RANS-LES is shown in Fig. 8.25.

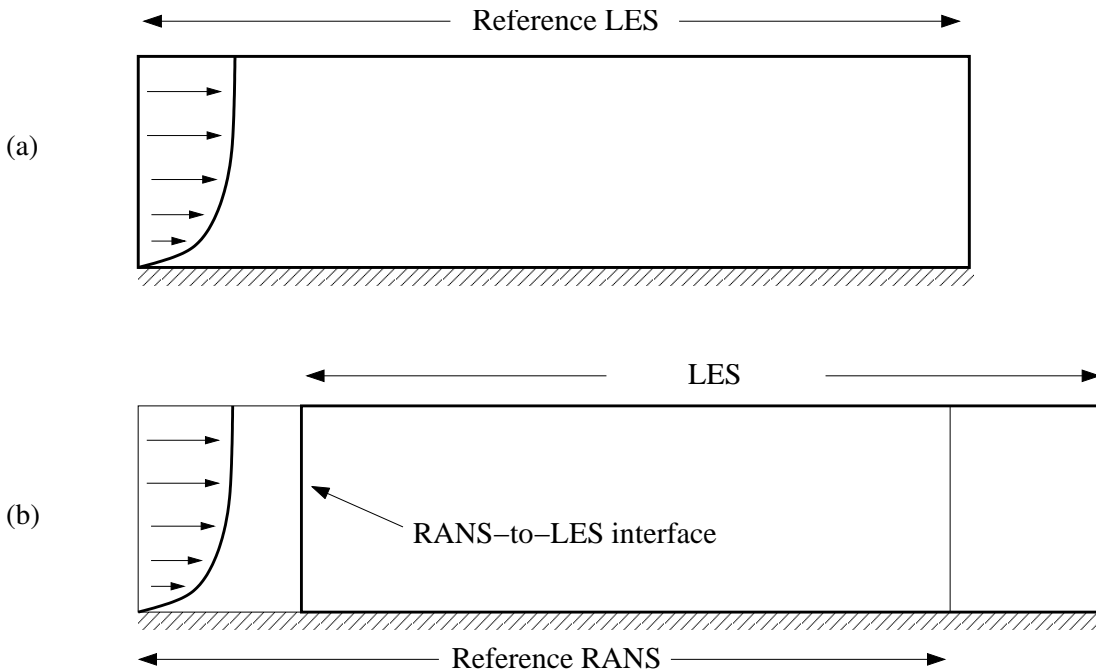


Figure 8.25: Sketch of the configuration of (a) the reference LES and (b) the hybrid RANS-LES simulations of the turbulent boundary layer over a flat plate.

The same grid is used for the reference LES and the LES region of the hybrid simulations. It uses 300 cells in the streamwise direction ($\Delta x^+ \approx 50$), 42 cells in the wall-normal direction (with $\Delta y^+_{\min} \approx 2$) and 72 cells in the spanwise direction ($\Delta z^+ \approx 15$). The present grid spacings in wall units are given at the inlet of the LES domain where they are at a maximum. In order to avoid interpolation at the RANS-LES interface, the same streamwise and wall-normal grid resolution is adopted for the RANS grid, with one cell in the spanwise direction. For all simulations, the time step Δt was adjusted so that the maximum CFL number remains lower than unity.

The SST model of Menter (1994) is used in the RANS region whereas the Smagorinsky model (with $C_S = 0.065$) and Van-Driest damping at the wall is used in the LES region.

The inflow data for the reference RANS and LES is generated using the recycling and rescaling method of Lund et al. (1998). The rescaling station is positioned at $8\delta_0$ downstream of the inlet. The same treatment as in the original Lund's method is applied to the velocity. When the SST model is used, the turbulent kinetic energy k and ω are rescaled by u_τ^2 and u_τ^2/v respectively before being recycled at the inlet plane. A no-slip boundary conditions is applied at the bottom wall. A special treatment is used for the boundary conditions on the top surface of the computational domain (Lund et al., 1998),

$$\frac{\partial u}{\partial y} = 0, \quad v = U_\infty \frac{d\delta^*}{dx}, \quad \frac{\partial w}{\partial y} = 0 \quad (8.9)$$

where δ^* is the boundary layer displacement thickness. The derivative $d\delta^*/dx$ is computed by performing a linear regression on the streamwise distribution of δ^* to determine the average slope. This boundary condition has the advantage that flow is sucked out of the computational domain through the top boundary which ensures that the boundary layer does not accelerate and the mean streamwise pressure gradient is zero. At the exit plane the standard outlet boundary condition implemented in *Code_Saturne* (see page 97 in Chapter 5) is applied.

The boundary conditions for the LES domain of the hybrid simulations are prescribed as follows. A no-slip boundary conditions is applied at the bottom wall, and the standard outlet boundary condition implemented in *Code_Saturne* is applied at the exit plane. At the top surface of the domain we impose, $\mathbf{u} = \mathbf{u}_{RANS}$, where \mathbf{u}_{RANS} is the constant velocity on the top surface of the RANS domain computed from Eq. (8.9). At the inlet plane of the LES domain, data are extracted from the RANS solution, and used for the generation of synthetic turbulence. Three hybrid simulations were performed using the SEM with the parametrization presented in Section 8.2, the spectral method of Batten et al. (2004) and the random method.

8.4.2 Results and discussion

In order to study the development of the boundary layer mean velocity profile, we show on Fig. 8.26 the streamwise development of the coefficient of friction,

$$C_f = \frac{\tau_w}{\frac{1}{2}\rho U_\infty^2}, \quad (8.10)$$

as a function of Re_θ defined as,

$$Re_\theta = \frac{U_\infty \theta}{v}. \quad (8.11)$$

For comparisons, the results from the momentum integral estimate based on Cole's Law of the wake (Coles, 1956) calculated as described in Appendix C of Lund et al. (1998) are included. It can be noted that for a given Re_θ the coefficient of friction is underestimated by the reference RANS simulation and

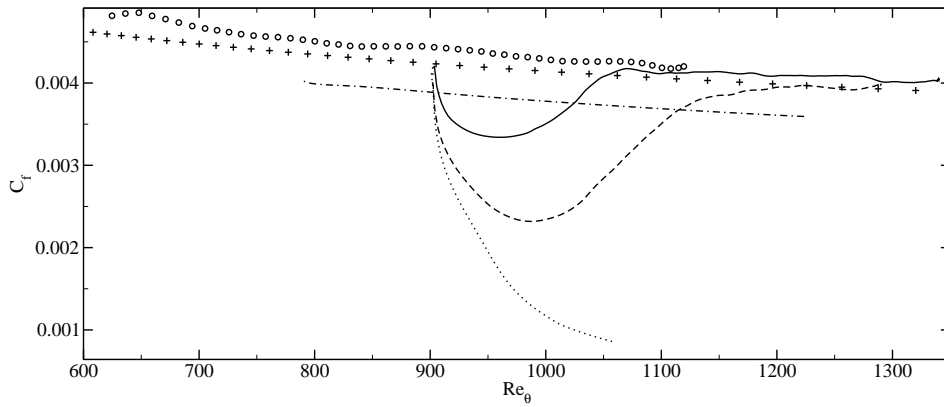


Figure 8.26: Hybrid RANS-LES simulation of a zero pressure gradient turbulent boundary layer. Streamwise evolution of the coefficient of friction C_f as a function of Re_θ : ——, SST model solution; ······, LES solution with uncorrelated random numbers at interface; - - - - , LES solution with the method of Batten et al. (2004) at interface; —, LES solution with the SEM at interface; ○○○, reference LES; + + +, momentum integral estimate.

slightly overestimated by the reference LES (see Fig. 8.26 (b)). Overall the agreement between the reference RANS and LES using Lund's method and the analytical law is very good. In the case of the hybrid simulations, the random method leads to a laminarization of the flow and the coefficient of friction decreases over the whole LES domain. With the SEM and Batten's method, the coefficient of friction decays downstream of the inlet before recovering towards the reference LES value at $Re_\theta = 1,050$ and $Re_\theta = 1,200$, respectively. This corresponds approximately to about $8\delta_0$ and $20\delta_0$ downstream of the inlet for the SEM and Batten's method, respectively. Using the friction velocity at the inlet of the LES domain, $8\delta_0$ corresponds to approximately 3,000 wall units. The behavior of the coefficient of friction in the present boundary layer flow is thus in very good agreement with previous investigations on the channel flow case, where it was also shown that the coefficient of friction recovers correct values after approximately 3,000 wall units. Additionally, it can be noted that the LES approach (when the SEM or Batten's method was used) managed to correct the initial inaccuracies in the coefficient of friction of the SST solution.

Fig. 8.27 shows the development of the shape factor H (ratio of displacement thickness to δ^* to momentum thickness θ) as a function of Re_θ . The predictions of the reference LES using Lund's method are again in excellent agreement with the analytical law, whereas the SST solution overpredicts the shape factor of about 10% over the whole RANS domain. In the case of the hybrid simulations, the random

method gives again very poor results. The shape factor steadily increases over the LES region towards the laminar value of 2.6. With the SEM and Batten's method, the shape factor initially increases downstream of the inlet before slowly decreasing towards the reference LES solution value. In the case of Batten's method however, the initial transient downstream of the inlet causes an increase of the shape factor which is not corrected by the end of the domain.

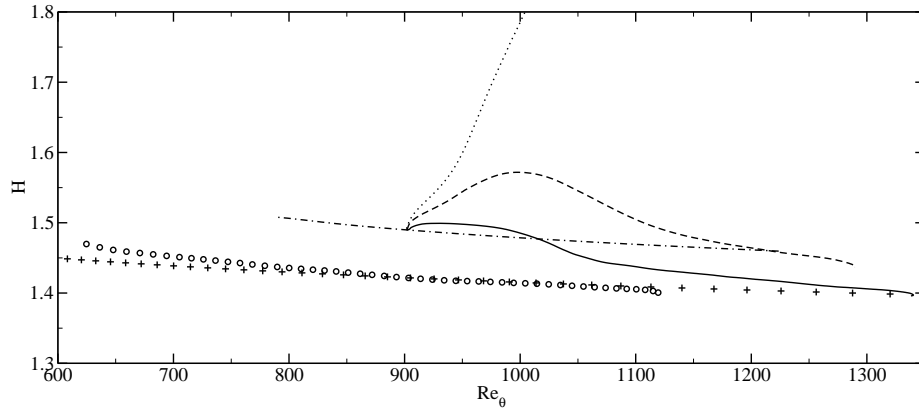


Figure 8.27: Hybrid RANS-LES simulation of a zero pressure gradient turbulent boundary layer. Streamwise evolution of the shape factor H as a function of Re_θ . Same legend as in Fig. 8.26.

We wish now to study the spatial growth of the boundary layer downstream of the RANS-LES interface. Fig. 8.28 shows the downstream development of the momentum thickness θ . It should be noted that the growth rate of the reference RANS solution is slightly underestimated compared to the reference LES, although the overall agreement is relatively good. In the case of the hybrid simulations, the boundary layer never grows at the correct rate when the random method is used. With Batten's method, there is an initial transient of about 10δ before the boundary layer grows at the correct rate. This transient generates an offset which causes the momentum thickness to be about 5% lower than predicted by the SST. With the SEM, there is also an initial transient during which, on the contrary to Batten's method, the boundary layer grows faster than expected which. This causes the momentum thickness to be overestimated by about 5% compared to the SST predictions. For $x > 10\delta_0$, the boundary layer in the hybrid simulations using the random method and Batten's method grow at the same rate as the boundary layer of the upstream RANS solution.

Mean velocity profiles at different streamwise locations are shown on Fig. 8.29. All profiles are normalized by the local boundary layer thickness δ and boundary layer edge velocity U_e (maximum mean streamwise velocity). Profiles extracted from the reference LES using Lund's method at $Re_\theta = 1,100$

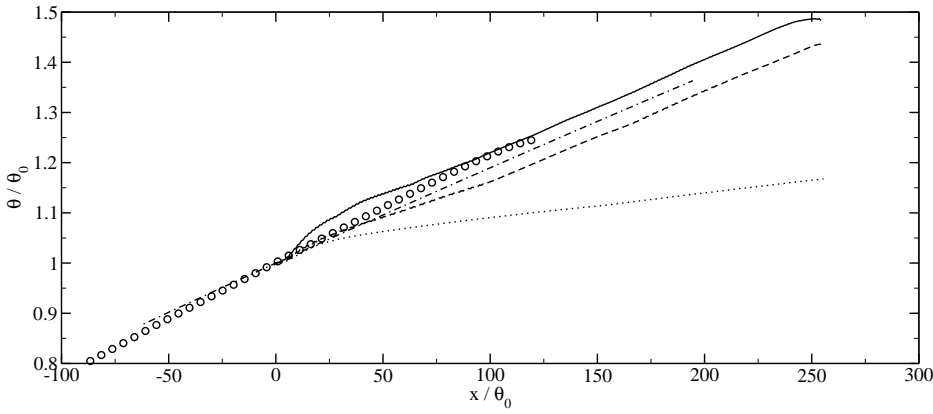


Figure 8.28: Hybrid RANS-LES simulation of a zero pressure gradient turbulent boundary layer. Streamwise evolution of the momentum thickness θ . Same legend as in Fig. 8.26.

are included for comparisons. The random method leads to anomalous behavior of the profiles that amplify as it evolves downstream. The main discrepancies with the reference LES data can be observed in the near-wall region where the profile tends towards a laminar profile. With Batten's method, an important transient can also be observed in the near-wall region and in the log-layer where the mean velocity is underestimated. On the contrary to the random method, the near-wall behavior of the mean velocity improves after the first station ($x/\delta_0 = 5$) because turbulence is produced at the wall, but the mean velocity remains significantly underestimated in the outer layer of the boundary layer. The SEM produces a smaller transient than the other two methods, and about $10\delta_0$ downstream of the inlet the agreement with the reference LES is good.

Turbulent kinetic energy and Reynolds shear stress profiles are shown at different streamwise locations on Fig. 8.30. Again profiles extracted from the reference LES using Lund's method at $Re_\theta = 1,100$ are included for comparisons. As in the channel flow simulations, the fluctuations prescribed with the random method are almost entirely dissipated before the first station ($x/\delta_0 = 5$) and no sign of regeneration of turbulent kinetic energy is visible further away downstream. The collapse of the profiles for Batten's method is quite poor at all streamwise locations represented. The decay of the turbulent kinetic energy and Reynolds shear stress in the near-wall region especially appear to be quite important up to $x/\delta_0 = 10$. As in the case of the channel flow, overly large values of Reynolds shear stress and turbulent kinetic energy due to the overprediction of the outer layer inflow time scale can be observed at the last station. With the SEM the collapse of the profiles is much better than with the other two methods, especially for the turbulent kinetic energy profiles which are in good agreement with the DNS data by the first

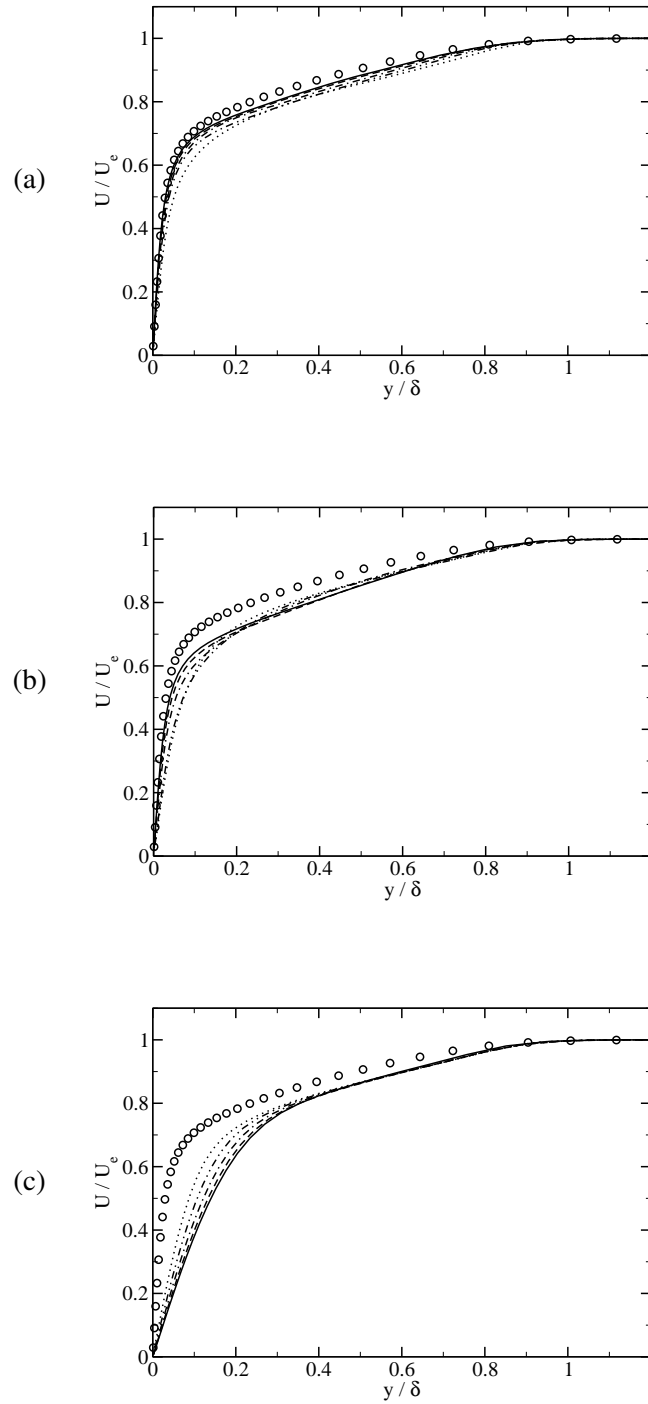


Figure 8.29: Hybrid RANS-LES simulation of a zero pressure gradient turbulent boundary layer. Profiles of the mean velocity at various streamwise locations: (a) SEM inlet conditions, (b) Batten's method inlet conditions and (c) random number method inlet conditions. , $x/\delta_0 = 5$; -·-, $x/\delta_0 = 10$; -·-, $x/\delta_0 = 15$; —, $x/\delta_0 = 20$; ○○○, reference LES.

station.

Velocity fluctuations in the near-wall region for the hybrid calculations and the reference LES are compared on Fig. 8.31. In the case of the reference LES, the fluctuations are fully developed from the inlet and no transient is visible. The observation of the fluctuations in the case of the hybrid simulations confirms previous findings: fluctuations generated by the SEM trigger the near-wall cycle of production of turbulence after a shorter distance (about $x/\delta_0 = 8$) downstream of the inlet than Batten's method (about $x/\delta_0 = 20$) and fluctuations prescribed by the random method are dissipated immediately downstream of the inlet.

The features of the flow in the outer layer of the boundary layer can be observed on Fig. 8.32. With Batten's method, the lack of turbulent kinetic energy production in the near-wall region downstream of the inlet and the overly large time scale in the outer layer lead to a large transient downstream of the inlet. The boundary layer grows faster than with the other methods when the SEM is used to generate the inflow data, which is consistent with the previous analysis of the evolution of the momentum thickness on Fig. 8.28. Once again no turbulent fluctuations can be observed when the random method is used.

8.5 Duct Flow Results

8.5.1 Presentation of the case

Turbulent flow along a streamwise corner occur in many practical engineering applications such as flows in turbomachinery and heat exchangers, or flows in rivers. These flows are characterized by the existence of a secondary mean flow created by the turbulent motion (Huser and Biringen, 1993). Although this secondary flow is only 2 – 3% of the mean streamwise velocity, it has a significant impact on the wall shear stress distribution and heat transfer rates at the walls.

In the present section, we investigate the ability of the SEM to generate inlet conditions for turbulent flow along a streamwise corner. The turbulent flow through a square duct is simulated because of its simple geometry. The Reynolds number based on the bulk velocity U_b and the duct width D is 10,513. This corresponds approximately to a friction Reynolds number of $Re_\tau = u_\tau D / \nu = 600$. Data extracted from the DNS of Huser and Biringen (1993) performed at the same Reynolds number will be used to validate the present LES results.

Four simulations are performed: a reference LES (domain size: $2\pi D \times D \times D$) using periodic boundary conditions in the streamwise direction and three hybrid RANS-LES simulations. The LES domain of the hybrid calculations starts at $x = 0$ and has dimensions $5\pi D \times D \times D$ to allow for realistic fluctuations to develop downstream of the inlet. The RANS equations are solved in a domain of dimensions

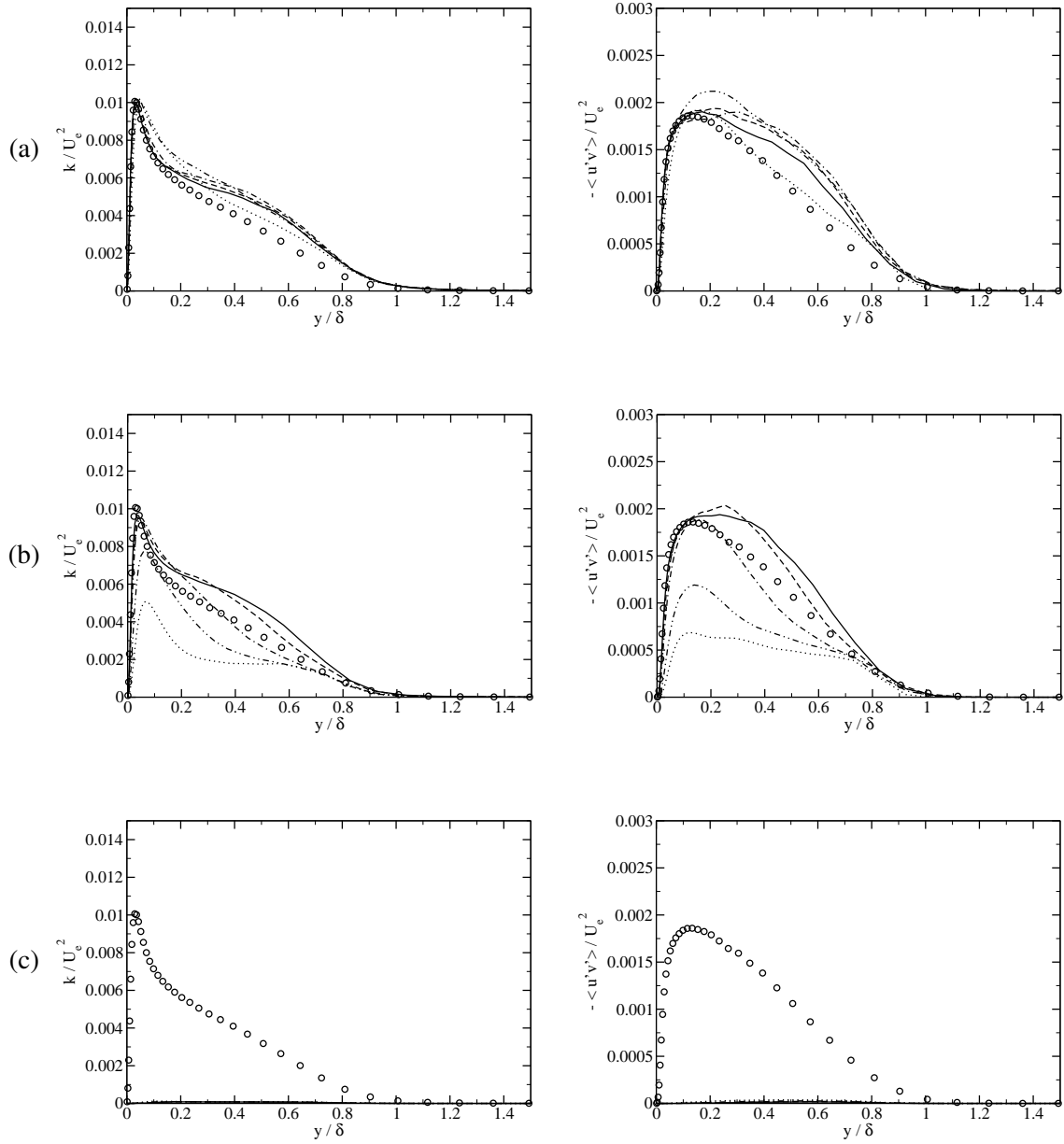


Figure 8.30: Hybrid RANS-LES simulation of a zero pressure gradient turbulent boundary layer. Profiles of turbulent kinetic energy (left) and Reynolds shear stress (right) at various streamwise locations: (a) SEM inlet conditions, (b) Batten's method inlet conditions and (c) random number method inlet conditions. Same legend as in Fig. 8.29.

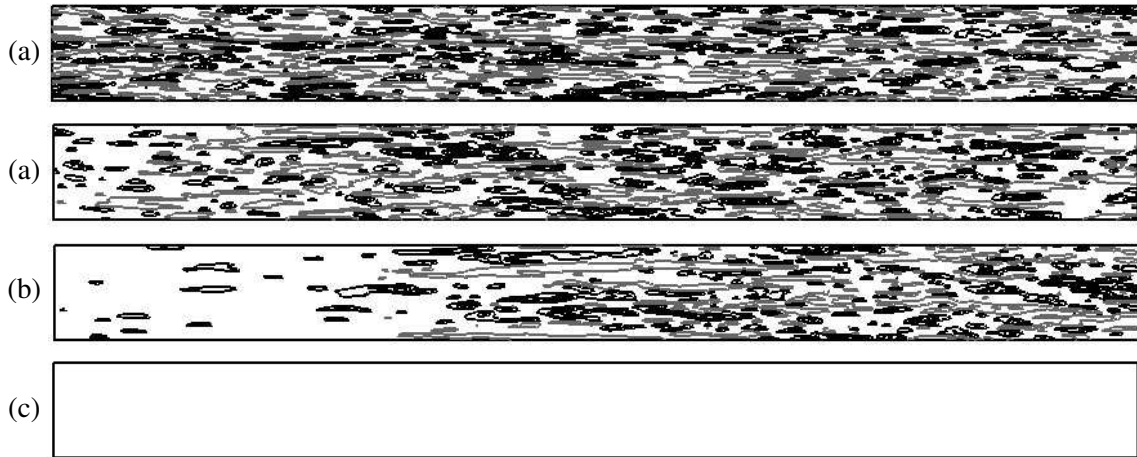


Figure 8.31: Hybrid RANS-LES simulation of a zero pressure gradient turbulent boundary layer at $Re_\theta = 900$. Contours of the instantaneous streamwise velocity fluctuations u^+ at $y^+ = 5$: (a) SEM inlet conditions, (b) Batten et al. (2004) inlet conditions and (c) random method inlet conditions. Contour lines are evenly spaced at $\pm 2, \pm 3, \pm 4, \pm 5$ and ± 6 . Grey lines indicate negative value contours.

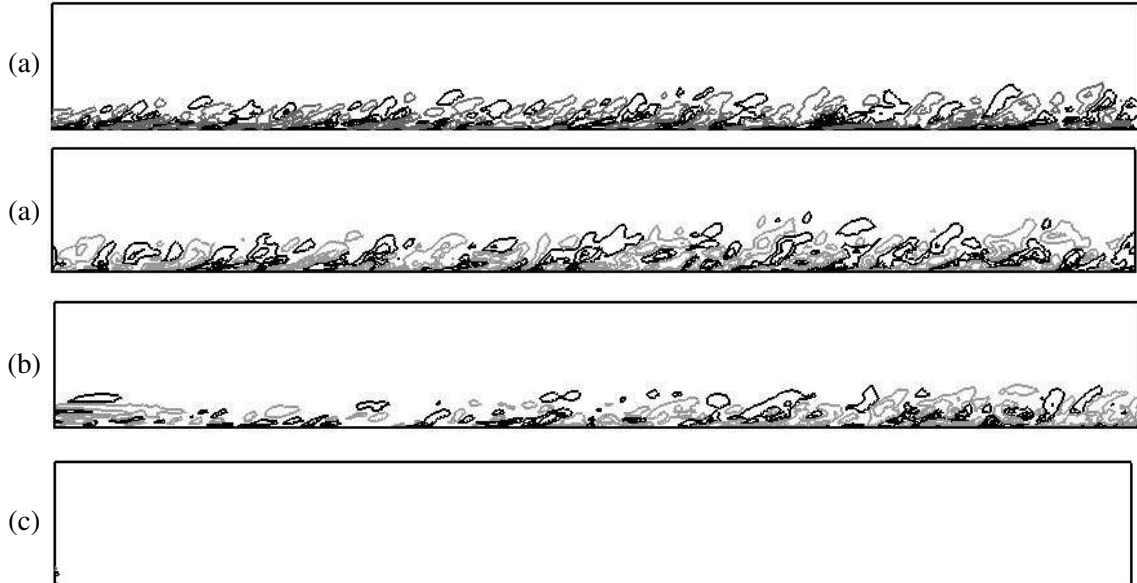


Figure 8.32: Hybrid RANS-LES simulation of a zero pressure gradient turbulent boundary layer at $Re_\theta = 900$. Contours of spanwise velocity fluctuations w^+ on a plane of constant z : (a) SEM inlet conditions, (c) Batten et al. (2004) inlet conditions and (d) random method inlet conditions. Contour lines are evenly spaced at $\pm 0.5, \pm 1.5, \pm 2.5, \pm 3.5$ and ± 4.5 . Grey lines indicate negative value contours.

$0.1D \times D \times D$ upstream of the LES domain.

The LES mesh of the hybrid calculations has $360 \times 72 \times 72$ cells in the x , y and z directions, respectively. The grid spacing is homogeneous in the streamwise direction ($\Delta x^+ \approx 26$), and decreases in the two transverse directions at the walls ($\Delta y_{\max}^+ \approx 15$ and $\Delta y_{\min}^+ \approx 1.7$). The same grid refinement is used for the reference LES mesh. Given the shorter streamwise dimension of the reference LES domain, the mesh thus only requires 144 cells in the streamwise direction. In the case of the RANS simulation, only one cell is used in the streamwise direction. For all simulations, the time step Δt was adjusted so that the maximum CFL number remains lower than one.

A no-slip boundary condition is applied at the four walls of the ducts for all simulations. In the case of the reference LES and RANS simulations, periodic boundary conditions are applied in the streamwise direction. In the case of the hybrid calculations, different methods of generation of inflow data for LES are used to prescribe the inlet conditions at the inlet plane of the LES domain, and are compared in the following section. The required input statistics are extracted from the upstream RANS. At the exit plane of the LES domain, the standard outlet boundary condition implemented in *Code_Saturne* (see page 97 in Chapter 5) is used.

The Smagorinsky model (with $C_S = 0.065$) and Van-Driest damping at the wall is used in the LES region, whereas the SST model of Menter (1994) is used in the RANS region.

Once steady state is reached, the statistics are averaged over a time period $T = 60D/u_\tau$ (about 120 flow through time of the reference LES) and then spatially averaged over the eight symmetries of a cross-section.

8.5.2 Results and discussion

Reference LES and SST results

In this section, we analyse the results of the fully developed LES and SST simulations. Fig. 8.33 displays the mean streamwise velocity distribution and transverse velocity vectors for the present LES and SST simulations, and the reference DNS of Huser and Biringen (1993). Two corner vortices are clearly visible in the present LES and in the reference DNS. On the contrary, the SST solution, as expected, does not exhibit any secondary motion. All turbulence models based on the isotropy of Reynolds stresses are unable to generate secondary flows in non-circular ducts. In order to model accurately secondary flows with RANS models, non-linear eddy viscosity or Reynolds stress models have to be used (Demuren and Rodi, 1984). A noticeable difference in the secondary motion topology between the reference DNS and the LES is that the vortex centres are slightly further from the wall in the LES ($z/D \approx 0.3$, $y/D \approx 0.11$)

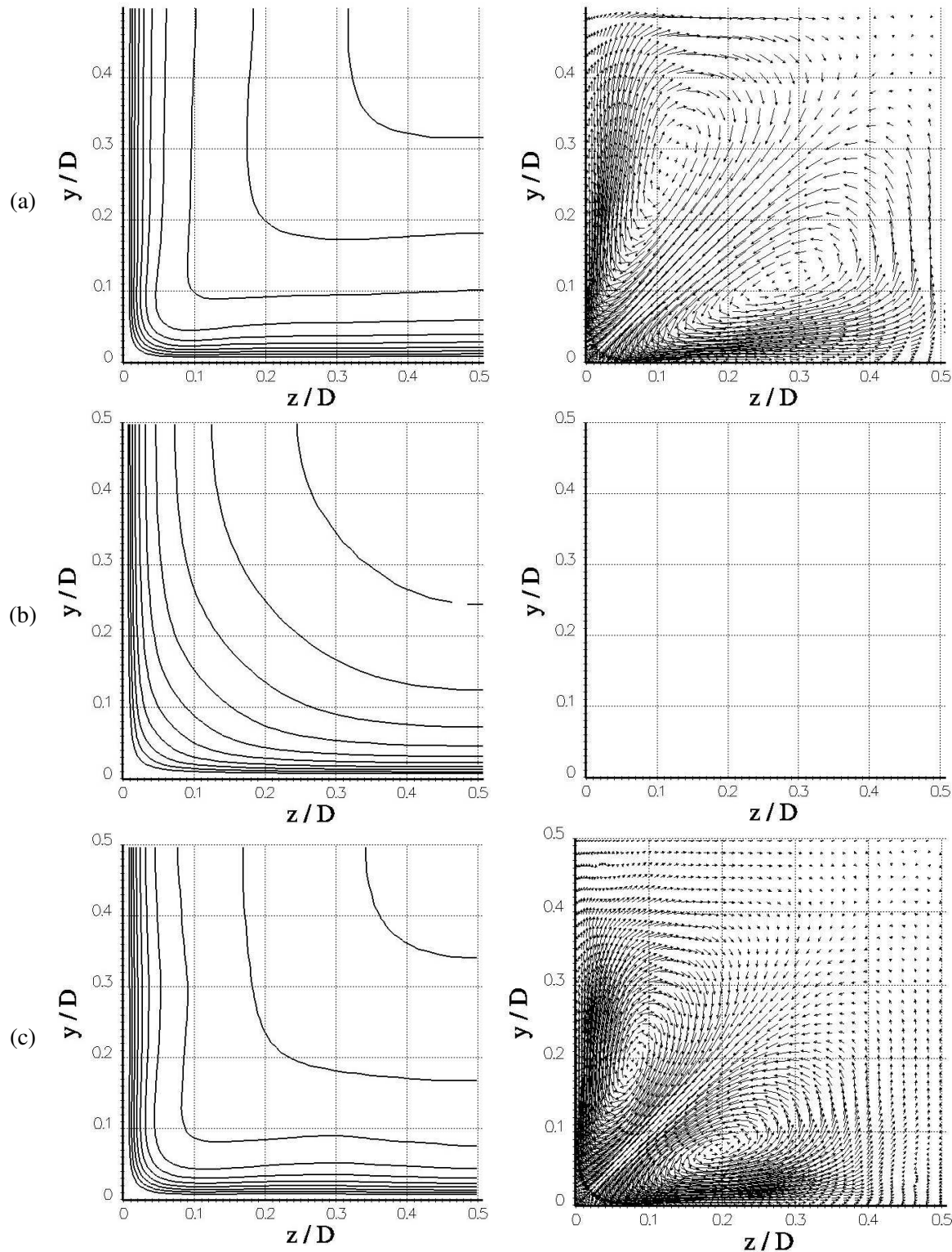


Figure 8.33: Comparison of mean streamwise velocity contours (left) and transverse velocity vectors (right) between (a) the LES, (b) the SST, and (c) the reference DNS data of Huser and Biringen (1993). Contours lines are evenly space between 0.3, 0.4, ..., 1.2.

Run	$Re = U_b D / \nu$	U_b / u_τ	U_c / U_b	V_{\max} / U_b
DNS	10,320 (-)	17.2 (-)	1.23 (-)	1.99% (-)
Ref. LES	10,518 (+1.9%)	16.99 (-1.2%)	1.24 (-1.9%)	2.03% (+2.0%)
Ref. SST	10,518 (+1.9%)	17.52 (+1.9%)	1.26 (+2.4%)	0.0% (-100%)

Table 8.2: Mean flow properties obtained from LES computations of the periodic duct flow.

than in the DNS data ($z/D \approx 0.2$, $y/D \approx 0.08$). In the LES, 72 cells were used in the y and z directions compared to 100 in the reference DNS grid. The difference in the topology of the secondary motion between the present LES and the DNS of Huser and Biringen (1993) is thus likely to be suppressed by refining the LES grid in the two transverse directions. The effect of the secondary motion on the mean streamwise velocity distribution is to convect momentum from the central region of the duct to the walls along the corner bisectors, which explains the curvature of the U isocontours towards the corner in the LES and DNS. This feature of the streamwise velocity distribution is not reproduced by the SST solution (since there is no secondary motion). Another effect of the secondary motion is to convect momentum from the corners to the centre along the walls. Due to the different positions of the secondary vortices in the LES and in the reference DNS, the streamwise velocity distribution is different in the centre of the duct. A noticeable difference is that the LES exhibits a local minimum of U at the wall bisector (U contours bent towards the duct centre) whereas the reference DNS exhibits a local maximum of U (U contours bent towards the wall).

The main properties of the mean flow are summarized on Table 8.2. The agreement between the LES and the DNS data of Huser and Biringen (1993) is excellent: all the errors (especially the error in the intensity of the secondary motion) do not exceed 2%. In the following section, the LES will thus be used as a reference simulation to asses the development of the turbulence in the LES region of the hybrid simulations.

Hybrid RANS-LES results

The streamwise development of the coefficient of friction at the wall averaged along a x cross-section,

$$\overline{C_f}(x) = \frac{1}{4D} \int_{\Gamma} C_f(x, l) dl$$

is shown in Fig. 8.34. As a benchmark, the value of $\overline{C_f}$ obtained in the reference periodic LES is also represented. Similarly to other wall flows studied earlier, the random method exhibits very poor results. The coefficient of friction decreases indicating that the mean flow profile becomes laminar. Results using Batten's method are also very poor: the coefficient of friction decays significantly and never recovers fully

developed values as was the case in previous studies on channel and boundary layer flows. As explained in Section 8.3, Batten's method destroys spatial velocity correlations in the direction of non-homogeneity of the flow. In the present case, the upstream k and ω profiles extracted from the SST solution and transmitted to Batten's method are non-homogeneous in the two transverse directions. Consequently Batten's method does not generate any two-point velocity correlations in the inlet plane. The better results obtained than when using the random method can be explained by the better time correlation of the inflow data generated using Batten's method. The results using the SEM are again superior to results obtained using the random method and Batten's method. The $\overline{C_f}$ decays downstream of the inlet, before recovering its fully developed value after about $4D$. This corresponds to 2,400 wall units, which conforms to previous observations that the SEM manages to sustain fully developed turbulence in the near-wall region of wall bounded flows about 3,000 wall units downstream of the inlet. It can also be observed in Fig. 8.34 that, as in the case of the channel flow, the coefficient of friction is slightly overestimated compared to its fully developed value (about 7%).

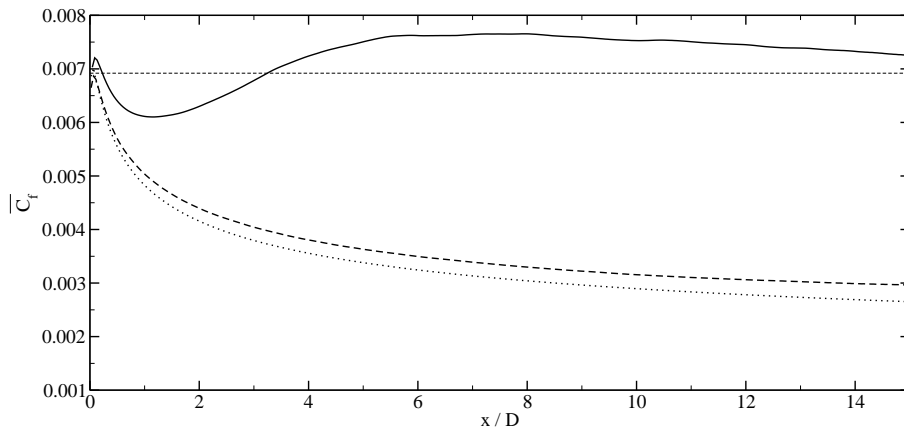


Figure 8.34: Development of the coefficient of friction averaged in the lateral direction along the bottom wall $\overline{C_f}(x)$: , random method; - - - , Batten's method; — , SEM; and - - - , Periodic LES target value.

The development of the secondary motion downstream of the inlet in the LES region is now studied. Fig. 8.35 shows the downstream development of the maximum mean transverse velocity V_{\max} normalized by U_b . Since the upstream SST solution does not exhibit any secondary motion, $V_{\max}/U_b = 0$ at the inlet of the LES domain for all hybrid simulations.

All the simulations exhibit a non-zero maximum mean transverse velocity immediately downstream of the inlet because of the turbulent motion imposed at the inlet. However with the random method and

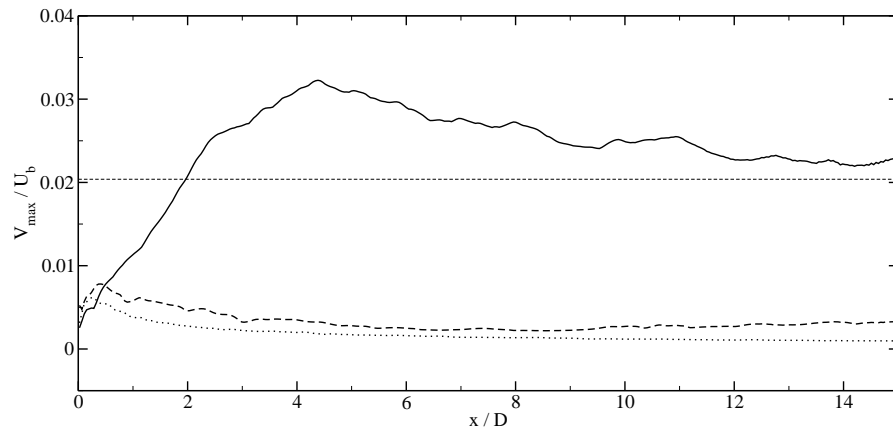


Figure 8.35: Development of the maximum intensity of the secondary motion V_{\max}/U_b . Same legend as in Fig. 8.34.

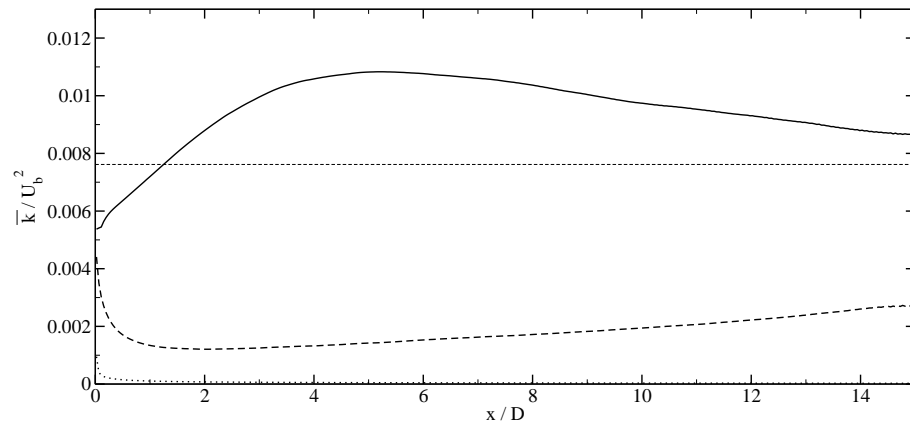


Figure 8.36: Development of the kinetic energy over a duct cross-section $\bar{k}(x)$. Same legend as in Fig. 8.34.

Batten's method, the intensity of the secondary motion is strongly underestimated at the inlet and slowly decreases downstream. In the case where the SEM is used, the secondary motion intensifies downstream of the inlet to exceed of approximately 50% the intensity of the secondary motion in fully developed turbulence at $x/D = 4$, before slowly recovering its fully developed value further downstream. The mean secondary motion is created by the non-zero turbulent fluctuations near the duct corners. In order to understand the origin of the overestimation of the intensity of the secondary motion, the development of the turbulent kinetic energy averaged on a duct cross-section \bar{k} is shown on Fig. 8.36. The turbulent kinetic energy exhibits the same behavior as the coefficient of friction and the intensity of the secondary motion: it increases downstream of the inlet down to about $x/D = 5$ where it is overestimated by almost 40%, before slowly recovering towards fully developed values. As in the case of the channel flow, this overprediction of the turbulent fluctuations can be shown to be restricted to the core of the duct, and it can be reduced by using a more accurate inlet profile and reducing the length and time scale of the synthetic fluctuations in the core of the channel.

The topology of the mean flow is now studied at two different streamwise locations. At $x/D = 2$, the simulation using the SEM exhibits two mean streamwise counter-rotating vortices in the corner of the duct, as shown in Fig. 8.37 (a). Although these vortices are closer to the corner than in fully developed turbulence (see Fig. 8.37 (d)), their topology and intensity is very similar. Due to the existence of this secondary motion, momentum is convected from the central region to the walls along the corner bisectors. This is illustrated on Fig. 8.38 which shows isocontours of U at the same location ($x/D = 2$). Further downstream at $x/D = 15$, the simulation using the random method still does not exhibit any secondary motion (see Fig. 8.39 (c)). With Batten's method, two very weak streamwise corner vortices can be observed, but their weak intensity does not alter the mean streamwise velocity distribution in the correct manner as shown on Fig. 8.40 (b). On the contrary, the simulation using the SEM exhibits two strong streamwise vortices whose centre location and topology are in very good agreement with those from the reference fully developed LES. Due to the persistent action of the secondary motion, the mean streamwise velocity distribution (see Fig. 8.40 (a)) is in excellent agreement with the one from the reference LES, and thus the mean flow can be considered as fully developed.

Finally, streamwise velocity fluctuations on the plane $y^+ = 5$ are shown on Fig. 8.41. As expected, the fluctuations prescribed at the inlet are immediately dissipated when the random method or the method of Batten et al. (2004) are used. On the contrary, the simulation using the SEM exhibits realistic near-wall velocity fluctuations immediately downstream of the inlet.

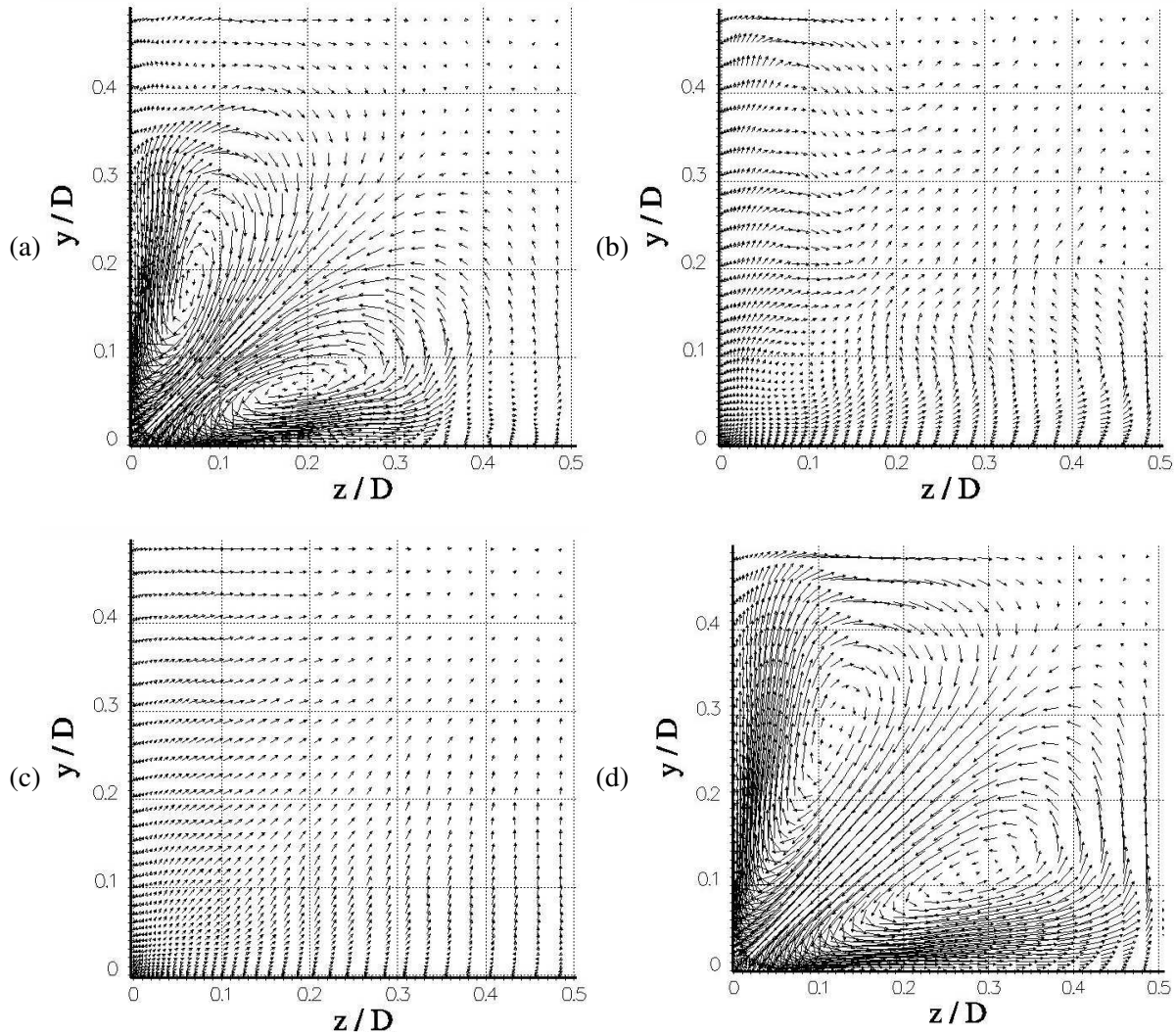


Figure 8.37: Transverse velocity vectors at $x/D = 2$: Hybrid simulations with (a) SEM, (b) Batten's method, (c) the random method and (d) reference periodic LES.

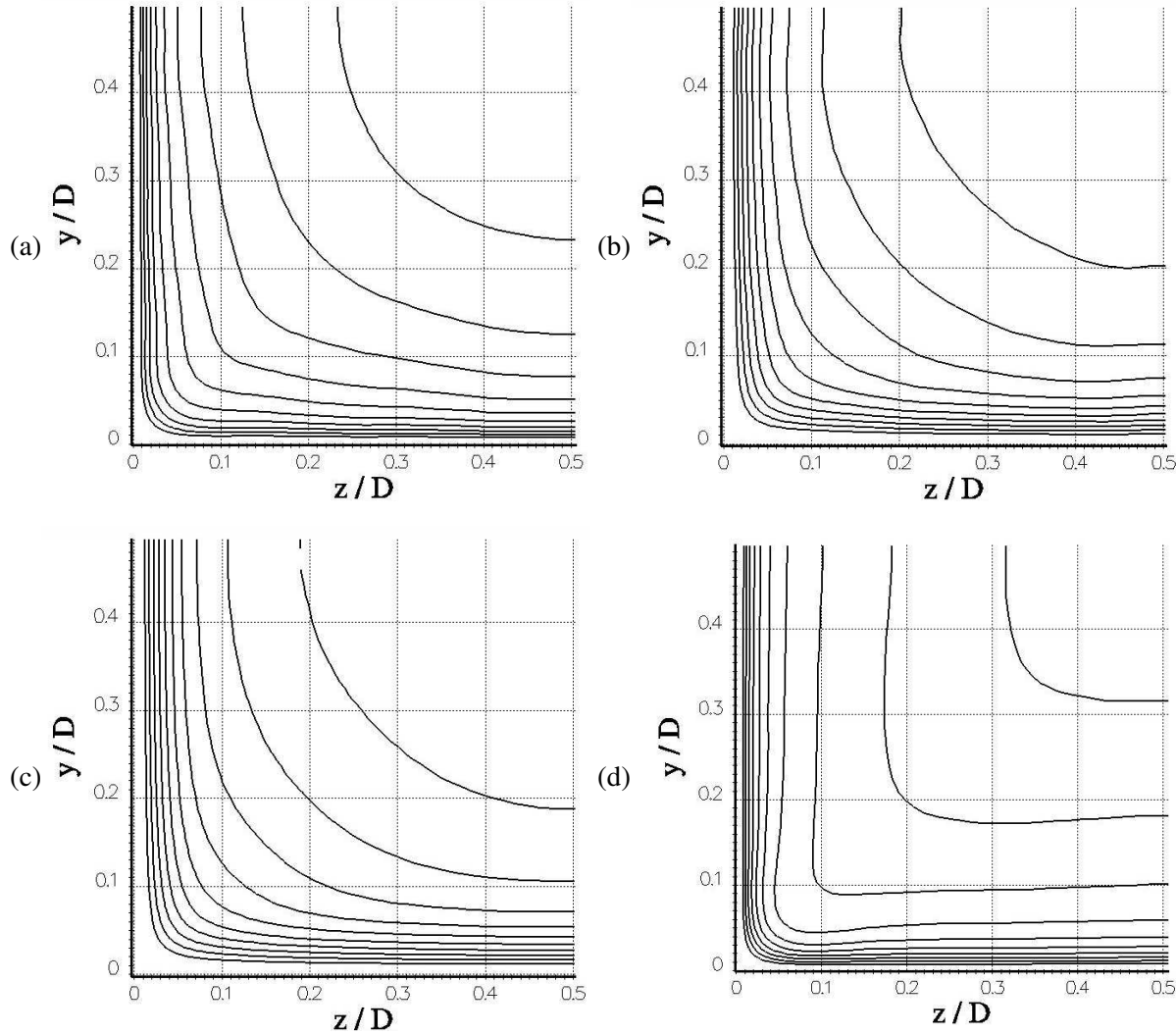


Figure 8.38: Mean streamwise velocity U distribution normalized by U_b at $x/D = 2$: Hybrid simulations with (a) SEM, (b) Batten's method, (c) the random method and (d) reference periodic LES. Contours lines are evenly space between 0.3, 0.4, ..., 1.2.

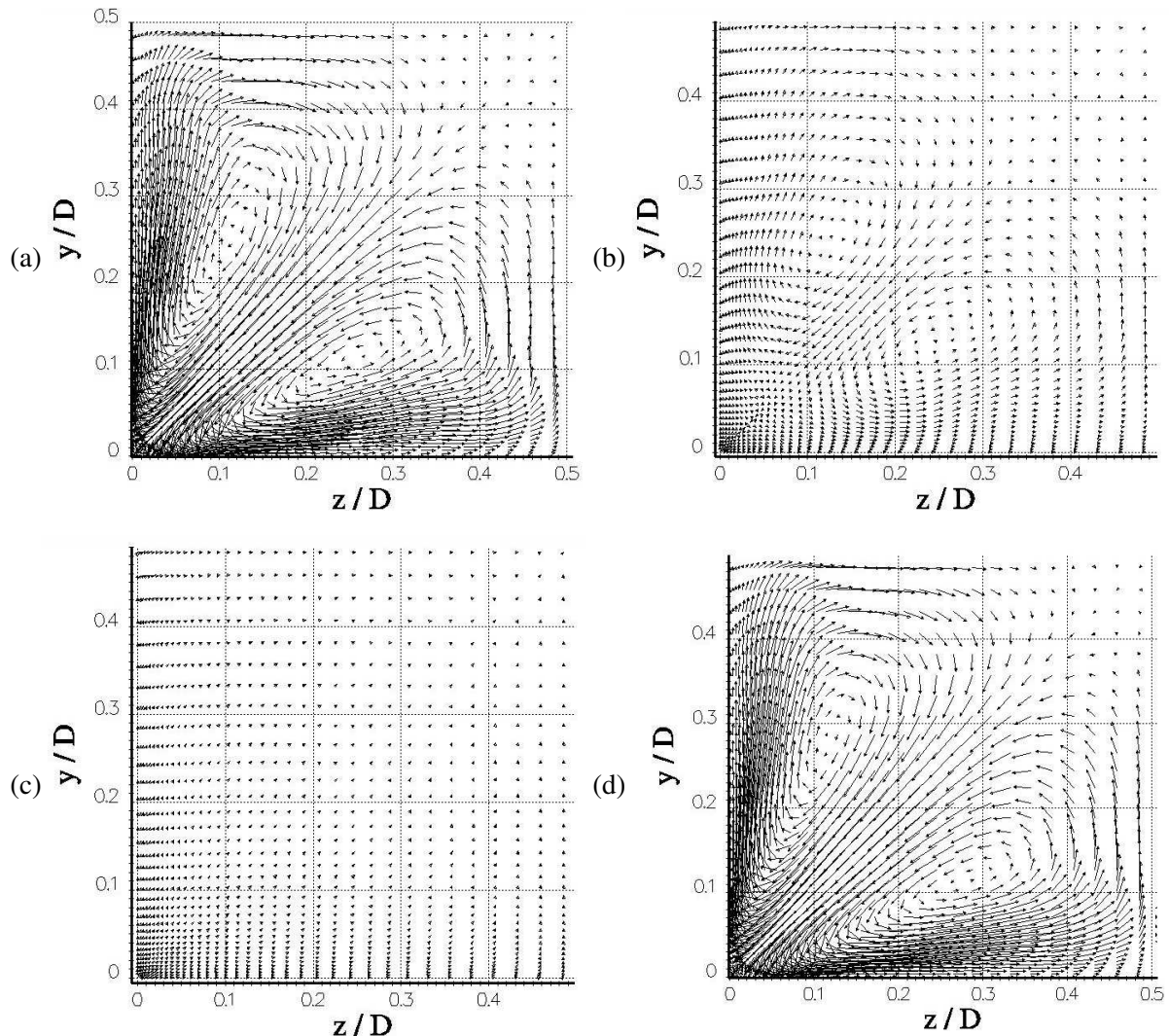


Figure 8.39: Transverse velocity vectors at $x/D = 15$: Hybrid simulations with (a) SEM, (b) Batten's method, (c) the random method and (d) reference periodic LES.

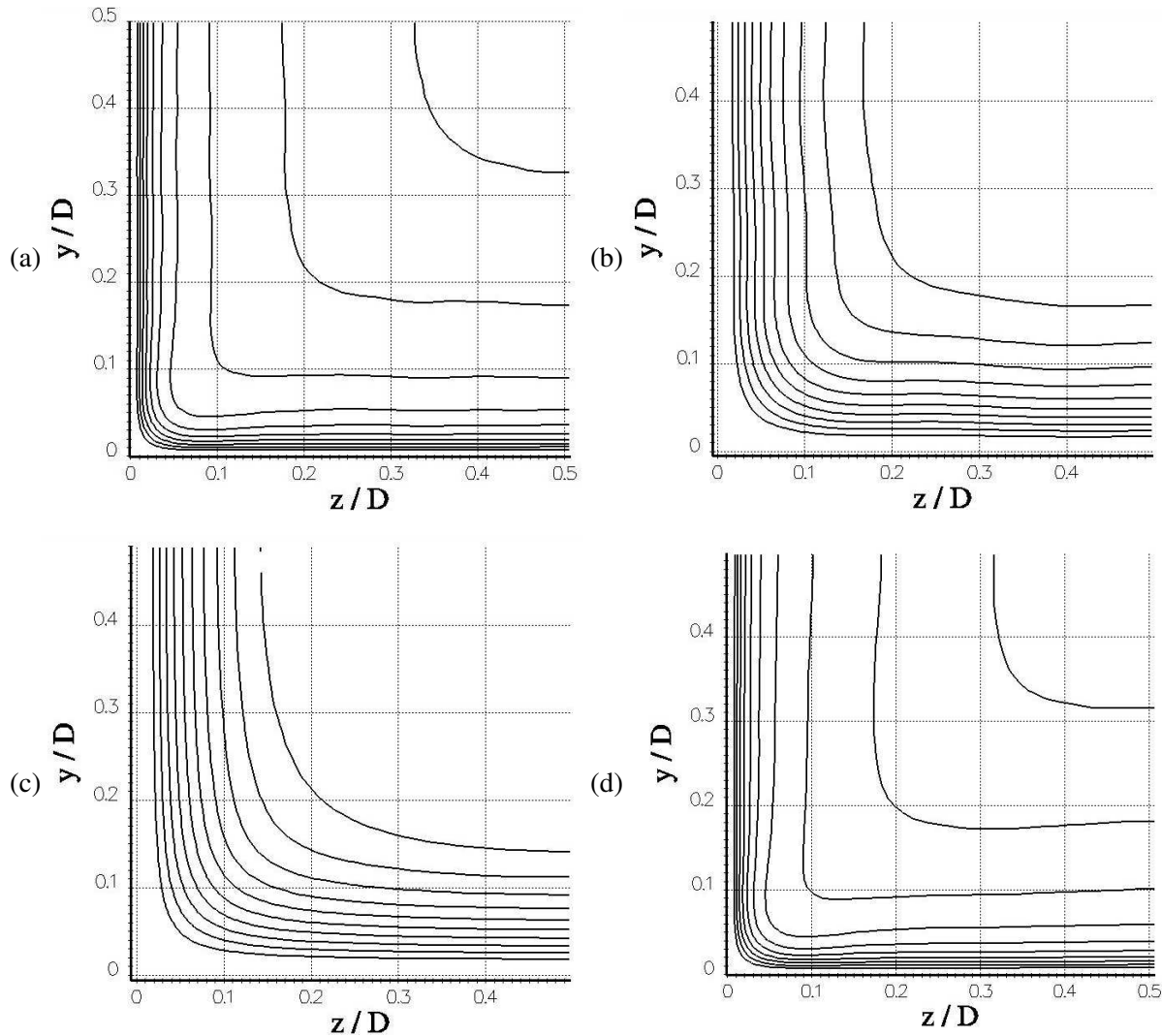


Figure 8.40: Mean streamwise velocity U distribution normalized by U_b at $x/D = 15$: Hybrid simulations with (a) SEM, (b) Batten's method, (c) the random method and (d) reference periodic LES. Contours lines are evenly space between 0.3, 0.4, ..., 1.2.

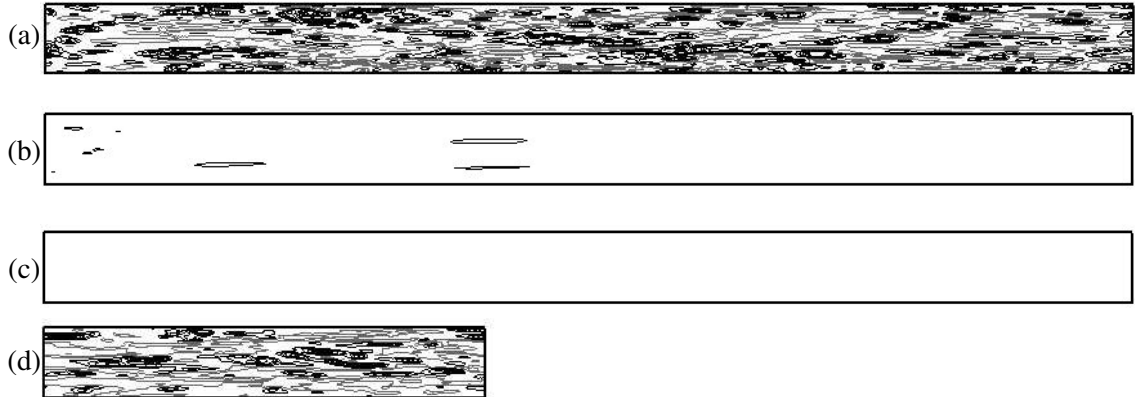


Figure 8.41: Streamwise velocity fluctuations at $y^+ = 4$: Hybrid simulations with (a) SEM, (b) Batten's method, (c) the random method and (d) reference periodic LES. Contour lines are evenly spaced at ± 1 , ± 2 , ± 3 , ± 4 and ± 5 . Grey lines indicate negative value contours.

8.6 Concluding Remarks

The SEM has been used to generate inlet conditions for LES of simple wall-bounded flows using only the reduced information available from a SST simulation. Building up on the experience gained from the sensitivity analysis performed in Chapter 7, the SEM input parameters have been set to minimize user intervention and produce realistic inflow data for LES from simple RANS statistics.

The present method has been used to generate interface conditions between an upstream SST simulation and a downstream LES in the case of a turbulent plane channel flow, a zero-pressure gradient flat plate turbulent boundary layer and a square duct flow. The three tests cases confirmed that when the SEM is used to generate inlet conditions, first and second order statistics are in good agreement with fully developed turbulence statistics after a distance of about 3,000 wall units.

The SEM was also compared to other methods of generation of inflow data for LES. As expected, the random method using uncorrelated random numbers leads to a rapid laminarization of the flow. The method of Batten et al. (2004) was shown to be inadequate to generate turbulence in complex non-homogeneous situations encountered in practical engineering flows. Even in the simple case of the channel flow, Batten's method yields fully developed turbulence after a transition region about three times longer than when the SEM is used.

The present results have been derived in the case of simple wall-bounded flows where the near-wall turbulence is fully developed. In the following chapter, we perform similar hybrid RANS-LES simulations in more complex flows involving recirculation.

Chapter 9

Interface Conditions for RANS-to-LES Coupling of Wall Flows with Recirculation

9.1 Introduction

In this chapter, the effect of the upstream boundary conditions on the LES of turbulent flows with recirculation is investigated. These flows occur in many practical engineering applications such as diffusers (Kaltenbach et al., 1999), or combustion chambers (Akselvoll and Moin, 1996), for internal flows and trailing edge flows (Wang and Moin, 2000), or flows around bluff bodies (Brunn and Nitsche, 2006). In all these situations the upstream boundary layer separates from the solid surface, before it reattaches further downstream forming a recirculation bubble.

Hybrid RANS-LES calculations of two types of recirculating flows are performed (i.e. the flow over a backward facing step and over an airfoil trailing edge). In both flows, the LES region only encloses the region of interest where separation occurs. The effects on separation of (a) the position of the RANS-to-LES interface and of (b) the method of generation of LES inflow data are investigated.

The first case studied in this chapter is the turbulent flow over a backward facing step (Section 9.2). In this case the location of the separation point is fixed by the flow geometry. The simulation was conducted at a relatively low Reynolds number Re_h of 5,100 based on the step height h and inlet free-stream velocity U_0 . The Reynolds number Re_θ - based on the momentum thickness θ and inlet free-stream velocity - is 670. The present results will be compared to the DNS data of Le et al. (1997) and the measurements of Jovic and Driver (1994) which were both obtained under the same flow conditions.

The second flow simulated is the turbulent flow over an airfoil trailing edge (Section 9.3). In this case the location of the separation point depends on the upstream flow history, and on pressure gradient

and/or surface curvature effects. The Reynolds number is 1.017×10^5 based on the airfoil thickness h and free-stream velocity. The Reynolds number Re_θ of the boundary layer upstream of the recirculation region is approximately 3,000. The present simulation will be compared to reference data taken from the experiment of Blake (1975) and from the finely resolved LES of Wang and Moin (2000).

Finally, Section 9.4 summarizes the conclusions drawn from the simulations performed in this chapter.

9.2 Flow Over a Backward Facing Step

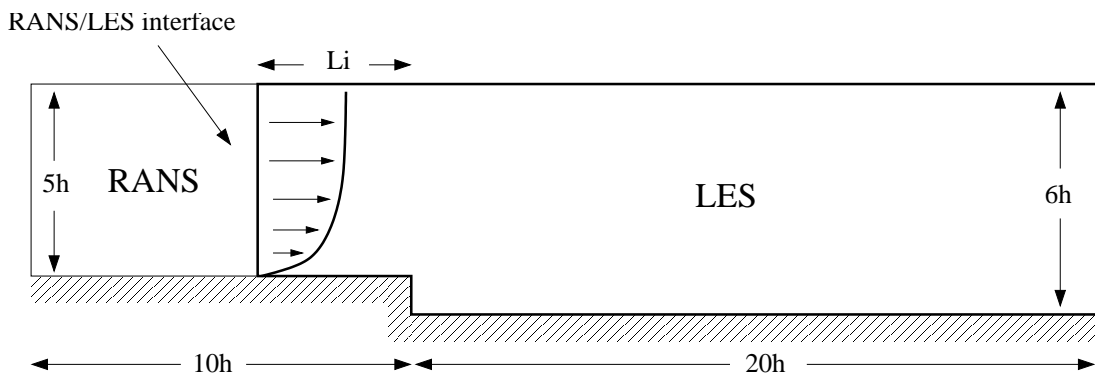


Figure 9.1: Sketch of the hybrid RANS-LES simulations of the backward facing-step flow configuration.

9.2.1 Presentation of the case

Flow configuration

Fig. 9.1 shows a two-dimensional sketch of the computational domain. The step is located at $x/h = 0$. The inlet section upstream of the step has a streamwise length of $10h$, a spanwise width of $4h$ and a vertical height of $5h$. The expansion ratio (which is defined as the ratio of the domain height downstream of the step to that upstream) is 1.2. The computational domain extends $20h$ downstream of the step.

As already mentioned in this chapter's introduction, all simulations were conducted at a Reynolds number Re_h of 5,100 based on the step height h and inlet free-stream velocity U_0 . The boundary layer at the inlet of the RANS computational domain is a zero-pressure gradient turbulent boundary layer at $Re_\theta = 670$. The boundary layer thickness is $\delta = 1.2h$. The present simulations match the previous DNS of Le et al. (1997) in expansion ratio, Reynolds number Re_θ of the boundary layer at the inlet and Reynolds number Re_h .

Computational methodology

The RANS domain extends over the whole computational domain between $x/h = -10$ and $x/h = 20$. In order to reduce the computational cost of the simulation, the LES domain is embedded in the RANS domain and only begins at $x/h = -L_i$. Different LES domains with different length of the inlet section will thus be used.

The Smagorinsky model (with $C_S = 0.065$) and Van-Driest damping at the wall is used in the LES region; the SST model of Menter (1994) is used in the RANS region.

The mean inflow velocity profile imposed at the RANS inlet is obtained from the DNS of Spalart (1988) of a flat-plate turbulent boundary layer at $Re_\theta = 670$. The turbulent variables k and ω required by the SST at the inlet are extracted from the DNS data. For all simulations performed, a no-slip boundary conditions is applied at the wall, and the standard outlet boundary condition implemented in *Code_Saturne* (see page 97 in Chapter 5) is applied at the exit plane. At the top surface of the domain, we impose a symmetry condition (see page 98 in Chapter 5). At the inlet plane of the LES domain, data are extracted from the RANS solution, interpolated onto the LES grid, and used for the generation of synthetic turbulence.

The same grid refinement in the streamwise and wall-normal directions are used for the full domain RANS and LES. A total of 300 cells are used in the streamwise direction, 100 of which are positioned before the step. A non-uniform mesh distribution is used in the streamwise direction with fine grid spacings near the step. The grid spacing in wall units is $\Delta x^+ \approx 40$ near the inlet and the outlet and $\Delta x^+ \approx 13$ near the step. In the wall-normal direction, a non-uniform mesh distribution is used with finer grid spacing near the wall upstream and downstream of the step. A total of 112 cells are used, of which 48 are placed below $y < h$. The grid spacing in wall units is $\Delta y^+ \approx 1.6$ along the horizontal walls upstream and downstream of the step, $\Delta y_{\max}^+ \approx 10$ within the step and $\Delta y_{\max}^+ \approx 300$ at the top of the computational domain. The grid spacing is uniform in the spanwise direction for all LES grids. 64 cells are used in the spanwise directions which in terms of grid spacing gives $\Delta z^+ \approx 15$, based on the boundary layer friction velocity of the DNS data at $x/h = -10$. For the RANS simulation, only one cell is used in the spanwise direction. This results in a grid of 28,800 cells for the RANS simulation and 1,843,200 cells for the LES simulation of the full computational domain. For the LES runs using a shorter inlet section upstream of the step, the same grid refinement as in the full domain LES is used. Fig. 9.18 shows the LES computational mesh near the step.

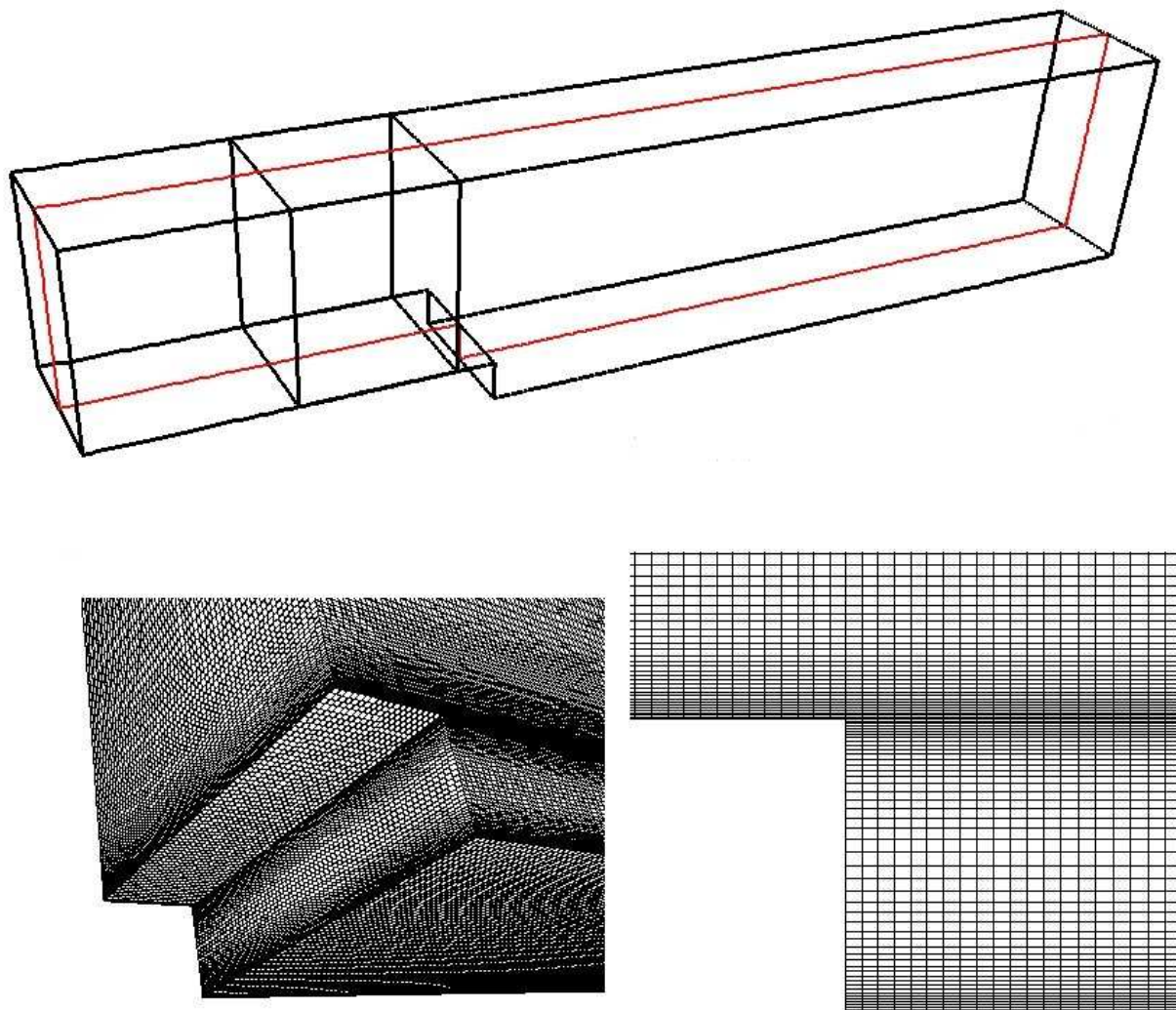


Figure 9.2: RANS (red line) and embedded LES (black line) computational domains used in the hybrid simulations (top), and different close-up views of the shortest LES mesh near the step (bottom).

Run	LES inlet section	Inflow method	Input statistics
S1	1h	Synthetic Eddy Method	RANS
S2	5h	Synthetic Eddy Method	RANS
S3	10h	Synthetic Eddy Method	RANS
B3	10h	Batten et al. (2004)	RANS
R3	10h	Random Method	RANS
P3	10h	Precursor simulation	×

Table 9.1: Parameter settings used in the hybrid RANS/LES computations of the backward facing step. The parameters not listed here are kept constant for all simulations.

Simulations performed

The simulations performed are summarized on Table 9.1. The inflow data in run P3 is generated from a precursor LES of a zero pressure gradient flat plate turbulent boundary layer, using the method of Lund et al. (1998). In order to avoid interpolation in space and in time of the inflow velocities, the precursor LES has the same grid refinement and the same time step as the main simulation. In the precursor LES, time series of inflow velocities are stored on disk at the streamwise location where the thickness of the boundary layer matches the thickness of the boundary layer at the inlet of the hybrid simulations domain ($\delta/h = 1.2$). Since the mean flow profile predicted by the precursor simulation is different from the mean flow profile prescribed at the inlet of the hybrid simulations domain, the inflow data is finally transformed as follows,

$$u_i = U_i^{\text{RANS}} + (u_i^{\text{prec}} - U_i^{\text{prec}}) \quad (9.1)$$

where U_i^{RANS} is the RANS mean velocity, and $u_i^{\text{prec}} - U_i^{\text{prec}}$ is the fluctuating velocity extracted from the precursor LES. Simulation P3 has thus the same mean inlet velocity profile as the reference DNS and the other hybrid simulations but the velocity fluctuations are extracted from the LES of a zero pressure gradient boundary layer.

Run P3 is then used as a comparison point for all other cases using synthetic turbulence and a reduced LES inlet section upstream of the step. First the SEM (run S3), the random method (run R3) and the method of Batten et al. (2004) (run B3) are used to generate synthetic inlet conditions on the large LES domain with an inlet section of 10h upstream of the step. The inlet statistics are extracted from the full domain SST simulation, and the input parameters of the SEM are calculated as described in Section 8.2 of Chapter 8.

The influence of the length of the upstream LES inlet section on the flow downstream of the step is

then investigated. Two hybrid simulations using shorter LES domains with an inlet section of length $5h$ (run S2) and $1h$ (run S3) are also performed. Since the same grid refinement as in the full domain LES is used, the grids have 1,507,328 cells and 1,687,552 cells for S1 and S2, respectively.

9.2.2 Results and discussions

Validation of the reference LES

Run P3 which uses time series of inflow velocities extracted from a precursor LES will be the baseline simulation with which all simulations using synthetic turbulence will be compared. Before analyzing the results of the hybrid simulations, we first validate the results of run P3 by verifying that the main features of the mean flow are correctly predicted,

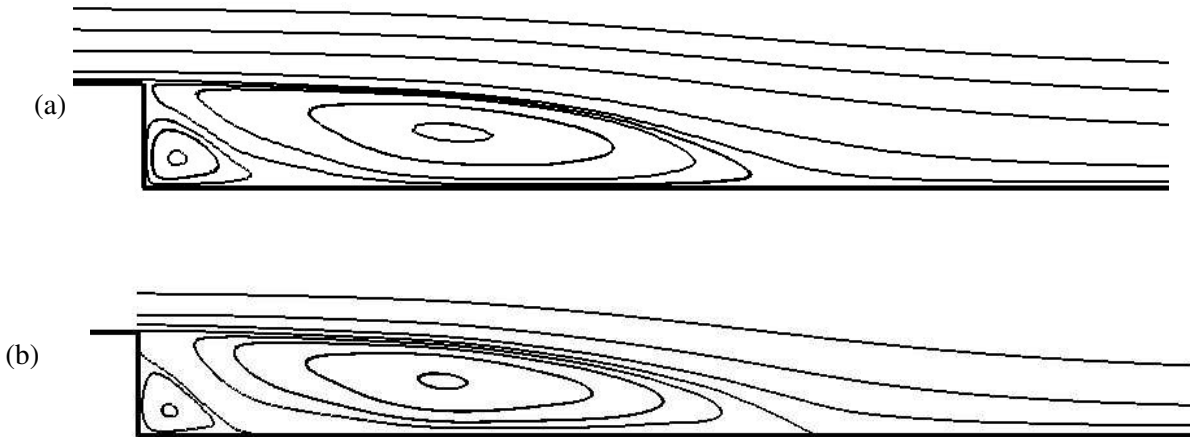


Figure 9.3: Streamlines of the mean flow: (a) reference LES run P3, and (b) DNS of Le et al. (1997).

Fig. 9.3 compares the streamlines of the mean flow for run P3 and the reference DNS of Le et al. (1997). Both simulations exhibit two large recirculation bubbles downstream of the step. The coefficient of friction

$$C_f = \frac{\tau_w}{\frac{1}{2}\rho U_0^2} \quad (9.2)$$

near the step is shown on Fig. 9.4. The agreement between run P3, the DNS data of Le et al. (1997) and the measurements of Jovic and Driver (1994) is excellent over the whole computational domain. The mean reattachment length X_r is calculated on Fig. 9.3 as the location at which the coefficient of friction (or the wall shear stress) is zero. Run P3 predicts a mean recirculation length $X_r = 6.5h$, (less than 4% of variation compared to the DNS data where $X_r = 6.28h$).

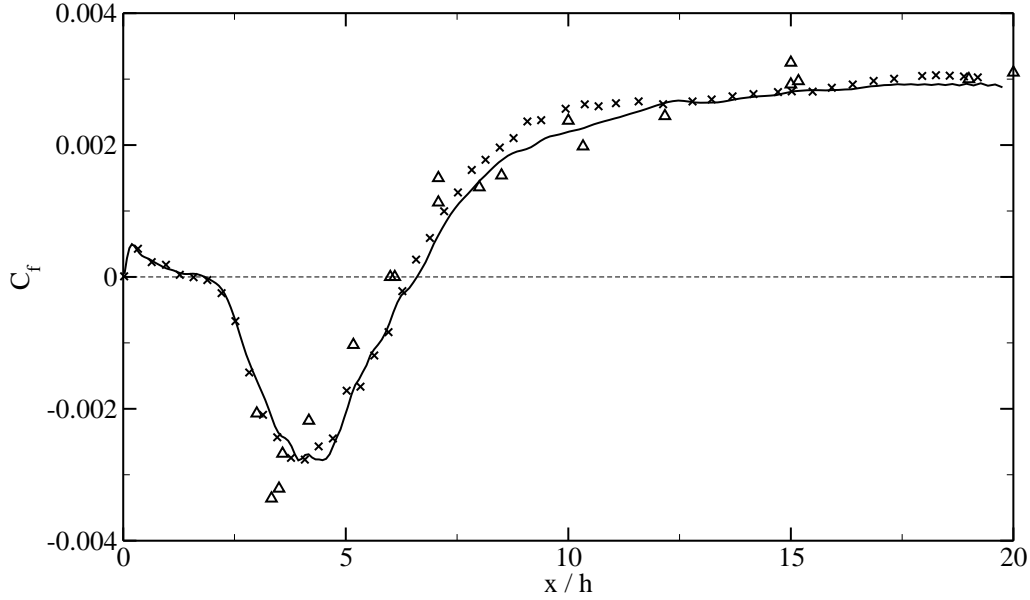


Figure 9.4: Comparison of coefficient of friction C_f between run P3 (—), the DNS of Le et al. (1997) (×), and the experiment of Jovic and Driver (1994) (△).

Comparisons of methods of generation of inflow data

Fig. 9.5 shows the streamlines of the mean flow for runs P3, S3, R3 and B3. Run S3 predicts accurately the position and size of the main and secondary recirculation bubbles. On the contrary, runs R3 and B3 significantly overpredicts the size of the secondary recirculation bubble, and consequently the reattachment length. Comparison of the coefficient of friction downstream of the step, as shown on Fig. 9.6, gives more insight into the quantitative differences between the four simulations. Excellent agreement is obtained between the simulation using the SEM and the reference LES near the step. There is less than 1% variation between the size of the secondary recirculation bubble (calculated as the distance from the step at which $C_f = 0$) in run S3 ($1.79h$) and in run P3 ($1.82h$). The large peak of negative skin friction in the main recirculation bubble is also well reproduced by run S3, and the reattachment length ($X_r = 6.17h$) is only underestimated of 5% compared to the reference LES. On the contrary, results using Batten's method and the random method are poor: the size of the secondary bubble and the reattachment length are underestimated, as is the peak of the negative skin friction in the main recirculation bubble. The size of the secondary bubble is $2.87h$ with Batten's method and $3.20h$ with the random method, corresponding to +63% and +82% error compared to the DNS data, respectively. The reattachment length is $X_r = 7.22h$ with Batten's method (+11% error) and $X_r = 7.28h$ with the random method (+12% error). Further downstream of the reverse flow region ($x > 10h$) the agreement between

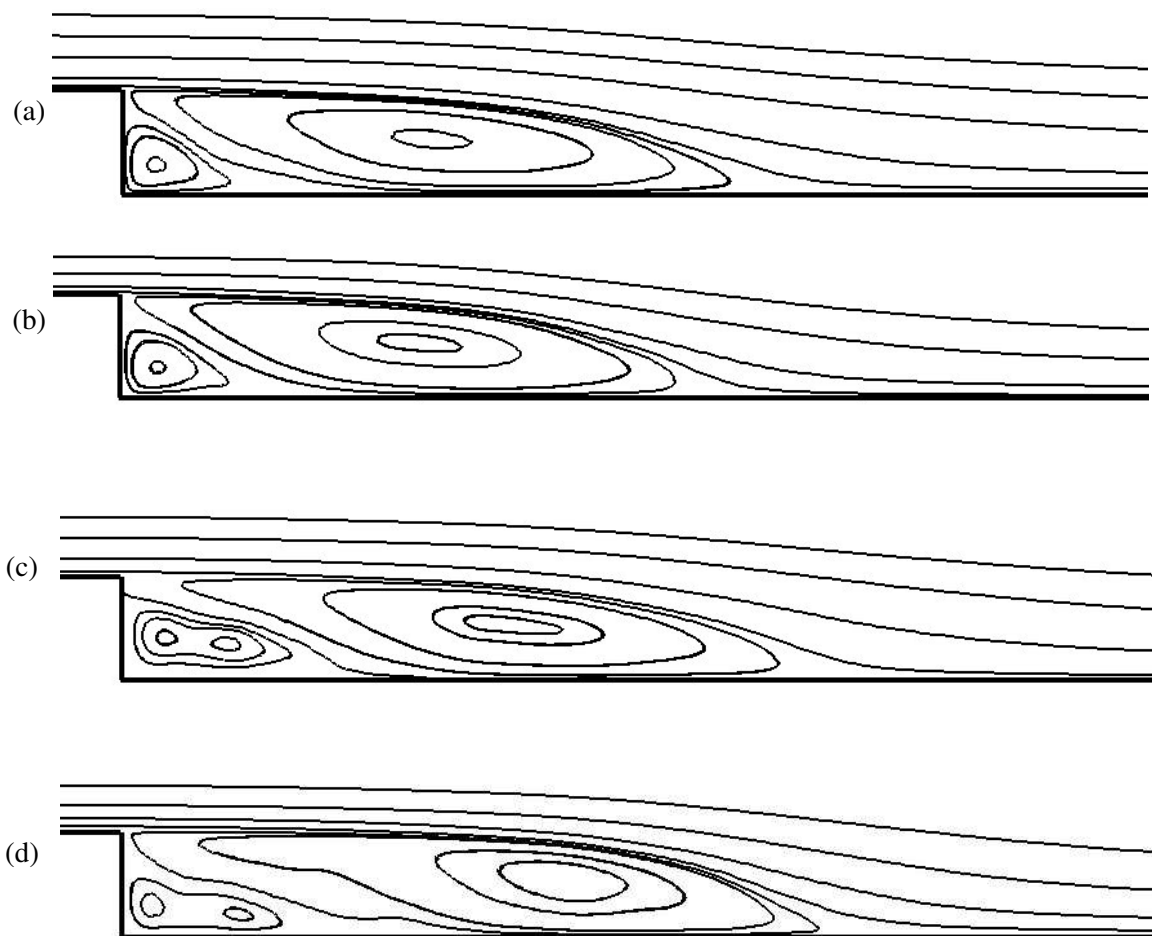


Figure 9.5: Streamlines of the mean flow for different methods of generation of inflow data: (a) precursor simulation (run P3); (b) SEM (run S3); (c) Batten's method (run B3); (d) random method (run R3).

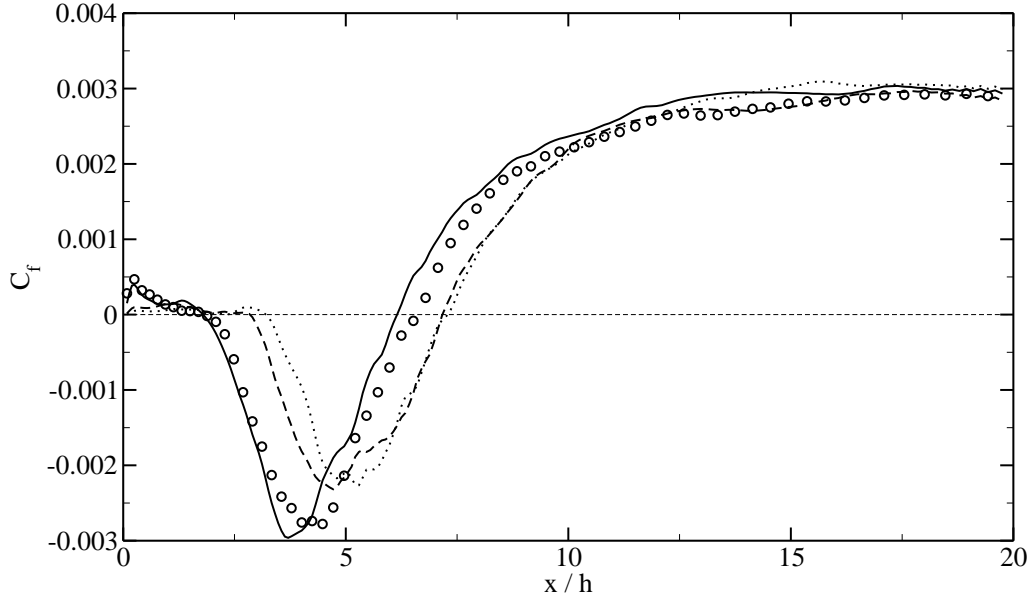


Figure 9.6: Coefficient of friction C_f for different methods of generation of inflow data: —, SEM (run S3); ---, Batten's method (run B3); ·····, random method (run R3); ○○○, precursor simulation (run P3).

the present LES and the DNS data is very good.

Velocity profiles at five representative streamwise locations are shown in Fig. 9.7. Very good agreement between run S3 and the reference LES is obtained at all locations. On the contrary, as expected from the study of the mean flow streamlines, runs R3 and B3 predict a longer reattachment length: at location $x/h = 6$ the flow has almost reattached in run S3, whereas we are still in the main recirculation bubble in run B3 and R3.

The origin of the strong discrepancies observed in the mean flow features between runs S3, R3 and B3 will now be investigated. Fig. 9.8 shows the development of the integrated turbulent kinetic energy profile,

$$\bar{k}(x) = \frac{1}{(y_t - y_w)} \int_{y_w}^{y_t} k(x, y) dy. \quad (9.3)$$

y_t and y_w are the y -coordinates of the upper domain boundary and of the wall, respectively. Run B3 strongly underestimates the turbulent kinetic energy in the boundary layer upstream of the step. As expected from the previous chapter investigations, all the turbulent fluctuations prescribed using the random method have been dissipated immediately downstream of the inlet in run R3. On the contrary, the levels of \bar{k} in run S3 using the SEM are in very good agreement with the reference LES. The present results for the inlet section can be related with the results obtained in the preceding chapter for the boundary

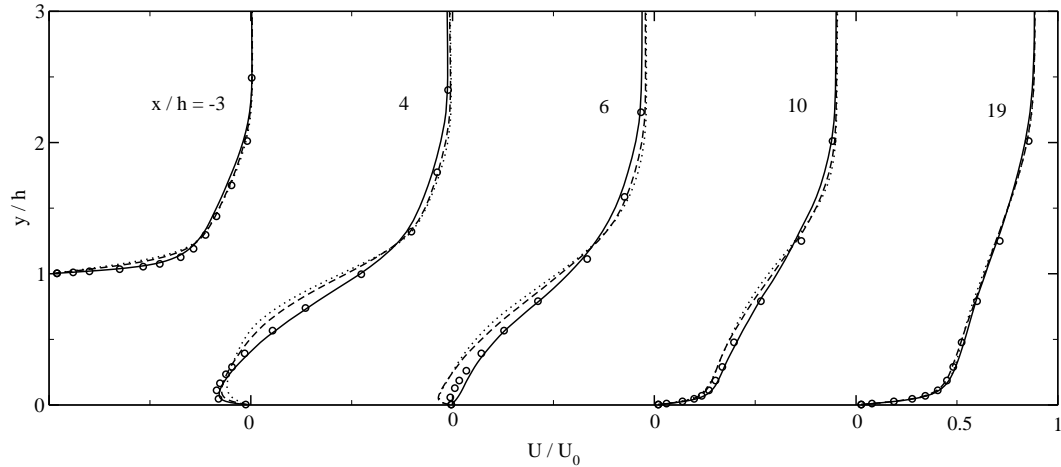


Figure 9.7: Mean streamwise velocity profiles for different methods of generation of inflow data: —, SEM (run S3); - - -, Batten's method (Run B3); , random method (run R3); ○○○, precursor simulation (run P3).

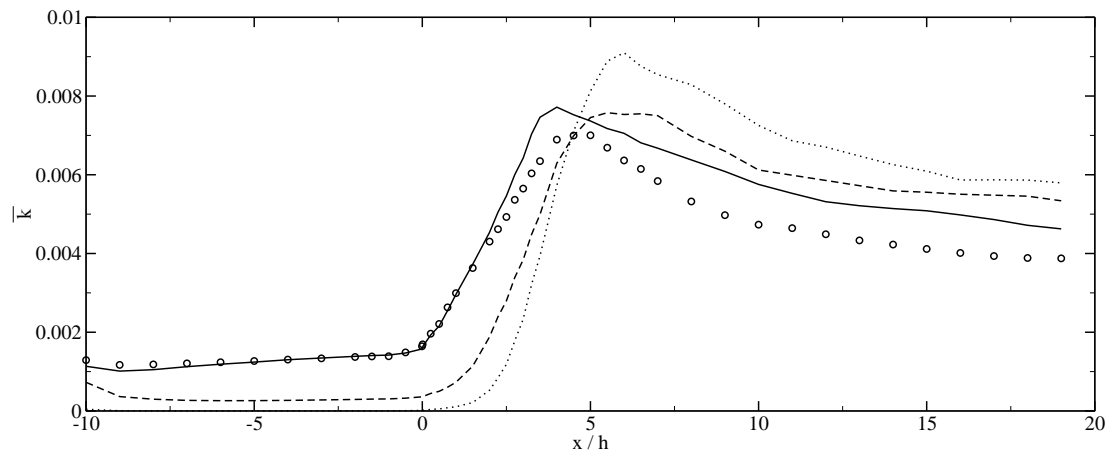


Figure 9.8: Evolution of the integrated turbulent kinetic energy profile \bar{k} in the inlet section boundary layer and downstream of the step: —, SEM (run S3); - - -, Batten's method (Run B3); , random method (run R3); ○○○, precursor simulation (run P3).

layer since the inlet section upstream of the step is essentially a flat plate boundary layer with a very weak pressure gradient. The length of the inlet section is approximately $9\delta_0$ (or 2,400 wall units). At this distance away from the inlet, the turbulent kinetic profiles using the SEM are slightly overestimated but still in very good agreement with the reference data (see Fig. 8.30 (a)) and the near-wall structures are fully developed (see Fig. 8.31 (a)). On the contrary, when Batten's method is used, the coefficient of friction reaches its minimum (see Fig. 8.26), the turbulent kinetic energy profile is largely underestimated (see Fig. 8.30 (b)) and the near-wall streaks have not been yet generated (see Fig. 8.31 (b)).

Fig. 9.8 also shows that the levels of turbulent kinetic energy downstream of the step are strongly influenced by the upstream flow conditions. In run S3 and P3, the upstream boundary layer destabilizes the shear layer immediately downstream of the step and large levels of turbulent kinetic energy are produced. In run B3 and R3, there is a transition region extending down to $1.5h - 2.5h$ downstream of the step where no turbulent kinetic energy is produced. This is not the expected physical behavior of a sudden expansion which is fed by a fully developed turbulent boundary layer. This is illustrated in Fig. 9.9 showing contours of wall-normal velocity fluctuations. In runs S3 and P3, the shear layer is destabilized by the velocity fluctuations in the upstream boundary layer, hence producing turbulent fluctuations immediately downstream of the step. In runs R3 and B3, there is a transition region downstream of the step where the mixing layer is essentially laminar. The presence of a transitional mixing layer decreases the rate of mixing of momentum below the step and hence increases the size of the secondary bubble and of the reattachment length.

Further downstream of the step, significant variations of \bar{k} among the four simulations can be observed on Fig. 9.8. The growth of large scale coherent structures in the laminar shear layer downstream of the step can explain the strong overestimation of the turbulent fluctuations observed in run R3 and B3. In run S3 the presence of fluctuations in the upstream boundary layer - and more specifically streamwise coherent vortices - rapidly destabilizes the large scale coherent structures, thus preventing their growth and producing small scale turbulence. This can be observed on Fig. 9.10 which shows the isosurfaces $Q = 0.5U_0^2/h$ around the step. As expected, the boundary layer upstream of the step does not contain any coherent vortices in runs B3 and R3. Consequently, there is a transition of the shear layer immediately downstream of the step from a laminar state to a turbulent state which is characterized by the formation of quasi two-dimensional spanwise Kelvin-Helmotz vortices. These vortices are the dominant coherent structures in transitional mixing layers, and can also be observed in the strong alternating positive and negative v contours for $x/h < 6$ on Fig. 9.9. Although they are present in all runs, they are the largest in run R3 and B3 and they remain dominant in the flow as they are carried away downstream. These vortices are then distorted by streamwise vortices (see Fig. 9.10 (b)) which causes various pairings and

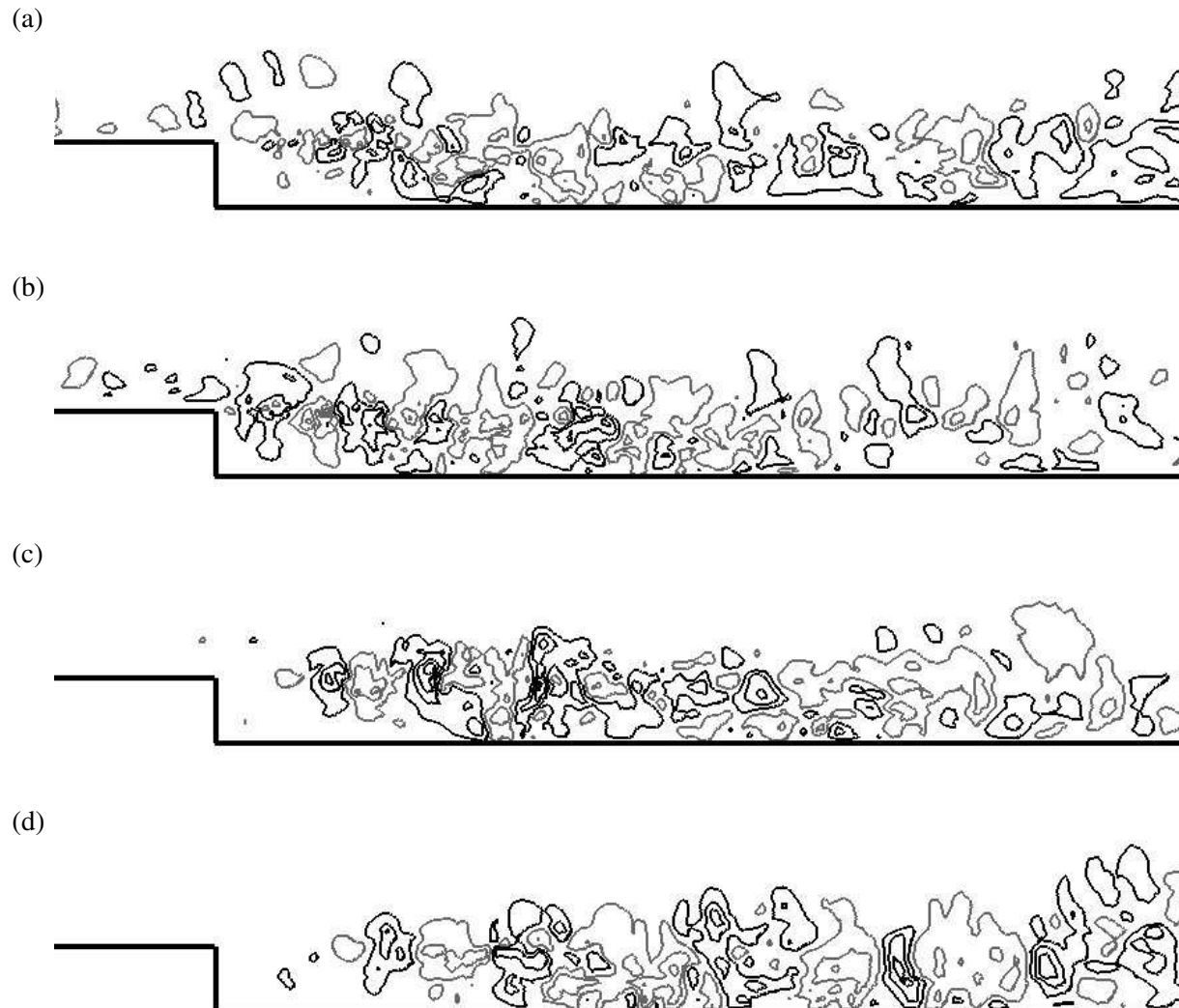


Figure 9.9: Contours of wall-normal velocity fluctuations with different methods of generation of inflow data: (a) precursor simulation (run P3); (b) SEM (run S3); (c) Batten's method (run B3); (d) random method (run R3). Contour lines are evenly spaced at ± 0.5 , ± 1.5 , ± 2.5 , ± 3.5 and ± 4.5 . Grey lines indicate negative value contours.

the development of small scale turbulence.

Finally the rms profiles of the longitudinal fluctuations $\langle u'^2 \rangle^{1/2}/U_0$, the vertical fluctuations $\langle v'^2 \rangle^{1/2}/U_0$, and the Reynolds shear stress $-\langle u'v' \rangle/U_0^2$ are plotted at five streamwise locations in Fig. 9.11. The agreement between run S3 and run P3 is good for all Reynolds stress components both in the upstream boundary layer and downstream of the step. The small discrepancies observed between run S3 and the reference LES are localized far away from the wall ($y/h > 1.5$), in a region of the flow which was already shown in the previous chapter to be affected by the inflow data more than 20 boundary layer thicknesses downstream of the inlet. Profiles for runs R3 and B3 confirm previous conclusions drawn from the analysis of the integrated turbulent kinetic energy profiles. The upstream boundary layer contains little levels of Reynolds stresses and for about $x/h > 3$, the unphysical transition of the shear layer overproduces Reynolds stresses which remain in the flow until the outlet of the computational domain.

Influence of the inlet section length

In this section, we investigate the influence of the length of the LES inlet section L_i on the flow when the SEM is used. Fig. 9.12 shows little difference between the streamlines of the mean flow for runs S1 ($L_i = 1h$), S2 ($L_i = 5h$) and S3 ($L_i = 10h$). Fig. 9.13 shows the coefficient of friction for runs S1, S2, S3 and the reference LES (run P3). Reducing the length of the LES inlet section only slightly decreases the magnitude of the peak of negative skin friction and increases the reattachment length. However the predictions of the size of the main and secondary recirculation bubbles are in excellent agreement for the four simulations (within 5% error between one another).

Fig. 9.14 shows the development of the integrated kinetic energy profile \bar{k} for runs S1, S2, S3 and P3. As expected the inlet section in runs S1 and S2 is too short to recover accurate boundary layer fluctuations before the step. However the shear layer further downstream begins producing turbulence immediately downstream of the step for all four simulations. This suggests that the fluctuations in the upstream boundary layer in runs S1 and S2, even though underestimated, are efficient in causing a rapid transition to a turbulent mixing layer downstream of the step.

These observations are confirmed by the isosurfaces of $Q = 0.5U_0^2/h^2$ shown in Fig. 9.16. Due to a short inlet section upstream of the step, the density of near-wall streaks is lower at the step in run S2 than in the reference LES, and realistic streamwise elongated near-wall streaks have not yet developed at the step in run S1. However the shear layer becomes turbulent immediately downstream of the step (as in the reference LES) irrespective of the size of the inlet section. This explains why the mean recirculation bubble predicted by the three simulations are in excellent agreement.

Further downstream of reattachment, Fig. 9.14 shows that run S1 significantly overpredicts the inten-

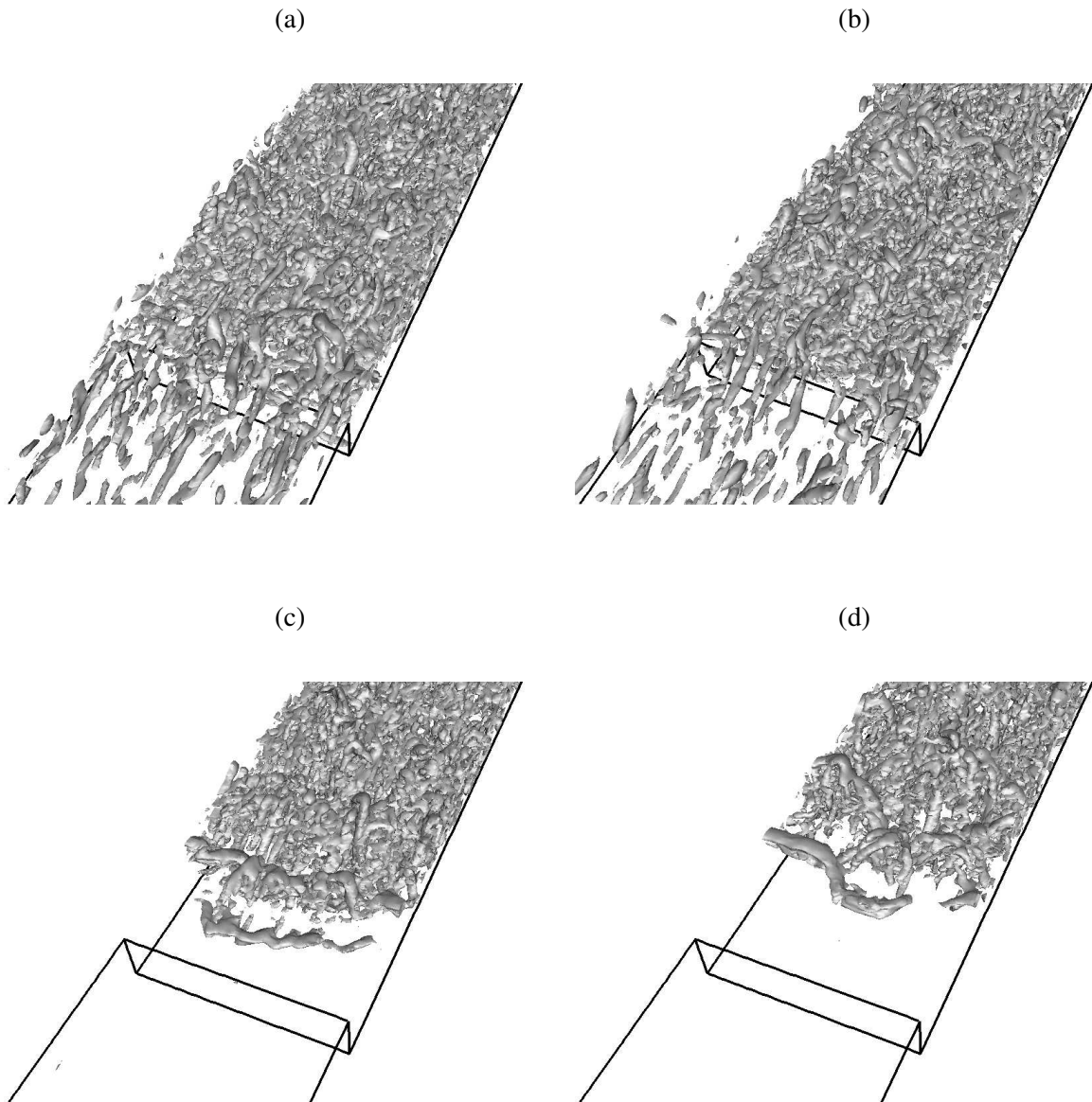


Figure 9.10: Isosurfaces $Q = 0.5U_0^2/h$ with different methods of generation of inflow data: (a) precursor simulation (run P3); (b) SEM (run S3); (c) Batten's method (run B3); (d) random method (run R3).

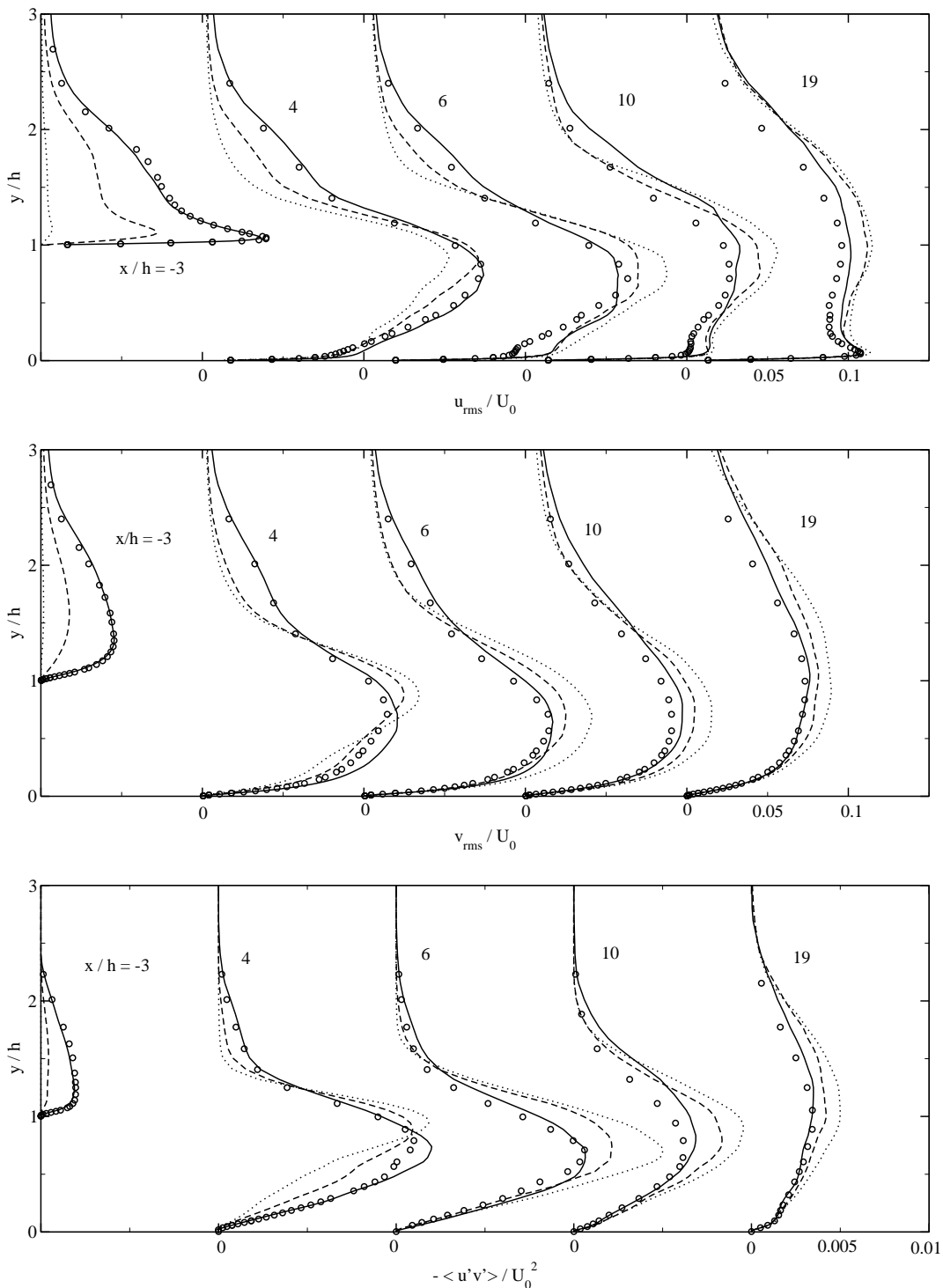


Figure 9.11: Profiles of Reynolds stresses with different methods of generation of inflow data. From top to bottom: $\langle u'^2 \rangle^{1/2} / U_0$, $\langle v'^2 \rangle^{1/2} / U_0$ and $-\langle u'v' \rangle / U_0^2$: —, SEM (run S3); - - -, Batten's method (Run B3); ·····, random method (run R3); ○○○, precursor simulation (run P3).

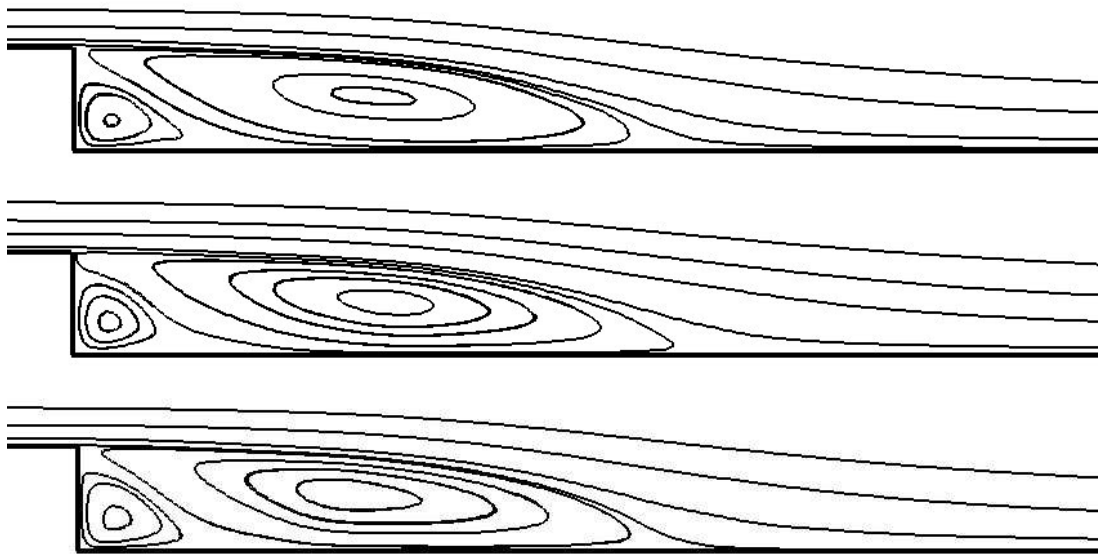


Figure 9.12: Streamlines of the mean flow for different lengths of the inlet section: (a) run S1 ($L_i = 10h$); (b) run S2 ($L_i = 5h$); and (c) run S3 ($L_i = 1h$).

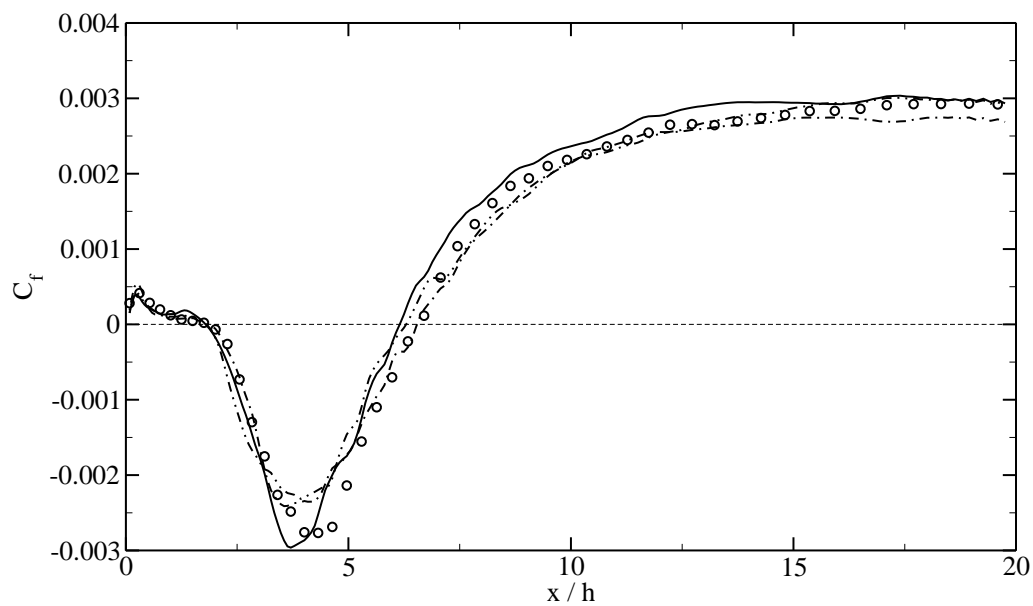


Figure 9.13: Coefficient of friction using the SEM for different lengths of the inlet section: —, run S1 ($L_i = 10h$); -·-, run S2 ($L_i = 5h$); -··-, run S3 ($L_i = 1h$); ○○○, run P3 ($L_i = 10h$).

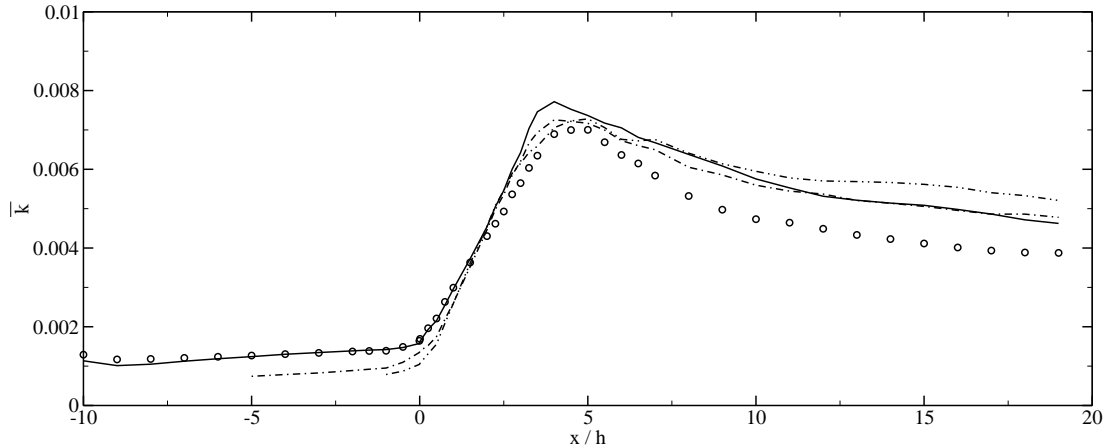


Figure 9.14: Coefficient of friction using the SEM for different lengths of the inlet section: —, run S1 ($L_i = 10h$); - - -, run S2 ($L_i = 5h$); - · - , run S3 ($L_i = 1h$); ○○○, run P3 ($L_i = 10h$).

sity of the turbulent fluctuations. Profiles of individual Reynolds stresses at different streamwise location are shown on Fig. 9.15. Although the general agreement between the profiles is very good in the re-circulation region, a small overprediction of the turbulent fluctuations can be observed at the last station $x/\delta = 19$ for runs S1 and S2. This can be attributed to the underprediction of the turbulent kinetic energy in the upstream boundary layer, which prevents the break-up of large-scale coherent structures in the mixing layer downstream of the step. These large-scale structures remain in the flow whereas they should break up into smaller structures, which results in the small excess of energy observed in the boundary layer by the end of the domain.

9.3 Flow Over an Airfoil Trailing Edge

9.3.1 Presentation of the case

Flow configuration

Fig. 9.17 shows a two-dimensional view of the airfoil trailing edge flow configuration. The airfoil considered is a two-dimensional flat strut with a circular leading edge and an asymmetric beveled trailing edge with a 25° tip angle. It is placed in a uniform stream at zero-degree angle of attack. The Reynolds number based on the freestream velocity U_0 and the airfoil thickness h is 1.017×10^5 . The strut has a chord to thickness ratio $C/h = 21.125$. The flow simulated corresponds to the experiment performed by Blake (1975). The geometry of the airfoil and the flow conditions are described by Wang (1997) and by Wang and Moin (2000).

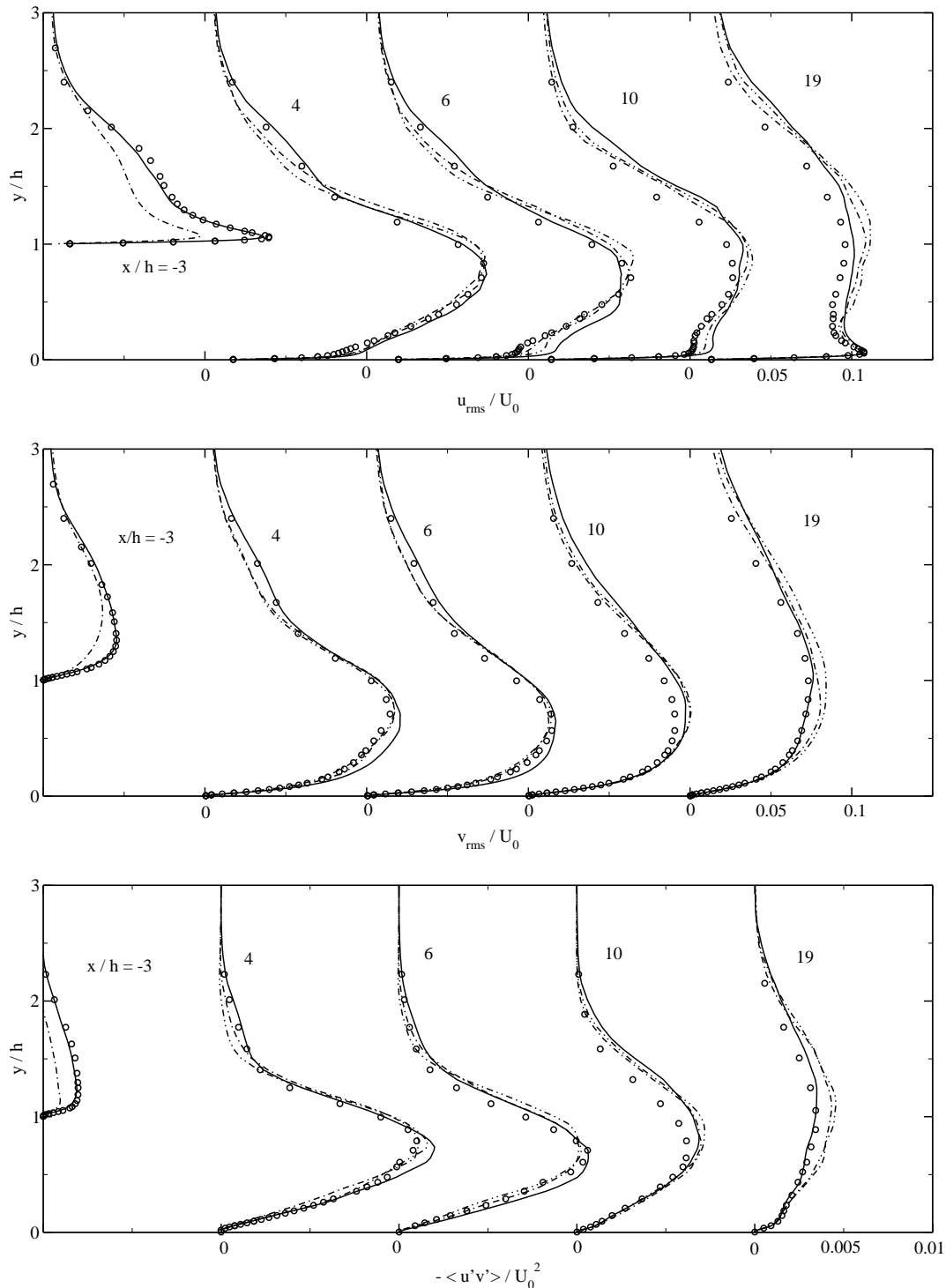


Figure 9.15: Profiles of Reynolds stresses using the SEM for different lengths of the inlet section. From top to bottom: $\langle u'^2 \rangle^{1/2} / U_0$, $\langle v'^2 \rangle^{1/2} / U_0$ and $-\langle u'v' \rangle / U_0^2$: —, run S1 ($L_i = 10h$); -·-, run S2 ($L_i = 5h$); -··-, run S3 ($L_i = 1h$); ○○○, run P3 ($L_i = 10h$).

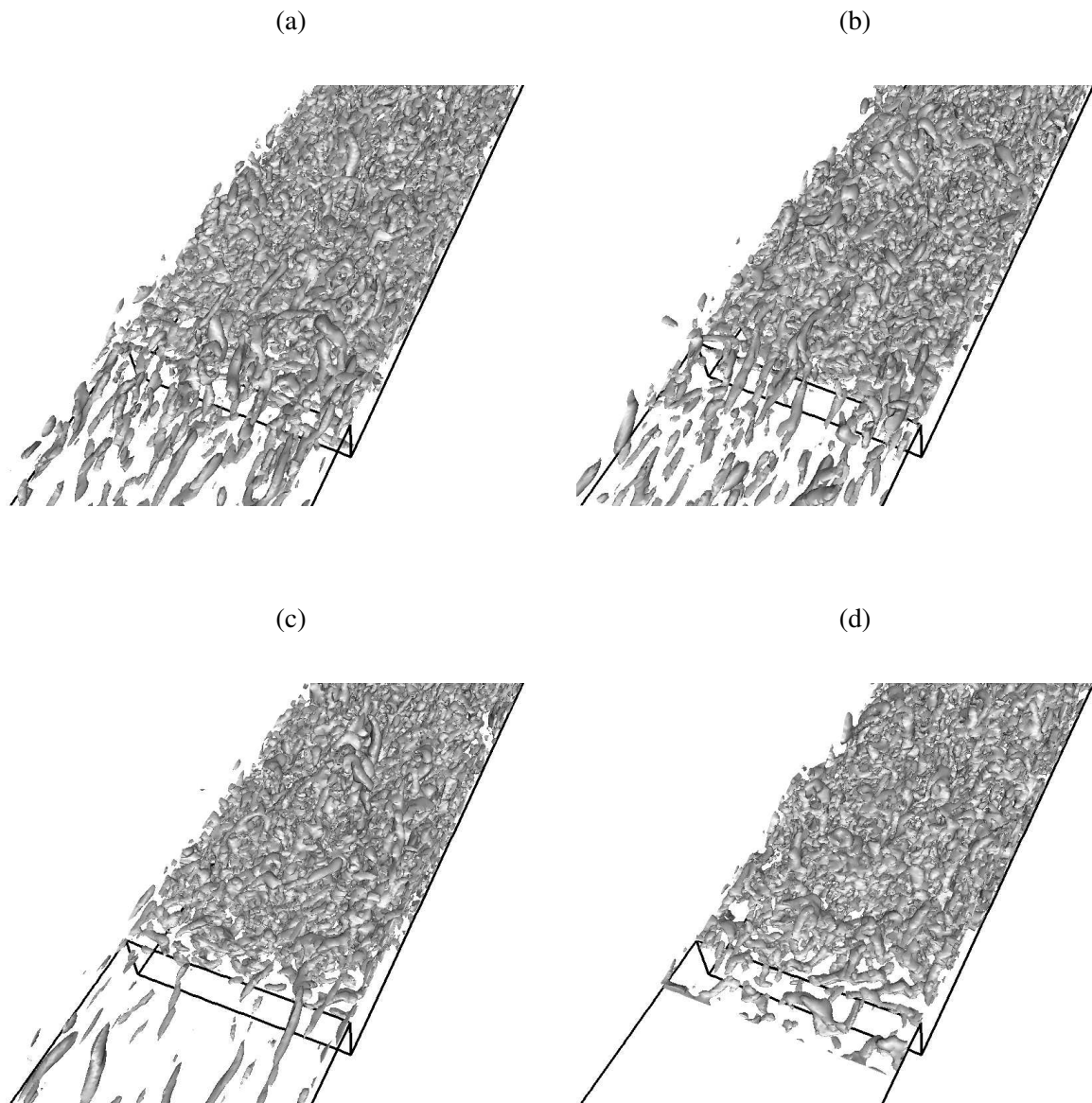


Figure 9.16: Isosurfaces $Q = 0.5U_0^2/h$ with different methods of generation of inflow data: (a) run P3 ($L_i = 10h$); (b) run S3 ($L_i = 10h$); (c) run S2 ($L_i = 10h$); (d) run S1 ($L_i = 10h$).

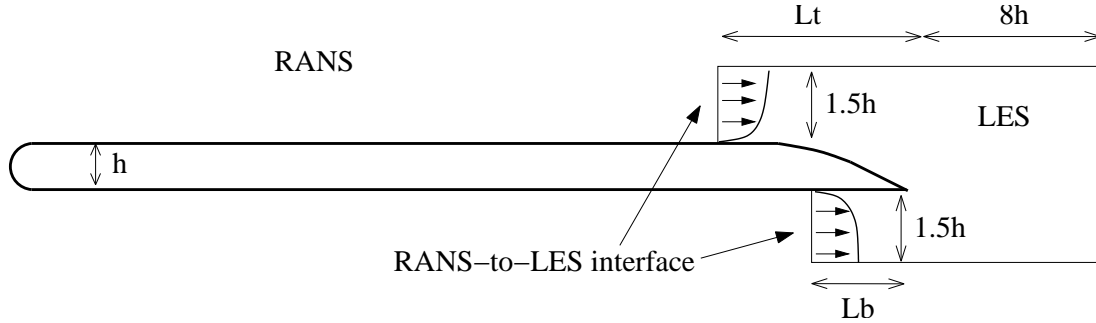


Figure 9.17: Sketch of the hybrid RANS-LES simulations of the airfoil trailing edge.

The asymmetric trailing edge shape produces a mean circulation around the airfoil. On the high-pressure side the flow is essentially a zero-pressure gradient turbulent boundary layer. On the low-pressure side, the boundary layer first experiences a favorable pressure gradient as it approaches the trailing edge, causing flow acceleration, followed by a region of adverse pressure gradient leading to flow deceleration and eventually separation. Further downstream, this results in the near wake of the trailing edge in a mixing layer with complex interactions between the low-pressure side separated boundary layer and the high-pressure side attached boundary layer.

Computational methodology

Several hybrid RANS-LES simulations of this flow are performed. As shown on Fig. 9.17, the RANS domain encloses the entire airfoil and only the rear part of the trailing edge and the near wake are simulated with LES (the non-equilibrium region of the flow).

The RANS simulation is conducted on a C-grid domain, as shown on Fig. 9.18. The top and bottom boundaries are placed $20h$ from the strut to minimize the effect of the boundary conditions. In the wake, the exit plane is located $8h$ downstream of the trailing edge. Three embedded LES domains have been used for the hybrid simulations, which differ from one another on the lengths of the inlet section L_t and L_b upstream of the trailing edge on the top and bottom surface, respectively. All the LES domain extend $8h$ downstream of the trailing edge in the wake, and the top and bottom boundaries are placed $1.5h$ away from the nearest wall.

The SST model of Menter (1994) is used in the RANS region; the Smagorinsky model (with $C_S = 0.065$) and Van-Driest damping at the wall is used in the LES region.

For all simulations performed, a no-slip boundary conditions is applied at the wall, and the standard outlet boundary condition implemented in *Code_Saturne* (see page 97 in Chapter 5) is applied at the exit

plane. At the top and bottom surfaces of the domain, we impose a symmetry condition (see page 98 in Chapter 5) in the RANS calculation whereas in the LES, we impose $\mathbf{u} = \mathbf{u}_{RANS}$, where \mathbf{u}_{RANS} is the velocity of the RANS solution interpolated onto the LES grid. At the inlet plane of the LES domain, data are extracted from the RANS solution, interpolated onto the LES grid, and used for the generation of synthetic turbulence.

The mesh used in the RANS simulation is structured, two-dimensional and has 131,840 cells. 2,060 cells are used in the streamwise direction, with the refinement increasing both near the leading edge and near the trailing edge. 1,000 cells are used along the upper surface and 700 are used along the lower surface. 360 cells are distributed along the wake line. 64 cells are used in the wall-normal direction with a clustering of cells at the wall. Using the friction velocity corresponding to the peak of the coefficient of friction, the grid spacing in wall units is reduced from $\Delta x^+ \approx 300$ at the middle of the airfoil to $\Delta x^+ \approx 76$ at the trailing edge. The grid spacing in the wall-normal direction for the first layer of cells adjacent to the surface remains unchanged along the airfoil $\Delta y^+ \approx 2$. SST simulations on coarser meshes have been performed and the results did not exhibit any difference with the present SST solution.

For the LES mesh, 644 cells are uniformly distributed along the upper surface, and 384 along the lower surface. Using the same friction velocity as earlier gives a grid spacing in wall units of $\Delta x^+ = 65$ and $\Delta x^+ = 68$ on the upper and lower surface, respectively. At the inlet of the LES, this reduces to $\Delta x^+ = 41$ and $\Delta x^+ = 34$ on the upper and lower surfaces, respectively. 150 cells are non-uniformly distributed along the wake line. The wall-normal grid spacing increases as the upper and lower walls are approached. 64 cells are used and the near-wall grid spacing is at a minimum at the walls, with $\Delta y^+ \approx 2$. In the spanwise direction, 64 cells are uniformly distributed. The grid spacing in wall units on the upper surface is approximately $\Delta z^+ = 41$ at its coarsest, and around 26 at the inlet of the LES domain. In total, the LES mesh used on the large domain has about 5.4×10^6 cells. Fig. 9.18 shows the LES computational mesh near the airfoil trailing edge.

Simulations performed

The simulations performed are summarized in Table 9.2. Results are compared with the finely resolved LES of Wang and Moin (2000). The LES domain used by Wang and Moin (2000) begins at $x/h = -8$ upstream of the trailing edge on both sides of the airfoil, and the top and bottom boundaries are placed $20h$ from the airfoil. The grid refinement is similar to the present hybrid simulations except in the spanwise direction where it is coarser (48 cells compared 64 cells in the present hybrid simulations). A RANS domain enclosing the entire airfoil provides boundary conditions for the LES domain outside the boundary layers. Inside the boundary layers on both side of the airfoil, time series of inflow velocities are

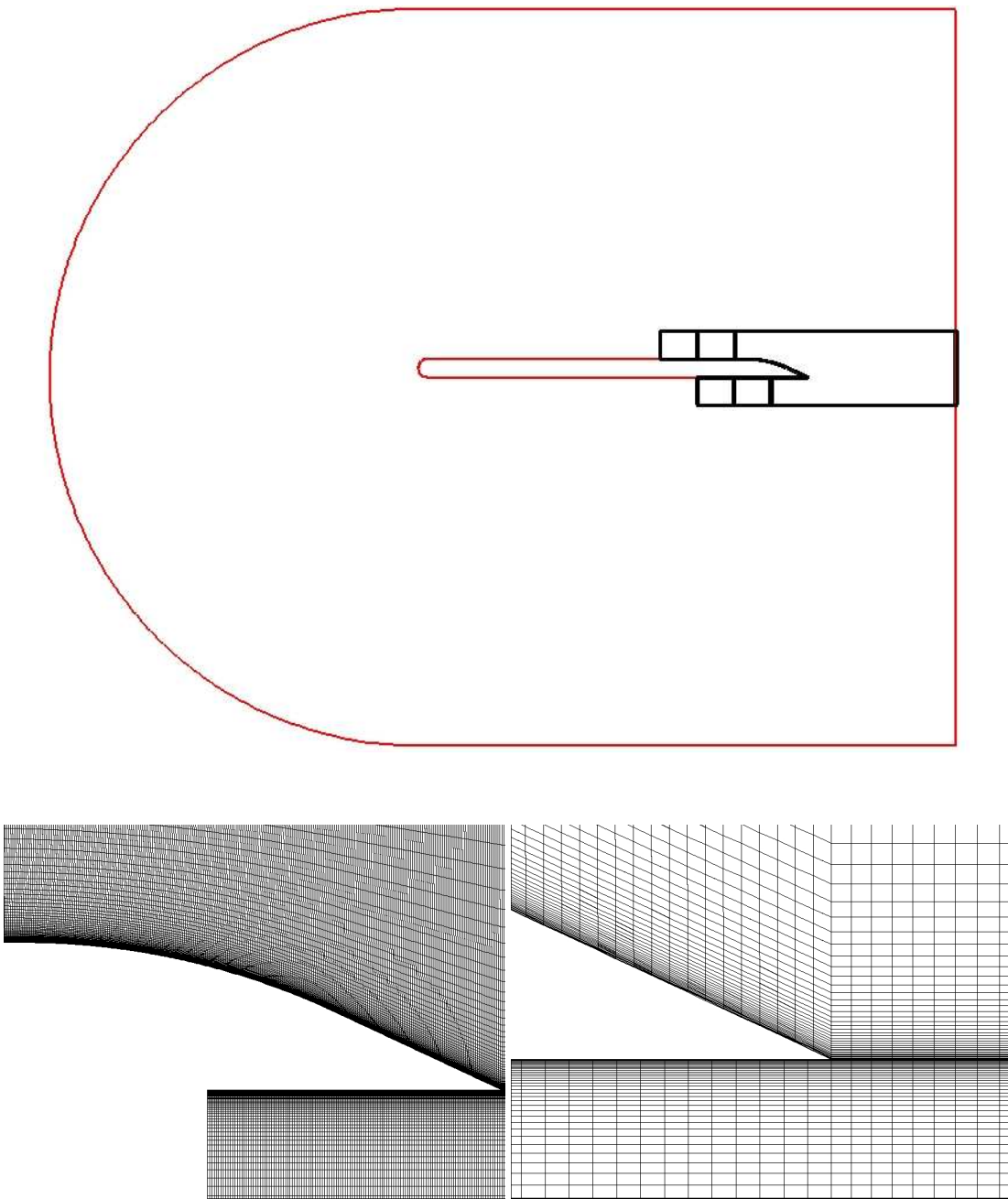


Figure 9.18: RANS (red line) and embedded LES (black line) computational domains used in the hybrid simulations (top), and different close-up views of the LES mesh near the airfoil trailing edge (bottom).

Run	LES inlet section (low- and high-pressure side)	Inflow method	Input statistics
S1	$8h, 6h$	SEM	RANS
S2	$6h, 4h$	SEM	RANS
S3	$4h, 2h$	SEM	RANS
B3	$4h, 2h$	Batten et al. (2004)	RANS
R3	$4h, 2h$	Random Method	RANS

Table 9.2: Parameter settings used in the hybrid RANS/LES computations of the flow over an airfoil trailing edge. The parameters not listed here are kept constant for all simulations.

generated using two precursor LES of zero pressure gradient flat plate turbulent boundary layers, using the method of Lund et al. (1998).

We first wish to study the ability of hybrid simulations using the SEM to generate accurate inlet conditions for the non-equilibrium region of the flow within as short a distance as possible. Three different LES domains were used. Run S1 uses the computational domain with the longest inlet section on the airfoil which has been presented in the previous subsection. It begins at $x/h = -8$ and $x/h = -6$ upstream of the trailing on the top and bottom surface, respectively. The LES domains with shorter inlet sections have the same grid refinement as the mesh used in run S1. The grids used in run S2 and S3 have 4.2×10^6 cells ($L_t/h = 6$ and $L_b/h = 4$) and 3.0×10^6 cells ($L_t/h = 4$ and $L_b/h = 2$), respectively.

Hybrid simulations are also performed in order to test the influence of the method of generation of inflow data for the LES region. The SEM (run S3) is then compared with the random method (run R3) and the method of Batten et al. (2004) (run B3). These simulations are performed on the shortest LES domain.

9.3.2 Results and discussions

The results obtained from the SST simulation are analyzed first. The results of the hybrid simulations are then presented, focusing on the influence of the size of the LES domain and on the method used to generate the LES inflow data.

RANS results

The flow is characterized by a mean circulation around the airfoil, which in the present coupling methodology is entirely controlled by the RANS model. In order to study the intensity of this mean circulation,

Fig. 9.19 (a) shows the velocity at the top of the boundary layer U_e on the lower and upper surface of the airfoil. As a comparison, the edge velocity at the inlet plane of the reference LES of Wang and Moin (2000) is also represented. The velocity overshoot on the upper side of the airfoil due to the presence of a lifting surface is overestimated in our simulation. In the present SST simulation, $U_e \approx 1.131U_0$ on the upper surface, compared with $U_e \approx 1.093U_0$ in the SST simulation of Wang and Moin (2000) and $U_e \approx 1.071U_0$ in the experiment of Blake (1975). The origin of the discrepancies between the present SST simulation and the SST simulation of Wang and Moin (2000) is not clear. Grid convergence studies have shown that the present solution is independent of further grid refinement. Therefore the only possible source of errors is the particular implementation of the SST model in *Code-Saturne* and the code used by Wang and Moin (2000). Fig. 9.19 (b) shows that the boundary layer momentum thickness θ (on the low-pressure side of the airfoil) predicted by the present SST simulation is in excellent agreement with the reference LES predictions.

Hybrid RANS-LES using the SEM (large LES domain results)

Fig. 9.20 compares the coefficient of friction on the low-pressure side near the trailing edge for run S1, the SST calculation and the reference LES. As expected in the hybrid simulation, the coefficient of friction decays downstream of the LES inlet, before recovering the SST solution value (but not the reference LES value) only $1h$ downstream of the inlet. Further downstream the discrepancies between the hybrid simulation and the reference LES are quite significant. The benchmark LES of Wang and Moin (2000) uses a different code, a different mesh and different inlet conditions than the present hybrid simulations. The benchmark LES against which to compare the hybrid simulations using synthetic turbulence should then ideally be a full domain LES, or say a hybrid simulation using inflow data extracted from a precursor simulation using the same code and the same grid. For computational reasons, such a simulation has not been performed yet. In what follows, the LES of Wang and Moin (2000) will thus still be considered as the benchmark solution.

Fig. 9.21 shows instantaneous streamwise velocity fluctuations on the plane $y^+ = 1$ along the low-pressure side wall. All the instantaneous features of a trailing edge boundary layer are well reproduced by the present LES (see Chong et al. (1998) or De Prisco et al. (2007) among others for a study of coherent structures in non-equilibrium boundary layers). The regular streaky structure of the boundary layer can be observed for $-7 < x/h < -5$. In the region where the boundary layer accelerates, fluctuations reorganise in longer and more stable streamwise streaks ($-5 < x/h < -2.5$). After the removal of the pressure gradient, there is a rapid re-transition to a more turbulent state ($-2.5 < x/h < -1$) followed by an unsteady separation ($-1 < x/h < 0$).

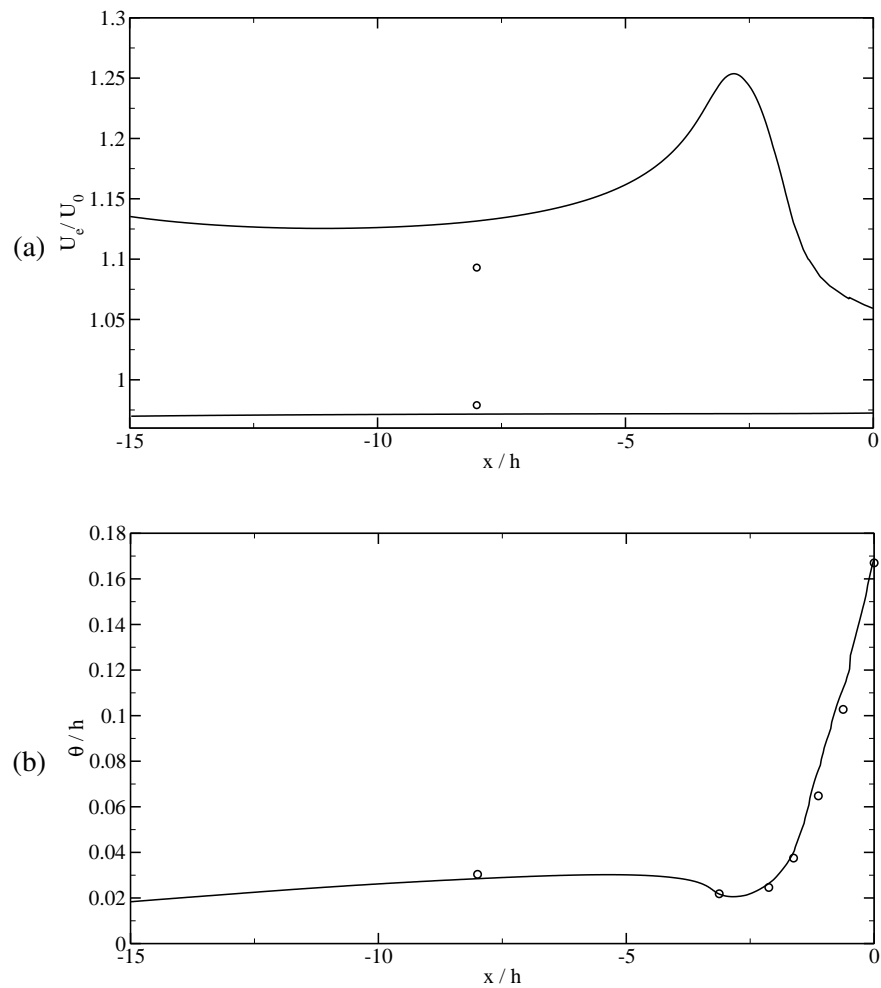


Figure 9.19: Comparison between the full domain trailing edge SST solution (—) and the reference LES data of Wang and Moin (2000) (○ ○ ○): (a) Boundary layer edge velocity U_e of the lower and upper boundary layer, (b) boundary layer momentum thickness θ on the upper surface near the trailing edge.

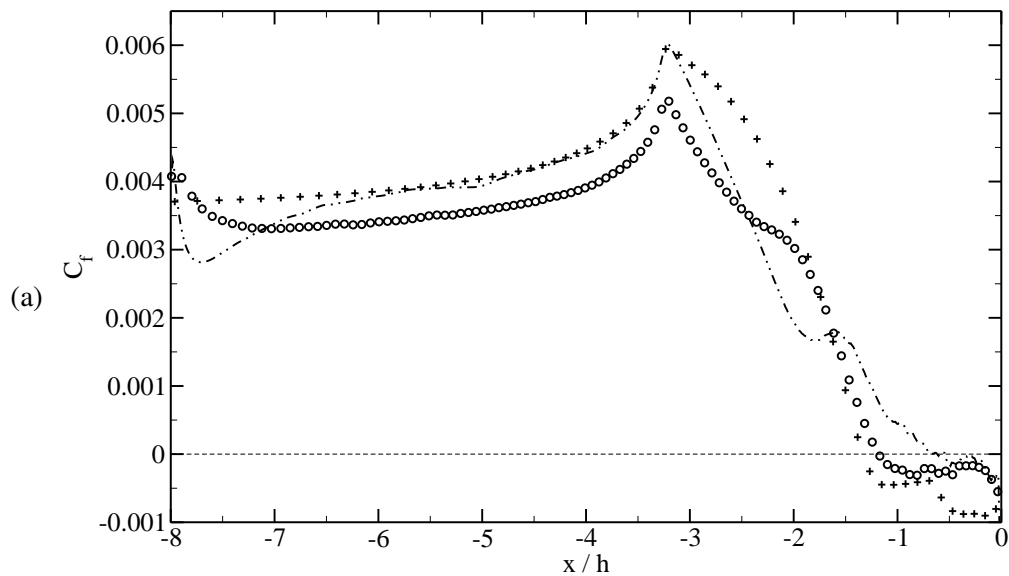


Figure 9.20: Coefficient of friction on the low-pressure side near the trailing edge: — · — , Hybrid RANS-LES run S1; + + +, Full domain SST; ○ ○ ○, reference LES of Wang and Moin (2000).

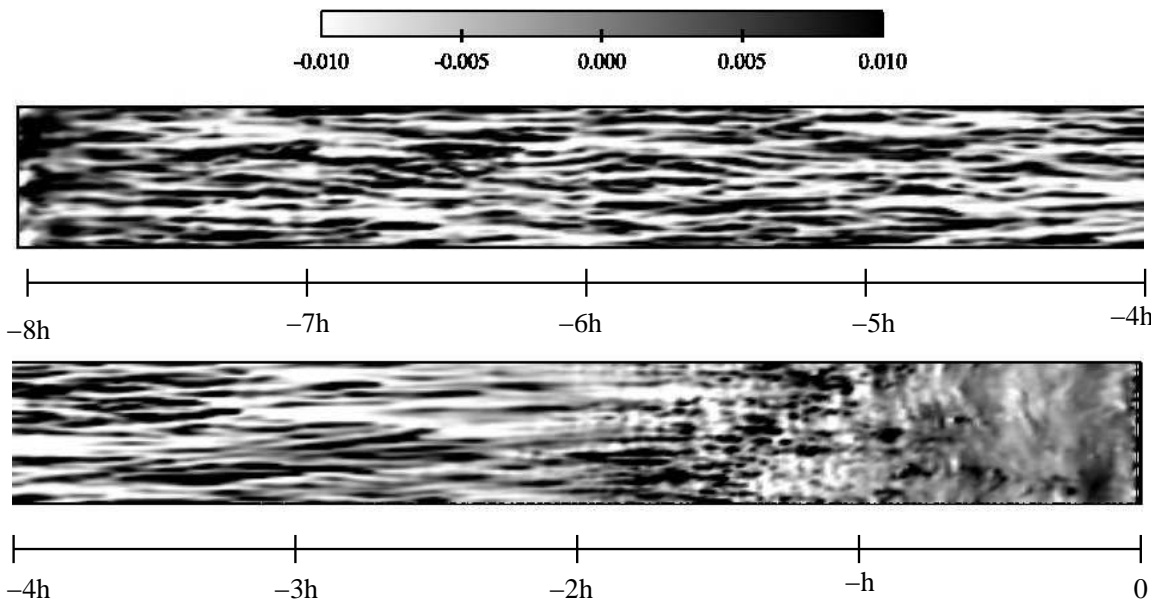


Figure 9.21: Streamwise velocity fluctuations in a plane parallel to the wall at $y^+ = 1$ on the low-pressure side (run S1).

Fig. 9.22 compares the mean velocity magnitude $\tilde{U} = (U^2 + V^2)^{1/2}$, normalized by its value at the boundary layer edge \tilde{U}_e at different streamwise stations on the upper wall of the airfoil for run S1 and the reference LES. The agreement is excellent at all locations except at the last two stations, where the boundary layer (which is subject to a strong adverse pressure gradient) remains attached to the wall in run S1 longer than in the reference LES. This could also be observed in Fig. 9.20 where it is showed that separation is delayed in the hybrid simulation compared to the reference LES.

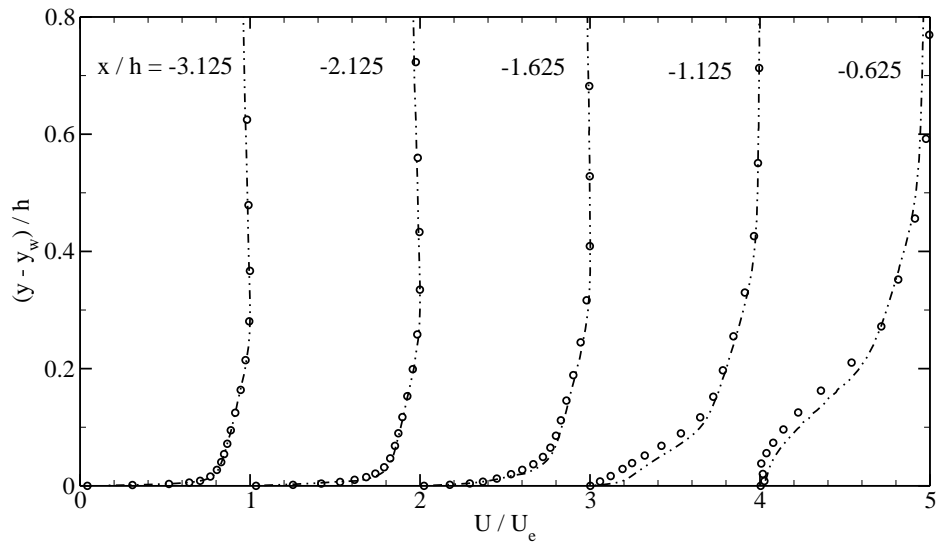


Figure 9.22: Profiles of the mean velocity magnitude normalized by the edge velocity as a function of vertical distance from the upper surface, at $x/h = -3.125, -2.125, -1.625, -1.125, -0.625$: $\cdots\cdots$, Hybrid RANS-LES run S1; $\circ\circ\circ$, reference LES of Wang and Moin (2000).

Fig. 9.23 compares the rms streamwise velocity fluctuations normalized by the edge velocity at different streamwise stations on the upper surface of the airfoil for run S1 and the reference LES. The agreement is good at all stations. The overestimation of the turbulent fluctuations in the outer layer of the boundary layer downstream of the inlet can be observed at $x/h = -4.625$ and; a phenomenon already observed in the simulation of several wall bounded flows in the previous chapter. An overestimation of the fluctuations in the near-wall region which can be held responsible for the delayed separation in the present LES can also be observed at $x/h = -1.625$.

Fig. 9.24 shows profiles of the mean streamwise velocity at several near-wake stations. The corresponding rms streamwise velocity fluctuations profiles are depicted on Fig. 9.25. The agreement between the hybrid simulation (run S1) and the reference LES is excellent at all stations.

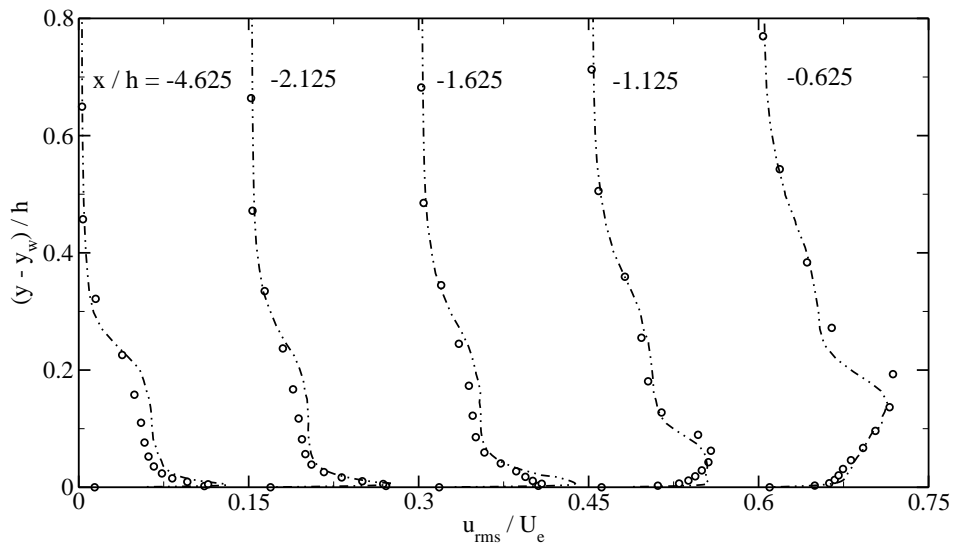


Figure 9.23: Profiles of the rms streamwise velocity fluctuations normalized by the edge velocity as a function of vertical distance from the upper surface, at $x/h = -4.625, -2.125, -1.625, -1.125, -0.625$:
 ---, Hybrid RANS-LES run S1; ○○○, reference LES of Wang and Moin (2000).

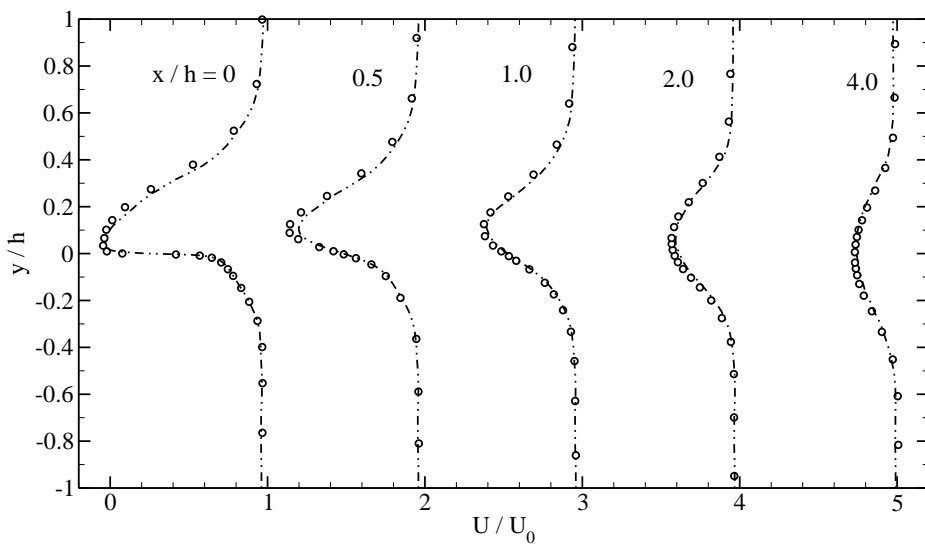


Figure 9.24: Profiles of the mean streamwise velocity normalized by the free-stream velocity at $x/h = 0, 0.5, 1, 2, 4$: ---, Hybrid RANS-LES run S1; ○○○, reference LES of Wang and Moin (2000).

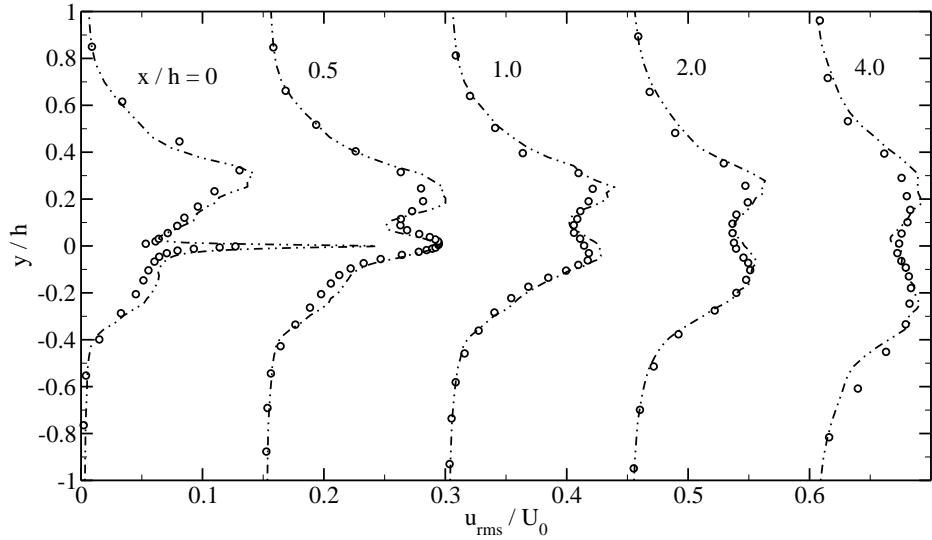


Figure 9.25: Profiles of the rms streamwise velocity fluctuations normalized by the free-stream velocity at $x/h = 0, 0.5, 1, 2, 4$: $\cdots \circ \circ \circ$, Hybrid RANS-LES run S1; $\circ \circ \circ$, reference LES of Wang and Moin (2000).

Influence of LES inlet section length

Two hybrid RANS-LES simulations (runs S2 and S3) are performed with a shorter LES domain than in run S1. The coefficient of friction near the trailing edge is shown on Fig. 9.26. As expected, all hybrid simulations exhibit a short (about one airfoil thickness) transition region downstream of the inlet characterized by a drop of the coefficient of friction. Consequently the coefficient of friction peak is lower in run S3 than in the other hybrid calculations due to the proximity of the LES inlet. However the agreement between all hybrid simulations is excellent for $x/h > -3$ in the adverse pressure gradient region and in the region of separation.

Profiles of mean velocity magnitude and rms streamwise velocity fluctuations at several locations on the upper surface of the airfoil on Fig. 9.27 confirm that the position of the LES inlet has little effect on the downstream development of the turbulence statistics. The most important differences between the three hybrid simulations are observed at $x/h = -1.125$ and at $x/h = -0.625$, where the mean velocity profiles in the near-wall region are fuller in runs S1 and S2 than in run S3, due to the proximity of the LES inlet, downstream of which the mean flow undergoes a short laminarization process. It can also be noted that the fluctuations are slightly higher at station F and G in run S3 than in run S1 and S2, due again to the proximity of the inlet plane.

In the wake of the airfoil, the profiles of mean streamwise velocity and rms velocity fluctuations

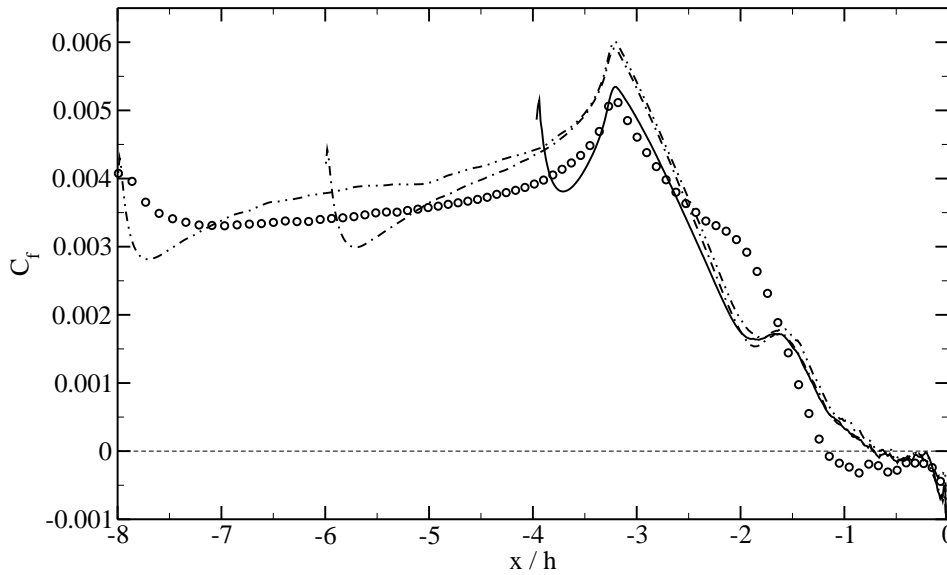


Figure 9.26: Coefficient of friction on the low-pressure side near the trailing edge for run S1, run S2, run S3 and the reference LES: \cdots , Hybrid run S1; $\cdots\cdots$, Hybrid run S2; $-$, Hybrid run S3; $\circ\circ\circ$, reference LES of Wang and Moin (2000).

shown on Fig. 9.28 for the three hybrid simulations are again very similar.

Streamwise velocity fluctuations in a plane parallel to the low-pressure side wall are shown on Fig. 9.29. In the region where the boundary layer accelerates, the fluctuations have the same magnitude for the three simulations as already noted from the study of rms streamwise velocity fluctuation profiles. However, the turbulent structures are larger in run S1 than in the other two hybrid simulations. The inflow fluctuations prescribed have a lack of structural information which cannot be generated in the short inlet section in run S1. This lack of structural information can also account for the underprediction of the coefficient of friction peak in run S1. Further downstream in the recirculation region, both the magnitude of the fluctuations and the size of the structures are very similar in the three simulations.

Comparison of methods of generation of inflow data

The SEM is compared with the random method (run R3) and Batten's method (run B3) on the shortest LES domain (given the good results obtained with the SEM on this domain). Fig. 9.30 shows the coefficient of friction on the low-pressure side. The hybrid simulations using the random method and Batten's method initially laminarize, and show very early separation at $x/h = -2.4$ and $x/h = -2.1$, respectively. This is followed by a region where the boundary layer has a non-physical behavior, reattaching, before de-

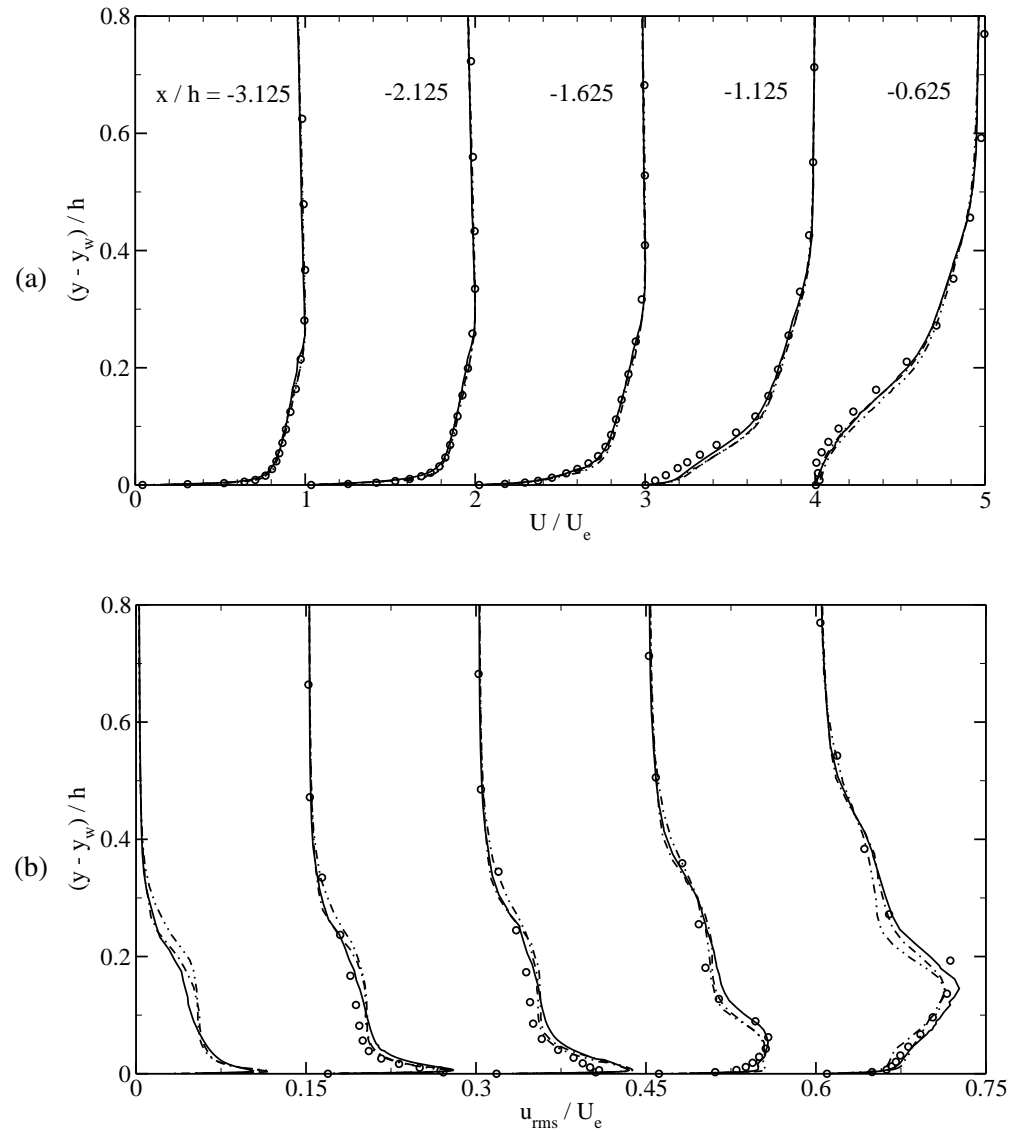


Figure 9.27: Profiles of (a) the mean velocity magnitude and (b) the rms streamwise velocity fluctuations normalized by the edge velocity as a function of vertical distance from the upper surface, at $x/h = -3.125, -2.125, -1.625, -1.125, -0.625$: \cdots , Hybrid run S1; $\cdots\cdots$, Hybrid run S2; $-$, Hybrid run S3; $\circ\circ\circ$, reference LES of Wang and Moin (2000).

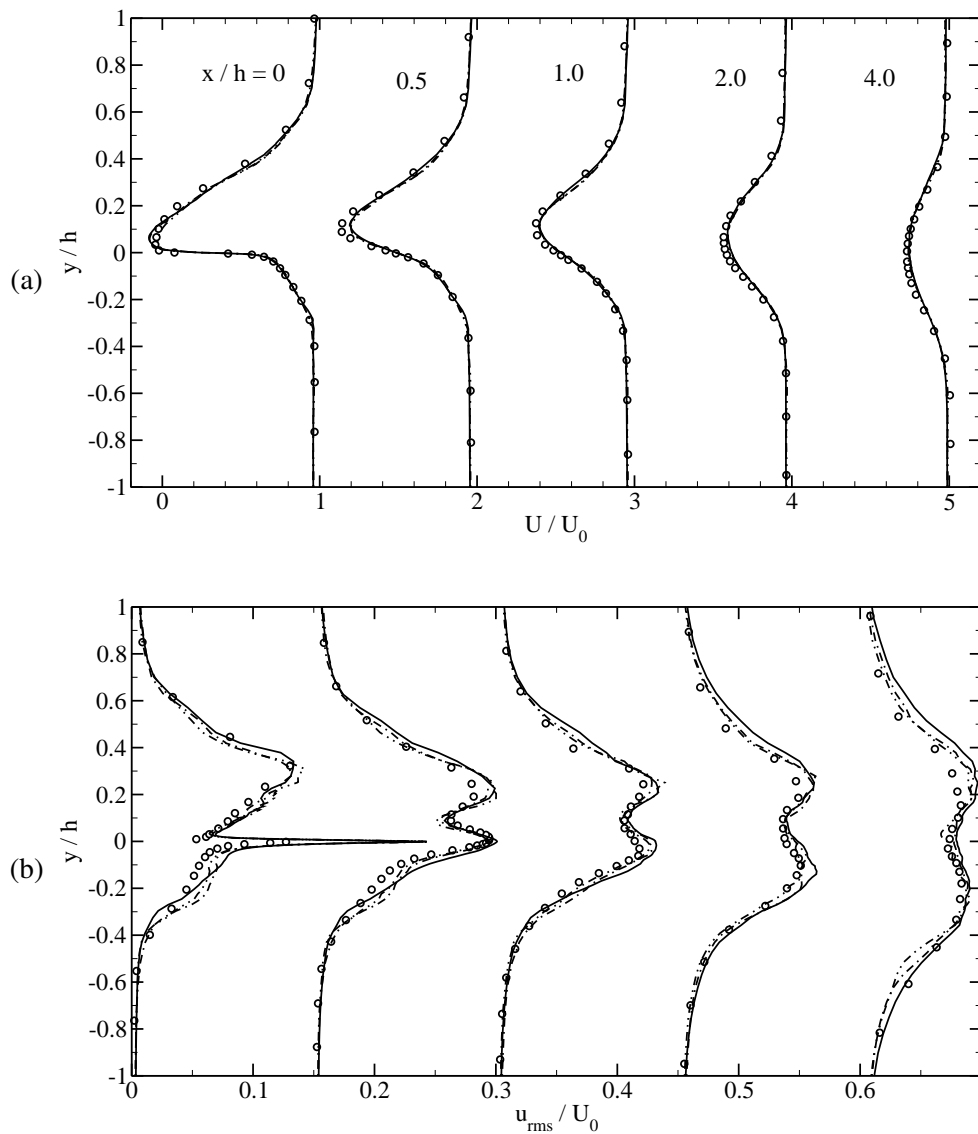


Figure 9.28: Profiles of (a) the mean streamwise velocity and (b) the rms streamwise velocity fluctuations normalized by the free-stream velocity at $x/h = 0, 0.5, 1, 2, 4$: —·—, Hybrid run S1; -·-, Hybrid run S2; —, Hybrid run S3; ○○○, reference LES of Wang and Moin (2000).

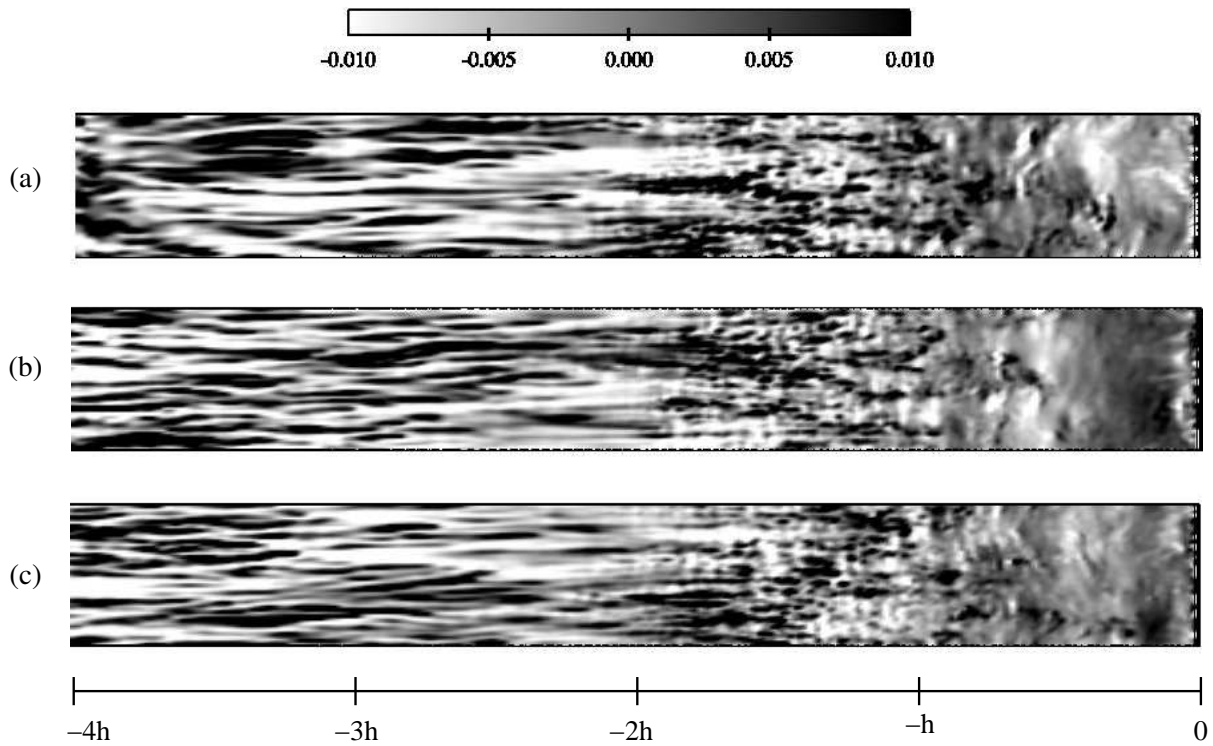


Figure 9.29: Streamwise velocity fluctuations in a plane parallel to the wall at $y^+ = 1$ for hybrid simulations with different LES domains: (a) run S1, (b) run S2, and (c) run S3.

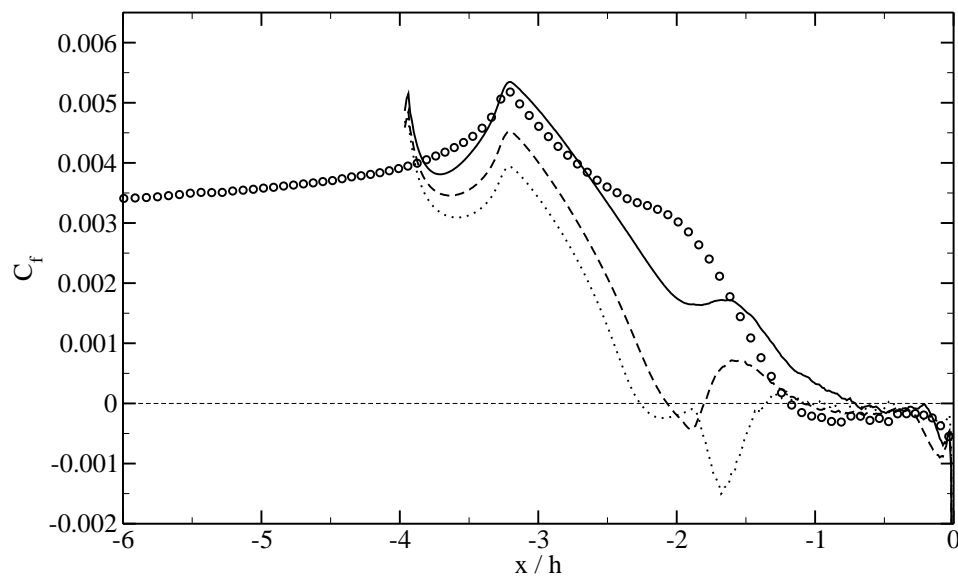


Figure 9.30: Coefficient of friction C_f for different methods of generation of inflow data: —, SEM; ---, Batten et al. (2004); ·····, random method; ○○○, reference LES of Wang and Moin (2000).

taching again. The hybrid simulation using the SEM detaches at $x/h = -0.75$, slightly after the reference LES ($x/h = -1.17$).

Profiles of mean velocity magnitude and streamwise velocity fluctuations on the low-pressure side of the airfoil are shown in Fig. 9.31. The early separation of the boundary layer in the simulation using Batten's method (or the random method) is clearly visible on the different mean flow profiles. This is again caused by the lack of coherence of the prescribed inlet fluctuations which are underestimated at the first station. Further downstream the presence of a large separation bubble in run B3 and R3 produces larger levels of fluctuations in the recirculation region (see Fig. 9.31 (b) at $x/h = -1.125$ and at $x/h = -0.625$). When the SEM is used the profiles are in much better agreement with the reference LES.

The fluctuations generated by the larger recirculation in run B3 and R3 are convected into the wake of the airfoil. Consequently, the streamwise velocity fluctuations profiles are overestimated as shown in Fig. 9.32 (b). The agreement between the mean flow profiles of run S3 and the reference LES is excellent. On the contrary, the mean flow profiles are poorly predicted in run B3 and R3 in the near wake due to the upstream flow history, and the discrepancies are reduced as the flow is convected away from the trailing edge.

The effect of the inflow data on the turbulent structures will now be described. Streamwise velocity fluctuations along the upper surface of the airfoil are shown in Fig. 9.33. The simulation using Batten's method - although leading to early separation and weak magnitude fluctuations in the near wall region - still shows features similar to the simulation using the SEM: the weak near-wall streaks are elongated in the streamwise direction (due to the favorable pressure gradient experienced by the boundary layer), followed by a rapid transition towards a more turbulent state (after the removal of the pressure gradient), before finally separating from the wall. With the random method, no turbulent structures are present in the near-wall region of boundary layer downstream of the inlet, which also leads to early separation. However in this case, the separation is laminar and leads to the formation of large scale two-dimensional Kelvin-Helmotz vortices in the subsequent shear layer. This scenario is confirmed in Fig. 9.34 showing isosurfaces of $Q = 10U_0^2/h^2$ on the low-pressure side of the airfoil. Large scale two-dimensional spanwise vortices are formed in the laminar boundary layer around $x/h = -2$ when the random method is used.

Fig. 9.35 shows v' -velocity fluctuations in the near-wake for the three simulations using different inflow data. Alternating positive and negative v contours indicate the presence in all simulations of Kelvin-Helmotz vortices. However the size and the intensity of these vortices are significantly overestimated with the random method or Batten's method, due to the lack of fluctuations in the boundary layer before separation. It was noted previously that the turbulent statistics in the wake of the airfoil were affected by the upstream boundary layer inlet conditions. It appears now that the large fluctuations observed with

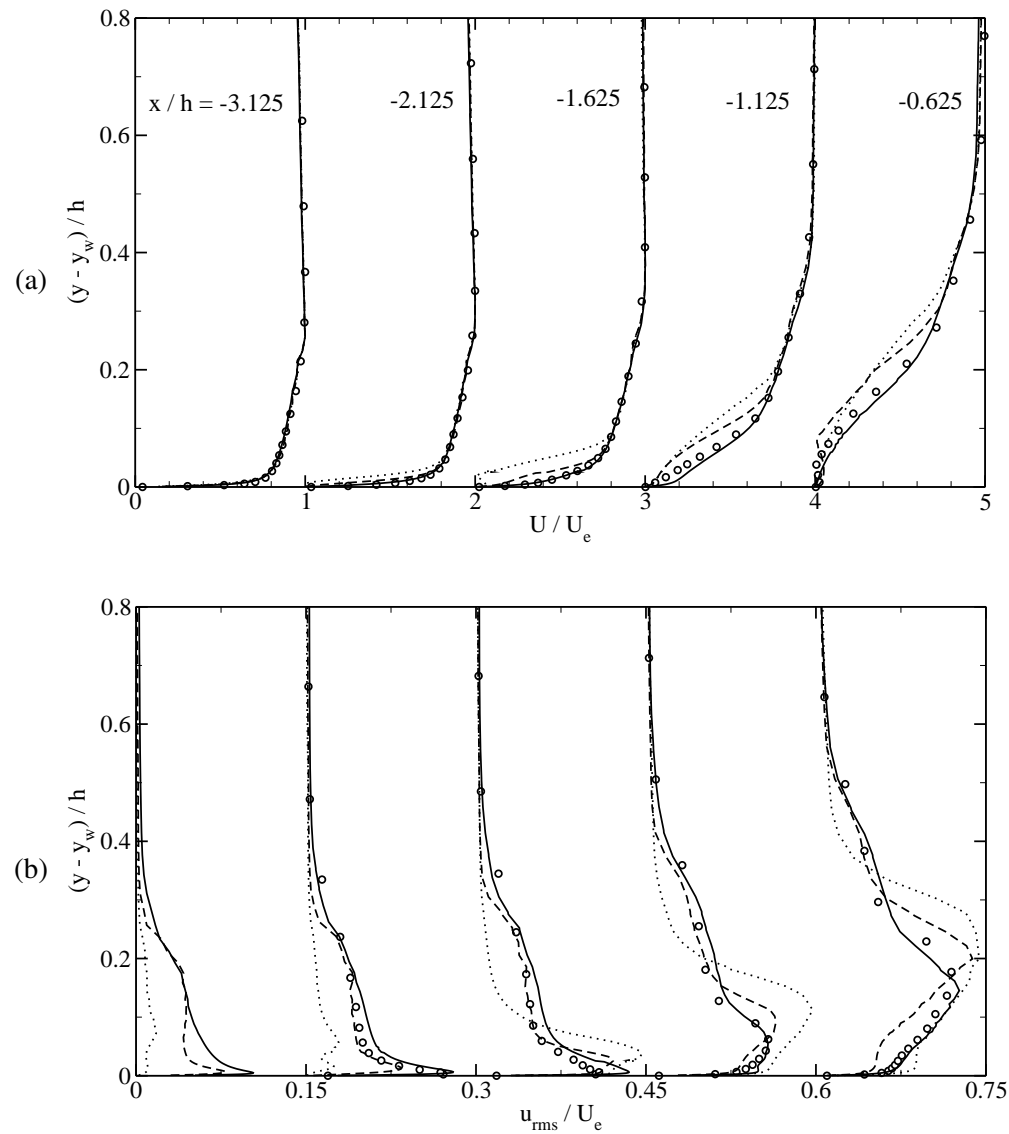


Figure 9.31: Profiles of (a) the mean velocity magnitude and (b) the rms streamwise velocity fluctuations normalized by the edge velocity as a function of vertical distance from the upper surface, at $x/h = -3.125$, -2.125 , -1.625 , -1.125 , -0.625 : —, SEM; - - -, Batten et al. (2004); ······, random method; ○○○, reference LES of Wang and Moin (2000).

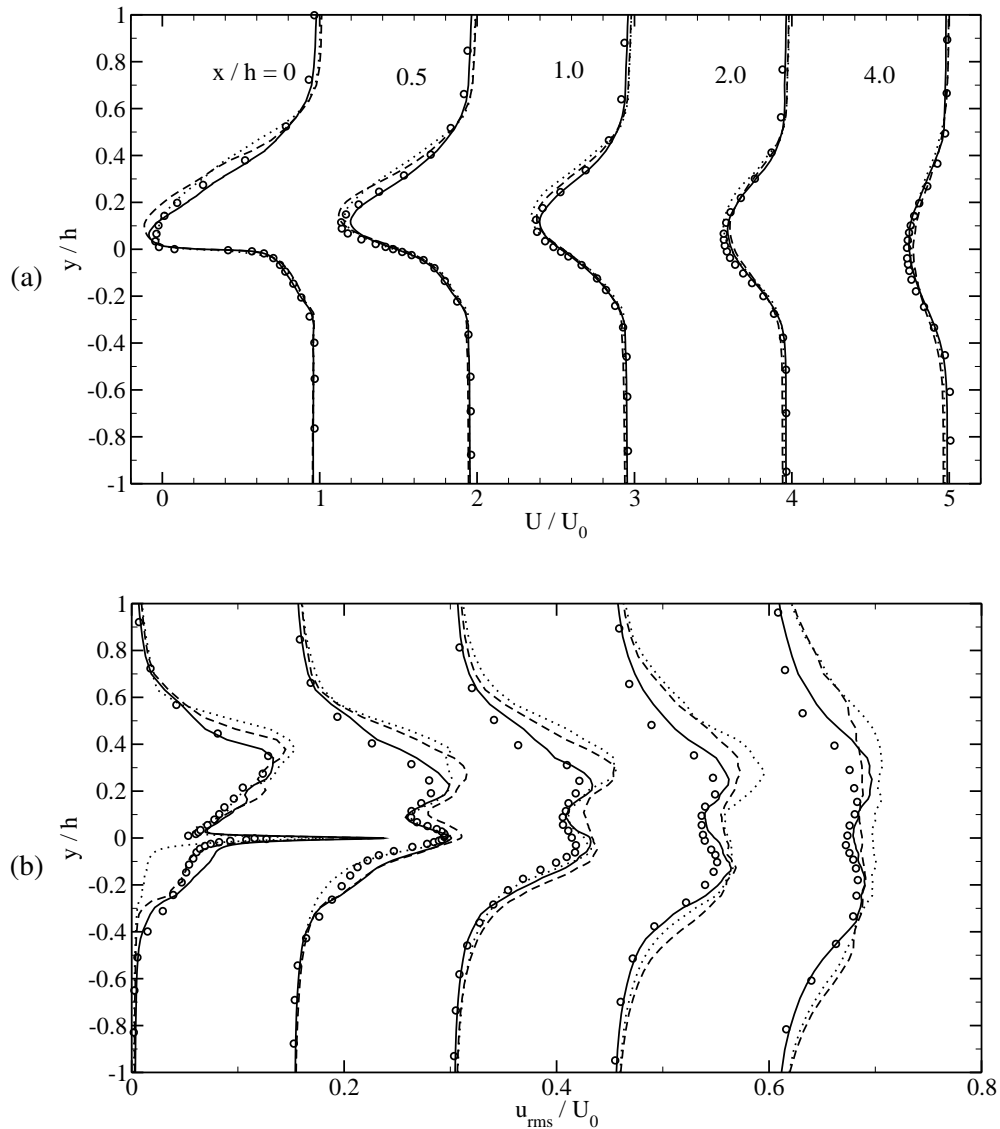


Figure 9.32: Profiles of (a) the mean streamwise velocity and (b) the rms streamwise velocity fluctuations normalized by the free-stream velocity at $x/h = 0, 0.5, 1, 2, 4$. Same legend as in Fig. 9.31.

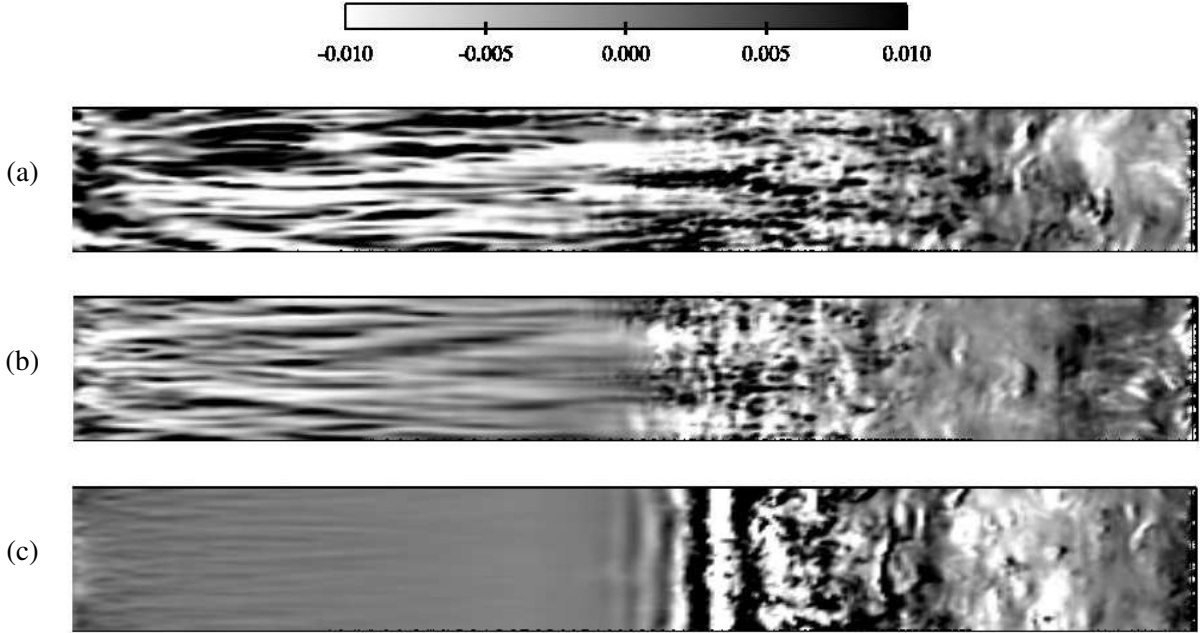


Figure 9.33: Streamwise velocity fluctuations in a plane parallel to the wall at $y^+ = 1$ for hybrid simulations with different LES inflow data: (a) SEM, (b) method of Batten et al. (2004) and (c) random method.

the random method or with Batten's method are due to the formation of large scale coherent vortices upstream of the airfoil trailing edge.

Fig. 9.36 shows the frequency spectrum of the v -fluctuations at x/h downstream of the trailing edge. A strong peak around $fh/U_0 = 0.6$ can be observed with the random method and Batten's method, indicating the presence in the flow of Kelvin-Helmotz vortices shedding in the wake of the airfoil. On the contrary the frequency spectrum in the case of the SEM does not exhibit any peak, in agreement with observations of instantaneous fluctuations in the near-wake which did not exhibit any clear vortex shedding. This is the physical behavior of the flow observed in the reference LES of Wang and Moin (2000).

9.4 Concluding Remarks

Hybrid RANS-LES simulations of the turbulent flow over a backward-facing step and over an airfoil trailing edge have been performed using several methods of generation of inlet conditions for the LES region. The different inlet conditions tested were shown to have a strong effect on the mean flow, on the turbulent statistics and on the coherent structures upstream of the recirculation, in the recirculation region and far away downstream of the recirculation.

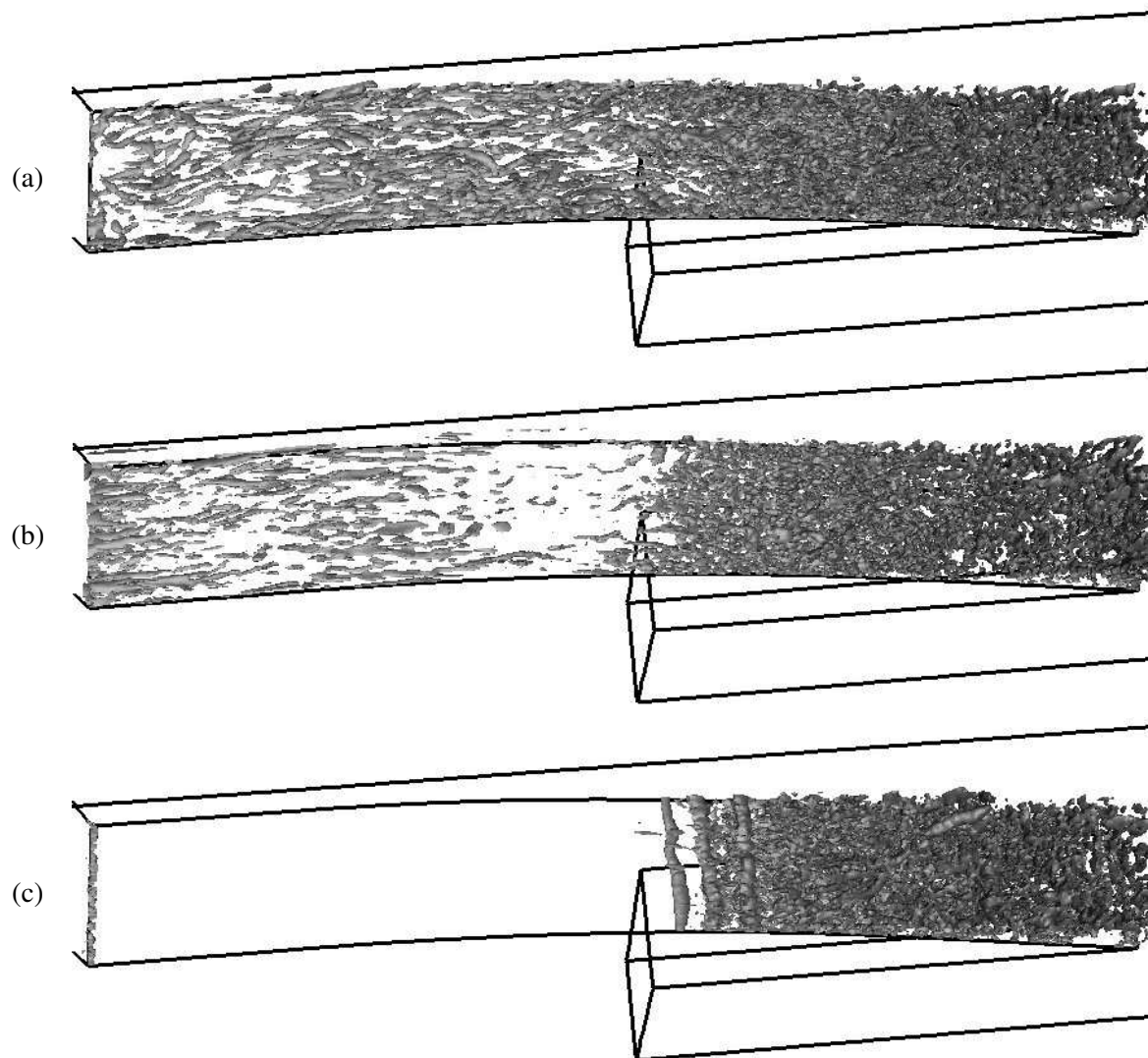


Figure 9.34: Isosurfaces $Q = 10U_0^2/h^2$ for hybrid simulations with different LES inflow data: (a) SEM, (b) method of Batten et al. (2004) and (c) random method.

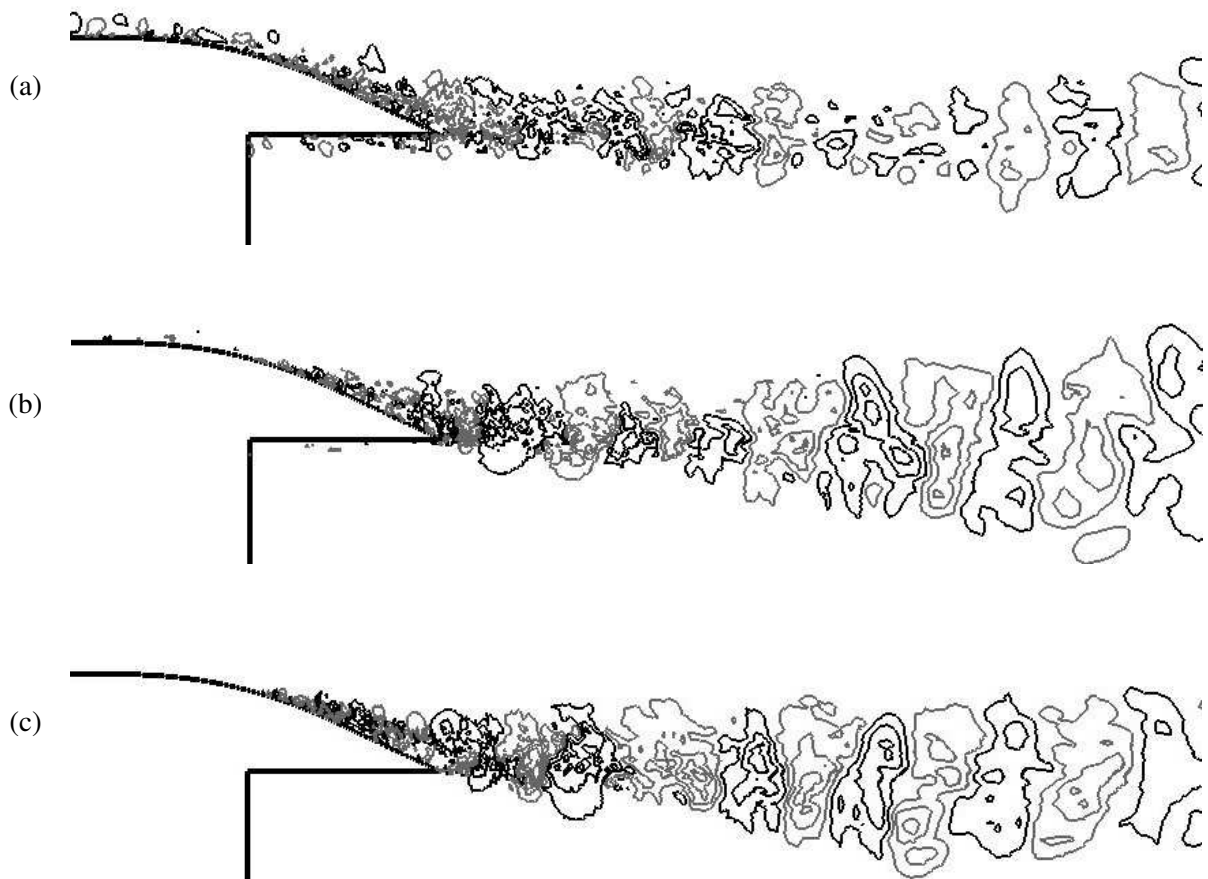


Figure 9.35: Contours of v' -velocity fluctuations with different LES inflow data: (a) SEM, (b) method of Batten et al. (2004) and (c) random method. Contour lines are evenly spaced at ± 0.05 , ± 0.015 , ± 0.025 , ± 0.035 and ± 0.045 . Grey lines indicate negative value contours.

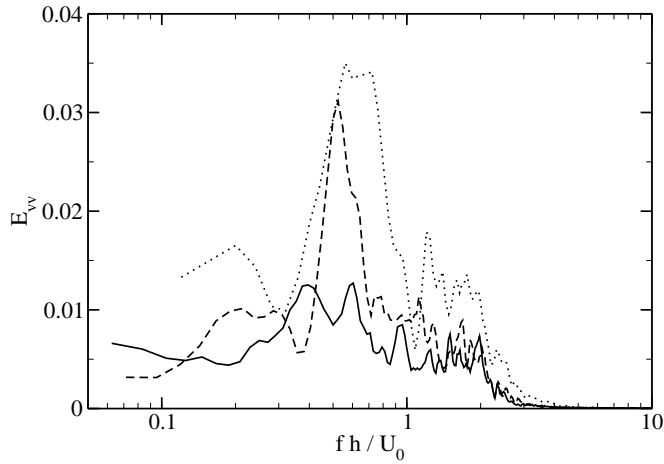


Figure 9.36: Frequency spectrum of the v fluctuations in the near wake at $x/h = 4$ and $y/h = 0.5$: —, SEM; - - -, Batten et al. (2004); and , random method.

With the random method, the fluctuations prescribed at the inlet of the LES domain are rapidly dissipated leading to an essentially laminar boundary layer immediately downstream of the inlet. In the case of the trailing edge flow, the absence of coherent structures in the boundary layer upstream of the non-equilibrium region of the flow leads to a very early separation. Both flows simulated (i.e. the backward facing step and the trailing edge flow) were characterized by the presence of a laminar separation, followed by a transitional shear-layer. The production of two-dimensional large scale Kelvin-Helmotz vortices in the shear layer was then responsible for an overestimation of the turbulent fluctuations in the downstream flow.

We saw in the previous chapter that Batten's method requires a very long transition region to generate fully developed turbulence in simple wall flows. The LES domains used in the hybrid simulations of the backward facing step and of the trailing edge flow did not allow the method to yield realistic fluctuations upstream of the region of interest. Similarly to the random method, it resulted in an overestimation of the size of the recirculation bubble which led to a higher production of Reynolds stresses, and hence an overestimation of the velocity fluctuations further away downstream of the recirculation region.

Results using the SEM were in good agreement with the reference data both for the backward facing step and the trailing edge flows. The SEM managed to generate realistic boundary layer fluctuations upstream of the region of interest which led to accurate prediction of the separation point in the case of the trailing edge and accurate predictions of the reattachment length in the case of the step. For both flows the position of the LES inlet section was shown to have little influence on the statistics in the region of

interest.

The use of smaller LES domains (without significant loss of accuracy) in the hybrid simulations using the SEM led to substantial savings in terms of number of cells used (and hence in terms of CPU time). In the case of the airfoil trailing edge, the reduction in terms of CPU time achieved with the smallest LES domain is over 40% when compared to the domain used in the reference LES of (Wang and Moin, 2000), and over 80% when compared to a full domain LES enclosing the entire airfoil.

Chapter 10

Conclusions and Future Directions

10.1 Conclusions

This thesis has described the development and validation of a new method of generation of synthetic inlet conditions for LES, the Synthetic Eddy Method (SEM).

This research was motivated by the growing interest in the engineering community in LES and hybrid RANS-LES methods, and the need for a cost effective, robust and accurate method of generation of inflow data for LES. The SEM requires as an input statistical quantities typically available from an experiment or from a RANS simulation, and synthesizes instantaneous velocity fluctuations with a prescribed mean velocity, Reynolds stresses, length and time scale distribution. The method is based on the classical view of turbulence as a superposition of eddies. The velocity signal is thus expressed as a sum of synthetic eddies with random position and intensity. The characteristics of the synthetic eddies are calculated from the input statistical quantities, and determine the characteristics of the synthesized signal. The SEM has been implemented into an unstructured finite volume code, *Code_Saturne*, with which all the simulations presented in this thesis have been performed.

A benchmark simulation using the SEM to generate inlet conditions for a LES of a spatially developing turbulent plane channel flow was first performed. Input statistics for the SEM were extracted from a periodic LES of fully developed turbulence in a channel at the same Reynolds number. It was shown that the coefficient of friction and the Reynolds stresses decay downstream of the inlet, before recovering their fully developed value. In the near-wall region, realistic turbulent structures are generated immediately downstream of the inlet, and a distance of only 10δ is required (where δ is the channel half-width) for the turbulence statistics to be in good agreement with the reference statistics. In the core of the channel however, the development length of the turbulent eddies is substantially increased (about 25δ).

A sensitivity analysis of the effect of the SEM input parameters on the turbulence downstream of the inlet in plane channel flow was then carried out. It was shown that the mean velocity, the turbulent kinetic energy, the integral length scale, and time scale all have a great influence on the development of the turbulence downstream of the inlet. The correct estimation of these physical quantities at the inlet is therefore of paramount importance to provide a LES with accurate boundary conditions.

The SEM was then used to generate inlet conditions for a LES domain using only information available from an upstream RANS simulation. Equations to compute all of the input parameters of the SEM from simple RANS statistics were proposed. This hybrid RANS-LES coupling strategy was tested on several simple wall-bounded flows (i.e. turbulent channel, boundary layer and duct flow). The SEM was systematically compared to other existing methods of generation of synthetic turbulence; the random method and the method of Batten et al. (2004). With the SEM, the development length of the eddies in the near wall region was shown to be approximately 3,000 wall units for all the cases simulated. This offers significant promise for the application of the method to high Reynolds number flows of engineering interest. With the random method, the velocity fluctuations prescribed at the inlet were immediately dissipated and the flow became laminar. With Batten's method, the use of Fourier harmonics with spatially varying wavelengths leads to a destruction of the spatial correlations of the signal in the direction of non-homogeneity of the flow. The SEM, because it uses local shape functions instead of global Fourier harmonics, is designed to generate non-homogeneous turbulence in complex geometries. Consequently with Batten's method the drop of the coefficient of friction and turbulent statistics is more severe than with the SEM, and the development length of the near-wall eddies is about three times that of the SEM.

Finally hybrid simulations of more complicated turbulent flows involving separation and reattachment (i.e. the flow over a backward facing step and over an airfoil trailing edge) were performed. With the SEM, realistic turbulence is generated upstream of the separation, and thus flow predictions downstream of the separation are in good agreement with the reference data. The LES inlet was moved to different locations upstream of the separation with the intent of reducing the size of the LES domain without altering the results. In the case of the step, good results were obtained with the inlet positioned only one step height upstream of the separation. In the case of the trailing edge, the inlet was positioned only 3 boundary layer thicknesses upstream of the location where the boundary layer experiences maximum acceleration, this without significant alteration of the results. Inlet conditions prescribed using the random method or Batten's method require a longer development length to generate realistic turbulence. The length of the LES inlet sections used in these latter cases did not allow either method to generate a realistic boundary layer upstream of the region of interest. In both cases, the lack of turbulent structures in the upstream boundary layer lead to an overestimation of the recirculation region, and hence a higher

production of turbulent kinetic energy; leading to the growth (after separation) of quasi two-dimensional structures characteristic of transitional flows.

10.2 Future Directions

The following research could be considered as direct extensions of the present work:

1. **Improvement of the SEM:** The shape function used in the simulation presented in this thesis is a tent function $f(r) = 1 - |r|$. Thus it has a non-continuous derivative at $r = 0$ and $r = \pm 1$. Spline functions are good candidates to derive a function that is easy to evaluate, and has compact support, with the prescribed smoothness properties as required by the SEM. An alternative to the tent function adopted in the present thesis could be for example, $f(r) = 2|r|^3 - 3|r|^2 + 1$, whose derivative is continuous on its support $[-1, 1]$. Another aspect of the SEM that has not been explored in this thesis is the incompressibility of the inflow data. The fluctuations generated by the SEM are not divergence-free, which is not physical and might generate spurious fluctuations in the pressure field. In order to render the inflow data divergence free, a possible simple solution would be to change the representation of the eddies in the SEM. Instead of seeing each eddy k as a velocity fluctuation $f(\mathbf{x} - \mathbf{x}^k) \epsilon^k$ along a velocity intensity vector ϵ^k , the eddies could be defined as two-dimensional vortices $(\mathbf{x} - \mathbf{x}^k) f(\mathbf{x} - \mathbf{x}^k) \times \epsilon^k$, around a vorticity intensity vector ϵ^k . Such a method has already been implemented but needs now to be tested and validated in an actual LES.
2. **Validation of the results:** In the cases of the backward facing step and of the airfoil trailing edge, the results of the hybrid calculations were compared to reference simulations which use a different turbulence model, a different code and different inlet conditions. Differences between the present simulations and the reference data might be caused by any of these aspects. Ideally the hybrid simulations using synthetic turbulence should be compared against a full domain LES or a hybrid calculation with inflow data extracted from a precursor simulation. Such simulations are under way in order to fully validate our approach.
3. **Influence of the upstream RANS model:** The present coupling methodology between an upstream SST solution and a LES solution could be extended to different RANS models (RSM, $k-\epsilon$ or Spalart and Allmaras (1992) for instance). Since different RANS models use different turbulent variables, this would probably require the derivation of new equations specific to the model used to compute the input SEM length scale.

4. **Generation of fluctuations for LES with near-wall modelling:** In the present work, the LES grids were always fine enough to discretize the near-wall structures. Detached-Eddy Simulations (DES) and other similar types of hybrid RANS-LES approaches use a RANS model in the near-wall region, and a LES model in the outer part of the flow. The reconstruction of turbulent fluctuations for such hybrid methods in the outer layer of the boundary layer has strong applications to the aeronautical industry where these types of hybrid approaches are routinely used. Deck et al. (2007) have successfully implemented and used the SEM to generate turbulent fluctuations for DES of a spatially developing boundary layer.
5. **Better integration of all boundary conditions in a general zonal RANS-LES coupling framework:** The coupling of a steady RANS solution with a downstream unsteady LES solution has been treated in this thesis. In order to further reduce the size of the LES domain, the problem of interfacing LES with a downstream RANS region (and thus the effect of the LES outlet conditions on the flow inside of the LES domain) should also be investigated. Possible solutions to this problem have recently been proposed by Quéméré and Sagaut (2002) or von Terzi et al. (2007).
6. **Further applications:** The SEM has already been tested and validated in a wide variety of turbulent flows. Further applications in aeronautics could include airfoils with camber (Moreau et al., 2006) and/or trailing edge aeroacoustics (Terracol, 2005). In nuclear power plant, the effect of the SEM on problems involving heat transfer and wall-temperature fluctuations predictions in complex hydraulic systems where an embedded LES approach is necessary could also be investigated (Peniguel et al., 2003). Other current applications of the SEM apart from RANS-to-LES coupling also include the reconstruction of turbulent fluctuations to simulate the flow around tidal turbine devices (Gant and Stallard, 2008). This work represents the first stage in the development of a coupling strategy between meta-scale simulations of environmental flows in an estuary or downstream from a submerged island (Stansby, 2003), and detailed small-scale simulations of the flow around the tidal turbine device.

Bibliography

- K. Adams. DNS of shock boundary-layer interaction - preliminary results for compression ramp flow. *CTR Annual Research Briefs, Stanford Univ.*, pages 329–338, 1997.
- Y. Addad, D. Laurence, C. Talotte, and M.C. Jacob. Large eddy simulation of a forward-backward facing step for acoustic source identification. *International Journal of Heat and Fluid Flow*, 24:562–571, 2003.
- J-L. Aider and A. Danet. Large-eddy simulation study of upstream boundary conditions influence upon a backward-facing step flow. *Comptes Rendus Mecanique*, 334(7):447–453, 2006.
- K. Akselvoll and P. Moin. Large-eddy simulation of turbulent confined coannular jets. *Journal of Fluid Mechanics*, 315:387–411, 1996.
- R.A. Antonia, M. Teitel, J. Kim, and L.J.B. Browne. Low Reynolds-number effects in a fully developed turbulent channel flow. *Journal of Fluid Mechanics*, 236:579–605, 1992.
- F. Archambeau, N. Mechitoua, and M. Sakiz. A finite volume method for the computation of turbulent incompressible flows - industrial applications. *International Journal on Finite Volumes*, 1(1), 2004.
- J.S. Baggett, J. Jimenez, and A.G. Kravchenko. Resolution requirements in large-eddy-simulations of shear flows. In *Annual research briefs*, pages 51–66. Center for turbulence research, Stanford, CA, 1997.
- E. Balaras, C. Benocci, and U. Piomelli. Two-layer approximate boundary conditions for large eddy simulations. *AIAA Journal*, 34:1111–1119, 1996.
- J. Bardina, J Ferziger, and W. Reynolds. Improved subgrid-scale models for large-eddy simulations. *AIAA Paper*, 4:80–1357, 1980.
- P. Batten, U. Goldberg, and S. Chakravarty. Interfacing statistical turbulence closures with large-eddy simulation. *AIAA Journal*, 42, 2004.

- W.K. Blake. A statistical description of pressure and velocity fields at the trailing edge of a flat strut. *David Taylor Naval Ship Research and Development Center, Report 241, Bethesda, Maryland*, 1975.
- M. Breuer and W. Rodi. Large-eddy simulation of turbulent flow through a straight square duct and a 180° bend. In P. Voke, R. Kleiser, and J. Chollet, editors, *Direct and Large Eddy Simulation I*, volume 26 of *Fluid Mechanics and its Applications*, pages 273–285, Munich, Germany, 2007.
- A. Brunn and W. Nitsche. Active control of turbulent separated flows over slanted surfaces. *International Journal of Heat and Fluid Flow*, 27:748–755, 2006.
- I.B. Celik, Z.N. Cehreli, and I. Yavuz. Index of resolution quality for large eddy simulations. *Journal of Fluids Engineering*, 127:949–958, 2005.
- B. Chaouat and R. Schiestel. A new partially integrated transport model for subgrid-scale stresses and dissipation rate for turbulent developing flows. *Physics of Fluids*, 17:1–19, 2005.
- D. Chapman. Computational aerodynamics development and outlook. *AIAA Journal*, 17:1293–1313, 1979.
- M.S. Chong, J. Soria, A.E. Perry, J. Chacin, B.J. Cantwell, and Y. Na. Turbulence structures of wall-bounded shear flows found using DNS data. *Journal of Fluid Mechanics*, 357:225–247, 1998.
- Y.M. Chung and H.J. Sung. Comparative study of inflow conditions for spatially evolving simulation. *AIAA Journal*, 35(2):269–274, 1997.
- D.E. Coles. The law of the wake in a turbulent boundary layer. *Journal of Fluid Mechanics*, 1, 1956.
- J. Dandois, E. Garnier, and P. Sagaut. Numerical simulation of active separation control by a synthetic jet. *Journal of Fluid Mechanics*, 574:25–58, 2007.
- L. Davidson. Using isotropic synthetic fluctuations as inlet boundary conditions for unsteady simulations. *Advances and Applications in Fluid Mechanics*, 1(1):1–35, 2007a.
- L. Davidson. Hybrid LES-RANS: Inlet boundary conditions for flows including recirculation. In *Proceedings of the 4th Int. Symp. on Turbulence and Shear Flow Phenomena*, volume 2, pages 689–694, Munich Germany, 2007b.
- L. Davidson and M. Billson. Hybrid RANS-LES using synthetized turbulence for forcing at the interface. In P. Neittaanmäki, T. Rossi, S. Korotov, E. Oñate, J. Périaux, and D. Knörzer, editors, *ECCOMAS*, 2004.

- L. Davidson and S. Dahlström. Hybrid LES-RANS: An approach to make LES applicable at high Reynolds number. *International journal of computational fluid dynamics*, 19:415–427, 2005.
- L. Davidson, D. Cokljat, J. Frohlich, M Leschziner, C. Mellen, and W. Rodi. Large-eddy simulation of flow around a high lift airfoil. Results of the project LESFOIL supported by the European Union 1998-2001. *Notes on Numerical Fluid Mechanics and Multiplidisciplinary Design*, 83, 2003.
- G. De Prisco, A. Keating, and U. Piomelli. Large-eddy simulation of accelerating boundary layers. In *AIAA Paper 2007-0725*, Reno, Nevada, June 2007.
- R.B. Dean. Reynolds number dependence of skin friction and other bulk flow variables in two-dimensional rectangular duct flow. *Trans. ASME I : Journal of Fluids Engineering*, 100:215, 1978.
- J.W. Deardorff. A numerical study of three-dimensional turbulent channel flow at large Reynolds numbers. *Journal of Fluid Mechanics*, 41:453–480, 1970.
- S. Deck, P.E. Weiss, M. Pamies, and E. Garnier. On the use of stimulated detached eddy simulation for spatially developing boundary layers. In *2nd Hybrid RANS-LES Symposium*, Corfu, Greece, 17-18 June 2007.
- J.C. del Alamo, J. Jimenez, P. Zandonade, and R.D. Moser. Scaling of the energy spectra of turbulent channels. *Journal of Fluid Mechanics*, 500:135–144, 2004.
- A.O. Demuren and W. Rodi. Calculation of turbulence-driven secondary motion in non-circular ducts. *Journal of Fluid Mechanics*, 140:189, 1984.
- J.M.J den Toonder and F.T.M. Nieuwstadt. Reynolds number effect in a turbulent pipe flow for low to moderate Re. *Physics of Fluids*, 9(11):3398–3409, 1997.
- L. di Mare, M. Klein, W.P. Jones, and J. Janicka. Synthetic turbulence inflow conditions for large-eddy simulation. *Physics of Fluids*, 18, 2006.
- P. Druault, S. Lardeau, Bonnet J.-P., F. Coiffet, J. Delville, E. Lamballais, J.F. Largeau, and L. Perret. Generation of three-dimensional turbulent inlet conditions for large-eddy simulation. *AIAA Journal*, 42(3):447–456, 2004.
- Y. Dubief and F. Delcayre. On coherent-vortex identification in turbulence. *Journal of Turbulence*, 11, 2000.

- P. A. Durbin. Near-wall turbulent closure modelling without damping functions. *Theoretical and computational fluid dynamics*, pages 1–13, 1991.
- J. Eggers and S. Grossmann. Effect of dissipation fluctuations on anomalous velocity scaling in turbulence. *Physical Review A*, 45(4):2360–2369, 1992.
- A. Ferrante and S.E. Elghobashi. A robust method for generating inflow conditions for direct simulation of spatially developing turbulent boundary layers. *Journal of Computational Physics*, 198:372–387, 2004.
- J.H. Ferziger and M. Perić. *Computational Methods for Fluid Dynamics*. Springer, New York, 1999.
- R. Friedrich and M. Arnal. Analysing turbulent backward-facing step flow with the lowpass-filtered Navier-Stokes equation. *Journal of Wind Engineering and its Applications*, 35:101–128, 1990.
- J.C. Fung, J.C. Hunt, N.A. Malik, and R.J. Perkins. Kinematic simulation of homogeneous turbulence by unsteady random Fourier modes. *Journal of Fluid Mechanics*, 236:281–318, 1992.
- S Gant and T. Stallard. Modelling a tidal turbine in unsteady flow. In *ISOPe conference*, Vancouver, Canada, July 2008.
- W.K. George and L. Davidson. Role of initial conditions in establishing asymptotic flow behavior. *AIAA Journal*, 42(3):438–446, 2004.
- M. Germano, U. Piomelli, P. Moin, and W. H. Cabot. A dynamic subgrid scale eddy viscosity model. *Physics of fluids*, 3:1760, 1991.
- D.J. Glaze and H. Frankel. Stochastic inlet conditions for large-eddy simulation of a fully turbulent jet. *AIAA Journal*, 41(6):1064–1073, 2003.
- R.R. Grinstein, E.J. Gutmark, T.P. Parr, D.M. Hanson-Parr, and U. Obeysekare. Streamwise and spanwise vortex interaction in an axysymmetric jet. a computational and experimental study. *Physics of Fluids*, 8(6):1515–1524, 1996.
- R.A. Handler, E. Levich, and L. Sirovich. Drag reduction in turbulent channel flow by phase randomization. *Physics of Fluids A*, 5(3):686–694, 1993.
- K. Hanjalic. Will RANS survive LES? A view of perspectives. *Journal of Fluids Engineering*, 127:831–839, 2005.

- M.R. Head and P. Bandyopadhyay. New aspects of turbulent boundary-layer structure. *Journal of Fluid Mechanics*, 107:297–338, 1981.
- P. Holmes, J.L. Lumley, and G. Berkooz. *Turbulence, Coherent Structures, Dynamical Systems and Symmetry*. Cambridge University Press, New-York, 1996.
- S. Hoyas and J. Jimenez. Scaling of the velocity fluctuations in turbulent channels up to $Re_\tau = 2003$. *Physics of fluids*, 18, 2006.
- X. Huai, R.D. Joslin, and U. Piomelli. Large-eddy simulation of boundary layer transition on a swept fence. *Journal of Fluid Mechanics*, 381:357–380, 1999.
- A. Huser and S. Biringen. Direct numerical simulation of turbulent flow in a square duct. *Journal of Fluid Mechanics*, 257:65–95, 1993.
- K. Iwamoto, Y. Suzuki, and N. Kasagi. Reynolds number effect on wall turbulence: Towards effective feedback control. *International Journal of Heat and Fluid Flow*, 23:678–689, 2002.
- K. Jansen. Large-eddy simulation of flow around a NACA 4412 airfoil using unstructured grids. *Annual Research Briefs, CTR, Stanford, USA*, pages 225–232, 1996.
- J. Jimenez and A. Pinelli. The autonomous cycle of near-wall turbulence. *Journal of Fluid Mechanics*, 389, 1999.
- J. Jimenez and A.A. Wray. On the characteristics of vortex filaments in isotropic turbulence. *Journal of Fluid Mechanics*, 373, 1988.
- P.S. Johansson and H.I. Andersson. Generation of inflow data for inhomogeneous turbulence. *Theoretical Computational Fluid Dynamics*, 18:371–389, 2004.
- W.P. Jones and B.E. Launder. The prediction of laminarization with a two-equation model of turbulence. *International Journal of Heat Mass Transfer*, pages 301–314, 1972.
- S. Jovic and D. Driver. Backward-facing step measurement at low Reynolds number, $Re_h = 5000$. *NASA Tech. Mem.*, 108807, 1994.
- H.J Kaltenbach, M. Fatica, R. Mittal, T.S. Lund, and P. Moin. Study of flow in a planar asymmetric diffuser using large eddy simulation. *Journal of Fluid Mechanics*, pages 151–185, 1999.
- A. Keating and U. Piomelli. A dynamic stochastic forcing method as a wall layer model for large-eddy simulation. *Journal of Turbulence*, 7(12):1–24, 2006.

- A. Keating, U. Piomelli, E. Balaras, and H-J. Kaltenbach. *A priori* and *a posteriori* test of inflow conditions for large-eddy simulation. *Physics of Fluids*, 16, 2004.
- A. Keating, G. De Prisco, U. Piomelli, and E. Balaras. Interface conditions for hybrid RANS/LES calculations. In W. Rodi and M. Mulas, editors, *Engineering Turbulence Modelling and Experiments 6*, Sardinia, Italy, 23-25 May 2005 2005.
- A. Keating, G. De Prisco, and U. Piomelli. Interface conditions for hybrid RANS/LES calculations. *International Journal of Heat and Fluid Flow*, 27, 2006.
- J. Kim, S.J. Kline, and W.C. Reynolds. The production of turbulence near a smooth wall in a turbulent boundary layer. *Journal of Fluid Mechanics*, 50:133–160, 1971.
- J. Kim, P. Moin, and R. Moser. Turbulence statistics in fully developed channel flow at low Reynolds number. *Journal of Fluid Mechanics*, 177:133–166, 1987.
- M. Klein, A. Sadiki, and J. Janicka. A digital filter based generation of inflow data for spatially developing direct numerical or large-eddy simulations. *Journal of Computational Physics*, 186:652–665, 2003.
- A.N. Kolmogorov. The equations of turbulent motion in an incompressible fluid. *Izvestia Acad. Sci., USSR; Phys.*, 6:56–58, 1942.
- A.N. Kolmogorov. The local structure of turbulence in incompressible viscous fluid for very large Reynolds number. *Dokl. Akad. Nauk SSSR*, 30:301–305, 1941.
- K. Kondo, S. Murakami, and A. Mochida. Generation of velocity fluctuations for inflow boundary conditions of LES. *Journal of Wind Engineering and Industrial Aerodynamics*, 67 & 68:51–64, 1997.
- A. Kourta and H. Minh. Semi-deterministic turbulence modelling for flows dominated by strong organized structures. In *Proc. 9th Int. Symp. on Turb. Shear Flows*, pages 1–6, Kyoto, Japan, 1993.
- R.H. Kraichnan. Diffusion by a random velocity field. *Physics of Fluids*, 13(1):22–31, 1969.
- A. Kravchenko, P. Moin, and R.D. Moser. Zonal embedded grids for numerical simulations of wall-bounded turbulent flows. *Journal of Computational Physics*, 127:412–423, 1996.
- E. Labourasse and P. Sagaut. Reconstruction of turbulent fluctuations using a hybrid RANS/LES approach. *Journal of computational physics*, 182:301–336, 2002.
- B. E. Launder and B. I. Sharma. Applications of energy-dissipation model of turbulence to the calculation of flow near a spinning disc. *Letters in Heat and Mass Transfer*, pages 131–138, 1974.

- B.E. Launder, G.J. Reece, and W. Rodi. Progress in the development of a Reynolds-stress turbulent closure. *Journal of Fluid Mechanics*, pages 537–566, 1975.
- H. Le, P. Moin, and J. Kim. Direct numerical simulation of turbulent flow over backward-facing step. *Journal of Fluid Mechanics*, 330:349–373, 1997.
- S. Lee, S.K. Lele, and P. Moin. Simulation of spatially evolving turbulence and the applicability of Taylor’s hypothesis in compressible flow. *Physics of Fluids A*, 4(7):1521–1530, 1992.
- M. Lesieur. *Turbulence in fluids, Thirs revised and enlarged edition*. Kluwer Academic Publishers, 1997.
- M. Lesieur and R. Rogallo. Large-eddy simulation of passive scalar diffusion in isotropic turbulence. *Physics of Fluids A*, 1:718–722, 1989.
- N. Li, E. Balaras, and U. Piomelli. Inflow conditions for large-eddy simulation of mixing layers. *Physics of Fluids*, 12(4):935–938, 2000.
- D.K. Lilly. The representation of small scale turbulence in numerical simulation experiments. In *IBM Scientific Computing Symposium on environmental sciences*, pages 195–210, Yorktown heights, 1967.
- J.L. Lumley. *Stochastic tools in turbulence*. Academic Press, New-York and London, 1970.
- T. Lund, X. Wu, and D. Squires. Generation of turbulent inflow data for spatially-developing boundary layer simulations. *Journal of Computational Physics*, 140:233–258, 1998.
- T.S. Lund and H.-J. Kaltenbach. Experiments with explicit filtering with LES using a finite difference method. *CTR Annual Research Briefs, Stanfort Univ.*, pages 91–105, 1995.
- C. Meneveau, T. Lund, and W. Cabot. A Lagrangian dynamic subgrid-scale model of turbulence. *Journal of Fluid Mechanics*, 319:353–385, 1996.
- F.R. Menter. Two-equation eddy-viscosity turbulence models for engineering applications. *AIAA Journal*, pages 1598–1605, 1994.
- F.R. Menter and Y. Egorov. Turbulence models based on the length-scale equation. In *Turbulence and Shear Flow Phenomena 4*, pages 941–946, Williamsburg, Virginia, 2005.
- P. Moin and J. Kim. Numerical investigation of turbulent channel flow. *Journal of fluid mechanics*, 118:341–377, 1982.

- P. Moin and R.D. Moser. Characteristic-eddy decomposition of turbulence in a channel. *Journal of Fluid Mechanics*, 200:471–509, 1989.
- S. Moreau, D. Neal, Y. Khalighi, M. Wang, and G. Iaccarino. Validation of unstructured-mesh LES of the trailing edge flow and noise of a controlled-diffusion airfoil. In *Centre for Turbulence Research, Proceedings of the Summer Program*, Stanford University, California, July 2006.
- R. Moser, J. Kim, and N. Mansour. Direct numerical simulation of turbulent channel flow up to $Re_\tau = 590$. *Physics of Fluids*, 11:943–945, 1999.
- S. Muzaferija and D. Gosman. Finite-volume CFD procedure and adaptive error control strategy for grids of arbitrary topology. *Journal of Computational Physics*, 138:766–787, 1997.
- Y. Na and P. Moin. Direct numerical simulation of a separated turbulent boundary layer. *Journal of Fluid Mechanics*, 374:379–405, 1998.
- B. Niceno, A.D.T. Dronkers, and K. Hanjalic. Turbulent heat transfer from a multi-layered wall-mounted cube matrix: an les. *International Journal of Heat and Fluid Flow*, 23:173–185, 2002.
- F. Nicoud and F. Ducros. Subgrid-scale stress modelling based on the square of the velocity gradient tensor. *Flow, Turbulence and Combustion*, 62(3):183–200, 1999.
- N.V. Nikitin, F. Nicoud, B. Wasistho, K.D. Squires, and P. Spalart. An approach to wall modelling in large eddy simulations. *Physics of fluids*, 10:1629–1632, 2000.
- S.A. Orszag and G.S. Patterson. Numerical simulation of three-dimensional homogeneous isotropic turbulence. *Phys. Rev. Letters*, 28:76–79, 1972.
- C. Peniguel, M. Sakiz, S. Benhamadouche, J.M. Stephan, and C. Vindedirhno. Presentation of a numerical 3D approach to tackle thermal striping in a PWR nuclear plant T-junction. In *ASME Pressure Vessels and Piping Conference*, Cleveland, Ohio, USA, July 20-24 2003.
- U. Piomelli. High Reynolds number calculations using the dynamics subgrid-scale stress model. *Physics of fluids A*, 5:1484–1490, 1991.
- U. Piomelli and J. Liu. Large-eddy simulation of rotating channel flows using a localized dynamic model. *Physics of Fluids*, 4:839–848, 1995.
- U. Piomelli, E. Balaras, E. Pasinato, K.D. Squire, and P. Spalart. The inner-outer later interface in large eddy simulation with wall layer models. *Interntional journal of heat and fluid flow*, 23:538–550, 2003.

- U. Piomelli, S. Kang, F. Ham, and G. Iaccarino. Effect of discontinuous filter width in large-eddy simulations of plane channel flow. *CTR, Proceedings of the Summer Program*, pages 151–162, 2006.
- S. Pope. *Turbulent flows*. Cambridge University Press, Cambridge, 2000.
- L. Prandtl. Bericht über die entstehung der turbulenz. *Z. Angew. Math. Mech.*, 5:136–139, 1925.
- W.H. Press, S.A. Teukolsky, W.T. Vetterling, and B.P. Flannery. *Numerical Recipes, The Art of Scientific Computing, Third Edition*. Cambridge University Press, New-York, 2007.
- P. Quéméré and P. Sagaut. Zonal multi-domain RANS/LES simulations of turbulent flows. *International Journal of Numerical Methods in Fluids*, 40:903–925, 2002.
- M.M. Rai and P. Moin. Direct numerical simulation of transition and turbulence in a spatially evolving boundary layer. *Journal of Computational Physics*, 109:169, 1993.
- W.C. Reynolds. The potential and limitations of direct and large-eddy simulations. In *Whither turbulence? Turbulence at the crossroads*, pages 313–342. E. Lumley, Ed. Springer-Verlag, 1990.
- C. M. Rhie and W. L. Chow. Numerical study of a turbulent flow past an airfoil with trailing edge separation. *AIAA journal*, 21:1525–1532, 1983.
- L.F. Richardson. *Weather prediction by numerical process*. Cambridge university Press, 1922.
- S.K. Robinson. Coherent motion in the turbulent boundary layer. *Annual Review of Fluid Mechanics*, 23: 601–639, 1991.
- R.S. Rogallo. Numerical experiments in homogeneous turbulence. *Nasa TM-81315*, 1981.
- M.M. Rogers and R.D. Moser. The three dimensional evolution of a plane mixing layer: the Kelvin-Helmholtz roll-up. *Journal of Fluid Mechanics*, 243:183–226, 1992.
- P. Sagaut. *Large Eddy Simulation for Incompressible Flows*. Springer, Berlin, 2001.
- P. Sagaut. Numerical simulations of separated flows with subgrid models. *La Recherche Aerospatiale*, pages 51–63, 1996.
- P. Sagaut, E. Garnier, E. Tromeur, L. Larcheveque, and E. Labourasse. Turbulent inflow conditions for LES of compressible wall bounded flows. *AIAA Journal*, 42(3), 2004.
- N.D. Sandham, Y.F. Yao, and A.A. Lawal. Large-eddy simulation of transonic turbulent flow over a bump. *International Journal of Heat and Fluid Flow*, 24:584–595, 2003.

- J.U. Schlüter, H. Pitsch, and P. Moin. Large-eddy simulation inflow conditions for coupling with Reynolds-averaged flow solvers. *AIAA Journal*, 42(3):478–484, 2004.
- U. Schumann. Subgrid scale model for finite difference simulations of turbulent flows in plane channels and annuli. *Journal of computational physics*, 18:676–404, 1975.
- E. Sergent. *Vers une Methodologie de Couplage entre la Simulation des Grandes Echelles et les Modeles Statistiques, PhD Thesis*. Ecole Centrale de Lyon, Lyon, France, 2002.
- J. Smagorinsky. General circulation experiments with the primitive equations: I The basic equations. *Monthly Weather Review*, 91:99–164, 1963.
- A. Smirnov, S. Shi, and I.B. Celik. Random flow generation technique for large-eddy simulations and particle-dynamics modeling. *Journal of Fluids Engineering*, 123:359–371, 2001.
- P. Spalart. Direct numerical simulation of a turbulent boundary layer up to $Re_\theta = 1410$. *Journal of Fluid Mechanics*, 187:61–98, 1988.
- P. Spalart, W. Jou, M. Strelets, and S. Allmaras. Comments of feasibility of LES for wings, and on a hybrid RANS/LES approach. In *International Conference on DNS/LES, Aug. 4-8, 1997, Ruston, Louisiana.*, 1997.
- P. Spalart, M. Strelets, and A. Travin. Direct numerical simulation of large-eddy breakup devices in a boundary layer. *International Journal of Heat and Fluid Flow*, 27:902–910, 2006.
- P.R. Spalart. Topics in detached-eddy simulation. In *Computational Fluid Dynamics 2004: Proceedings of the third international conference on computational fluid dynamics, ICCFD03*, Toronto, 12-16 July 2004. Springer Berlin Heidelberg.
- P.R. Spalart and S.R. Allmaras. A one equation turbulence model for aerodynamic flows. *AIAA Journal*, 94-439, 1992.
- P.R. Spalart and J.H. Watmuff. Experimental and numerical study of a turbulent boundary layer with pressure gradients. *Journal of Fluid Mechanics*, 249:337–371, 1992.
- C.G. Speziale. Turbulence modeling for time-dependant RANS and VLES: a review. *AIAA Journal*, 26: 179–184, 1998.
- C.G. Speziale, S.Sarkar, and T.B. Gatski. Modelling the pressure-strain correlation of turbulence: an invariant dynamical system approach. *Journal of Fluid Mechanics*, pages 245–272, 1991.

- A. Spille and H-J. Kaltenbach. Generation of turbulent inflow data with a prescribed shear-stress profile. In C. Liu, L Sakell, and T. Beutner, editors, *Third AFSOR Conference on DNS and LES*, Arlington TX, 5-9 August 2001.
- P.K. Stansby. A mixing-length model for shallow turbulent wakes. *Journal of Fluid Mechanics*, 495: 369–384, 2003.
- S. Stolz and N.A. Adams. An approximate deconvolution procedure for large-eddy simulation. *Physics of Fluids*, 11:1699–1701, 1999.
- L. Temmerman. *Large Eddy Simulation of separating flows from curved surfaces*. PhD thesis, Queen Mary University of London, 2004.
- L. Temmerman, M.A. Leschziner, C.P. Mellen, and J. Frohlich. Investigation of wall-function approximations and subgrid-scale models in large eddy simulation of separated flow in a channel with streamwise periodic constrictions. *International Journal of Heat and Fluid Flow*, 24, 2003.
- H. Tennekes and J.L. Lumley. *A first course in turbulence*. MIT Press, 1972.
- M. Terracol. Airframe noise prediction by mean of a zonal RANS/LES approach. In *Turbulence and Shear Flow Phenomena 4*, pages 1165–1169, Williamsburg, Virginia, USA, 27-29 June 2005.
- A.A. Townsend. *The structure of Turbulent Shear Flows, 2nd ed.* Cambridge University Press, New-York, 1976.
- J. Uribe, N. Jarrin, R. Prosser, and D. Laurence. Two-velocities hybrid RANS/LES of a trailing edge flow. In *IUTAM Symposium on Unsteady Separated Flows and their Control*, Corfu, Greece, 2007.
- J.P. Van Doormal and G. D. Taithby. Enhancement of the SIMPLE method for predicting incompressible fluid flows. *Numerical Heat transfer*, 7:147–163, 1984.
- E. R. Van Driest. On turbulent flow near a wall. *J. Aerospace Sci.*, 23:1007–1011, 1956.
- M. Van Dyke. *An Album of Fluid Motion*. The Parabolic Press, Stanford, California, 1982.
- I. Veloudis, Z. Yang, J.J Mc Guirk, and G.J. Page. Assessment of the digital filter approach for generating large eddy simulation inlet conditions. In W. Rodi, editor, *Engineering Turbulence Modelling and Experiments 6*, pages 307–316, Sardinia, Italy, 23-25 May 2005.
- T. von Karman. Mechanische ahnlichkeit und turbulenz. In *Proc. Third Int. Congr. Applied Mechanics*, pages 85–105, 1930.

- D.A. von Terzi, W. Rodi, and J. Frohlich. Scrutinizing velocity and pressure coupling conditions for LES with downstream RANS calculations. In S.-H. Peng and W. Haase, editors, *Notes on Numerical Fluid Mechanics and Multidisciplinary Design: Advances in Hybrid RANS-LES Modelling*, volume 97, Corfu, Greece, 2007. Springer.
- B. Vreman, B. Geurts, and H. Kuerten. Large-eddy simulation of the turbulent mixing-layer. *Journal of Fluid Mechanics*, 339:357–390, 1997.
- M. Wang. Progress in LES of trailing-edge turbulence and aeroacoustics. In *Annual research briefs*. Center for turbulence research, Stanford, CA, 1997.
- M. Wang and P. Moin. Computation of trailing-edge flow and noise using large-eddy simulation. *AIAA Journal*, 38:2201–2209, 2000.
- D.C. Wilcox. *Turbulence Modelling for CFD*. DCW industries, 1993.
- W. Yoshizawa. Statistical theory for compressible shear flows with the application of subgrid modelling. *Physics of Fluids*, 29(7):2152–2164, 1986.